

**Magnetic Correlations  
in  
Ruddlesden-Popper Ruthenates**

Inaugural-Dissertation

zur

Erlangung des Doktorgrades  
der Mathematisch-Naturwissenschaftlichen Fakultät  
der Universität zu Köln

vorgelegt von  
**Kevin Jenni**  
aus Trier

Köln, 2021

Diese Arbeit stellt eine von der Mathematisch-Naturwissenschaftlichen Fakultät der Universität zu Köln angenommene Dissertation dar.

Berichtersteller:

Prof. Dr. Markus Braden  
Prof. Dr. Markus Grüninger

Vorsitzender der Prüfungskommission:

Prof. Dr. Simon Trebst

Tag der mündlichen Prüfung:

10.12.2021

# Contents

<b>1</b>	<b>Introduction: Ruddlesden-Popper Ruthenates</b>	<b>1</b>
<b>2</b>	<b>SrRuO<sub>3</sub>: Impact of Spin-orbit Coupling on Magnetic Excitations</b>	<b>7</b>
2.1	Magnon Dispersion . . . . .	7
2.1.1	Introduction . . . . .	7
2.1.2	Results and Analysis . . . . .	8
2.1.3	Section Summary . . . . .	20
2.2	Fingerprint of Weyl Fermions in Spin Excitations . . . . .	21
2.2.1	Introduction . . . . .	21
2.2.2	Contribution to Publication and its Relevance in Thesis . . . . .	21
2.2.3	Publication . . . . .	23
2.3	Chirality of Spin Excitations . . . . .	29
2.3.1	Introduction . . . . .	29
2.3.2	Results and Analysis . . . . .	31
2.3.3	Section Summary . . . . .	40
2.4	Discussion . . . . .	42
2.5	Methods . . . . .	44
<b>3</b>	<b>Ca<sub>2</sub>RuO<sub>4</sub>: Entanglement of Structural, Electronic, and Magnetic Properties</b>	<b>51</b>
3.1	Current-Induced Insulator-Metal Transition . . . . .	51
3.1.1	Introduction . . . . .	51
3.1.2	Contribution to Publication and its Relevance in Thesis . . . . .	52
3.1.3	Publication . . . . .	53
3.2	Magnetic Correlations and Oxygen Moment . . . . .	64
3.2.1	Introduction . . . . .	64
3.2.2	Results and Analysis . . . . .	65
3.2.3	Section Summary . . . . .	70
3.3	Discussion . . . . .	71
3.4	Methods . . . . .	73
<b>4</b>	<b>Sr<sub>2</sub>RuO<sub>4</sub>: Characteristics of Magnetic Fluctuations</b>	<b>77</b>
4.1	Introduction . . . . .	77
4.2	Contribution to Publication and its Relevance in Thesis . . . . .	79
4.3	Publication . . . . .	80
4.4	Methods . . . . .	90
<b>5</b>	<b>Sr<sub>2</sub>Ru<sub>1-y</sub>Co<sub>y</sub>O<sub>4</sub>: Search for Magnetic Order</b>	<b>93</b>
5.1	Introduction . . . . .	93
5.2	Results and Analysis . . . . .	95

5.3	Discussion . . . . .	101
5.4	Methods . . . . .	103
<b>6</b>	<b>Experimental Methods</b>	<b>109</b>
6.1	Crystal Growth of layered Ruthenates . . . . .	110
6.1.1	Powder Sintering . . . . .	110
6.1.2	Mirror Furnace . . . . .	111
6.1.3	Sample Characterization . . . . .	112
6.2	Neutron Scattering . . . . .	115
6.2.1	Basics . . . . .	115
6.2.2	Polarization Analysis . . . . .	117
6.2.3	Triple-Axis Spectrometer . . . . .	123
6.2.4	Time-of-Flight Spectrometer . . . . .	125
<b>A</b>	<b>Appendix</b>	<b>127</b>
A.1	Phonons in SrRuO <sub>3</sub> . . . . .	127
A.2	Spin-density wave dynamics in Ca <sub>2-x</sub> Sr <sub>x</sub> RuO <sub>4</sub> . . . . .	130
	<b>Bibliography</b>	<b>133</b>
	<b>Abstract</b>	<b>145</b>
	<b>Kurzzusammenfassung</b>	<b>147</b>
	<b>List of Publications</b>	<b>149</b>
	<b>Danksagung</b>	<b>151</b>
	<b>Erklärung</b>	<b>153</b>

# Introduction: Ruddlesden-Popper Ruthenates

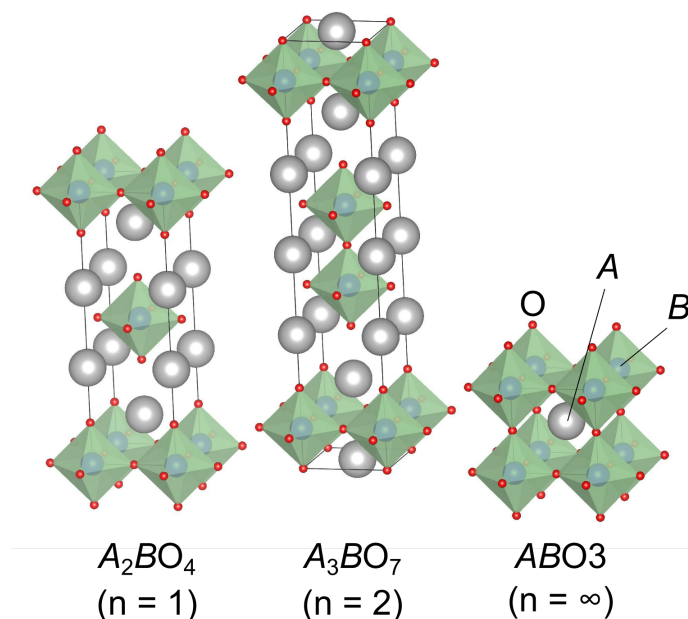


**Figure 1.1: Schematic representation of the layered crystal structures in the Ruddlesden-Popper oxides.** For the ruthenate series B represents Ru which can partly substituted with Ti or Co for example to study the characteristics of the parent compound. Depending on the (Ca,Sr) composition at position A the ruthenates exhibit a variety of magnetic, electronic and structural properties.

Historically the intense research of ruthenates was motivated by the discovery of high- $T_C$  superconductivity in  $(La,Ba)_2CuO_4$  cuprates by Bednorz and Müller in 1986 [1]. Following this discovery the question was asked if the Cu is necessary to trigger high-temperature superconductivity in oxides or it can also be achieved using other elements like Ti or Ru. Polycrystalline ruthenates with the three-dimensional perovskite structure  $(Ca,Sr,La)RuO_3$  were studied in 1988 by Maeno and Bednorz. The focus shifted then more to ruthenates with layered structure following the scheme of the series  $A_{n+1}B_nO_{3n+1}$ . This so-called Ruddlesden-Popper series was established by Ruddlesden and Popper in 1957 and 1958 in the Sr-Ti-O system [2, 3]. The structures follow a changing stacking scheme of the  $RuO_2$  layers (see Figure 1.1). Different layered ruthenates were synthesized from which first single crystals of the  $n = 1$  member of the Ruddlesden-Popper series  $Sr_2RuO_4$  were suc-

cessfully grown using the floating zone method [4]. In 1994, Maeno *et al.* measured the low temperature resistivity and susceptibility with these crystals and discovered superconductivity in the Cu-free oxide  $\text{Sr}_2\text{RuO}_4$  [5].

This discovery led to the beginning of an intense research of the Ruddlesden-Popper ruthenates to investigate and understand the mechanism of superconductivity. The investigation of higher layered ruthenates like  $\text{Sr}_3\text{Ru}_2\text{O}_7$  and  $\text{Sr}_4\text{Ru}_3\text{O}_{10}$  as well as the 'infinite layered' perovskite  $\text{SrRuO}_3$  resulted in findings which were not only important in the context of superconductivity but also interesting in themselves. The substitution of Sr in the series with La or Ca was from the very beginning a common method to manipulate the electronic environment of Ru which creates rich phase diagrams, especially for the Ca substitution. On the Sr side, there is the metallic superconductor  $\text{Sr}_2\text{RuO}_4$  while on the other Ca side the material is a Mott insulator which orders antiferromagnetically. For intermediate doping there appears interesting structural transitions and magnetic phenomena like spin-density-wave ordering [6] and metamagnetism [7]. Also in the other members of the Ruddlesden-Popper series one finds a variety of exotic phases and intriguing mechanism like nematic phases in  $\text{Sr}_3\text{Ru}_2\text{O}_7$  in magnetic field [8] or quantum criticality in  $\text{Ca}_{1-x}\text{Sr}_x\text{RuO}_3$  [9]. All the ruthenates of this series share the  $4d^4$  electronic configuration of the  $\text{Ru}^{4+}$  ion. The direct environment of Ru ion, i.e. the  $\text{RuO}_6$  octahedra, influences the electronic configuration where the octahedra shape gives the crystal field. The crystal field splitting results in the low-spin configuration ( $S = 1$ ) where all four electrons are dedicated to the  $t_{2g}$  level (see Figure 1.2). In combination with spin-orbit coupling and electron hopping one finds a scenario for  $\text{Ru}^{4+}$  where the corresponding energy scales are comparable. This creates correlated degrees of freedom which results in the variety of quantum phenomena in the Ruddlesden-Popper ruthenates.

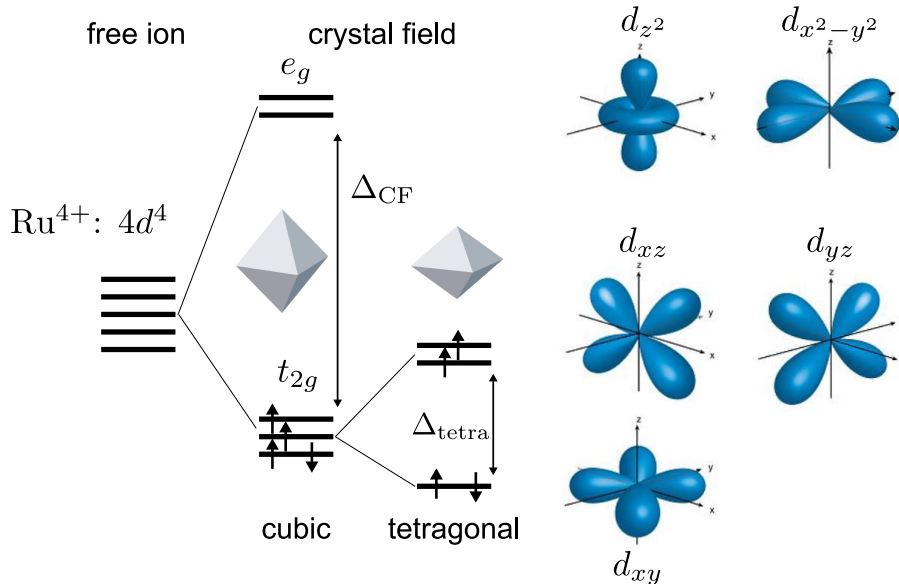


**Figure 1.2: Schematic electronic configuration of  $\text{Ru}^{4+}$  with the valence state  $4d^4$  in the low-spin configuration ( $S = 1$ ).** The crystal field in the  $\text{RuO}_6$  octahedron splits the five  $4d$  states into a threefold ( $t_{2g}$ ) and a twofold ( $e_g$ ) subshell. While for an undistorted octahedron the cubic crystal field conserves the degeneracy of the  $t_{2g}$  subshell, a distorted octahedron creates a tetragonal crystal field which lifts the degeneracy. The spatial density of the  $d$ -orbitals are displayed next to the corresponding subshells.

In this thesis we focus on three compounds which are all connected via the Ruddlesden-Popper series but show different and sometimes quite opposite characteristics. All have in common that they were grown in our institute by the floating zone method and studied with X-ray and neutron scattering techniques revealing intriguing parts of their structural and magnetic properties. In the following there will be an individual presentation of the general properties of these compounds.

### **SrRuO<sub>3</sub>**

SrRuO<sub>3</sub> has a perovskite-like structure and is referred to as the infinite layered Ruddlesden-Popper ruthenate ( $n = \infty$ ). Its deviation from the cubic perovskite structure as seen in SrTiO<sub>3</sub> comes from the rotation and tilting of the RuO<sub>6</sub> octahedra which reduces the symmetry to the orthorhombic space group  $Pnma$  with lattice parameters  $a = 5.5322(1) \text{ \AA}$ ,  $b = 7.8495(2) \text{ \AA}$ ,  $c = 5.5730(1) \text{ \AA}$  at room temperature [10]. Nevertheless the structure can be referred to as pseudo-cubic since the Ru positions follow still the cubic symmetry. The orthorhombic short axes  $a$  and  $c$  are therefore approximately  $\sqrt{2}a_c$  and the long axis  $b$  is approximately  $2a_c$  with  $a_c \approx 3.93 \text{ \AA}$ . SrRuO<sub>3</sub> is the only simple ruthenate that exhibits ferromagnetic order at ambient conditions. Its ferromagnetism inspired the proposal of  $p$ -wave superconductivity in Sr<sub>2</sub>RuO<sub>4</sub> where the pairing mechanism has to include ferromagnetic fluctuations [5, 11]. The magnetic moment of ferromagnetic SrRuO<sub>3</sub> amounts to  $1.6 \mu_B$  and the transition temperature occurs at 165 K [12]. The magnetization measurements reveal an anisotropy of  $M$  and  $\xi$  with the easy axis pointing along the longer of the two short orthorhombic axes  $c$ , parallel to the longest edge of the RuO<sub>6</sub> octahedron [13]. The magnetization density is not only concentrated at the Ru site but also the oxygen orbitals carry in sum a third of the total magnetic moment [14]. In addition the magnetization density at the Ru and O sites is highly anisotropic and follows the bonding and hybridization of Ru  $d$  and O  $p$  orbitals. The ferromagnetism is associated with strongly anomalous behavior in various properties which confirms the influence of spin-orbit coupling in SrRuO<sub>3</sub>. For example, thermal expansion shows an invar effect in the ferromagnetic phase [15, 16]. Also the switching of structural domains with magnetic field results in a magnetic shape memory effect making the magneto-elastic coupling evident [13]. At low temperature there is evidence for non-Fermi-liquid behavior that is strongly discussed in theory [17, 18]. The anomalous Hall effect exhibits an anomalous temperature dependence including a sign change [19, 20]. It is proposed that the anomalous Hall effect stems from the impact of Weyl points which can be understood as magnetic monopoles in reciprocal space. Magnetic exchange splitting in combination with spin-orbit coupling causes these Weyl points in the band structure which, according to DFT calculations, lay close to the Fermi level [21].

In Chapter 2 an extensive study of the magnetic excitations in SrRuO<sub>3</sub> is presented revealing their connection with the electronic degrees of freedom due to the Weyl points and testing general concepts like the handedness of magnons in ferromagnets.

## Ca<sub>2</sub>RuO<sub>4</sub>

The Ca counterpart of the superconductor Sr<sub>2</sub>RuO<sub>4</sub> differs fundamentally in its properties from the sister compound. The substitution of Sr by Ca with a smaller ionic radius leads to heavy rotation and tilting of the octahedra combined with orthorhombic distortion. This leads to a symmetry reduction from the tetragonal K<sub>2</sub>NiO<sub>4</sub> type structure of Sr<sub>2</sub>RuO<sub>4</sub> to an orthorhombic structure with space group *Pbca* (room temperature lattice parameters:  $a = 5.41 \text{ \AA}$ ,  $b = 5.512 \text{ \AA}$ ,  $c = 11.93 \text{ \AA}$  [22]). The rotation, tilting, and distortion of the octahedra in Ca<sub>2</sub>RuO<sub>4</sub> is strongly temperature dependent and drives the different phase transitions in this material. This compound exhibits a metal-insulator transition at 357 K; a jump in resistivity is accompanied by a flattening of the lattice [22, 23]. Upon further cooling flattening continues, the resistivity steeply increases [22], and at 110 K antiferromagnetic order sets in [22–24] accompanied by structural anomalies. The magnetic structure corresponds to the simple G-type antiferromagnetic order observed in many A<sub>2</sub>BO<sub>4</sub> materials with magnetic moments along the *b* direction (parallel to the planes). Two different magnetic structures concerning the stacking can appear in Ca<sub>2</sub>RuO<sub>4</sub>. In the A-centered structure the magnetic moments in the  $z = 0.5$  plane are coupled antiferromagnetically for the Ru positions (0.5, 0, 0.5). In the B-centered phase the magnetic moments in the  $z = 0.5$  plane are coupled antiferromagnetically for the Ru positions (0, 0.5, 0.5). In the pure Ca<sub>2</sub>RuO<sub>4</sub> the A-centered structure is dominant while samples with an oxygen excess seem to favor the B-centered structure [25]. The theoretical analysis of the electronic structure is quite complex due to the fact that there are four electrons per Ru site which occupy the three  $t_{2g}$  orbitals in a low-symmetry structure. As the orbital moment is not fully quenched there is sizeable spin-orbit coupling. Almost each of the sophisticated state-of-the-art methods to calculate correlated electron systems was applied to Ca<sub>2</sub>RuO<sub>4</sub> [26–35]. There seems to be consensus today concerning the fact that there is some orbital ordering ending in enhanced or full occupation of the  $d_{xy}$  orbital and that the remaining two electrons occupy the other  $d_{xz,yz}$  orbitals. Such interpretation only roughly corresponds to the measured ordered moment of  $1.3 \mu_B$  which is significantly below the expectation [23]. The most recently proposed theories [35] try to bridge the Mott state in Ca<sub>2</sub>RuO<sub>4</sub> with that in iridates (like Sr<sub>2</sub>IrO<sub>4</sub>) where spin-orbit coupling is the essential interaction to determine the magnetic ground state. For example in Sr<sub>2</sub>IrO<sub>4</sub> one frequently assumes an effective  $j - 1/2$  state through spin orbit coupling between the  $t_{2g}$  states. It is claimed that spin-orbit coupling is also the dominant interaction in Ca<sub>2</sub>RuO<sub>4</sub> [35]. Strong spin-orbit coupling can couple the spin and orbital moments to a non-magnetic  $j = 0$  ground state in Ca<sub>2</sub>RuO<sub>4</sub> so that magnetic moments only arise from the excited levels as in a van-Vleck material. This model, however, appears to underestimate the crystal fields arising from the strong structural distortions generating strong crystal fields and orbital polarization as well as the large hopping terms [32, 36, 37]. Nevertheless Ca<sub>2</sub>RuO<sub>4</sub> seems to be very well suited for studying the impact of strong spin-orbit coupling on a Mott insulator in close relation to the enormous efforts recently made on iridates.

In Chapter 3 the effects of current application in Ca<sub>2</sub>RuO<sub>4</sub> are presented displaying the emerging of phase coexistence creating a complex real structure. Furthermore details of the magnetic order and the magnetic correlations are studied using neutron scattering techniques.

## $\text{Sr}_2\text{Ru}_{1-y}\text{Co}_y\text{O}_4$

The superconductor  $\text{Sr}_2\text{RuO}_4$  is the most famous member of the Ruddlesden-Popper series. It crystallizes in the tetragonal  $\text{K}_2\text{NiO}_4$  structure (space group  $I4/mmm$ ) and is therefore isostructural to the high- $T_C$  superconductor  $\text{La}_{2-x}\text{Ba}_x\text{CuO}_4$ . The lattice parameters at room temperature are  $a = 3.87 \text{ \AA}$  and  $c = 12.74 \text{ \AA}$  [38]. Despite its structural relationship to the cuprates its physical properties differ significantly. The superconducting transition temperature in high-quality crystals of  $\text{Sr}_2\text{RuO}_4$  of 1.5 K [39] is well below the transition temperatures of the cuprates. While  $\text{La}_2\text{CuO}_4$  is an antiferromagnetic Mott insulator where metallic conductivity and superconductivity can be induced by doping, the normal state of  $\text{Sr}_2\text{RuO}_4$  is a paramagnetic metal whose thermodynamic properties can be well described by a quasi two-dimensional Fermi liquid [40]. Quantum oscillation measurements find three cylindrical Fermi surface sheets with enhanced effective electron masses consistent with the Fermi liquid behavior [41]. The Fermi surface sheets are formed by two one-dimensional bands  $\alpha$  and  $\beta$  and one two-dimensional band  $\gamma$  arising from the hybridized Ru  $4d$  orbitals,  $d_{xz}$ ,  $d_{yz}$ , and  $d_{xy}$  respectively. A very detailed picture of the normal-state electronic structure of  $\text{Sr}_2\text{RuO}_4$  is given by angle-resolved photoemission spectroscopy combined with DFT calculations in a study from 2013 [42]. Based on the large mass enhancement indicating strong carrier correlations and the ferromagnetism in the closely related  $\text{SrRuO}_3$  Rice and Sigrist suggested in 1995 that the superconducting state is formed by spin-triplet pairing with a  $p$ -wave symmetry [11]. They drew the connection to the superfluid state of  $^3\text{He}$  and proposed that ferromagnetic spin fluctuation drive the Cooper pairing. Many experiments confirmed the unconventional superconductivity while the  $p$ -wave spin-triplet pairing was supported by two key experiments (Knight shift [43] and polarized neutron scattering [44]) which have shown that the spin susceptibility stays constant with the onset of superconductivity. Muon spin resonance experiments have also revealed a time reversal breaking inside the superconducting state [45]. For a long time the chiral  $p$ -wave spin-triplet superconducting state was promoted in  $\text{Sr}_2\text{RuO}_4$ . In contrast were some experimental findings like the neutron scattering studies which found dominant antiferromagnetic fluctuations while ferromagnetic fluctuations were barely detectable [46–48]. Very recently the two key experiments supporting triplet pairing were revised and both Knight shift in NMR [49, 50] and polarized neutron scattering [51] found that the spin susceptibility indeed drops down in the superconducting state which is inconsistent with spin-triplet pairs. Following these events numerous proposals for the superconducting state were made which discuss mostly some sort of  $d$ -wave state or a complex combination of components [52–57]. In Chapter 4 an extended neutron scattering study of magnetic fluctuations in  $\text{Sr}_2\text{RuO}_4$  is presented supporting some reported results while contradicting others.

A way to study magnetic fluctuations in  $\text{Sr}_2\text{RuO}_4$  is the substitution of Ru by a dopant like Ti, Mn or Co to stabilize the fluctuations and analyze the appearing magnetic order. Introducing small amounts of isovalent, nonmagnetic Ti into  $\text{Sr}_2\text{RuO}_4$  stabilizes the antiferromagnetic fluctuations which leads to spin-density wave ordering [58]. The same magnetic order is achieved for  $\text{Ca}_{0.5}\text{Sr}_{1.5}\text{RuO}_4$  [6]. Ortman *et al.* found that Mn doping stabilizes the same state as Ti or Ca while Co doping results in short-range ferromagnetic order showing the competition of

antiferromagnetic and ferromagnetic fluctuations in  $\text{Sr}_2\text{RuO}_4$ [59]. In Chapter 5 we investigate the magnetic order in Co doped  $\text{Sr}_2\text{RuO}_4$  with neutron scattering and discuss character of the measured ferromagnetic order.

# SrRuO<sub>3</sub>: Impact of Spin-orbit Coupling on Magnetic Excitations

## 2.1 Magnon Dispersion

### 2.1.1 Introduction

The infinite-layer material of the Ruddlesden-Popper series  $\text{Sr}_{n+1}\text{Ru}_n\text{O}_{3n+1}$  attracts most interest due to its ferromagnetism. It is actually the only simple ruthenate to exhibit this long-range magnetic order at ambient conditions. This ferromagnetism led to the proposition of  $p$ -wave superconductivity in  $\text{Sr}_2\text{RuO}_4$  where the pairing mechanism has to include ferromagnetic fluctuations. But the magnetism in  $\text{SrRuO}_3$  itself is intriguing because of the connection to anomalies in various properties. At the ferromagnetic transition temperature of  $T_C = 165$  K there is a kink in the DC transport measurement [60] as well as a constant cell volume below  $T_C$  known as the invar effect [15]. The spin degree of freedom seems to be coupled to charge and lattice degrees of freedom. Magnetization measurements reveal a high anisotropy between the long orthorhombic  $b$  axis in space group  $Pnma$  and the orthorhombic  $c$  axis which can be identified as the easy axis [13]. This direction corresponds to the longer edge of the  $\text{RuO}_6$  octahedron. The estimated anisotropy field of  $\approx 10$  T points to strong spin-orbit coupling in this material. Combined with its metallic behavior  $\text{SrRuO}_3$  is one of the few transition-metal oxides which exhibit an itinerant magnetism. It is categorized as a 'bad metal' because the high temperature resistivity  $\rho_{\text{DC}}$  is passing through the Ioffe-Regel limit around 500 K and exhibits no saturation [16]. Based on pressure study of  $T_C$  this material has been classified as a moderately weak itinerant ferromagnet [61]. Metallic magnets always trigger the question which description of the underlying magnetic mechanism is the best suitable for this certain material. On the one side the picture of local moments following the Heisenberg model gives a precise framework for the description of magnetic insulators and can also be applied for magnetic metals. On the other side the magnetism of itinerant electrons where the electron states are localized in reciprocal space is treated as a band theory based on the Stoner theory. The reality lies often in between these two extremes. Both systems make different predictions for the distribution of spin fluctuations in reciprocal space. The local moments system allows only for collective spin wave modes which disperse in reciprocal space following the dispersion relation derived from the Heisenberg model. Following the Stoner theory the low  $q$  spin-wave dispersion goes over into a continuum of electron-hole pair excitations with opposite spins [62]. Therefore inelastic neutron scattering is a suitable tool to study the

magnon dispersion and analyze in what extend which description governs the spin-wave excitations. The investigation of the spin-wave dispersion gives insight into the extend of spin-orbit coupling, e.g. in form of an anisotropy gap. Furthermore the experimental evidence can assign where this material is located in between the two possible description of magnetism.

### 2.1.2 Results and Analysis

The magnon signal can be followed in  $\mathbf{Q}$ - $E$  space by using inelastic neutron scattering. The triple-axis spectrometer allows defined scans along given directions in reciprocal space for a given energy transfer. The possible energy transfer and the energy resolution is connected to the temperature of incoming neutrons. Therefore a combination of cold and thermal neutron sources with accordingly designed spectrometers yield sufficient access to study magnons. Typical neutron scattering data from three different spectrometers measuring the magnon signal are displayed in Figure 2.1. In the following all  $\mathbf{Q}$  vectors refer to the pseudo-cubic lattice since the crystals grown by the floating-zone method show usually structural multi-domains following the six possible orthorhombic twins [13]. It is therefore advantageous to use the cubic setting where the cubic  $[1,0,0]$  direction corresponds to a long orthorhombic  $b$  direction and the cubic  $[0,1,1]$  direction corresponds to a diagonal in the  $a, c$  plane. Constant energy scans along high-symmetry directions around the ferromagnetic zone center  $\mathbf{Q} = (1, 0, 0)$  reveal the magnon dispersion as the peak position changes with increasing energy transfer (panels (a) to (c)). Note here that the scans cover both sides of the magnetic zone center. Hence, the two peaks appearing in each scan visualize the symmetry of the magnon dispersion. The cold triple axis spectrometers 4F1 and PANDA with their high energy resolution enable a direct measurement of a possible magnon gap via a constant  $\mathbf{Q}$  scan at the zone center (Figure 2.1(d)). For the data description the MATLAB based software tool `Reslib` [63] is used where a given model cross section  $\mathcal{S}(\mathbf{q}, E)$  is convoluted with the instrumental resolution function of the specific instrument and fitted to the data (see Section 2.5). This procedure enables one to separate the pure excitation related physics from the effects of the instrumental resolution on the experimental data. The intensity of excitation is modeled by a Lorentzian  $\mathcal{L}(E)$  with the FWHM  $\gamma$  and the amplitude  $A$  (Equation 2.4) following . The  $\mathbf{q}$ - $E$  correlation is taken into account by the specified dispersion relation. To describe the low-energy data where the tail of the magnetic Bragg peak at the zone center influences the inelastic scattering a Gaussian  $\mathcal{G}(\mathbf{q}, E)$  centered at  $\mathbf{q}_0 = (0, 0, 0)$  and  $E_0 = 0$  is included in the model cross section.

The dispersion relation  $E(\mathbf{q})$  can be derived from the general Heisenberg Hamiltonian (Equation 2.2).

$$\mathcal{H} = \mathcal{H}_{SSI} + \mathcal{H}_{ZFI} + \mathcal{H}_{EZI} \quad (2.1)$$

$$= - \sum_{\langle ij \rangle} J \mathbf{S}_i \cdot \mathbf{S}_j - \sum_i K (S_i^z)^2 - \mu_B g \mathbf{B} \sum_i S_i^z \quad (2.2)$$

For the description of spin waves in SrRuO<sub>3</sub> three contributions have to be considered: (i) the spin-spin interaction (SSI)<sup>1</sup> with the exchange-coupling constant

<sup>1</sup>The sum is built over the pair  $\langle ij \rangle$  allowing all permutations with  $i \neq j$

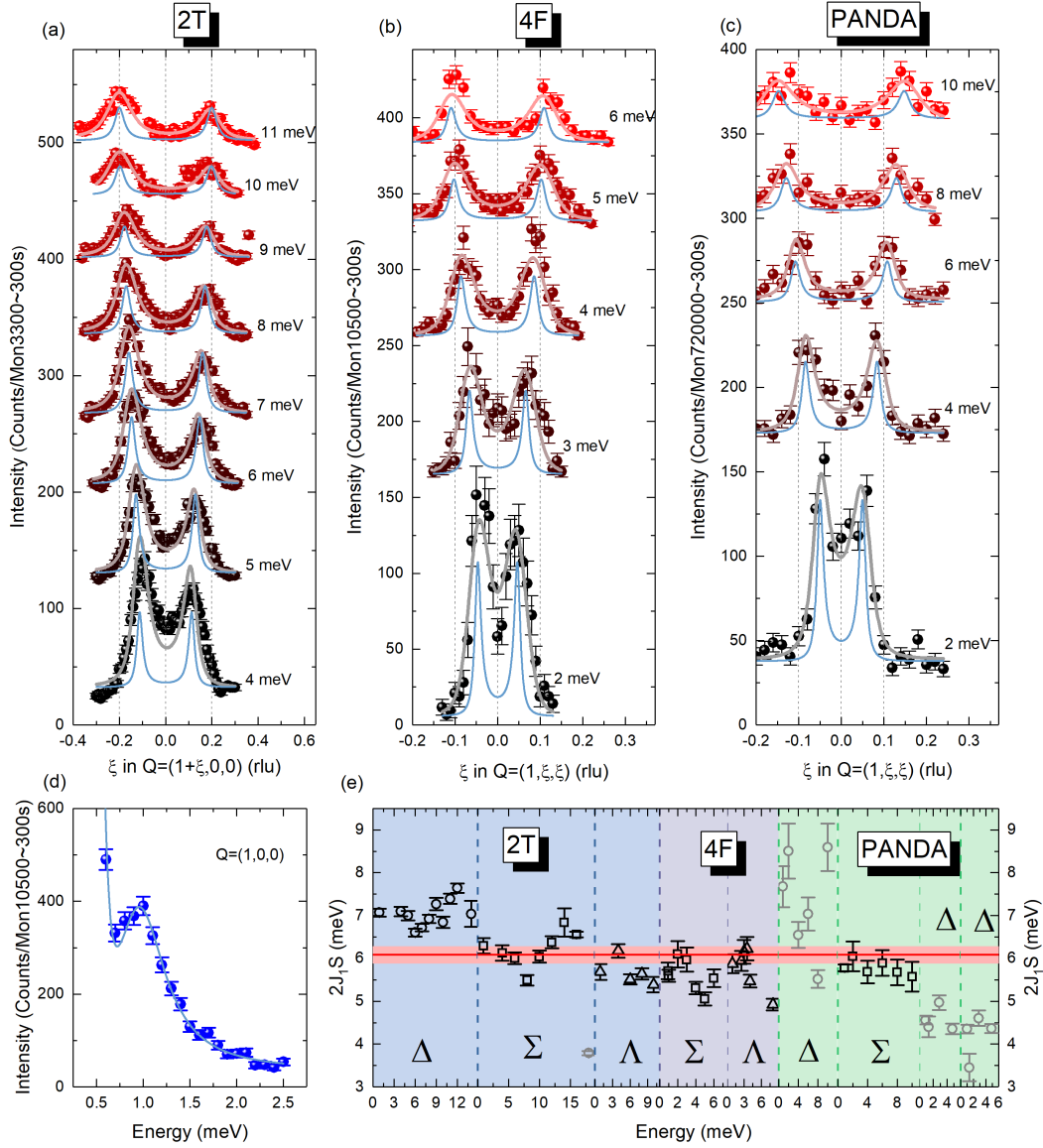


**Figure 2.1: Determination of ferromagnetic magnon dispersion using triple-axis spectrometer.** (a)-(c) Constant energy scans across the magnon dispersion in SrRuO<sub>3</sub> at various energies obtained at T=10 K on the cold triple-axis spectrometer 4F (LLB) and PANDA (MLZ), and on the thermal triple-axis spectrometer 2T (LLB). The light blue lines represent the modeled magnon contribution including a broadening term. Note here that the PANDA data were measured after detwinning the crystal assembly with magnetic field. To describe the data the magnon scattering was modeled following the ferromagnetic dispersion relation (light blue lines) and then folded with the  $Q$  and  $E$  dependent resolution function (colored lines). Data are vertically offset for clarity. (d) Constant  $Q$  scan at  $Q = (1, 0, 0)$  described with the same dispersion model showing the anisotropy gap at T = 10 K. (e) The fitting yields a value of  $2J_1S$  for each scan along different high symmetry cubic directions in different experiments. The data are distinguishable by colored background in respect to the instrument and by symbol shape in respect to the cubic direction (circle:  $\Delta = [\xi, 0, 0]$ ; square:  $\Sigma = [0, \xi, \xi]$ ; triangle:  $\Lambda = [\xi, \xi, \xi]$ ). The weighted average of  $2J_1S = 6.1(2)$  meV is represented by the red line while the light red area denotes its error margin. The data in gray are not used for the averaging.

$J$ , (ii) the zero-field interaction (ZFI) with the anisotropy parameter  $K^2$ , and (iii) the electron-Zeeman interaction (EZI) with the Landé factor  $g$  and the external field  $\mathbf{B}$ . Note that the sum indices  $i$  and  $j$  represent different spin. Without an external field  $\mathbf{B} = 0$  the dispersion relation for a ferromagnet with cubic lattice can be derived [64] (Equation 2.3). The anisotropy  $K$  results in a finite energy at  $\mathbf{q} = 0$  which is given by the anisotropy gap  $\Delta$ . The electron-electron interaction between six nearest neighbors in the cubic ferromagnet leads to a  $\cos(\mathbf{q})$  dependence which scales with the coupling constant  $2JS$  consisting of the exchange coupling  $J$  and the spin moment  $S$ .

$$E_{\mathbf{q}} = \Delta + 2JS(6 - 2 \sum_{i=x,y,z} \cos(2\pi q_i)) \quad (2.3)$$

$$\mathcal{L}(E) = \frac{A}{2\pi} \frac{\gamma}{(E - E_{\mathbf{q}})^2 + \gamma^2} \quad (2.4)$$

$$\mathcal{S}(\mathbf{q}, E) = \mathcal{G}(\mathbf{q}, E) + \mathcal{L}(\mathbf{q}, E) \quad (2.5)$$

The constant  $\mathbf{Q}$  scan at the zone center (Figure 2.1(d)) can be well described with the dispersion model and yields a value of  $\Delta=0.94(3)$  meV at 10 K for the magnon gap in SrRuO<sub>3</sub>. This gap is a manifestation of the single-ion anisotropy of Ru where spin-orbit coupling leads to a preferred alignment of spins along a certain crystallographic direction (easy axis). Its size is in agreement with the anisotropy field of  $\approx 10$  T from magnetization measurements [13] and with the energy of the ferromagnetic resonance of  $\approx 250$  GHz  $\hat{=}$  1.03 meV observed in time-resolved magneto-optical Kerr effect measurements [65]. In the following analysis the magnon gap is fixed in the model cross section at the determined value which confines the dependency of the peak position in the constant  $E$  scans to the single fitting parameter  $2JS$ . This parameter contains the coupling constant in the Heisenberg model  $J$  and is connected with the so called spin stiffness  $D$ . The magnon stiffness is defined by approximating the ferromagnetic dispersion relation (Equation 2.3) for small  $\mathbf{q}$ . The approximation yields a quadratic dispersion relation where the spin stiffness  $D$  represents the stretch of the parabola (Equation 2.6).

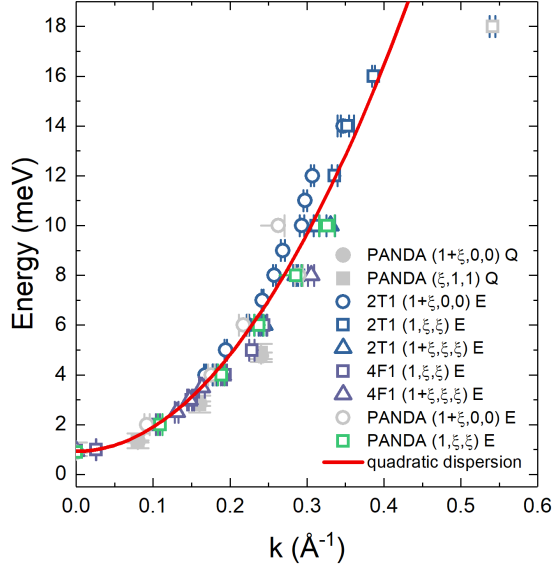
$$E_{\mathbf{k}} \approx \Delta + \underbrace{2JSa_c^2}_{D} \mathbf{k}^2 \quad (2.6)$$

The theoretical description of the experimental data are displayed by the lines in Figure 2.1(a)-(d). The light blue lines represent the cross section model for the  $\mathbf{q}$  and  $E$  values specific to each scan and the same colored lines as the data visualize the fitted result of convolution of the model with instrumental resolution. By comparison of the model with the convolution result the influence of the instrumental resolution on the experimental data become visible. The ellipsoid shape of the resolution function in  $\mathbf{Q}$ - $E$  space leads to a focusing effect where the magnon signal on one side of the constant  $E$  scan is increased. Additionally the instrumental function governs the width of the magnon peaks in the experimental data since it

---

<sup>2</sup>Here an easy axis anisotropy is assumed.

**Figure 2.2: Low energy magnon dispersion derived from triple-axis spectrometers.**  $E$ - $k$  dependency of the magnon signal shows parabolic behavior for low wave vectors. The  $k$  value is calculated with the fitted values of  $2JS$  (Figure 2.1(e)). The red line represents the parabolic magnon dispersion determined by Equation 2.6 with the averaged value of  $2JS$ .



significantly broadens the peaks derived from the model. Nevertheless the description of experimental data need a finite width of the model which indicates that the magnons are intrinsically broadened.<sup>3</sup> Such an intrinsic broadening can stem from the twinning in the here-used SrRuO<sub>3</sub> crystals since this superposes different directions of the orthorhombic lattice. The pseudo-cubic direction  $[1, 0, 0]_c$  is parallel to the long orthorhombic axis  $b$  (in  $Pnma$ ) of one twin. The other twins are oriented in such a way that this pseudo-cubic direction points along the in-plane diagonals meaning the  $[1, 0, 1]_o$  for the other twins [13]. If the short orthorhombic axes  $a$  and  $c$  were equal, i.e. a tetragonal structure, half the diagonal of the  $ac$  plane would be equal to the pseudo-cubic lattice constant  $a_c$ . In SrRuO<sub>3</sub> both short axes  $a$  and  $c$  differ by 0.037 Å at 10 K [15] which results in a relative deviation of the length of half the diagonal to  $a_c$  by 0.2%. Therefore the twinning related broadening does not account for the total amount. The sizable intrinsic broadening of the magnon results most likely comes from the coupling to electrons as seen in the kink at the ferromagnetic transition in the resistivity [60]. Hence, the intrinsic magnon broadening is experimental evidence for significant spin-orbit coupling in SrRuO<sub>3</sub>.

As mentioned before the peak positions in the constant  $E$  scans are determined by the  $2JS$  parameter which is fitted in the analysis of each scan. Figure 2.1(e) shows the resulting  $2JS$  values for each scan separated for the three instruments (background color) and the different high symmetry directions (symbol). Since the coupling constant describes the magnetic interaction of neighboring moments and is therefore a universal parameter of the system all scans should be describable with the same parameter. Unfortunately the fitting of all scans in a multi-fit routine using one set of generalized fitting parameter is not feasible with the used software tool due to the individual backgrounds of the different instruments. Therefore the results of fitting all scans are averaged and yield a general  $2JS$  of 6.1(2) meV. This translates to a spin stiffness in SrRuO<sub>3</sub> of  $D = 94.2 \pm 3.0 \text{ meV}\text{\AA}^2$ . This averaged spin stiffness describes the low energy data of all instruments reasonably well as one can see in the  $E$ - $k$  dependency for the magnon signal (Figure 2.2). Here the  $k$  values are calculated from the fitted  $2JS$  of each scan (Figure 2.1(e)) following

<sup>3</sup>The intrinsic width of the model is set to 40% of the specific energy.

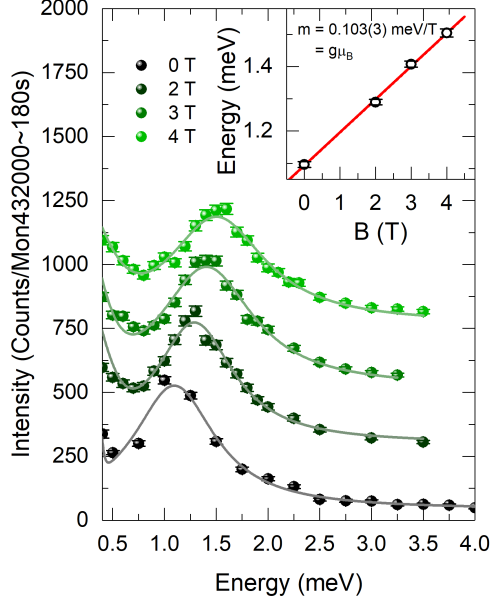


**Figure 2.3: Magnetic field dependency of the anisotropy gap.** Constant  $\mathbf{Q}$  scans at  $\mathbf{Q} = (0,1,1)$  are shown for different values of the applied magnetic field. The magnon signal is modeled with a Lorentzian profile combined with a Gaussian background taking the low energy contribution of the elastic line into account (lines). The data are shifted by a constant offset for better visibility. The inset depicts the magnon gap (Lorentzian peak position) in comparison to the magnetic field. This dependence is fitted by a linear function with slope  $m$  (red line).

the quadratic relation (Equation 2.6) and plotted against the energy. This differs from the determination of spin stiffness  $D$  in [66] where  $D$  is resulting from the approximated quadratic dispersion model for small  $q$  which is fitted to the  $E$ - $k$  data extracted from the constant energy scans. The coupling constant  $J$  can be estimated to  $3.8(1) \text{ meV}$  by using the saturation magnetization of  $1.6 \mu_B/\text{Ru}$  [13] and assuming a  $g$  factor of  $2$ .<sup>4</sup> A possibility to directly measure the  $g$  factor is the magnetic field dependency of the magnon gap. Applying an external magnetic field will add a Zeeman term to the dispersion relation of the magnon resulting from the electron-Zeeman interaction in Equation 2.2. We therefore have to modify equation Equation 2.3:

$$E_q = \Delta + 2JS(6 - 2 \sum_{i=x,y,z} \cos(2\pi q_i)) + g\mu_B B \quad (2.7)$$

This term increases the magnon energy at the zone center  $q = 0$  linearly with the applied magnetic field  $B$ . The Zeeman energy represents the potential energy of the spin magnetic moments in the external field. The magnetic field dependency of the magnon signal in constant  $\mathbf{Q}$  scans is displayed in Figure 2.3. The scans are measured at the ferromagnetic zone center  $\mathbf{Q} = (0, 1, 1)$ . It clearly shows the shift of the magnon gap to higher energies with increasing field. The gap value determined by the Lorentzian peak position of the fit indeed exhibits a linear correlation to the external field (Figure 2.3 inset). The slope  $m$  of the linear fit is equal to  $g\mu_B$  and a value of  $g$  can be derived. This analysis yields a  $g$  factor of  $1.78(5)$ . Using the experimental value of  $g$  the coupling constant  $J$  amounts to  $3.4(7) \text{ meV}$  because the averaged spin calculated with the saturation magnetization increases<sup>5</sup>. Usually the  $g$  factor in  $4d$  transition-metal oxides with a high crystal-field splitting

<sup>4</sup>The saturation magnetization is equal to the  $g$  factor multiplied with the averaged spin. Therefore we can determine the averaged spin and use it to extract  $J$  from  $2JS$ .  $\langle S_z \rangle M_{sat} = g\langle S_z \rangle \Leftrightarrow 1.6 \mu_B = 2\langle S_z \rangle \Rightarrow \langle S_z \rangle = 0.8$

<sup>5</sup> $M_{sat} = g\langle S_z \rangle \Rightarrow \langle S_z \rangle = 1.6/1.78(5) = 0.90(3)$

like SrRuO<sub>3</sub> is assumed to consist only of the spin contribution  $g_S = 2$  because the orbital moment is quenched and it therefore does not contribute to the magnetism. However in materials with sizable spin-orbit coupling the orbital moment can partly recover and the  $g$  factor deviates from 2 [67]. The orbital moment of SrRuO<sub>3</sub> is found by x-ray magnetic circular dichroism (XMCD) to be very small [68, 69]. While Okamoto *et al.* reported an orbital moment of  $0.04(4) \mu_B$  [68], Agrestini *et al.* give  $L_z/2S_z$  ratios of 0.01 with  $L_z = 0.01(1) \mu_B$  [69]. These experimental reports are confirmed by DFT calculations which report an orbital moment of three orders of magnitude smaller than the spin moment [14]. The orbital moment seems to be basically quenched which supports the assumption of a  $g$  factor of 2. Time-resolved magneto-optical Kerr effect measurements on SrRuO<sub>3</sub> thin films also quantify the linear field dependence of the ferromagnetic resonance [65]. They report a slope of  $\approx 17 \frac{\text{GHz}}{\text{T}}$  which corresponds to  $0.07 \frac{\text{meV}}{\text{T}}$ . This yields an even smaller  $g$  factor of 1.21. A possible explanation for this reduced factors may be connected to the sample geometry dependent demagnetization field. In a magnet a magnetic field is generated by the magnetization, i.e. demagnetizing field, which can oppose the magnetization depending on the sample shape and uniformity of the magnetization. The demagnetization field reduces the internal field. In our case of the multi-crystal assembly of cylindrical crystals, this internal field reduction would be small but increases the slope in Figure 2.3 which increases the calculated  $g$  factor. In thin films the effect of the internal field reduction by the demagnetizing field is expected to be even more pronounced because of the highly anisotropic sample shape. This results in the even smaller slope in the  $E$ - $B$  dependence. For these reasons the  $g$  factor will be assumed to be 2 in the following and the averaged spin is then fixed to 0.8.

The investigation of the magnon dispersion using triple-axis spectrometers becomes increasingly difficult for increasing energy. At higher energies the inelastic scattering can contain multiple contributions from phonons. In addition to sample related excitations the density of spurious increases at high energies with a triple-axis spectrometer. The distinguishing between magnon and phonon contribution in a single one-dimensional scan relies on a good understanding of the complex phonon dispersion with its multiple modes. The time-of-flight technique can deliver a complete picture of the Brillouin zone with its different excitations. It uses higher initial energies than the cold and thermal sources used to operate triple-axis spectrometers which increases the access to  $q$ - $E$  space. Therefore, it is easier to follow certain dispersion branches and distinguish between magnons and phonons. In the case of SrRuO<sub>3</sub> the magnon dispersion was studied using the time-of-flight spectrometer MERLIN at ISIS Neutron and Muon Source. Usually the time-of-flight technique enables one to collect data simultaneously for several incident energies. This creates comparable data sets with different energy resolution and range. The presented data are taken from the data sets with an incident energy of 22, 43, and 68 meV since they yield the most clear picture of the magnon signal. The magnon dispersion can be visualized by two-dimensional cuts through the four-dimensional  $\mathbf{Q}$ - $E$  space. Two different representations of the magnon dispersion are used here: (1) constant  $E$  cuts of the scattering plane  $[\xi, 0, 0]/[0, \xi, \xi]$  which represent horizontal cuts through the  $q$ - $E$  dispersion parabola (see Figure 2.4) and (2) constant  $\mathbf{Q}$  cuts which display the  $q$ - $E$  dependency of the magnon signal in the the cubic high-symmetry directions (see Figure 2.5). In the resulting maps the signal intensity

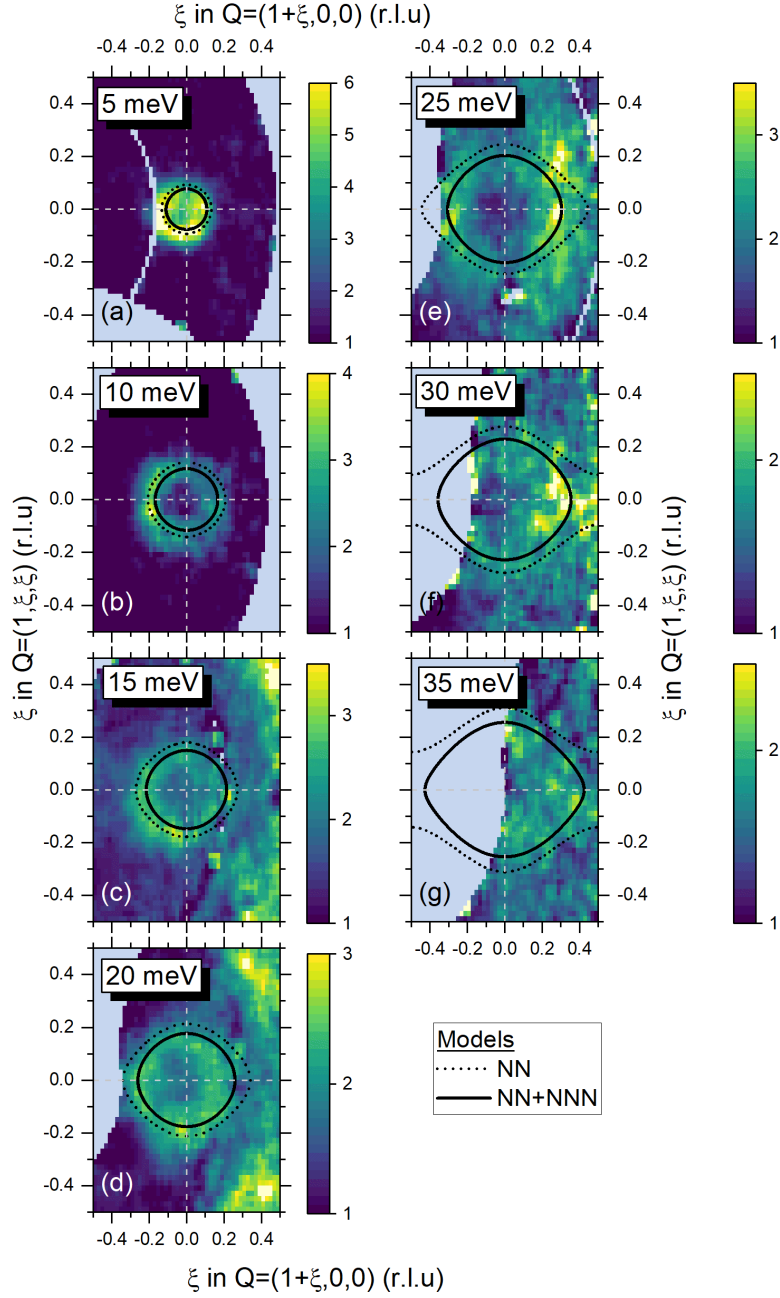


**Figure 2.4: Magnon dispersion measured by time-of-flight technique.** Constant  $E$  cuts at 10 K of the  $[\xi, 0, 0]/[0, \xi, \xi]$  plane for different energies display the ring shape of the magnon signal. The diameter of the ring is increasing with energy indicating the magnon dispersion. The axis length ratio is chosen to be  $1:\sqrt{2}$  to reflect the geometrical factor in the absolute lattice units between the two directions. The low energy data at 5 and 10 meV ((a),(b)) are taken with the incident energy of 22 meV while the energy data at 15 and 20 meV ((c),(d)) are taken with the incident energy of 43 meV and the energy data at 25, 30, and 35 meV ((e)-(g)) are taken with the incident energy of 68 meV. The used integration limits for these maps are  $-0.1 \leq \eta \leq 0.1$  in  $[1, -\eta, \eta]$  and  $E \pm 2.5$  meV. The time-of-flight data are overlaid with the ferromagnetic dispersion model with nearest-neighbor interaction (NN) taken from the analysis of the triple-axis spectrometer data as black dots and with nearest-neighbor and next-nearest-neighbor interaction (NNN) as black lines.

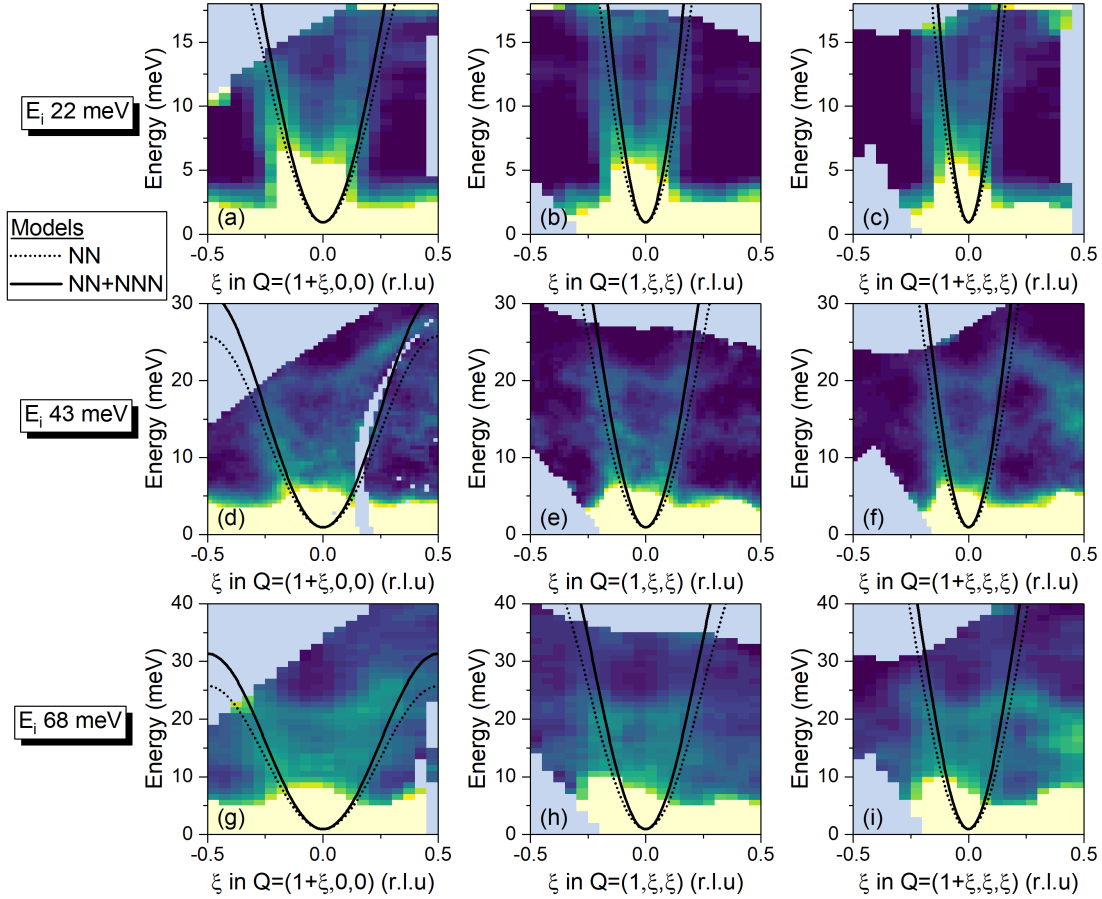


**Figure 2.5: Magnon dispersion measured by time-of-flight technique.** Constant  $\mathbf{Q}$  cuts at 10 K along the cubic high-symmetry directions around  $\mathbf{Q} = (1,0,0)$  show the magnon signal disperse in energy. The panels are sorted in rows where each row represent the data of a certain incident energy. From the top to the bottom the data are taken with 22 ((a)-(c)), 43 ((d)-(f)), and 68 meV ((g)-(i)) respectively. The intensity range (colorbar) is in the panels of every row the same for better comparability. The integration limits are  $-0.1 \leq \eta \leq 0.1$  in  $[1, -\eta, \eta]$  and  $-0.1 \leq \zeta \leq 0.1$  in the direction perpendicular to the respective high-symmetry direction. The time-of-flight data are overlaid with the ferromagnetic dispersion model with nearest-neighbor interaction (NN) taken from the analysis of the triple-axis spectrometer data as black dots and with nearest-neighbor and next-nearest-neighbor interaction (NNN) as black lines.

is encoded by color where bright means high intensity while dark color stands for low intensity. The data are integrated in  $[0, \xi, -\xi]$  by  $\pm 0.1$  r.l.u and in energy by  $\pm 2$  meV. To optimize the presentation of the magnon dispersion the different energies are taken from different incident energies since it influences the energy range and resolution. Figure 2.4(a) and (b) result from the data with  $E_i = 22$  meV, (c) and (d) are taken from the data with  $E_i = 43$  meV and (e)-(g) displays the data from  $E_i = 68$  meV. The branches of the magnon dispersion are not clearly visible in the higher incident energies ( $E_i = 120$  and  $180$  meV). In the two-dimensional constant  $E$  cuts the magnon exhibits a ring shape. As the energy increases the ring radius is increasing indicating the dispersion of the magnon. Figure 2.5 displays the two-dimensional constant  $\mathbf{Q}$  cuts along the three cubic high-symmetry directions where the dispersion parabola of the magnon becomes visible. Note here that the data are always integrated by  $\pm 0.1$  r.l.u in the two corresponding perpendicular directions. The low-energy part is dominated by the tail of the elastic (in-)coherent scattering which is visible by the bright area for all  $\xi$ . The expansion of the elastic scattering into the inelastic regime depends on the energy resolution and increases therefore with the incident energy. The magnon signal is clearly visible as a parabola in its  $q$ - $E$  dependency. Other phonon contributions and how they disperse can be seen for example in Figure 2.5(f),(i) at  $\mathbf{Q} = (1.5, 0.5, 0.5)$  around  $E = 15$  meV.

To compare the results of the time-of-flight measurement with the triple-axis spectrometer results the theoretical dispersion according to the Heisenberg model of a ferromagnet is overlaid on the experimental data. Firstly the model in Equation 2.3 is used with the coupling constant  $2J_1S$  and the anisotropy gap  $\Delta$  determined by the triple-axis experiments. This model takes only nearest neighbors (NN) into account. By comparison with the experimental time-of-flight data it is obvious that the model (black dotted line in Figure 2.4 and Figure 2.5 only describes the low energy part of the dispersion. This is expected since the triple-axis spectrometer data are also only available for energies up to 16 meV. In general the NN model seems to underestimate the magnon stiffness as the experimental parabolas are tighter and the rings smaller. The model is therefore modified by including next-nearest neighbor interaction in a cubic lattice with the coupling constant  $J_2$  (Equation 2.3). Figure 2.6 displays the connection between the NN ( $J_1$ ) and NNN ( $J_2$ ) coupling and the SrRuO<sub>3</sub> lattice.

$$E_{\mathbf{q}} = \Delta + 2J_1S(6 - 2 \sum_i \cos(2\pi q_i)) + 2J_2S(12 - 4 \sum_{ij, i \neq j} \cos(2\pi q_i)\cos(2\pi q_j)) \quad (2.8)$$

The coupling term  $2J_2S$  is determined by qualitatively comparing model and experiment for best visual overlap. Here the data in Figure 2.4 are used since the magnon is best visible. Including the NNN interaction does indeed tighten the ring shape for positive  $J_2$  especially for higher energies. The best overlap is achieved for  $2J_2S = 0.7$  meV which corresponds to  $J_2 = 0.4$  meV with  $S = 0.8$ . The modified model describes the parabolas in Figure 2.5 also better although the difference between the models is small for the displayed energy region in  $[0, \xi, \xi]$  and  $[\xi, \xi, \xi]$  direction. The data in Figure 2.5 suffer from heavy phonon contamination around  $\mathbf{Q} = (1.5, 0, 0)$  which can be easily mistaken as the magnon signal. This phonon contamination is also clearly visible in the in-plane scattering where it appears as intense scattering at the zone corners  $\mathbf{Q} = (1.5, 0.5, 0.5)$  and  $\mathbf{Q} = (1.5, -0.5, -0.5)$  for  $E = 15$  meV (Figure 2.4(c)). It disperses inwards and is visible as a strong

broad signal at  $\mathbf{Q} = (1.5, 0, 0)$  and  $E = 25$  meV (Figure 2.4(e)). The phonon dispersion study for SrRuO<sub>3</sub> has indeed revealed a phonon at the equivalent position  $\mathbf{Q} = (2.5, 0, 0)$  and the energy  $E = 25$  meV (Section A.1).

In a metallic ferromagnet the spin-wave dispersion following the Heisenberg model of localized moments is cut off at a finite energy above which magnetic excitations become electron-hole pair excitations between bands of opposite spin forming a continuous band, the so-called Stoner continuum [62]. The occurrence of these Stoner excitations in  $\mathbf{Q}$ - $E$  space can be complex since the band structure in a real material has multiple bands with changing band splittings throughout the Brillouin zone. The signature of Stoner excitations in neutron scattering is a broadening of the spin-wave excitations while their intensity decreases rapidly for increasing energy as they enter the continuum [70]. Indeed, especially in the data taken with  $E_i = 68$  meV, the intense magnon scattering seems to be abruptly reduced above 25 meV (Figure 2.5(h),(i)). Above this energy there seems to be still magnon scattering which follows distinct dispersion branches but its intensity is significantly lower. The same behavior is seen in Figure 2.4(f) and (g) where the ring shaped magnetic scattering is significantly lower at 30 meV and also seems to be broadened. Nevertheless the scattering is still structured as the ring shape is clearly visible. This could be an indication of the onset of the Stoner continuum. Admittedly the data quality suffers in general from the low-intensity signal of the magnetic excitations and the contamination of phonons. The time-of-flight experiments of three dimensional material like SrRuO<sub>3</sub> have a disadvantage since it is not possible to fully integrate over one dimension as it is done for example in two-dimensional layered materials which improves the statistic significantly. Nevertheless it is possible to identify the spin-wave excitation and to characterize its dispersion qualitatively.

Beside the analysis of the low-temperature magnon dispersion in the ferromagnetic phase we also studied the magnon dispersion close to the phase transition at 160 K. In Figure 2.7 and Figure 2.8 the high temperature data are directly compared to the low temperature in form of the same two-dimensional cuts of the  $\mathbf{Q}$ - $E$  space. Note here that for the incident energy of 68 meV no high temperature data were measured. As the intensity ranges represented by the color bars are scaled equally for both temperatures it becomes evident that the magnon signal increases with temperature. Inside the ferromagnetic phase the increase of magnetic scattering intensity can be explained by the Bose factor. However at 160 K, at the phase transition, the magnetic scattering should decrease faster than the Bose factor enhancement since the magnetization, i.e. the ordered moment, decreases. The strong

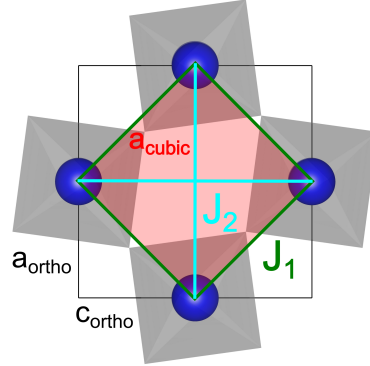


**Figure 2.6: Schematic representation of the orthorhombic  $ac$  plane in SrRuO<sub>3</sub> with the pseudo-cubic cell and the corresponding coupling directions.** The  $ac$  plane of the orthorhombic cell (black) is displayed including the Ru atoms (blue) and the oxygen octahedra (gray). The cubic cell with the lattice parameter  $a_c$  is given in red. The coupling constants  $J_1$  (green) and  $J_2$  (cyan) are connected to the lattice directions via the neighboring Ru atom relations nearest neighbors (NN) and next-nearest neighbors (NNN) respectively.

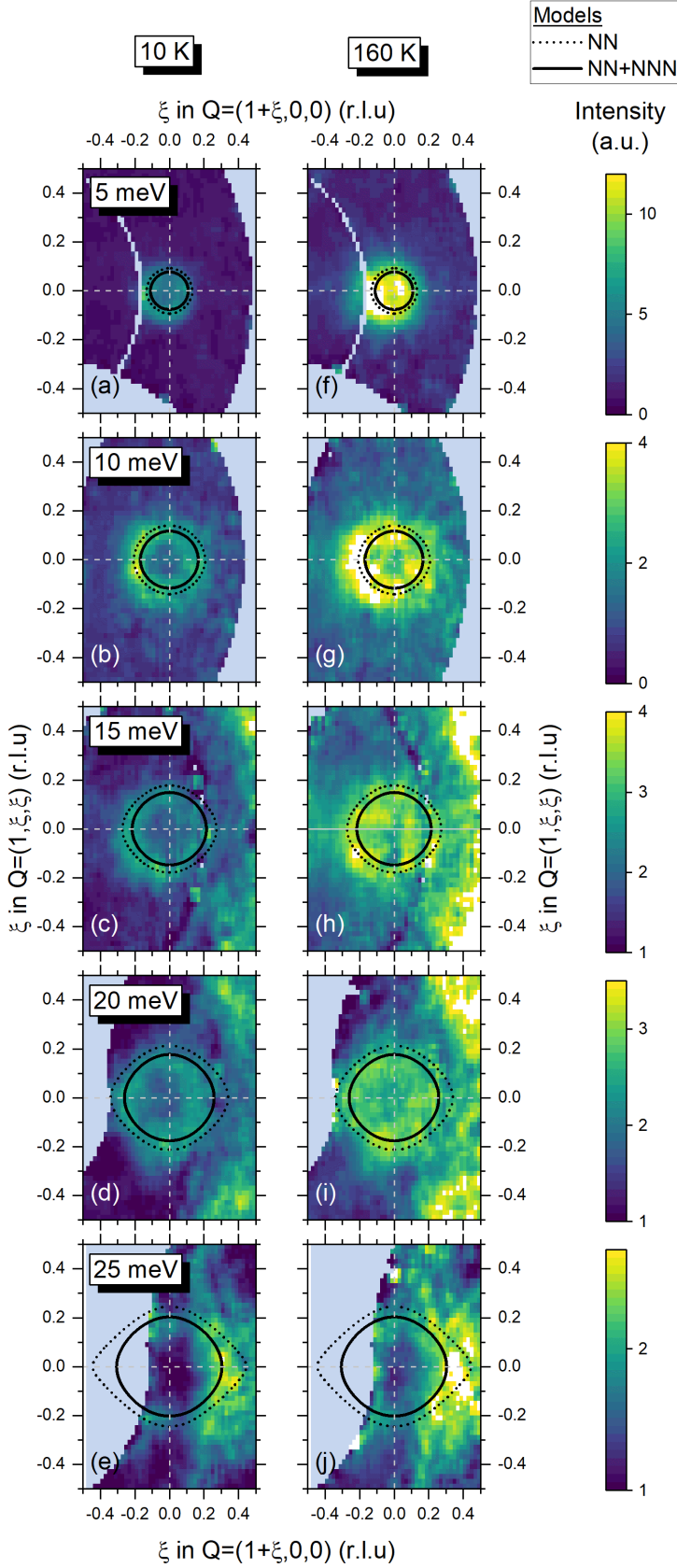


**Figure 2.7: Magnon dispersion measured by time-of-flight technique.** Constant  $E$  cuts of the  $[\xi, 0, 0]/[0, \xi, \xi]$  plane for different energies display the ring shape of the magnon signal. The diameter of the ring is increasing with energy indicating the magnon dispersion. The magnon signal in the ferromagnetic phase at 10 K ((a)-(e)) is compared with the magnon signal around the phase transition at 160 K ((f)-(g)). To compare the signal strength between temperatures the intensity range (colorbar) is the same for each energy. The axis length ratio is chosen to be  $1:\sqrt{2}$  to reflect the geometrical factor in the absolute lattice units between the two directions. The low energy data at 5 and 10 meV are taken with the incident energy of 22 meV while the higher energy data are taken with the incident energy of 43 meV. The time-of-flight data are overlaid with the ferromagnetic dispersion model with nearest-neighbor interaction (NN) as black dots and with nearest-neighbor and next-nearest-neighbor interaction (NNN) as black lines.

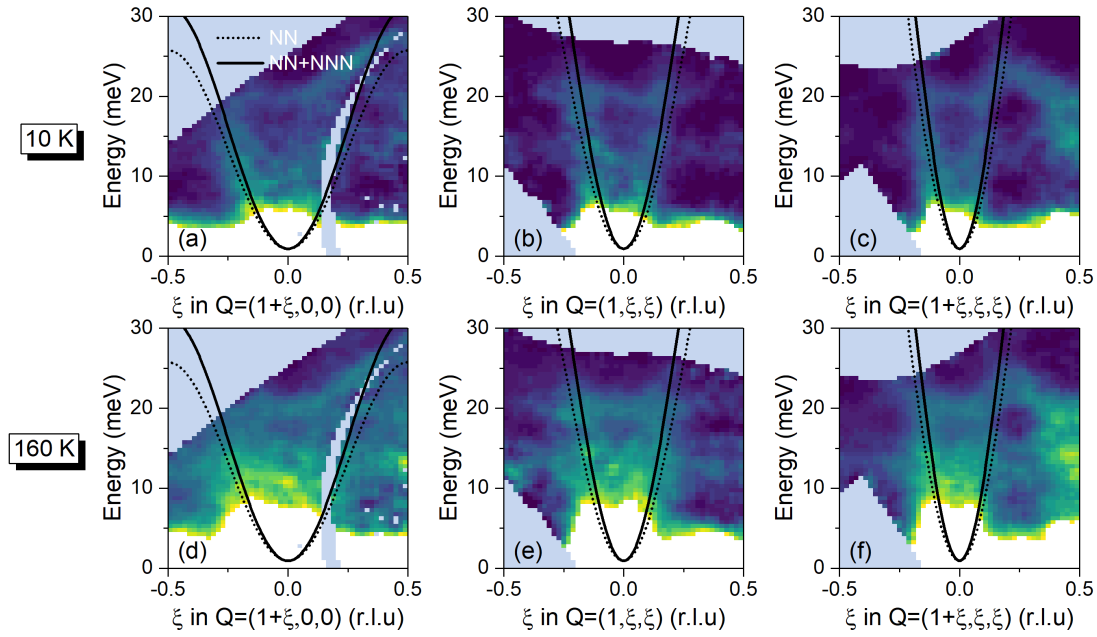


**Figure 2.8: Magnon dispersion measured by time-of-flight technique.** Constant  $\mathbf{Q}$  cuts along the cubic high-symmetry directions around  $\mathbf{Q} = (1,0,0)$  show the magnon signal disperse in energy. The data are taken with the incident energy of 43 meV. The top row ((a)-(c)) displays the low temperature data at 10 K while the bottom row ((d)-(f)) shows the data around the phase transition at 160 K. The intensity range (colorbar) is in all panels the same for better comparability. The time-of-flight data are overlaid with the ferromagnetic dispersion model with nearest-neighbor interaction (NN) as black dots and with nearest-neighbor and next-nearest-neighbor interaction (NNN) as black lines.

magnetic scattering at the phase transition can be explained by the existence of paramagnons outside of the ordered phase which seem to follow the same dispersion as the long-range order excitations. To analyze the change of the magnon dispersion the dispersion model derived from the low temperature data are also plotted in the high temperature data. There is no indication that the magnon stiffness changes significantly as the model still describes the data qualitatively. This supports the magnon softening at low temperatures reported in [66]. Normally one would expect the spin stiffness to decrease with increasing temperature following the magnetization [20]. In this case the spin stiffness stays constant which can be seen at the comparable diameter of the ring shaped scattering in Figure 2.7. Besides the signal increase and the comparable dispersion, the magnon is also broadened as the intensity spread, especially towards the zone center  $q = 0$ , is wider. The rings in Figure 2.7(f)-(i) are closing. This is also related to the transformation from long-range magnetic excitations into paramagnons outside the ordered phase.

### 2.1.3 Section Summary

The dispersion of spin-wave excitations in SrRuO<sub>3</sub> are studied by inelastic neutron scattering. The combination of triple-axis and time-of-flight spectrometers gives access to an extensive portion of  $\mathbf{Q}$ - $E$  space. The triple-axis data are analyzed taking the instrumental resolution into account and it can be described by the dispersion model following the Heisenberg model of localized moments of a ferromagnet. The spin-dynamic parameters like the anisotropy gap and the spin stiffness can be quantitatively determined by the model (Tab. 2.1). This model is compared with the magnon dispersion measured with the time-of-flight technique and extended. The extension of the model is still in the framework of the Heisenberg model and the high energy part of the magnon dispersion can be qualitatively described by including higher order interactions. The scattering intensity seems to be abruptly reduced above 25 meV which would be the fingerprint of Stoner excitations in an itinerant ferromagnet. The sizable anisotropy gap and the finite width of the magnon are both indicating the significant influence of spin-orbit coupling in SrRuO<sub>3</sub>. This analysis of the spin-wave excitation builds the groundwork for the following temperature dependent study of the spin-dynamic parameters. The comparison of low- and high-temperature data confirms the temperature dependence of the spin stiffness presented in Section 2.2 indicating magnon softening with increasing temperature. The magnetic scattering around the transition temperature is already dominated by paramagnons as the intensity and the width of the peaks increases. The temperature dependence of magnetic excitations in SrRuO<sub>3</sub> will be discussed further in Section 2.2.

**Table 2.1: Spin-dynamic parameters of SrRuO<sub>3</sub> determined by inelastic neutron scattering**

$\Delta$ [meV]	$D$ [meVÅ <sup>2</sup> ]	$2J_1S$ [meV]	$J_1$ [meV]	$2J_2S$ [meV]	$J_2$ [meV]
0.94(3)	94.2(2)	6.1(2)	3.8(1) <sup>6</sup>	0.7 <sup>7</sup>	0.4 <sup>6</sup>

## 2.2 Fingerprint of Weyl Fermions in Spin Excitations

### 2.2.1 Introduction

The discovery of the nonmonotonous temperature behavior of the anomalous Hall conductivity in SrRuO<sub>3</sub> led to the interpretation of magnetic monopoles close to the Fermi surface in  $\mathbf{k}$ -space [19]. These monopoles create the Berry phase curvature which makes the intrinsic contribution to the AHE measurable. Following the theory of Weyl semimetals these magnetic monopoles of the Berry curvature can be described as Weyl points, i.e. nondegenerate accidental band crossings. In ferromagnets the exchange splitting introduces band crossings between bands with different spin. Spin-orbit coupling opens a gap at the band crossing since it mixes the different spin components. These gaps occur at a two-dimensional surface in the three-dimensional momentum space and can close for a certain  $\mathbf{k}_0$ . This momentum  $\mathbf{k}_0$  constitutes a Weyl point. In Weyl semimetals where these Weyl points lay exactly at the Fermi energy their influence on transport phenomena is intensively studied [71]. In SrRuO<sub>3</sub> first evidence of Weyl points effecting the spin dynamics have been reported by Itoh *et al.* using neutron Brillouin scattering in powder samples [20]. The successful growth of large single crystals of SrRuO<sub>3</sub> in our institute [10] (see also Section 6.1) facilitates the extensive study of the magnon dispersion (see Section 2.1) and the temperature dependence of the spin dynamics in particular using inelastic neutron scattering. Our study extends the experimental fingerprint of Weyl points in the magnon dispersion and highlights the coupling of spin and charge degrees of freedom in SrRuO<sub>3</sub>.

The publication of these results in *Physical Review Letters* in 2019 is included in this thesis [66].

### 2.2.2 Contribution to Publication and its Relevance in Thesis

The single crystals used for the measurements were grown and characterized by S. Kunkemöller and by the author (Section 6.1) in cooperation with A.A. Nugroho. The neutron scattering data presented in this publication were measured by S. Kunkemöller and by the author. S. Kunkemöller conducted the experiment at 2T, LLB; the author conducted the experiments at 4F1, LLB and PANDA, FRM-II (see Table 2.2). The neutron experiments were accompanied and supervised by M. Braden and supported by the local contacts Y. Sidis and A. Schneidewind at the neutron facilities. The data analysis and modeling of the entire neutron data were conducted by the author. D. Brünig and T. Lorenz conducted the Hall effect measurements and their analysis. The theoretical model and the equations to describe the spin-dynamic parameters were deduced by A. Rosch and D.I. Khomskii. For the published text the author contributed all figures including their captions and contributed to several text sections.

---

<sup>6</sup>This value is calculated with  $S = 0.8$  given by  $M_{\text{sat}}$  and  $g = 2$ .

<sup>7</sup>The error can not be estimated since this value results from the model adjustments based on qualitative fitting of the TOF data in Figure 2.8.

The presented results arise from the temperature dependence study of the magnon dispersion which completes the findings about the magnon dispersion at low temperature described in Section 2.1 and give experimental evidence how spin-orbit coupling effects significantly magnetic correlations in the Ruddlesden-Popper ruthenates, specifically in SrRuO<sub>3</sub>.

## Interplay of Electronic and Spin Degrees in Ferromagnetic SrRuO<sub>3</sub>: Anomalous Softening of the Magnon Gap and Stiffness

K. Jenni,<sup>1</sup> S. Kunkemöller,<sup>1</sup> D. Brüning,<sup>1</sup> T. Lorenz,<sup>1</sup> Y. Sidis,<sup>2</sup> A. Schneidewind,<sup>3</sup> A. A. Nugroho,<sup>4</sup> A. Rosch,<sup>5</sup> D. I. Khomskii,<sup>1</sup> and M. Braden<sup>1,\*</sup>

<sup>1</sup>*II. Physikalisches Institut, Universität zu Köln, Zùlpicher Str. 77, D-50937 Köln, Germany*

<sup>2</sup>*Laboratoire Léon Brillouin, C.E.A./C.N.R.S., F-91191 Gif-sur-Yvette CEDEX, France*

<sup>3</sup>*Jùlich Centre for Neutron Science (JCNS) at Heinz Maier-Leibnitz Zentrum (MLZ), Forschungszentrum Jùlich GmbH, Lichtenbergstraße 1, 85748 Garching, Germany*

<sup>4</sup>*Faculty of Mathematics and Natural Science, Institut Teknologi Bandung, Jalan Ganesha 10, 40132 Bandung, Indonesia*

<sup>5</sup>*Institut für Theoretische Physik, Universität zu Köln, Zùlpicher Str. 77a, D-50937 Köln, Germany*



(Received 11 February 2019; published 3 July 2019)

The magnon dispersion of ferromagnetic SrRuO<sub>3</sub> was studied by inelastic neutron scattering experiments on single crystals as a function of temperature. Even at low temperature the magnon modes exhibit substantial broadening pointing to strong interaction with charge carriers. We find an anomalous temperature dependence of both the magnon gap and the magnon stiffness, which soften upon cooling in the ferromagnetic phase. Both effects trace the temperature dependence of the anomalous Hall effect and can be attributed to the impact of Weyl points, which results in the same relative renormalization in the spin stiffness and magnon gap.

DOI: 10.1103/PhysRevLett.123.017202

Strong spin-orbit coupling (SOC) causes intertwining of charge and spin degrees of freedom, which may result in various fascinating phenomena such as Weyl semimetals [1–3], multiferroics [4], or spin liquids with exotic excitations [5,6]. For a ferromagnetic metal the combination of magnetic exchange with strong SOC splits the bands and causes the emergence of Weyl points. These Weyl points possess strong impact not only on the charge transport [7] but also on the magnetic properties. The anomalous Hall effect can capture the impact of the Weyl points on the charge dynamics. As we will show below, the same physics influences also directly the magnon dispersion: the magnon anisotropy gap [8] and stiffness.

SrRuO<sub>3</sub> [9–11] with the *4d* ion Ru<sup>4+</sup> is a prime candidate to observe the impact of strong SOC in a ferromagnetic metal. It crystallizes in the cubic perovskite structure but undergoes two structural phase transitions at 975 and 800 K into an orthorhombic phase (space group *Pnma*) associated with rotations of the RuO<sub>6</sub> octahedra [9,12,13]. The ferromagnetic transition occurs at 165 K in our single crystals and at low temperature a magnetization of  $\sim 1.6\mu_B$  is observed at 6 T [14]. The electric resistivity is linear at moderate temperatures and breaks the Ioffe-Regel limit, but it drops in the ferromagnetic phase with a clear kink at the ferromagnetic  $T_c$  [15,16] attaining very low residual resistivity values of only  $3\ \mu\Omega\text{cm}$  in high-quality single crystals [14,17]. This coupling of ferromagnetic excitations and charge transport inspired the proposal of spin-triplet pairing in the superconducting sister compound Sr<sub>2</sub>RuO<sub>4</sub> [18], in which quasiferromagnetic excitations could only

recently be observed in neutron experiments [19]. The anomalous Hall effect in SrRuO<sub>3</sub> shows a peculiar temperature dependence undergoing a sign change [7,8,11,20–22]. Fang *et al.* [7] proposed that the anomalous Hall effect in SrRuO<sub>3</sub> arises from the impact of magnetic monopoles in momentum space associated with Weyl points. The magnetic exchange splitting combined with the impact of SOC causes Weyl points in the band structure [7,8], which DFT calculations predict to occur near the Fermi level [23].

More recently Itoh *et al.* argued that the Weyl points not only induce the peculiar temperature dependence of the anomalous Hall effect but also affect the spin dynamics. At each Weyl point, index *i*, two bands cross and the single-particle current  $j_n^{W,i} = e\sum_m v_{nm}^i \sigma^m$  and magnetization  $m_n^{W,i} = \sum_m g_{nm}^i \mu_B (\hbar\sigma^m/2)$  are proportional to each other [1]

$$\mathbf{m}^{W,i} = \frac{\hbar\mu_B}{2e} \mathbf{g}^i (\mathbf{v}^i)^{-1} \mathbf{j}^{W,i}, \quad (1)$$

where  $\mathbf{g}^i$  is the *g* tensor,  $n, m = x, y, z$ ,  $\mathbf{v}^i$  the tensor of Fermi velocities characterizing the Weyl point *i*, and  $\sigma^m$  are the Pauli matrices encoding the two crossing bands. The intimate relation of current, magnetization, and Berry phases will be tested by our Letter.

Inelastic neutron scattering (INS) experiments in Ref. [8] indeed find a temperature dependence of the magnon gap resembling that of the anomalous Hall effect while the magnon stiffness was claimed to exhibit a normal temperature dependence, i.e., a hardening upon cooling. However,

these measurements were performed with powder samples that do not give direct access to the parameters of the magnon dispersion. Here we report on INS, magnetization, and the anomalous Hall effect measurements on single-crystalline SrRuO<sub>3</sub>. We confirm a close similarity between the temperature dependencies of the magnon gap and the anomalous Hall conductivity, but the magnon gap differs from the powder experiment by almost a factor of 2. Furthermore, the magnon stiffness also softens upon cooling in the ferromagnetic phase in contrast to the powder INS study. We argue that this unusual temperature dependence originates from the coupling of current and magnetization thus confirming the impact of the anomalous Hall effect on magnetization dynamics.

Large single crystals of SrRuO<sub>3</sub> were grown by the floating-zone technique and characterized by resistivity and magnetization measurements [14]. For the INS experiments six crystals with a total mass of  $\sim 6$  g were coaligned in the [100]/[011] scattering plane in respect to the pseudocubic lattice with  $a_c \sim 3.92$  Å. INS experiments were performed on cold triple-axis spectrometers (TAS) 4F at the Laboratoire Léon Brillouin and PANDA at the Meier-Leibnitz Zentrum, and on the thermal TAS 2T at the Laboratoire Léon Brillouin. The anomalous Hall effect was measured on a rectangular sample with edge lengths of  $2.2 \times 1.64 \times 0.193$  mm<sup>3</sup> along the cubic directions [1 $\bar{1}$ 0], [001], and [110], respectively. We applied the electrical current  $I_x$  (typically 5 mA) along [1 $\bar{1}$ 0] (orthorhombic  $a$ ), the external magnetic field along [110] (the easy axis, orthorhombic  $c$ , up to  $\pm 7$  T) and measured the longitudinal ( $U_x || I_x$ ) and the transverse voltage  $U_y || [001]$  (orthorhombic  $b$ ). Using a SQUID magnetometer, we also measured the magnetization  $M$  of this sample for the same field direction in order to precisely determine the normal and anomalous Hall effects. Further experimental details are given in the Supplemental Material [24].

Figure 1 shows the INS data obtained by constant energy scans across the magnon dispersion on cold and thermal TAS. The peaks arising from the magnon on both sides of the (100) Bragg points are clearly visible and allow for a reliable determination of the dispersion. In order to quantitatively analyze these data we calculate the folding of the magnon dispersion with the resolution of the cold and thermal TAS using the RESLIB program package [25]. The lines superposed to the constant energy scans refer to this folding procedure with only a few global fit parameters. For small momenta, the magnon dispersion can approximately be described by  $E_0(\mathbf{q}) \approx \Delta + Dq^2$ , with the anisotropy gap  $\Delta$  and the magnon stiffness  $D$ . Magnetic anisotropy is sizable in SrRuO<sub>3</sub> as it can be inferred from the macroscopic magnetic anisotropy [14,26,27] and the shape memory effect [17] and from an optical study [28]. The small orthorhombic distortion of SrRuO<sub>3</sub> induces a tiny anisotropy in  $D$ , see below. Note, that throughout the Letter we use reduced reciprocal lattice units with respect to the

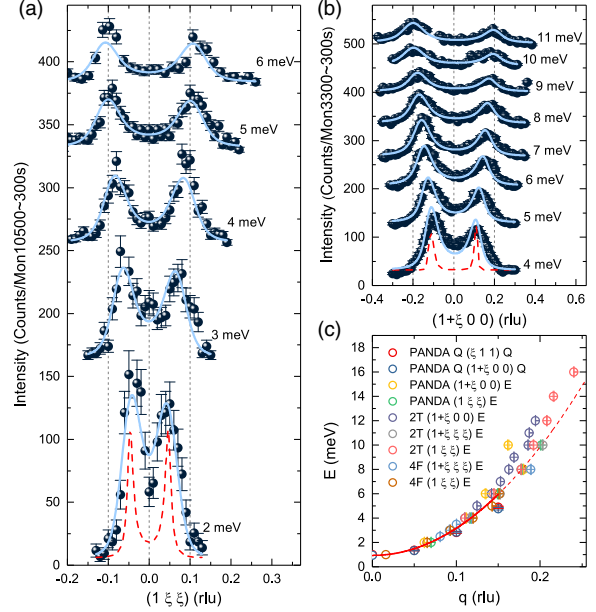


FIG. 1. (a) and (b) Constant energy scans across the magnon dispersion in SrRuO<sub>3</sub> at various energies obtained at  $T = 10$  K on the cold TAS 4F and on the thermal TAS 2T, respectively. Lines represent the folding of the modeled magnon dispersion including a broadening term with the resolution function of the spectrometer; data are vertically offset for clarity. Dashed lines illustrate the experimental resolution that would describe the data in the absence of any magnon broadening. (c) Combined magnon dispersion traced against the length of the magnon propagation vector  $|\vec{q}|$  in relative lattice units. The line reproduces the quadratic low- $q$  behavior defining the magnon stiffness.

pseudocubic cell,  $2\pi/a_c$ , but the stiffness is typically given in units of  $\text{meV \AA}^2$ . In order to describe the measured scan profiles we need to assume a width of the magnon modes that amounts to 40% of their energy. Part of this broadening can stem from the twinning of the crystals superposing different direction of the orthorhombic lattice, but due to the small orthorhombic distortion this broadening should be of the order of a few percent only. Magnons in SrRuO<sub>3</sub> thus exhibit strong scattering most likely due to the coupling to electrons, see also the kink in resistivity at  $T_c$  [15,16], and due to the presence of sizable SOC. The dispersion, which for small  $|\mathbf{q}|$  values is quadratic, is presented in Fig. 1(c). A consistent description of the data at low temperatures is obtained yielding  $D = 87(2)$   $\text{meV \AA}^2$  and  $\Delta = 0.94(3)$  meV and an energy width of  $0.4E_0(q)$ . Note that the gap  $\Delta$  is almost a factor of 2 smaller than the result obtained from the powder experiment, and also the stiffness  $D$  considerably differs [8].

With the better resolution of the cold TAS 4F we scanned across the magnon gap at the zone center; see Fig. 2. Again the gap can be directly read from the raw data in contrast to the previous powder INS experiment [8]. Our single-crystal INS result further agrees with the optical study [28] and

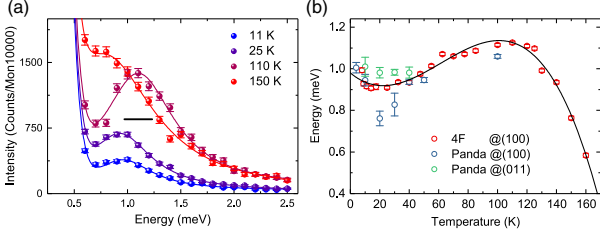


FIG. 2. (a) Energy scans at the magnetic (and nuclear) Brillouin zone center (100) across the magnon gap arising from anisotropy. The data are taken at the cold TAS 4F with final neutron energy of 4.98 meV. The resolution (full width at half maximum) is indicated by the horizontal bar. (b) The resulting gap values as a function of temperature. Data taken on the cold TAS PANDA taken on an untwinned crystal are included; the line is a guide to the eye.

with the extrapolation of the anisotropic magnetization [17]. The easy axis of SrRuO<sub>3</sub> is found along the orthorhombic  $c$  direction in  $Pnma$  notation [17] and therefore two anisotropy gaps can be expected for the orthorhombic system, i.e., for rotating the magnetic moments towards the  $a$  and  $b$  directions. Our data indicate little splitting for the two gaps that were examined with an untwinned smaller crystal on PANDA. This crystal was first mechanically detwinned [14] and then mounted with its cubic [011] direction parallel to a magnetic field in a vertical field cryostat. After applying a magnetic field of 3 T a fully monodomain crystal was obtained [17] with the orthorhombic  $c$  axis, the magnetic easy axis, parallel to cubic [011], and thus  $a \parallel [011]$  and  $b \parallel [100]$ . The gaps measured at the scattering vectors  $\mathbf{Q} = (100)$  and  $(011)$  correspond thus to the rotation of the moments towards  $a$  and  $b$ , respectively. In agreement with the macroscopic analysis in Ref. [17] the  $a$  direction is only slightly softer than  $b$ . The anomalies of the gap temperature dependence are qualitatively confirmed by these monodomain measurements, but the temperature dependence of the averaged gap profits from higher statistics. From the constant  $\mathbf{Q}$  scans at the zone center we deduce the temperature dependence of the anisotropy gap by fitting a Gaussian peak; see Fig. 2(b). In only qualitative agreement with the powder INS [8] there is a rather anomalous softening and rehardening of the gap upon cooling deep in the ferromagnetic phase, while the closing of the gap upon heating above the Curie temperature corresponds to the expected behavior.

Figure 3 summarizes the temperature dependence of the magnon stiffness. We recorded constant energy scans at 8 meV between 13 and 280 K that were analyzed by fitting the  $D$  value through the folding of the resolution with the dispersion. The characteristic two peak structure remains visible even well above the Curie temperature, which underlines the persistence of ferromagnetic correlations. This scattering agrees with the expectation for a nearly ferromagnetic metal, which still exhibits a paramagnon

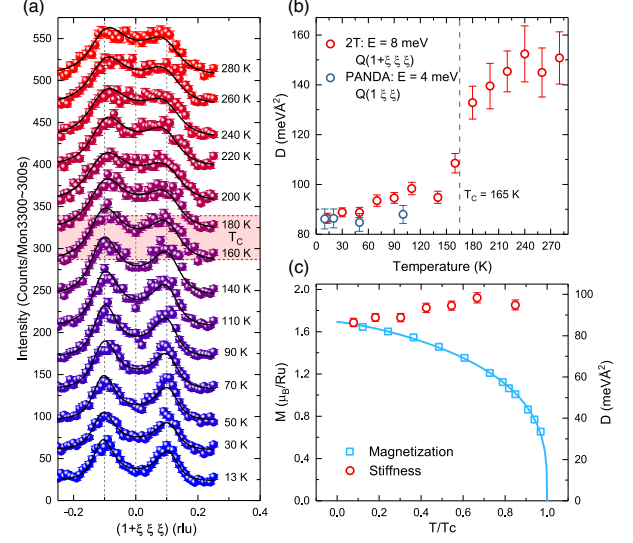


FIG. 3. (a) Constant energy scans across the magnon dispersion in SrRuO<sub>3</sub> at 8 meV obtained at the thermal TAS 2T. Lines represent the folding of the magnon dispersion including a broadening term with the resolution function of the spectrometer. (b) Temperature dependence of the magnon stiffness obtained from the data in (a) and from additional measurements on the cold TAS PANDA. Above the ferromagnetic transition  $D$  just describes the position of the paramagnon scattering, see text. (c) Comparison of the temperature dependencies of the magnetization and that of the magnon stiffness.

signal very similar to that of the ferromagnetic material with broad magnons [29]. The fitted  $\bar{q}$  positions can be directly transformed into temperature-dependent stiffness constants,  $D$ , by taking the temperature dependent anisotropy gaps into account, Fig. 3(b). The magnon stiffness clearly softens upon cooling well below the Curie temperature, while the magnetization increases. In Fig. 3(c) we compare the stiffness to the spontaneous magnetization, because in a usual system one expects the two quantities to scale. In contrast, in SrRuO<sub>3</sub> the stiffness softens upon cooling well below  $T_c$ . Scaling the magnetization  $M_s$  and  $D$  by the low-temperature values, one recognizes that at 0.8 times  $T_c$  the stiffness is almost twice as large as what follows from  $D \propto m$ . In contrast, the powder INS experiment [8] just reported such a scaling relation for the magnon stiffness [30].

The dynamics of small-amplitude, long-wavelength oscillations of the magnetization in a ferromagnet polarized in the  $z$  direction can be described by the action [8]

$$S \approx \frac{1}{2} \int d^3r dt \alpha(T) \left( \frac{dm_x}{dt} m_y - \frac{dm_y}{dt} m_x \right) - \kappa(T) (m_x^2 + m_y^2) - A(T) ((\nabla m_x)^2 + (\nabla m_y)^2) + \dots \quad (2)$$

up to higher order corrections and damping terms. From the corresponding Euler-Lagrange equations one obtains

$$\Delta = \frac{\kappa(T)}{\alpha(T)}, \quad D = \frac{A(T)}{\alpha(T)}. \quad (3)$$

In the absence of spin-orbit coupling  $\alpha$  is exactly given by  $\alpha_0 = \{1/[2m(T)\mu_B]\}$ , where  $m(T)$  is the magnetization density. Taking SOC and the Weyl points into account  $\alpha(T)$  is determined not only by  $m(T)$  but also by the anomalous Hall effect [8,24]

$$\alpha(T) \approx \frac{1}{g\mu_B m(T)} + c(T)\sigma_{xy}^a(T). \quad (4)$$

This equation arises because the time-dependent magnetization induces currents close to the Weyl points; see Eq. (1) and Ref. [24]. Because of the Berry curvature of the Bloch bands, both a transverse current and a transverse magnetization are generated, modifying  $\alpha(T)$ .

Neglecting the  $T$  dependence of  $\kappa(T)$ ,  $c(T)$ , and  $A(T)$ , we obtain from Eqs. (3) and (4) for the spin gap  $\Delta$  [8] and the stiffness  $D$  the same temperature dependence parametrized by

$$\Delta(T) \approx \frac{a_\Delta m(T)/m_0}{1 + b(m(T)/m_0)(\sigma_{xy}(T)/\sigma_0)},$$

$$D(T) \approx \frac{a_D m(T)/m_0}{1 + b(m(T)/m_0)(\sigma_{xy}(T)/\sigma_0)}, \quad (5)$$

where  $m_0 = m(T=0)$  and  $\sigma_0 = (e^2/2\pi\hbar a_c)$ .

In order to verify the scaling between the anomalous Hall effect and the two characteristic parameters of the magnon dispersion in SrRuO<sub>3</sub> we also measured the magnetization and anomalous Hall effect on a single crystal. The magnetization obtained by extrapolating field-dependent magnetization curves to  $H = 0$  T is shown in Fig. 3(c) and can be described by a stretched power law  $m(T) = m_0[1 - (T/T_c)^a]^\beta$  with the parameters  $m_0 = 1.69\mu_B$ ,  $a = 1.27$ , and  $\beta = 0.304$ . The field-dependent magnetization was inserted in the analysis of the anomalous Hall effect measurement performed on the same sample. The comparison of our and previous Hall conductivity results is shown in Figs. 4(a) and 4(b). Because of the larger thickness of the single-crystalline sample the Hall voltage is smaller, but it offers the advantage of more precise magnetization data. Our single-crystal data of the Hall conductivity  $\sigma_{xy}$  agree with previous single-crystal data but only qualitatively with powder and thin film data [8,31]. There is a sign change in  $\sigma_{xy}$  slightly below the ferromagnetic transition. Differences may stem from the twinning and different orientations of the distorted orthorhombic lattices in the powder and thin-film experiments and from differences in sample quality. The temperature dependence of the anomalous Hall effect was fitted by a polynomial and then inserted in Eq. (5) to describe the anomalous softening of the magnon gap in the ferromagnetic phase; see Fig. 4(b). This analysis well reproduces the main

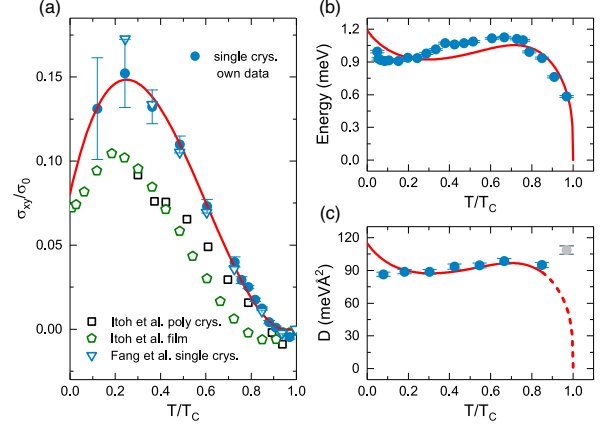


FIG. 4. Comparison of the anomalous Hall effect with the magnon gap and stiffness. (a) Temperature dependence of the anomalous Hall effect normalized to  $\sigma_0$  measured on single crystals and analyzed with the magnetization curves obtained on the same samples [31]. (b) Temperature dependence of the magnon gap (circles) compared to that of the anomalous Hall effect described by the relation (5). (c) Temperature dependence of the magnon stiffness analyzed in comparison to the anomalous Hall effect, relation (5).

feature with  $a_\Delta = 1.66$  meV and  $b = 4.98$ . The same temperature dependence of the anomalous Hall effect was used to describe the softening of the stiffness compared to a normal behavior proportional to the magnetization,  $a_D = 160.90$  meV Å<sup>2</sup>. Again good agreement is obtained, see Fig. 4(c). Taking into account that Eq. (5) completely neglects corrections arising, e.g., from the  $T$  and magnetization dependence of  $K(T)$ ,  $A(T)$ ,  $c(T)$  and from the broadening of the spin waves, the semiquantitative agreement is satisfactory. The temperature dependencies of these entities should be below 10%, while the entire renormalization amounts to about 50%. We emphasize, that the identical correction, i.e., the same  $b$  value, describes the deviation of both the gap and the stiffness from being proportional to the magnetization. This clearly supports a common origin of the unusual softening of spin gap and spin stiffness towards lower temperatures, explained by the coupling of magnetization and current and by the  $T$  dependence of the anomalous Hall effect.

At the phase transition, where  $m(T)$  vanishes, Eq. (5) predicts that  $D(T)$  vanishes also. However, in this temperature regime the broad spin waves smoothly transform into paramagnon scattering [29] with a very similar shape and thus a drop of  $D(T)$  cannot be extracted from the measured neutron scattering data.

In conclusion, we have studied the magnetization, anomalous Hall effect, and magnon dispersion in SrRuO<sub>3</sub> using high-quality single crystals. The magnon modes exhibit sizable broadening, revealing strong scattering by most likely charge carriers. The magnon gap and the magnon stiffness do not follow the temperature dependence

of the spontaneous magnetization. Both quantities soften upon cooling over a large temperature range in the ferromagnetic phase and at least the magnon gap passes through a minimum. These findings can be well explained by the effect of Weyl points situated close to the Fermi level. Such Weyl points possess a well-established impact on the anomalous Hall effect and cause an additional term in the magnetic Hamiltonian. The latter leads to a reduction of both the magnon gap and the stiffness, which scales with the anomalous Hall effect. Our data agree with this scaling between the anomalous Hall effect and the magnon dispersion.

We thank I. Lindfors-Vrejoiu for discussions. This work was funded by the Deutsche Forschungsgemeinschaft (DFG, German Research Foundation)—Project No. 277146847—CRC 1238, projects A02, B01, B04, C02, and C04.

\*braden@ph2.uni-koeln.de

- [1] A. A. Burkov and L. Balents, *Phys. Rev. Lett.* **107**, 127205 (2011).
- [2] X. Wan, A. M. Turner, A. Vishwanath, and S. Y. Savrasov, *Phys. Rev. B* **83**, 205101 (2011).
- [3] S. Murakami, *New J. Phys.* **9**, 356 (2007).
- [4] D. Khomskii, *Physics* **2**, 20 (2009).
- [5] A. Kitaev, *Ann. Phys. (Amsterdam)* **321**, 2 (2006).
- [6] J. c. v. Chaloupka, G. Jackeli, and G. Khaliullin, *Phys. Rev. Lett.* **105**, 027204 (2010).
- [7] Z. Fang, N. Nagaosa, K. S. Takahashi, A. Asamitsu, R. Mathieu, T. Ogasawara, H. Yamada, M. Kawasaki, Y. Tokura, and K. Terakura, *Science* **302**, 92 (2003).
- [8] S. Itoh, Y. Endoh, T. Yokoo, S. Ibuka, J.-G. Park, Y. Kaneko, K. S. Takahashi, Y. Tokura, and N. Nagaosa, *Nat. Commun.* **7**, 11788 (2016).
- [9] J. J. Randall and R. Ward, *J. Am. Chem. Soc.* **81**, 2629 (1959).
- [10] A. Callaghan, C. W. Moeller, and R. Ward, *Inorg. Chem.* **5**, 1572 (1966).
- [11] G. Koster, L. Klein, W. Siemons, G. Rijnders, J. S. Dodge, C.-B. Eom, D. H. A. Blank, and M. R. Beasley, *Rev. Mod. Phys.* **84**, 253 (2012).
- [12] C. W. Jones, P. D. Battle, P. Lightfoot, and W. T. A. Harrison, *Acta Crystallogr. Sect. C* **45**, 365 (1989).
- [13] B. Chakoumakos, S. Nagler, S. Mixture, and H. Christen, *Physica (Amsterdam)* **241–243B**, 358 (1997).
- [14] S. Kunkemöller, F. Sauer, A. A. Nugroho, and M. Braden, *Cryst. Res. Technol.* **51**, 299 (2016).
- [15] P. B. Allen, H. Berger, O. Chauvet, L. Forro, T. Jarlborg, A. Junod, B. Revaz, and G. Santi, *Phys. Rev. B* **53**, 4393 (1996).
- [16] L. Klein, J. S. Dodge, C. H. Ahn, G. J. Snyder, T. H. Geballe, M. R. Beasley, and A. Kapitulnik, *Phys. Rev. Lett.* **77**, 2774 (1996).
- [17] S. Kunkemöller, D. Brüning, A. Stunault, A. A. Nugroho, T. Lorenz, and M. Braden, *Phys. Rev. B* **96**, 220406(R) (2017).
- [18] T. M. Rice and M. Sigrist, *J. Phys. Condens. Matter* **7**, L643 (1995).
- [19] P. Steffens, Y. Sidis, J. Kulda, Z. Q. Mao, Y. Maeno, I. I. Mazin, and M. Braden, *Phys. Rev. Lett.* **122**, 047004 (2019).
- [20] M. Izumi, K. Nakazawa, Y. Bando, Y. Yoneda, and H. Terauchi, *J. Phys. Soc. Jpn.* **66**, 3893 (1997).
- [21] Y. Kats, I. Genish, L. Klein, J. W. Reiner, and M. R. Beasley, *Phys. Rev. B* **70**, 180407(R) (2004).
- [22] N. Haham, Y. Shperber, M. Schultz, N. Naftalis, E. Shimshoni, J. W. Reiner, and L. Klein, *Phys. Rev. B* **84**, 174439 (2011).
- [23] Y. Chen, D. L. Bergman, and A. A. Burkov, *Phys. Rev. B* **88**, 125110 (2013).
- [24] See Supplemental Material at <http://link.aps.org/supplemental/10.1103/PhysRevLett.123.017202> for additional information about experimental details and about the calculation.
- [25] Reslib-manual, Reslib, <http://www.neutron.ethz.ch/research/resources/reslib.html>, Neutron Scattering Sciences Division, Oak Ridge National Laboratory, Oak Ridge, 2007.
- [26] A. Kanbayasi, *J. Phys. Soc. Jpn.* **41**, 1876 (1976).
- [27] G. Cao, S. McCall, M. Shepard, J. E. Crow, and R. P. Guertin, *Phys. Rev. B* **56**, R2916 (1997).
- [28] M. C. Langner, C. L. S. Kantner, Y. H. Chu, L. M. Martin, P. Yu, J. Seidel, R. Ramesh, and J. Orenstein, *Phys. Rev. Lett.* **102**, 177601 (2009).
- [29] T. Moriya, *Spin Fluctuations in Itinerant Electron Magnetism* (Springer-Verlag, Berlin Heidelberg, 1985).
- [30] The discrepancies between our and the previous powder INS results seem to arise from a bad definition of the magnon signal in the powder experiment, where it remains hidden in the elastic line.
- [31] Note that there is an inconsistency in the sign of the AHE data published on SrRuO<sub>3</sub>. In the low-temperature range the AHE is parallel to the normal Hall effect, which corresponds to electron charge carriers, and therefore  $\sigma_{xy} \approx -(\rho_{xy}/\rho_{xx}^2)$  is positive in our notation.

## Interplay of electronic and spin degrees in ferromagnetic SrRuO<sub>3</sub>: anomalous softening of magnon gap and stiffness - supplemental material

- *INS experiments* - INS experiments were performed on cold triple-axis spectrometers (TAS) 4F at the Laboratoire Léon Brillouin and PANDA at the Meier-Leibnitz Zentrum, and on the thermal TAS 2T at the Laboratoire Léon Brillouin. All instruments were equipped with pyrolytic graphite (002) monochromator and analyzer crystals. Scans were performed with constant final energies of 14.7 and 4.98 meV and pyrolytic graphite and cooled Be filters were inserted behind the sample on 2T and 4F and PANDA, respectively.

- *AHE experiments* - The sample for the AHE measurements was cut from a larger single crystal that was mechanically detwinned yielding typically  $\approx 85\%$  single-domain crystals. Fully detwinning is achieved when a magnetic field is applied along the [110] direction, which then becomes the magnetic easy-axis  $c$ . In order to compensate the misalignment of the  $U_y$ -contact positions, we antisymmetrized the raw data of  $U_y$  by calculating  $U_H(B) = (U_y(+B) - U_y(-B))/2$  and derived the Hall resistivity  $\rho_{xy}(B) = U_H d / I_x$  where  $d = 0.193$  mm denotes the sample thickness and  $I_x$  the applied current of typically 5 mA. The normal and the anomalous Hall constants  $R_N$  and  $R_A$ , respectively, were determined from fits of  $\rho_{xy}(B) = R_N B + R_A \mu_0 M(B)$  using the  $M(B)$  data obtained from magnetization loops measured with a SQUID magnetometer on the sample sample for the same field orientation. The anomalous Hall resistivity  $\rho_{xy}(B = 0) = R_A \mu_0 M_s$  with the spontaneous magnetization  $M_s$  is obtained through linear extrapolations  $M_s = M(B \rightarrow 0)$  of the measured  $M(B)$  loops. In order to convert  $\rho_{xy}(B = 0)$  to the anomalous Hall conductivity  $\sigma_{xy} = -\rho_{xy}/(\rho_{xx}^2 + \rho_{xy}^2)$  we use the zero-field resistivity  $\rho_{xx} = U_x A_x / (I_x d_x)$  where  $d_x = 0.64$  mm is the distance of the  $U_x$  contacts and  $A_x = 0.425$  mm<sup>2</sup> the sample's cross section.

- *Magnetization dynamics and calculation of  $\alpha$*  - A description of the magnetization dynamics by a simple (classical) Heisenberg model  $H = \sum_{ij} J \mathbf{S}_i \cdot \mathbf{S}_j - K S_{i,z}^2$  with anisotropy  $K$  predicts  $\Delta = K \langle S_z \rangle$  and  $D = 2J \langle S_z \rangle a_c^2$  with  $J=3.5(1)$  meV ( $\langle S_z \rangle=0.8$  is estimated from the magnetization assuming a  $g$  factor of 2). Such a description is, however, of limited validity for the metallic SrRuO<sub>3</sub> and cannot predict the temperature dependence of  $\Delta$  and  $D$ . Instead, one can use the effective field theory, Eq. (2) of the main text.

In the absence of spin-orbit coupling, the factor  $\alpha(T)$  is exactly given by  $\alpha(T) = 1/(2\mu_B m(T))$ . This can be obtained from commutation relation  $[S_x, S_y] = i\hbar S_z$ , where the total spin  $S_z$  can in the thermodynamic limit be replaced by  $\langle S_z \rangle = V m(T)/(g\mu_B)$  with  $g = 2$  and the system volume  $V$ . In an itinerant system with spin-orbit coupling,  $\alpha(T)$  arises from integrating out of the electrons and is given by the transverse qcomponent of the

inverse of the bare electron susceptibility

$$\alpha = - \lim_{\omega \rightarrow 0, \mathbf{q} \rightarrow 0} \frac{(\chi_0^{-1}(\mathbf{q}, \omega))_{xy}}{i\omega} \quad (1)$$

$\alpha$  is therefore computed from a correlation function of the total magnetization of the conduction electron. Using that close to each Weyl nodes the electric current and the magnetization are proportional to each other, the total magnetization can be written as

$$\mathbf{m} \approx \mathbf{m}_0 + \frac{\hbar\mu_B}{2e} \sum_i \mathbf{g}^i (v^i)^{-1} (\mathbf{j}^{W,i} - \mathbf{j}^{W,\bar{i}}) \quad (2)$$

where  $\mathbf{m}_0$  are contributions to the magnetization not related to the Weyl points, while we used Eq. (1) (main text) to express the magnetization close to the Weyl points by current operators. Here we use the SrRuO<sub>3</sub> is inversion symmetric. Weyl points therefore occur in pairs connected by inversion symmetry which are denoted by the indices  $i$  and  $\bar{i}$ . Inversion symmetry maps  $\mathbf{j}^{W,i}$  to  $-\mathbf{j}^{W,\bar{i}}$ . Weyl points can be viewed as source of Berry curvature in momentum space, which is the origin of the anomalous Hall effect and thus are expected to give the main contribution to this quantity and its temperature dependence. The anomalous Hall conductivity is given the current-current correlation function  $\sigma_{xy}^a = \frac{\langle j_x j_y \rangle_\omega}{i\omega} \approx \sum_i \frac{\langle j_x^{W,i} j_y^{W,i} \rangle_\omega}{i\omega}$ , where we assumed that it is dominated by contributions close to the Weyl points and that corrections from scattering between different Weyl nodes give only small contributions to the anomalous Hall effect. Under these conditions

$$\alpha(T) \approx \frac{1}{g\mu_B m(T)} + c(T) \sigma_{xy}^a(T) \quad (3)$$

where we approximate the contribution from  $\mathbf{m}_0$  by its value without spin-orbit coupling. The constant  $c(T) \sim (\hbar\mu_B g / (ev\chi_{0,xx}))^2$  is proportional to  $\chi_{0,xx}^{-2}$ . The bare transverse susceptibility is approximately given by  $\chi_{0,xx} \approx m/B_{ex}$  where  $B_{ex} \sim Jm$  is the exchange field. Therefore  $c(T)$  is expected to depend only weakly on temperature.

The physical mechanism behind Eq. (3) is that the time-dependent magnetization induces forces on the electrons which can be described as electric fields proportional to  $d\mathbf{m}/dt$ . These forces have opposite sign on Weyl fermions at momenta related by inversion symmetry, thus the net current vanishes. The Berry curvature of the Bloch bands, however, has the effect that  $d\mathbf{m}_x/dt$  induces at each Weyl node currents in the  $\pm y$  direction inducing a net magnetization  $m_y$ . This mechanism leads to a correction to  $\alpha$  and thus, according to Eq.(3) in the main text, to corrections to the spin stiffness and the spin gap.

## 2.3 Chirality of Spin Excitations

### 2.3.1 Introduction

The handedness of spin-wave excitations arises from the quantum dynamics of spin and is therefore governed by the commutation relation of spin components  $[S^\alpha, S^\beta] = i\hbar\epsilon_{\alpha\beta\gamma}S^\gamma$  with  $\alpha, \beta, \gamma = x, y, z$  and the Levi-Cevita symbol  $\epsilon_{\alpha\beta\gamma}$ . This relation determines the direction of spin precession of the total magnetization in ferromagnets to be right-handed. The spin dynamics are governed by the Heisenberg Hamiltonian (Equation 2.2). The time dependence of a spin at site  $j$  in a one-dimensional and ferromagnetically ordered chain can be derived in a semiclassical approach [62]. Here the Hamiltonian reduces to

$$\mathcal{H} = -2 \sum_i J \mathbf{S}_i \cdot \mathbf{S}_{i+1} \quad (2.9)$$

Using the Schrödinger equation the time dependence of the expected value for the spin at site  $j$  is

$$\frac{d\langle \mathbf{S}_j \rangle}{dt} = \frac{1}{i\hbar} \langle [\mathbf{S}_j, \mathcal{H}] \rangle \quad (2.10)$$

$$= \frac{2J}{\hbar} \langle \mathbf{S}_j \times (\mathbf{S}_{j-1} + \mathbf{S}_{j+1}) \rangle. \quad (2.11)$$

In the ground state all spins (treated as classical vectors) are aligned along the  $z$  axis (arbitrary choice), so that  $S_j^z = S$ ,  $S_j^x = S_j^y = 0$ . When the excited state is considered only to deviate slightly from the ground state so that  $S_j^z \approx S$  and  $S_j^x, S_j^y \ll S$ , the time dependence of the single spin components become

$$\frac{dS_j^x}{dt} \approx \frac{2JS}{\hbar} (2\mathbf{S}_j^y - \mathbf{S}_{j-1}^y - \mathbf{S}_{j+1}^y) \quad (2.12)$$

$$\frac{dS_j^y}{dt} \approx -\frac{2JS}{\hbar} (2\mathbf{S}_j^x - \mathbf{S}_{j-1}^x - \mathbf{S}_{j+1}^x) \quad (2.13)$$

$$\frac{dS_j^z}{dt} \approx 0. \quad (2.14)$$

These equations can be solved with a normal mode ansatz

$$S_j^{x,y} = A_{x,y} \exp(i(jqa - \omega t)) \quad (2.15)$$

which yields  $A_x = iA_y$ . The  $x$  and  $y$  component of the spin motion are therefore  $\pi/2$  out of phase. The spin component perpendicular to the  $z$  axis can be written as

$$\mathbf{S}_\perp = A \begin{pmatrix} \cos(jqa - \omega t) - i \sin(jqa - \omega t) \\ \sin(jqa - \omega t) + i \cos(jqa - \omega t) \\ 0 \end{pmatrix}. \quad (2.16)$$

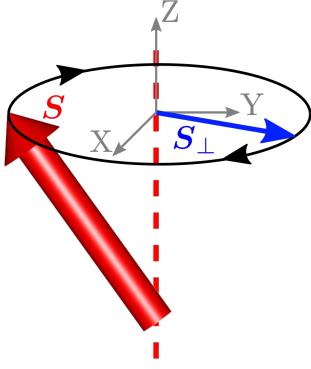


**Figure 2.9: Spin precession in a spin wave.** The spin  $\mathbf{S}$  at site  $i$  in the excited state precesses around the quantization axis  $Z$  clockwise (when looking along  $Z$ ). The perpendicular component  $\mathbf{S}_\perp$  follows Equation 2.16.

the direction of spin precession, i.e. handedness of spin excitation, as the following:

$$C_\phi^{xy} = \frac{1}{2V} \sum_{m,m',\mathbf{k}} \frac{f(\epsilon_{m'\mathbf{k}}) - f(\epsilon_{m\mathbf{k}})}{(\epsilon_{m\mathbf{k}} - \epsilon_{m'\mathbf{k}})^2} \cdot |\langle m\mathbf{k}|S^+|m'\mathbf{k}\rangle|^2. \quad (2.17)$$

In a system without spin-orbit coupling the band  $m$  decomposes into the spin part  $\sigma$  and the orbital part  $n$ . In this case the matrix element  $\langle m\mathbf{k}|S^+|m'\mathbf{k}\rangle$  containing the ladder spin operator is only nonzero for the states  $|n\mathbf{k}\uparrow, \downarrow\rangle$ . Their energy difference  $\epsilon_{n\mathbf{k}\uparrow} - \epsilon_{n\mathbf{k}\downarrow}$  represents the ferromagnetic exchange energy splitting and is therefore negative. This results in a negative difference of the Fermi-Dirac distribution  $f(\epsilon_{m'\mathbf{k}}) - f(\epsilon_{m\mathbf{k}})$  which yields a negative sign of the coefficient  $C_\phi^{xy}$ . When spin-orbit coupling is introduced this proof does not hold anymore since the band  $m$  cannot be split into spin and orbital part. Now two states  $|m\mathbf{k}\rangle$  and  $|m'\mathbf{k}\rangle$  can produce a nonzero matrix element for which the energy and the corresponding Fermi-Dirac distribution difference becomes positive. This would lead to a positive coefficient and therefore to a left-handed spin excitation.

On basis of their theoretical derivations they formulate four necessary conditions for the realization of the left-handed magnon in a ferromagnet: (i) basically quenched orbital moment, (ii) strong spin-orbit coupling, (iii) finite contribution of the majority and minority spins at  $E_F$ , and (iv) band degeneracy near the Fermi level. Onoda *et al.* proposed SrRuO<sub>3</sub> as a candidate material for the realization of the left-handed magnon or at least for a partial change of the chirality, because SrRuO<sub>3</sub> seems to perfectly fulfill these conditions. The general impact of spin-orbit coupling on the magnon dispersion in this material beyond the simple anisotropy gap is well established, see Section 2.1 and [66].

The authors also suggested polarized neutron scattering as the most suitable experimental method to search for left-handed spin-wave excitations. The neutron polarization is only determined by the sign of the correlation function and does not depend on the sign of the effective  $g$  factor as it does in electronic spin resonance experiments. With the large crystal volume (Section 2.5) it is possible to conduct the

The motion of  $\mathbf{S}_\perp$  corresponds to an anti-clockwise rotation around the  $z$  axis and is therefore right-handed (Figure 2.9).

Although the handedness is based on a basic principle of quantum physics there is the possibility to reverse it given the right conditions. Using electric and magnetic resonances simultaneously in a certain frequency range the handedness of propagating electromagnetic waves can be changed from right to left [72]. It is worth to search for the analogous phenomena in magnetic systems.

Onoda, Mishchenko and Nagaosa investigated the handedness of magnons in a ferromagnet taking spin-orbit coupling into account [73]. They identify the coefficient of the linear term in the spin wave dynamics whose sign determines

polarization analysis of inelastic scattering in great detail. Therefore the magnetic scattering at a ferromagnetic zone center is studied in four spin-flip channels to extract the chiral scattering contribution and to determine the handedness of the magnon. In addition the temperature dependence of the magnon chirality close to the phase transition is investigated.

### 2.3.2 Results and Analysis

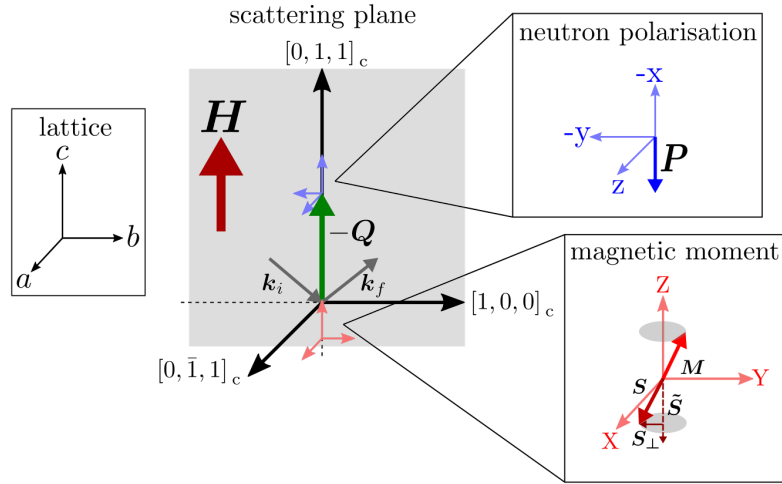


**Figure 2.10: Schematic representation of the scattering geometry of the experiment.** The scattering geometry given by the spectrometer configuration is shown including three additional coordinate systems relative to the scattering plane which are relevant for the analysis. All coordinate systems are given by the external magnetic field  $\mathbf{H}$  since it determines the sample orientation (black), the neutron polarization (blue), and the magnetic moment (spin) of the sample (red).

The anisotropy gap is measured by constant  $\mathbf{Q}$  scans at the ferromagnetic zone center  $\mathbf{Q} = (0, 1, 1)$  following the pseudo-cubic lattice. A horizontal magnetic field of 3.8 T is applied parallel to  $\mathbf{Q}$  and flippers are used in front (F1) and behind (F2) the sample to facilitate a full polarization analysis. Figure 2.10 displays a schematic representation of the scattering plane and the orientation of relevant coordinate systems relative to it. This should help to clarify the relative orientations of important vectors relevant for the analysis of this experiment. The scattering plane is given by the orientation of the sample lattice. The magnetic field determines the orientation of the sample lattice as all twins orient along the easy axis when the sample is cooled down in field. This results in a mono-domain state with the orthorhombic  $c$  axis pointing along the external field [13]. The scattering vector  $\mathbf{Q} = \mathbf{k}_i - \mathbf{k}_f$  (green) is given by the spectrometer configuration determining the incoming  $\mathbf{k}_i$  and outgoing  $\mathbf{k}_f$  vectors of the neutrons. Here the scattering vector is chosen to be  $\mathbf{Q} = (0, 1, 1)$  (in the pseudo-cubic lattice) which therefore points along the orthorhombic  $c$  axis. The coordinate system of the neutron polarization (blue) is defined by the scattering vector (see Section 6.2.2). The neutron polarization  $\mathbf{P}$  has to be collinear to the magnetic field and is therefore also collinear to  $\mathbf{Q}$ . In the case of IN12 the neutron polarization is antiparallel to the guide field and therefore also to the external field  $\mathbf{H}$  at the sample (see Section 2.5). The  $Z$  axis of the coordinate system of the

magnetic moment  $\mathbf{M}$  (red) points along the magnetic field. Since the electron spin points in the opposite direction as the magnetic moment the spins in the ground state are parallel to  $\mathbf{Q}$ . The unit vector of spin points therefore in  $-Z$  direction and is labeled  $\tilde{\mathbf{S}}$ . The spin-wave excitation creates a contribution perpendicular to the  $Z$  axis  $\mathbf{S}_\perp$  (Equation 2.16) which gives a scattering contribution since only magnetic moment perpendicular to  $\mathbf{Q}$  contributes to the scattering cross section (see Section 6.2.2).

To summarize, the following conditions hold for the experimental setup:

- $\mathbf{H}$  is antiparallel to  $\tilde{\mathbf{Q}} \rightarrow (\tilde{\mathbf{H}} \cdot \tilde{\mathbf{Q}}) = -1$
- $\mathbf{H}$  is antiparallel to  $\tilde{\mathbf{P}} \rightarrow (\tilde{\mathbf{H}} \cdot \tilde{\mathbf{P}}) = -1$
- $\mathbf{H}$  is antiparallel to  $\tilde{\mathbf{S}} \rightarrow (\tilde{\mathbf{H}} \cdot \tilde{\mathbf{S}}) = -1$

$$\Rightarrow (\tilde{\mathbf{Q}} \cdot \tilde{\mathbf{S}}) = 1 \text{ and } (\tilde{\mathbf{P}} \cdot \tilde{\mathbf{Q}}) = 1$$

Unit vectors are marked by  $\tilde{\square}$ .

$$\left( \frac{d^2\sigma}{d\Omega dE} \right) \propto [1 + (\tilde{\mathbf{Q}} \cdot \tilde{\mathbf{S}})^2 - 2(\tilde{\mathbf{P}} \cdot \tilde{\mathbf{Q}})(\tilde{\mathbf{Q}} \cdot \tilde{\mathbf{S}})] \quad (2.18)$$

With this experimental setup the chiral contribution of magnetic scattering can be measured since the neutron polarization  $\mathbf{P}$  is collinear with the scattering vector  $\mathbf{Q}$ . Following the definitions in Section 6.2.2 the intensities measured in this configuration are labeled  $I_x$ . Furthermore the measured intensities are labeled with a + or - according to the flipper states of the respective channels. Here + means the flipper is switched off while - denotes an active flipper. These flipper states correspond to the neutron polarization states via the experimental setup which leads to the following correlation:

- +  $\equiv \downarrow$ : when the flipper is switched off the neutron polarization is **antiparallel** to the guide field
- -  $\equiv \uparrow$ : when the flipper is switched on the neutron polarization is **parallel** to the guide field

With this nomenclature we can define the four spin-flip channels for this particular experimental setup: nSFoff =  $I_x^{++} = I_x^{\downarrow\downarrow}$ , nSFon =  $I_x^{--} = I_x^{\uparrow\uparrow}$ , SF1 =  $I_x^{-+} = I_x^{\downarrow\uparrow}$ , and SF2 =  $I_x^{+-} = I_x^{\uparrow\downarrow}$ . Note here that the first superscript is related to the spin flipper in front of the sample or the polarization state of the incoming neutron with  $k_i$  and the second superscript is related to the flipper after the sample or the polarization state of the outgoing neutron with  $k_f$ . The non-spin-flip channels nSFoff and nSFon measure the purely nuclear scattering contribution while the spin-flip channels collect the magnetic scattering contribution containing the chiral scattering. Using Equation 2.18 taken from Section 6.2.2 the scattering contribution of the creation (positive energy transfer) of a right-handed magnon appears in the spin-flip channel  $I_x^{-+}$  (SF1) where the first spin flipper is active while the second one behind the sample is switched off. If the first flipper is switched off, the neutron polarization  $\mathbf{P}$  is parallel to  $\mathbf{Q}$  which lets the scattering cross section of the creation of a

right-handed magnon in eqn:SRO-magnon-creation vanish. By switching the first flipper in front of the sample on the neutron polarization is antiparallel to the scattering vector which results in  $(\tilde{\mathbf{P}} \cdot \tilde{\mathbf{Q}}) = -1$ . This produces a non-zero cross section. Scattering from a left-handed magnon would correspondingly appear in the channel  $I^{+-}$  (SF2) because the minus sign in Equation 2.18 is reversed for the creation of left-handed magnons. Therefore we can define a criterion for the handedness of the measured magnon using the definition of the chiral ratio CR:

$$\text{CR} = \frac{I_x^{\downarrow\downarrow} - I_x^{\downarrow\uparrow}}{I_x^{\downarrow\downarrow} + I_x^{\downarrow\uparrow}} = \frac{I_x^{-+} - I_x^{+-}}{I_x^{-+} + I_x^{+-}} \begin{cases} > 0 \rightarrow \text{right-handed} \\ < 0 \rightarrow \text{left-handed} \end{cases} \quad (2.19)$$

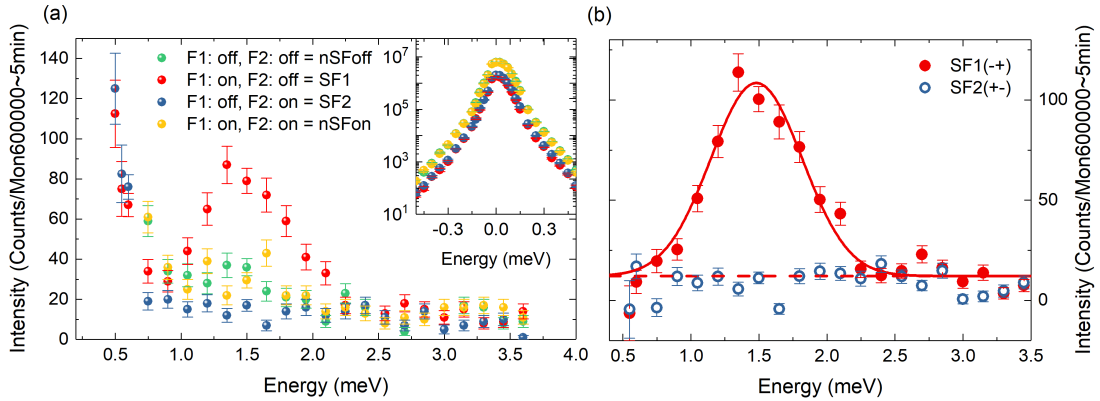


**Figure 2.11: Polarization analysis of the magnon gap.** (a) Constant  $\mathbf{Q}$  scans at  $\mathbf{Q} = (0, 1, 1)$  and  $T = 10$  K are shown using a horizontal magnetic field and different flipper configurations. The magnetic signal of the anisotropy gap in the inelastic response can be distinguished from nuclear contributions by the polarization analysis. The inset displays the elastic line for all four flipper configurations. (b) The magnon signal in the corrected SF1 channel is fitted with a Gaussian and constant background.

Following this criterion the experimental data are analyzed and the handedness of the magnon extracted. Figure 2.11(a) displays the constant  $\mathbf{Q}$  scans in all four scattering channels at 10 K. The inset shows the elastic scattering at  $\mathbf{Q} = (0, 1, 1)$ . The two non-spin-flip channels measure the nuclear contribution of the scattering and have very similar intensities. The spin-flip channels measure the magnetic scattering contribution which is expected to be zero in the elastic regime for this experimental setup since there is no static magnetic component perpendicular to  $\mathbf{Q}$ . The elastic signal in the spin-flip channels originate essentially from nuclear scattering and illustrates the finite flipping ratios of the polarization analysis. There can be a correction applied for this finite polarization efficiency. The details of the correction will be discussed in detail in Section 2.5. Another source of elastic intensity can be multiple scattering since the rules of polarization analysis only apply for single scattering events. Multiple scattering can be identified by changing the neutron beam path through the sample, i.e. measuring at an equivalent reflection, which was not feasible in this experiment <sup>8</sup>.

<sup>8</sup>The relative rotation of the sample to the magnetic field could lead to displacements in the coaligned crystal setup.

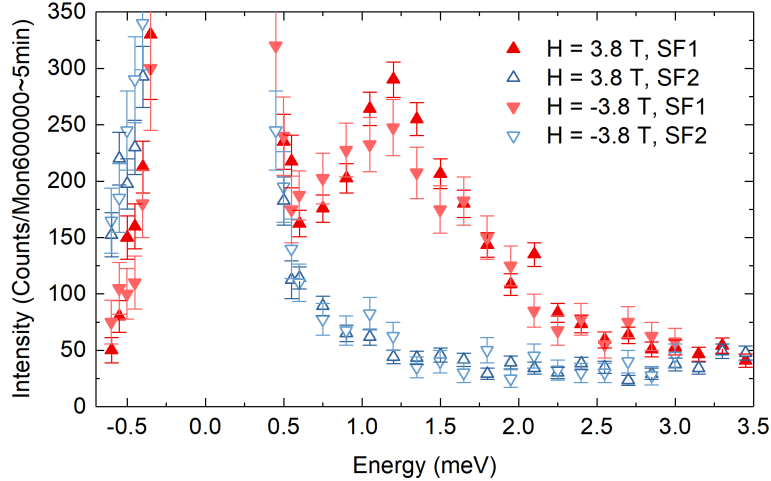


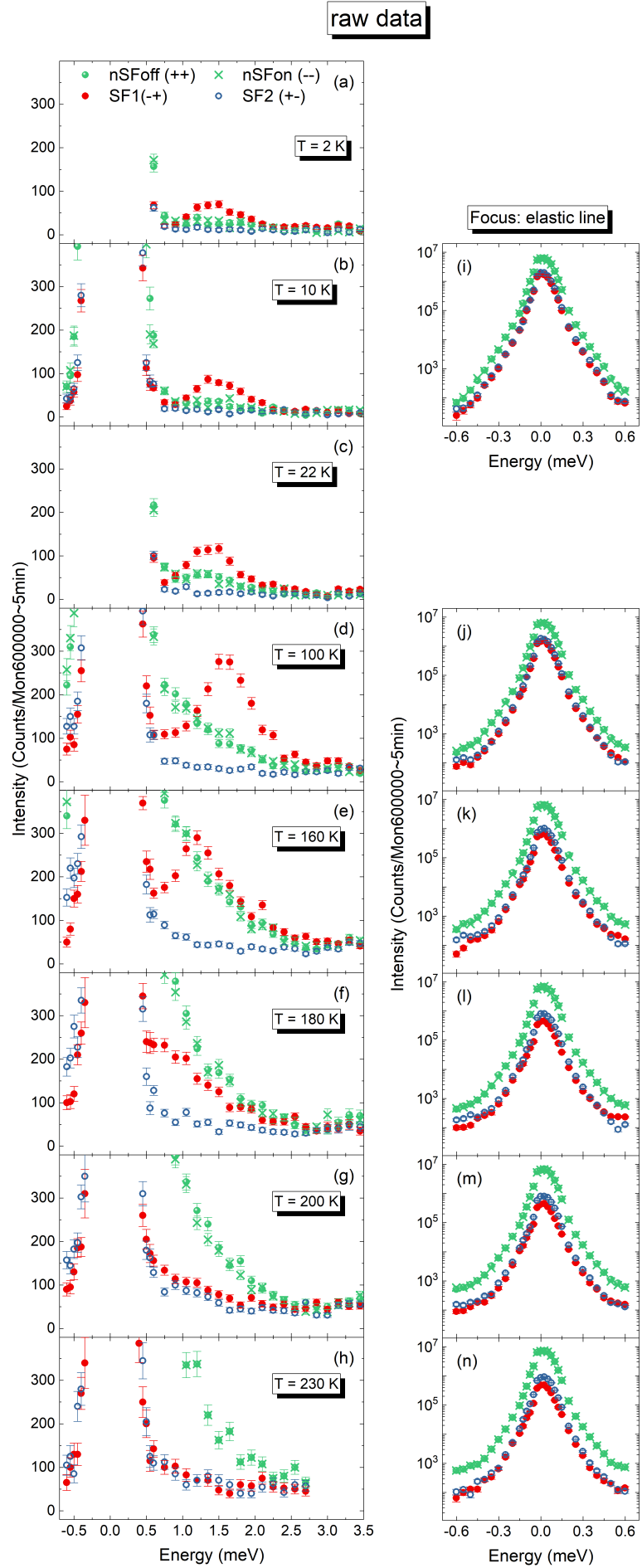
**Figure 2.12: Influence of magnetic field direction on magnon signal.** The constant  $\mathbf{Q}$  scan at the ferromagnetic zone center is measured for two different field directions at 160 K in both spin-flip channels.

The magnon signal is clearly visible in the inelastic part of only one channel, namely SF1. There seems to be no significant scattering in the other spin-flip channel. The fact that the magnon is only measurable in one spin-flip channel confirms that the only magnetic scattering contribution measurable in this experimental configuration stems from the chiral part created by the magnetic moment precession. The peak position of the magnon signal in SF1 can be determined by fitting a Gaussian with constant background (see Figure 2.11(b)). This yields a magnon gap value of 1.48(2) meV at 3.8 T and 10 K and is in agreement with the linear dependence between the magnon gap and an external field presented in Figure 2.3. The difference  $I_x^{-+} - I_x^{+-}$  is positive which confirms that the spin waves in SrRuO<sub>3</sub> at low temperature are right-handed. They follow the description in the Heisenberg model governed by the standard commutation relation of spin components.

Based on Equation 2.18 the criterion in Equation 2.19 is independent of whether the magnetic field direction and the scattering vector are parallel or antiparallel. A reversal of the magnetic field  $\mathbf{H}$  results in a reversal of the neutron polarization  $\mathbf{P}$  as well as the spin unit vector  $\tilde{\mathbf{S}}$  which produces sign reversals in both scalar products and the last term in Equation 2.18 does not change. Similarly a reversal of the scattering vector  $\mathbf{Q}$  would not change the expression. This means that the analysis of magnon handedness is not dependent of the exact definition of the scattering vector and magnetic field direction. Figure 2.12 confirms this result experimentally as there is no difference in the magnon signal in SF1 visible under field reversal.

Since the magnon gap and the spin stiffness exhibit an anomalous temperature dependence connected to the coupling of spin and charge degrees of freedom in SrRuO<sub>3</sub> (Section 2.2) it is worth to evaluate whether the magnon chirality exhibits any anomalous behavior connected to temperature. In addition it is possible to study the chirality close to the ferromagnetic transition temperature  $T_C$  as moments increasingly fluctuate from the external field direction. Using the same experimental configuration as before the constant  $\mathbf{Q}$  scan at  $\mathbf{Q} = (0, 1, 1)$  in all four channels

**Figure 2.13: Comparison of all four spin channels nSFoff, nSFon, SF1, SF2 for various temperatures.** The left column ((a)-(h)) focuses on the inelastic part of the constant  $Q$  scan at  $Q = (0, 1, 1)$  with the magnon signal while the right column ((i)-(n)) depicts the elastic part at the according temperature. The magnon signal in the inelastic part of SF1 represents the magnon gap at the zone center. There is no inelastic scattering visible in SF2 at low temperatures. The two non-spin-flip channels are as expected almost identical.



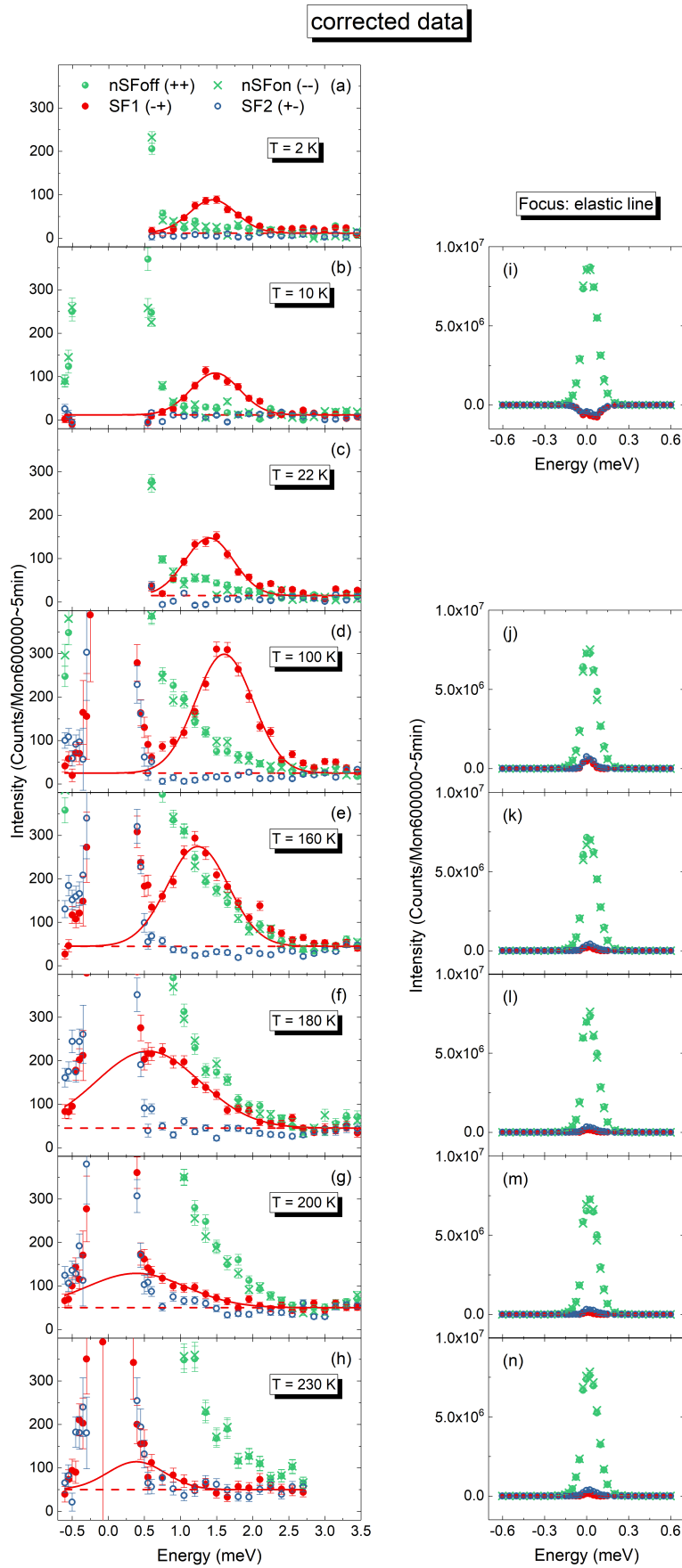


**Figure 2.14: Comparison of all four spin channels nSFoff, nSFon, SF1, SF2 for various temperatures after applying a finite polarization efficiency correction. (a)-(h) After correction the difference between the two spin-flip channels are even more pronounced. The magnon signal in SF1 is fitted with a Gaussian and a constant background. (i)-(n) The right column shows the corrected data around the elastic line. Note that the correction of data can lead to negative intensities (overcorrection) which can be only represented in a linear scale.**

is performed at various temperatures. Figure 2.13 depicts the raw data of these channels. The data are visually split into two columns where the left column focuses on the low intensity inelastic part and the right column depicts the elastic part (which was not measured for all temperatures). The magnon signal is visible in the SF1 channel of the inelastic part which implies the right handedness. As the temperature increases the phononic scattering contributions in the low-energy regime increase which results in an increase of the non-spin-flip scattering in the energy region of the magnon signal. Due to the finite polarization efficiency this leads to increasing contamination of the spin-flip channels which can distort the analysis of the chirality. For a quantitative analysis of the temperature dependence of the magnon signal and its chirality the data are corrected following the discussion in Section 2.5. The corrected data are displayed in Figure 2.14 where the magnon signal in SF1 is fitted by a Gaussian with constant background. The magnon signal exhibits an expected temperature dependence. Its amplitude increases with temperature above 100 K and decreases below 160 K again. This can be attributed to the 'competition' between Bose factor and susceptibility which contribute both to the scattering amplitude. As the temperature increases the Bose factor increases while the susceptibility does not change significantly inside the ferromagnetic phase. Close to  $T_C$  the susceptibility drops down faster as the Bose factor increases and the scattering amplitude decreases in total. Note here that the transition area is smeared out significantly around  $T_C$  due to the external magnetic field. Therefore the magnon can be measured well above  $T_C$ . Beside this usual behavior concerning the amplitude the peak position representing the magnon gap exhibits again the anomalous behavior reported in Section 2.2, even in high magnetic field. At low temperatures the gap stays rather constant, then increases up to 100 K. The gap decreases above 100 K until the susceptibility is too low and the gap value too close to the elastic line that the magnon can be measured and fitted properly. Therefore the values at 200 K and 230 K were determined by a constrained fit where the peak position is fixed at 0.39 meV which corresponds to the magnon gap energy created by a magnetic field of 3.8 T. These results are summarized in Figure 2.15(a) where the gap value is compared to the field-cooled magnetization at 4 T. Here the above described temperature dependence of the magnon gap becomes clear. The nonmonotonous behavior is identical to that found in Section 2.2 at zero field where the gap is renormalized in respect to the magnetization with the anomalous Hall effect.

The magnon signal is for all temperatures only measurable in the SF1 channel which collects the 'right-handed' scattering. The 'left-handed' scattering in channel SF2 after the correction exists only above the transition temperature where the magnon signal in SF1 significantly decreases and both spin-flip channels show similar scattering. This could indicate that the magnetic excitations above the ordered phase consist of a mixture of right- and left-handed excitations. However, since the magnon gap decreases significantly around the phase transition, the magnetic inelastic scattering shifts into the energy region of elastic line given by the instrumental resolution which weakens the experimental evidence for this interpretation.

The corrected data of the elastic line in the four spin-flip channels (Figure 2.14(i)-(n)) show still elastic scattering intensity for the spin-flip channels. In theory the corrected spin-flip channels should not show any elastic scattering intensity because there is no possibility to measure magnetic elastic scattering in this experimental

configuration. The finite elastic intensities in the spin-flip channels can be attributed to the correction artefact when correcting very high intensities with low flipping ratios. A slight deviation between the measured and real flipping ratios leads to an under- or overcorrection of the data. Especially since the polarization efficiency in this experiment is hampered by the experimental circumstances (Section 2.5) this artefact is more likely to appear.

A measure to quantize the chirality of the signal is the chiral ratio (CR) which was introduced in Equation 2.19). The chiral ratio is determined using the scattering intensities without background at the fitted peak position and depicted in Figure 2.15(b). At low temperatures the chiral ratio is around +1 which confirms the expected high chirality of the magnon scattering. It does not change significantly in the ferromagnetic phase up to 180 K. At 200 K and 230 K the data suggest no chirality. However, for these temperatures the gap value is decreased so far that the magnon signal merges with the elastic line and cannot be fitted properly. The intensity values at the fixed peak position are influenced heavily by the elastic line and therefore do not represent the magnon anymore. The magnon chirality exhibits no anomalous temperature behavior. The spin wave is right-handed and does not change its handedness.

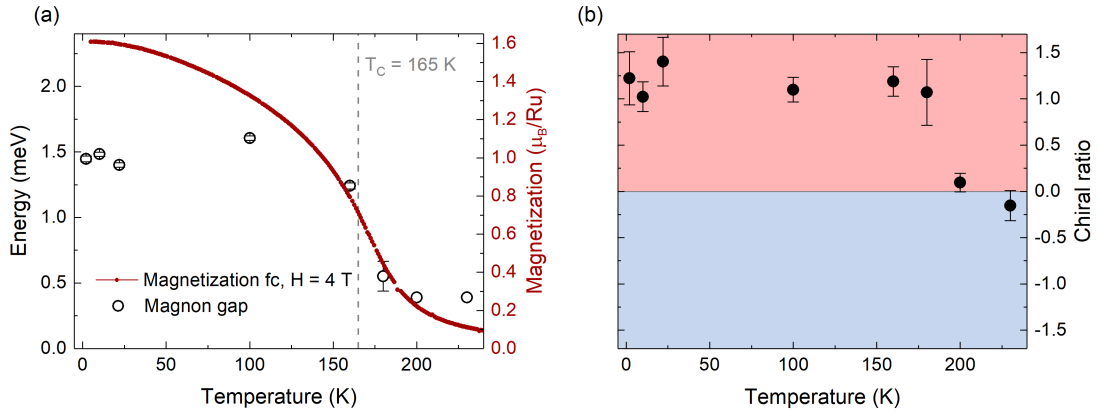


**Figure 2.15: Temperature dependence of the magnon gap and the chirality of the magnon.** (a) The magnon gap as peak position of the fits of the corrected data in Figure 2.14 (black circles) are compared to the field-cooled magnetization at 4 T with field parallel to  $[0,1,1]$  direction (red dots). (b) The chiral ratio as the normalized difference of both spin flip channels represents the chiral part of the magnetic scattering and exhibits no pronounced temperature dependence in the ferromagnetic phase for the magnon. The chiral ratio is based on corrected data.

While the inelastic scattering does not imply a change of chirality at any temperature there seems to be some temperature dependency in the quasi-elastic regime. In the constant  $Q$  scans of the elastic line in the right column of Figure 2.13 there are differences between the two spin-flip channels visible which become more pronounced at higher temperatures. Around  $E = \pm 0.6$  meV the intensities of SF1 and SF2 are reversed. Additionally the scattering in the quasi-elastic regime of channel SF1 is reduced at higher temperatures. The difference between the spin-flip channels can be quantified by the chiral ratio as done before. On this account the chiral ratio is calculated for energy transfers around zero for selected temperatures (Figure 2.16(a)-(d)) based on the corrected data. Comparing negative and positive energy transfers

there is a clear sign reversal visible while the absolute value of the ratio increases with increasing temperature. The sign reversal and the temperature dependence identify the source of scattering in this energy region as the spin wave excitation. Resulting from Equation 6.27 the scattering of magnon creation and annihilation have to appear in different spin-flip channel which produces the reversed sign of the chiral ratio. The absolute value at  $E = \pm 0.6$  meV can be explained by the temperature dependent shift of the magnon gap combined with the temperature dependent scattering amplitude. At low temperature the gap is big enough and the instrumental resolution small enough so that the inelastic magnon scattering does not contribute to the scattering intensity at 0.6 meV. Furthermore the Bose factor at these temperatures is small which is reflected in the small signal. As the Bose factor increases with increasing temperatures the scattering amplitude and the tail of the magnon signal becomes measurable at 0.6 meV. This effect is even larger than the anomalous increase of the gap which is pushing the tail further to higher energies. In the area of the transition at 160 K the scattering amplitude does not increase further with the Bose factor since the susceptibility drops down. However the scattering contribution of the magnon at 0.6 meV becomes maximum since the gap decreases and the peak shifts closer to the elastic line. The decrease of chiral signal after 160 K is again connected with the further drop of the magnetization. This low-energy chiral scattering has overall a positive sign and is therefore right-handed which connects it again with the magnon measured in the inelastic part at higher energies. This behavior is mirrored for the negative energy transfer as the absolute value of the chiral ratio shows the same behavior but with a negative sign.

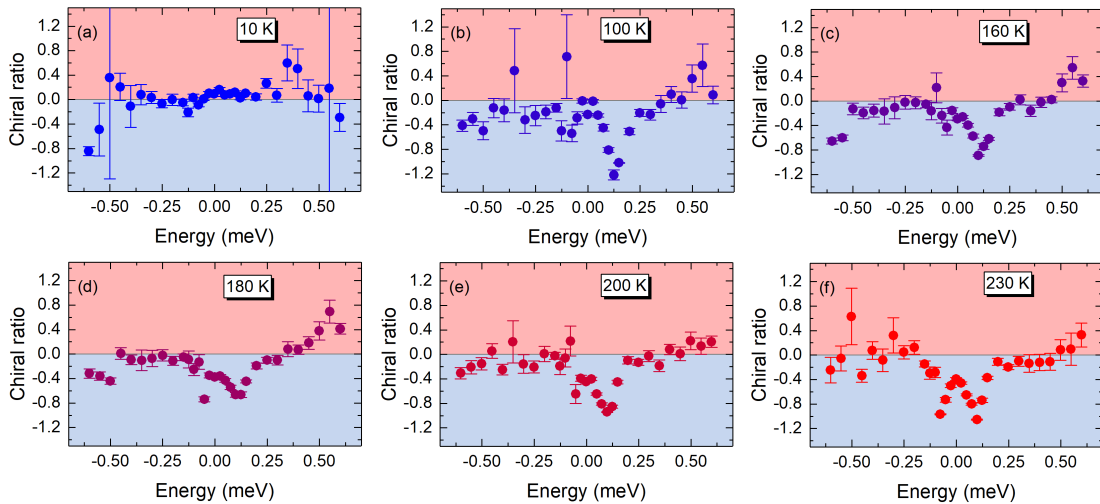


**Figure 2.16: Temperature dependence of the chiral ratio around the elastic line contains the signature of magnon creation and annihilation. (a)-(d)** The chiral ratio for energies around  $E = 0$  meV is calculated based on the corrected data in Figure 2.14 and displayed for all temperatures.

The most pronounced feature in Figure 2.16 is the increase of negative chiral ratio around  $E = 0$  meV with increasing temperature which indicates 'left-handed' scattering. In this experimental configuration the elastic signal in the spin-flip channels cannot stem from the magnetic Bragg peak of the commensurate ferromagnetic structure because there is no static magnetic component perpendicular to the scattering vector. A measurable static chirality is normally connected to modulated

spin structures where Bragg peak satellites appear at incommensurate  $\mathbf{Q}$  vectors. Single-layered SrRuO<sub>3</sub> seems to exhibit a chiral spin structure which is indicated by resonant soft X-ray scattering where two satellite peaks in reciprocal space with opposite chirality could be measured [74]. The destabilization of the magnetic order in this ultra-thin film can mimic the destabilization due to temperatures close to the ferromagnetic transition which could connect the measured chiral signal in the neutron experiment with the thin film results. However the measured constant  $\mathbf{Q}$  scans do not resolve the distribution of the chiral signal in reciprocal space and if it originates from satellite peaks around the Bragg peak. A quasi-elastic chiral scattering contribution which increases with increasing temperature could also stem from low-energy spin-wave excitations. Close to the ferromagnetic transition temperature the magnetic order is destabilized which results in short-range magnetic order and low-energy spin waves can be excited. Since the scattering on these spin wave have to follow Equation 6.27 there should be also a sign reversal of the chiral ratio for positive (creation) and negative (annihilation) energy transfer which the data do not show. The main part of the elastic signal which appears in both spin-flip channels originates most likely from nuclear contamination due to the finite flipping ratios. The finite polarization efficiency correction is not precise enough for the elastic region because of the high intensity values and the low flipping ratios. Taken this into account the temperature dependent difference of the elastic signal in the spin-flip channels can be explained by a temperature dependent polarization performance of the instrument in combination with systematic errors from the correction. A detailed discussion of the polarization efficiency and its correction is given in Section 2.5.

### 2.3.3 Section Summary

The study of the magnon gap with polarized neutron scattering is used to determine the handedness of the spin-wave excitation. The spin wave creates a dynamical chirality since the moments precess around the magnetic field direction. This gives rise to a magnetic moment component perpendicular to  $\mathbf{Q}$  which can be measured by neutron scattering. The rotation direction gives the handedness and, following the commutation relation of spin components, is right-handed in a Heisenberg ferromagnet with local moments. Using a horizontal magnetic field which polarizes incoming neutrons along the scattering vector  $\mathbf{Q}$  and the magnetization  $\mathbf{M}$  in addition to two flippers enables the full polarization analysis with which the chiral part of the magnetic scattering can be extracted. By thorough analysis of the important vectors for the used experimental setup a criterion can be formulated in which scattering channels a right-handed and left-handed scattering source can be detected. The chiral contribution of the magnon scattering at a ferromagnetic zone center is isolated and its sign implies a right-handed spin-wave. Following the anomalous temperature dependence of magnon gap and magnon stiffness (Section 2.2) the temperature dependence of the magnon chirality is studied to evaluate whether an anomalous behavior can be found. The magnon chirality stays positive (right-handed) with a maximum chiral ratio of 1 inside the ferromagnetic phase. Only above 180 K the chirality drops, simultaneously with the vanishing of magnetization. In this temperature range the analysis is inconclusive since the magnon signal is small and merges with the elastic line. While the magnon chirality does not show any evidence for

sign reversal the chirality in the quasi-elastic regime becomes negative for temperatures close to and above  $T_C$ . Possible sources of such a left-handed scattering are discussed but most likely the feature is connected to a temperature dependent polarization performance of the experimental setup and the numerical constrictions of the polarization efficiency correction.

## 2.4 Discussion

The research on the infinite layered compound of the Ruddelsden-Popper series SrRuO<sub>3</sub> is always related to two issues. Firstly, as a metallic ferromagnet, it has to be considered in what extend the Heisenberg model of local moments or the band theory of itinerant electrons are applicable to describe the magnetic properties in this material. Secondly, as the magnetism is governed by the 4d electrons of Ruthenium, the impact of spin-orbit coupling can be significant and, as such, influence the magnetic behavior strongly. Any results have to be discussed accordingly.

The growth of high-quality single crystals of SrRuO<sub>3</sub> in the II. Institute of Physics at University of Cologne facilitates the extensive study of magnetic excitations with inelastic neutron scattering. At low temperature the magnon dispersion in this metallic ferromagnet is studied using triple-axis spectrometer and time-of-flight spectrometer. Combining these complementary techniques one achieves a complete picture of the low-energy spin-wave excitations. The dispersion can be described by the relation following the Heisenberg model in a cubic ferromagnet. A single-ion anisotropy term has to be included as the sizable magnon gap of around 1 meV can be measured directly at the zone center. This anisotropy gap confirms the anisotropy field measured in the magnetization along the crystallographic axis and is one direct consequence of strong spin-orbit coupling. The single-ion anisotropy as a magnetocrystalline anisotropy arises from the electrostatic interaction of the *d* orbitals containing unpaired electrons. The crystal field stabilizes particular orbitals to which magnetic moments couple by the spin-orbit interaction. Thus the moments are aligned along a particular crystallographic direction. Beside the gap value, the dispersion relation also gives a value for the magnon stiffness *D* which is connected to the exchange coupling *J*. The spin-dynamic parameters derived from the dispersion model are summarized in Table 2.1. The spin-orbit coupling becomes also visible in the intrinsic width of the magnon. Correcting the data for instrumental resolution one can extract the intrinsic width of the excitation. In the case of SrRuO<sub>3</sub> the spin-wave excitations are broadened significantly which can be partly explained by the superposition of orthorhombic directions in twinned crystals. However, given the magnitude of the broadening of 40% of magnon energy, it is likely that the magnons exhibit strong scattering due to coupling to electrons. The coupling between electrons and magnetism is seen in the kink of the resistivity at T<sub>C</sub> [60].

The Stoner theory of itinerant magnetism predicts the spin-wave excitation spectrum to consist of two parts: On the one hand there is a spin wave dispersing according to the ferromagnetic dispersion relation arising from the Heisenberg model of local moments. On the other hand there are Stoner excitations which represent the electron-hole excitations between two bands of opposite spin. These excitations add up to a continuum whose lower energy boundary begins at the exchange splitting energy and *q* = 0 at the zone center and decreases linearly with increasing *q* [62]. The transition from conventional spin-wave excitation to Stoner continuum can be measured by inelastic neutron scattering as it has been done for iron [70]. The magnon signal abruptly decreases in intensity and broadens in width at the boundary. Such a behavior can be found in SrRuO<sub>3</sub> where the magnetic scattering intensity drops abruptly above 25 meV. This confirms the classification as a weak itinerant ferromagnet. The low energy excitation spectrum shows no deviation from

the local moment picture, as expected.

The time-of-flight experiment reveals already an anomalous temperature dependence of the spin stiffness as the magnon dispersion does not change significantly at the transition temperature. The broadening of the excitations indicate the onset of short-range excitations, i.e. paramagnons. The temperature dependence of the spin-dynamic parameters, namely the magnon gap and magnon stiffness, measured with triple-axis spectrometer reveal a nonmonotonous behavior which arises from Weyl physics in SrRuO<sub>3</sub>. Experimental evidence for Weyl points close to the Fermi surface have been found in the temperature dependence of the anomalous Hall effect where the Weyl points act as magnetic monopoles in  $k$  space [19]. These Weyl points form due to spin-orbit coupling as the due to spin-orbit interaction gapped spin bands can close at certain points in  $k$  space. Besides their effect on the Hall effect they also couple locally magnetization and current which leads to the renormalization of magnon gap and magnon stiffness. The softening of the magnon upon cooling scales with the temperature behavior of the anomalous Hall effect and is evidence for the coupling of spin and charge degrees of freedom. The reported behavior of the spin-dynamic parameter is experimental evidence for the existence of Weyl fermions in SrRuO<sub>3</sub>, beside the anomalous Hall effect. This result has been recently substantiated by quantum transport measurements [75].

Onoda, Michenko and Nagaosa proposed SrRuO<sub>3</sub> as a candidate for finding the left-handed magnon [73]. They declare four specific conditions for which the fundamental property of right-handed spin precession in a ferromagnet can be reversed: (i) basically quenched orbital moment, (ii) strong spin-orbit coupling, (iii) finite contribution of the majority and minority spins at  $E_F$ , and (iv) band degeneracy near the Fermi level. The study of the magnon handedness is possible by polarized neutron scattering as it enables the extraction of the chiral contribution of magnetic scattering. The results state clearly that the spin wave is right-handed, even in the vicinity of the phase transition, which indicates an insufficient fulfillment of the above stated conditions. Although there is no confirmation of the theoretical concept of Onoda *et al.* for the magnon mode itself, the quasi-elastic scattering of the ferromagnetic Bragg peak shows evidence for left-handed scattering which becomes pronounced above the phase transition. Whether this feature is connected to a physical origin like the onset of a chiral spin structure or low-energy short-range and left-handed spin-wave excitations is inconclusive. The feature can also be explained by a temperature dependent polarization performance of the experimental setup whose correction in the elastic regime is constraint by the measurement errors of the flipping ratios.

## 2.5 Methods

### Material Information



**Figure 2.17: Coaligned multi-crystal assembly for neutron scattering experiments.** The single crystals of nearly cylindrical shape with a diameter of around 4 mm and a length of up to 1.5 cm are individually fixed in aluminium clamps which are attached to two aluminium rods. This setup enables each crystal to be rotated individually around two axis for easy coalignment.

SrRuO<sub>3</sub> crystallizes in an orthorhombic lattice (space group  $Pnma$ ) at room temperature after undergoing two structural transition: from cubic to tetragonal at 975 K and from tetragonal to orthorhombic at 800 K. This symmetry reduction results in six possible twin domain orientations which imitate the cubic symmetry. Therefore the pseudo-cubic lattice (space group  $Pm\bar{3}m$ ) with lattice parameter  $a_{pc} = 3.93 \text{ \AA}$  is used here and all  $\mathbf{Q}$  vectors are given according to this lattice. The relation between orthorhombic lattice parameters and the cubic directions are as follows:  $\mathbf{a} \parallel [1, 0, 1]_c$ ,  $\mathbf{b} \parallel [0, 1, 0]_c$ , and  $\mathbf{c} \parallel [\bar{1}, 0, 1]_c$  with  $a \approx c \approx \sqrt{2a_{pc}}$  and  $b = 2a_{pc}$  [13]. The sample can be detwinned by applying a magnetic field of more than 1 T above  $T_C$  and then cooling down into the ferromagnetic phase. It develops a single domain state where the easy axis (orthorhombic  $c$  or  $[\bar{1}01]_c$ ) is pointing along the applied field. This state persists at low temperatures even when the field is turned off [13]. This magnetic detwinning is used in experiments at the triple-axis spectrometer PANDA and IN12 to reach a single domain state.

The data presented in this chapter were collected using single crystals grown by the floating-zone method in the II. Institute of Physics at the University of Cologne (Section 6.1). The growth was conducted by S. Kunkemöller and the author and the crystals were characterized by X-ray diffraction, resistivity and magnetization measurements (Section 6.1). The grown crystals exhibit ferromagnetic order below  $T_C = 165 \text{ K}$  with a saturation magnetization  $M_{\text{sat}} = 1.6 \mu_B/\text{f.u.}$  [10]. The coaligned multi-crystal assembly which was used for most of the neutron scattering experiments is depicted in Figure 2.17. The compact crystal assembly facilitates a high material density in a sample volume of roughly  $2 \text{ cm} \times 2 \text{ cm} \times 2 \text{ cm}$ . This enables extensive inelastic neutron scattering studies even with polarized neutrons.

### Neutron Scattering

The neutron scattering experiments were conducted at triple-axis spectrometers at the Laboratoire Léon Brillouin (LLB) in Saclay, France, at the Institute Laue Langevin (ILL) in Grenoble, France, and at the Forschungs-Neutronenquelle Heinz Maier-Leibnitz (FRM-II) in Garching, Germany. The time-of-flight data were collected at the ISIS Neutron and Muon source in Didcot, United Kingdom. All involved beam times including the instrument and the experimental setting are listed in Table 2.2. This chapter includes data from beam times (in the years 2014-2015)

which were not conducted by the author as experiment responsible. This data are added to the data measured by the author and analyzed together.

The sample is oriented in the  $[1, 0, 0]_c/[0, 1, 1]_c$  scattering plane for all scattering experiments. The triple-axis spectrometers are used with pyrolytic graphite crystals as monochromator and analyzer with a fixed  $k_f$ . A filter in front of the analyzer or a velocity selector is used to suppress higher order scattering.

### Polarized Neutron Scattering

For the polarized neutron scattering experiments on IN12 at ILL the neutron beam is polarized by a transmission polarizing cavity in front of the monochromator. These polarizers transmit neutrons with a polarization antiparallel to the guide field. In combination with two Mezei-flippers in front and behind the sample and a Heusler analyzer all four spin-flip channels can be measured. The here-used Heusler analyzer consists of  $\text{Cu}_2\text{MnAl}$  single crystals where the structure factor excludes scattering of neutron with a polarization parallel to the guide field. Only neutrons with polarization antiparallel to the guide field pass the analyzer. Without an active spin flipper this setup measures therefore the non-spin-flip channel  $I^{\uparrow\downarrow}$ . In the case of  $\text{SrRuO}_3$  a horizontal magnet (Model 134OXHV38 at ILL) was used to enable a neutron polarization collinear to  $\mathbf{Q}$ . Unfortunately the magnetization of the ferromagnetic  $\text{SrRuO}_3$  produces such a strong field around the crystal assembly that the neutrons are depolarized significantly by the sample. Therefore a high external field of 3.8 T (maximum field value of the magnet) had to be applied to overcome the sample field and conserve the neutron polarization. However the high external field creates high stray fields outside the magnet (especially for this kind of horizontal field magnet) which hinder the efficiency of the flippers. Especially flipper 2 is effected by this since it is closer to the magnet than flipper 1 which is located in the neutron beam in front of the monochromator. To counter this and maximize the flipper efficiency the flipper currents were optimized for the spectrometer range used in the experiment. The flipping ratio is determined by the comparison of (attenuated) direct beam intensity in non-spin-flip and spin-flip channel when no sample is mounted in the cryostat. The flipping ratio for flipper 1 amounts to  $\approx 24$  while for flipper 2 the ratio is strongly reduced to  $\approx 14$ . Although the flipper currents are optimized analyzing the flipping ratios of the direct beam to account for the stray field of the magnet as a function of the angle between the magnetic field  $H$  and  $k_f$ , flipper 2 is less effective. In addition the sample when mounted in the neutron beam depolarizes the neutron beam which leads to a further decrease of the polarization performance. This depolarization is connected to the sample magnetization as a source of magnetic field which can depend on the sample shape creating inhomogeneous fields around the multi-crystal setup. Since the magnetization increases with decreasing temperature due to the magnetic order it is expected that the depolarization is strongest at lowest temperature.

The temperature dependent polarization performance of the experimental setup when the sample is mounted inside the magnet is visualized in Figure 2.18. The sample flipping ratios are determined by comparison of intensity of the Bragg reflection  $\mathbf{Q} = (0, 1, 1)$  in the different spin-flip channels. For this experimental setup with the magnetization collinear to the scattering vector there should be no magnetic elastic scattering contribution at this Bragg reflection and the spin-flip channels measure only the nuclear contamination coming from the non-spin-flip channel. The

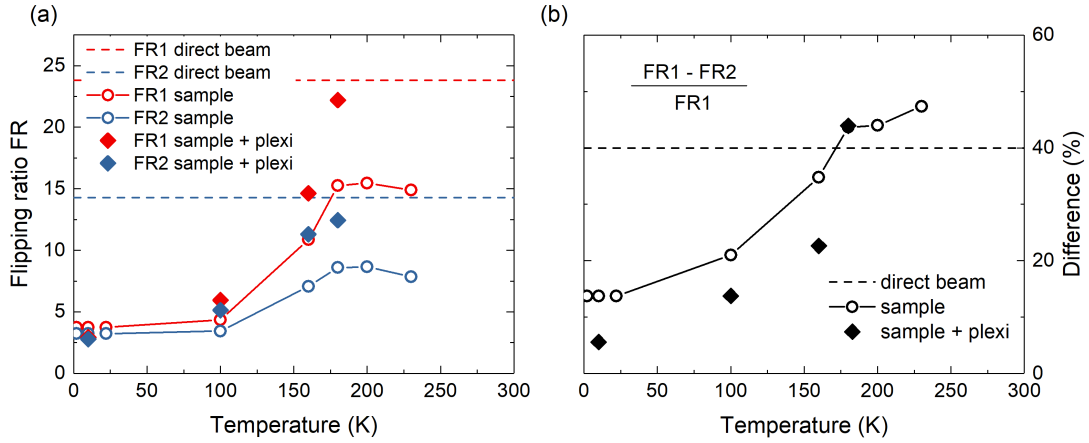


**Figure 2.18: Temperature dependence of the flipping ratio (FR).** The flipping ratios are measured using the direct beam and the Bragg reflection  $Q = (0, 1, 1)$  of the sample with and without attenuation. FR1 is the ratio in relation to flipper 1 (before the sample) and FR2 in relation to flipper 2 (after the sample). (a) Comparison of the dependence of the ratios in relation to the sample temperature with the values obtained from the direct beam measurement. (b) Relative difference of the two flipping ratios.

intensities are taken on the one hand from the elastic line in the constant  $Q$  scans (Figure 2.13) and on the other hand were determined for few temperatures by single counts with attenuation by a plexiglas attenuator. Without attenuation the nuclear scattering is so strong that the detectors are saturated which will lead to loss of absolute signal. This becomes clear in the comparison of the flipping ratios with and without attenuation where the ratios determined with attenuation are bigger than without. Nevertheless the elastic signal in the non-spin-flip channels of the scans can still be used to analyze relative changes in the temperature dependence of flipping ratios and reveal tendencies. The flipping ratios exhibit a strong temperature dependence. At low temperature the ratios are strongly reduced compared to the direct beam measurement pointing to a strong depolarization due to the sample magnetization. This depolarization decreases with increasing temperature which is also visible in the flipping ratios since they increase and stay constant above the ferromagnetic transition. The flipping ratio derived from the scans do not reach the original ratios of the direct beam because of the detector saturation in the non-spin-flip intensities. However the values with attenuation show that the ratios are already close to the original direct beam values which indicates again that the  $(0, 1, 1)$  reflection is suitable for measuring the flipping ratio. Beside the recovery of the flipping ratios in the paramagnetic phase also the difference of the two flippers increase with increasing temperature until it reaches similar relative values as in the direct beam measurement (Figure 2.18(b)). Most interestingly the difference is almost zero at low temperature. This strong temperature dependence of the polarization performance can be explained by the competition of two factors which decrease the polarization analysis performance. Firstly the high stray field of the horizontal field magnet leads to a big difference between the two flippers as it influences flipper 2 more than flipper 1. Secondly the neutron polarization is influenced strongly by the sample magnetization which causes a temperature dependent depolarization of the neutron beam. This leads to an overall decrease of flipping ratios so that the different flipper performances do not play an important role anymore. At higher temperatures and

especially in the paramagnetic phase the depolarization due to the sample becomes negligible and the different flipper performances dominate the overall polarization analysis performance indicated by the increasing flipping ratio difference up to the original values of the direct beam measurement.

To apply a quantitative correction of data taking into account the temperature dependent polarization performance the general polarization used in the standard correction for finite polarization efficiency has to be broken down. The general polarization,  $P$ , of the instrument is related to the flipping ratio,  $FR$ , through

$$FR = \frac{1 + P}{1 - P} \Leftrightarrow P = \frac{FR - 1}{FR + 1}. \quad (2.20)$$

The neutron beam consists relatively of  $x = \frac{P+1}{2}$  parallel polarized neutrons and  $1-x$  antiparallel polarized neutrons. When the polarization is symmetric before and after the sample the probability that the polarization including the complete experimental setup corresponds to the majority of  $\frac{1+x}{2}$  is  $(\frac{1+x}{2})^2 \approx x$ . The probability for the wrong process amounts to  $\frac{1-x}{2}$ . For the presented experiment the general finite polarization is separated from the efficiency of the second flipper  $\eta$  which is reduced by the horizontal field. However, only when the flipper is switched on, the reduced flipper efficiency applies and the ratio  $\eta$  describes the desired polarization while a ratio  $1 - \eta$  corresponds to neutrons with unchanged polarization. In the following the four intrinsic intensities in the four channels of polarizations are described by  $I_{++}, I_{+-}, I_{-+}$ , and  $I_{--}$  (+ no spin flip, - spin flip, first index incoming and second outgoing beam). The superscript  $O$  represents the observed intensities in these channels. Only for the intrinsic intensities one may further simplify  $I_{++}=I_{--}$ . The data correction is based on the following matrix equation where the vector of the observed intensity has to be multiplied by the inverse of the matrix which yields the intrinsic intensities.

$$\begin{pmatrix} I_{++}^o \\ I_{+-}^o \\ I_{-+}^o \\ I_{--}^o \end{pmatrix} = \begin{bmatrix} \left(\frac{1+x}{2}\right)^2 & \frac{1-x^2}{4} \\ \eta \frac{1-x^2}{4} + (1-\eta) \left(\frac{1+x}{2}\right)^2 & \eta \left(\frac{1+x}{2}\right)^2 + (1-\eta) \frac{1-x^2}{4} \\ \frac{1-x^2}{4} & \left(\frac{1-x}{2}\right)^2 \\ \eta \left(\frac{1-x}{2}\right)^2 + (1-\eta) \frac{1-x^2}{4} & \eta \frac{1-x^2}{4} + (1-\eta) \left(\frac{1-x}{2}\right)^2 \end{bmatrix} \begin{pmatrix} I_{++} \\ I_{+-} \\ I_{-+} \\ I_{--} \end{pmatrix} \quad (2.21)$$

The parameters  $x$  and  $\eta$  have to be determined from the measurement of the direct beam or a purely nuclear Bragg reflection where  $I_{++}=I_{--}=I_0$  and  $I_{+-}=I_{-+}=0$ . With this conditions the observed intensities become:

$$I_{++}^o = \left( \left( \frac{1+x}{2} \right)^2 + \left( \frac{1-x}{2} \right)^2 \right) I_0 \quad (2.22)$$

$$I_{+-}^o = \left( 2\eta \frac{1-x^2}{4} + (1-\eta) \left[ \left( \frac{1+x}{2} \right)^2 + \left( \frac{1-x}{2} \right)^2 \right] \right) I_0 \quad (2.23)$$

$$I_{-+}^o = 2 \frac{1-x^2}{4} I_0 \quad (2.24)$$

$$I_{--}^o = \left( \eta \left( \frac{1+x}{2} \right)^2 + \eta \left( \frac{1-x}{2} \right)^2 + 2(1-\eta) \frac{1-x^2}{4} \right) I_0 \quad (2.25)$$

From here, the polarization parameter  $x$  can be calculated from the first and third equations

$$\frac{1-x^2}{2} = \frac{I_{-+}^o}{I_{++}^o + I_{-+}^o} \Leftrightarrow x = \left[ 1 - \frac{2I_{-+}^o}{I_{++}^o + I_{-+}^o} \right]^{0.5}. \quad (2.26)$$

while  $\eta$  is determined by:

$$\eta = \frac{I_{+-}^o - I_{++}^o}{I_{-+}^o - I_{++}^o} \quad \text{or} \quad \eta = \frac{I_{--}^o - I_{-+}^o}{I_{++}^o - I_{-+}^o}. \quad (2.27)$$

The temperature-independent efficiency of the second flipper was determined by measurements in the direct beam, and the polarization parameter  $x$  is deduced from the temperature dependent analysis of the Bragg intensity at (011) with attenuation<sup>9</sup>.

---

<sup>9</sup>For 200 and 230 K there was no data with attenuation measured. The non attenuated data in Figure 2.18(a) indicate that the flipping ratios at 180, 200, and 230 K stay the same. Therefore the intensities at 180 K with attenuation were also used to correct the data at 200 and 230 K.

**Table 2.2: Involved beam times with the instrumental settings.**

Beam Time	Facility	Instrument	$k_f$ [ $\text{\AA}^{-1}$ ] ( $E_i$ [meV])	Mono./Ana.	Filter	comment
03-2014	LLB	2T1	2.662	PG(002)/PG(002)	PG	data analysis
03-2015	ISIS	MERLIN	(22,43,120)	—	—	data analysis
04-2017	LLB	4F1	1.55	PG(002)/PG(002)	cooled Be	
02-2018	FRM-II	PANDA	1.5	PG(002)/PG(002)	cooled Be	vertical field for detwinning
06-2018	ILL	IN12	1.5	PG(002) <sup>a</sup> /Heusler(111)	velocity selector	full polarization analysis
10-2019	ILL	IN12	1.5	PG(002)/Heusler(111)	velocity selector	full polarization analysis

<sup>a</sup>A transmission polarizing cavity polarizes the neutron beam before it scatters on the monochromator.



# Ca<sub>2</sub>RuO<sub>4</sub>: Entanglement of Structural, Electronic, and Magnetic Properties

## 3.1 Current-Induced Insulator-Metal Transition

### 3.1.1 Introduction

In strongly correlated materials a variety of different phases compete due to the interaction of orbital, magnetic, and lattice degrees of freedom. A certain phase can be favored by introducing a small stimulus like applying an electrical field. Especially the electrical control of different phases increases the possibility of technical application [76]. The influence of Joule heating and/or microscopic phase separation requires a thorough experimental effort to exclude it and to establish a true non-equilibrium phase since their relevance has been reported in many *3d* transition-metal oxides [77, 78]. We studied the antiferromagnetic Mott insulator Ca<sub>2</sub>RuO<sub>4</sub> which exhibits a insulator-metal transition (IMT) at 357 K [23, 79, 80]. This transition can be induced also by substitution with Sr [36], by applying hydrostatic pressure [24, 81], and by applying an electrical field [82]. Especially the discovery of the current-induced phase transition lead to a variety of different studies which investigated the influence of current to the electronic system and established a current-induced quasi-metallic state [83–86]. Even a strong diamagnetism and anomalous transport properties at low temperatures under moderate current densities were reported [83]. While the evidence of strong diamagnetism arises from an experimental artefact [87] the magnetoresistance turns negative and the Hall coefficient changes its sign at low temperatures. Nano-imaging optical techniques report nanostripe structured regions of alternating metallic and insulating phases for moderate current densities [86]. This evidence promotes a possible nonhomogeneous real structure in Ca<sub>2</sub>RuO<sub>4</sub> under application of current. The insulator-metal transition in general is accompanied by strong structural changes where the RuO<sub>6</sub> octahedra elongate vertically and contract horizontally. This changes translate into an increase of the *c* lattice parameter with increased temperature while the in-plane parameters decrease [22, 24, 25]. The lattice-parameter difference between metallic and insulating phase in Ca<sub>2</sub>RuO<sub>4</sub> enables a temperature and current dependent investigation of phase changes by using diffraction methods. By expanding our experimental setups of neutron and X-ray diffraction for the application of current we could study the current-induced transition behavior of Ca<sub>2</sub>RuO<sub>4</sub>.

The publication of these results in *Physical Review Materials* in 2020 is included in this thesis [88].

### 3.1.2 Contribution to Publication and its Relevance in Thesis

The single crystals used for the measurements were grown and characterized by S. Kunkemöller and by the author Section 6.1. The quasi-static transport measurements were conducted in the scope of the bachelor thesis of L. Berger [89] under the author's supervision. The time-resolved transport measurements and their analysis were conducted by K. Dietrich and J. Hemberger and the according text section in the publication was provided by J. Hemberger. The neutron and X-ray scattering data presented in this publication were measured partly in the scope of the bachelor thesis of F. Wirth [90] under the author's supervision. Building up on these first measurements the scattering data set was extended by measurements conducted by the author. The neutron experiments were accompanied and supervised by M. Braden and supported by the local contacts at the neutron facilities. The data analysis of the neutron and X-ray data was conducted by the author. For the published text the author contributed all figures, except Fig. 3, including their captions. The author was involved in the writing of all parts of the published text, except part III.B.

The published results arise from a thorough study of  $\text{Ca}_2\text{RuO}_4$  by combining transport measurements and scattering techniques. This required the expansion of sample environments of the existing experimental setups to enable temperature and current dependent measurements. The new experimental setups made it possible to form a clear picture of the complex transition behavior in  $\text{Ca}_2\text{RuO}_4$  when applying current. The impact of current on the insulator-metal transition is evidence for the strong correlations in this Mott insulator which couples electronic with structural properties. It also promotes the consideration of phase coexistence in the interpretation of experimental results.

Evidence for current-induced phase coexistence in  $\text{Ca}_2\text{RuO}_4$  and its influence on magnetic orderK. Jenni,<sup>1</sup> F. Wirth,<sup>1</sup> K. Dietrich,<sup>1</sup> L. Berger,<sup>1</sup> Y. Sidis,<sup>2</sup> S. Kunkemöller,<sup>1</sup> C. P. Grams <sup>1</sup>,  
D. I. Khomskii,<sup>1</sup> J. Hemberger <sup>1</sup> and M. Braden <sup>1,\*</sup><sup>1</sup>*II. Physikalisches Institut, Universität zu Köln, Zùlpicher Strasse 77, D-50937 Köln, Germany*<sup>2</sup>*Laboratoire Léon Brillouin, C.E.A./C.N.R.S., F-91191 Gif-sur-Yvette CEDEX, France*

(Received 4 May 2020; revised 29 June 2020; accepted 13 July 2020; published 3 August 2020)

Combining quasistatic and time-resolved transport measurements with x-ray and neutron diffraction experiments we study the nonequilibrium states that arise in pure and in Ti-substituted  $\text{Ca}_2\text{RuO}_4$  under the application of current densities. Time-resolved studies of the current-induced switching find a slow conductance relaxation that can be identified with heating and a fast one that unambiguously proves an intrinsic mechanism. The current-induced phase transition leads to complex diffraction patterns. Separated Bragg reflections that can be associated with the metallic and insulating phases by their lattice parameters, indicate a real structure with phase coexistence that strongly varies with temperature and current strength. A third contribution with a  $c$  lattice constant in between those of metallic and insulating phases appears upon cooling. At low current densities, this additional phase appears below  $\sim 100$  K and is accompanied by a suppression of the antiferromagnetic order that otherwise can coexist with current carrying states. A possible origin of the intermediate phase is discussed.

DOI: [10.1103/PhysRevMaterials.4.085001](https://doi.org/10.1103/PhysRevMaterials.4.085001)

## I. INTRODUCTION

The interaction of magnetic, orbital, and lattice degrees of freedom in strongly correlated electron materials frequently leads to the competition of different phases. As a result, small external stimuli can trigger phase transitions and exotic quantum states. Specifically, the electric control of nonthermal phase transitions is of wide interest in view of possible applications [1,2]. It is, however, very difficult to establish a true nonequilibrium character of a new phase and to fully exclude Joule heating or microscopic phase separation, which were shown to be relevant in many  $3d$  transition-metal oxides [3,4]. For electric-field-induced phenomena it was shown that the motion of defects can be essential [5,6]. Therefore, a thorough understanding of the transition mechanisms is essential for the interpretation of any nonequilibrium phase.

In this paper, we investigate the antiferromagnetic (AFM) Mott insulator  $\text{Ca}_2\text{RuO}_4$ , which is a “bad metal” (with low conductance) at high temperatures in thermal equilibrium and which transforms into a Mott insulator upon cooling below 357 K [7–9]. The metal-insulator transition is accompanied by strong structural changes [10–12]. At the transition the  $c$  lattice parameter shrinks and in-plane parameters elongate, coupled with a transition from elongated  $\text{RuO}_6$  octahedra at high temperature to flattened octahedra in the insulating state. This seems to be the essential element to change the orbital occupation and to induce insulating behavior [13,14]. But upon cooling also the tilting of the  $\text{RuO}_6$  octahedra increases and the octahedron basal plane becomes elongated along the orthorhombic  $b$  direction [10–12]. This later distortion seems to pin the magnetic moment parallel to the  $b$  axis [15]. The strong structural changes are not restricted to the metal-insulator

transition at 357 K but extend over a large temperature interval down to about the onset of AFM order at  $T_N = 110$  K. Note, that  $\text{Ca}_2\text{RuO}_4$  is a layered material resulting in rather low three-dimensional AFM ordering temperatures.

Besides by heating, the metal-insulator transition can be induced by applying hydrostatic pressure above 0.5 GPa [12,16], by substitution, for example, with Sr [17] and by applying an electric field [18]. The electric field needed to drive the phase transition is unusually small ( $E = 40$  V/cm) compared to the Mott energy gap; it is about two orders of magnitude below a typical break-through field of a Mott insulator [19,20]. Following this discovery [18] several other studies confirmed current-induced quasimetallic states in  $\text{Ca}_2\text{RuO}_4$  [21–24]. In particular, by using a noncontact infrared thermometer it was shown that the metallic phase can be stabilized by an external current at a sample temperature well below the metal-insulator transition [23]. The low-temperature observation of the quasimetallic states suggests a truly electric mechanism and thus excludes Joule heating of the entire sample as the origin [21–23]. However, if the sample becomes inhomogeneous and splits in metallic and insulating parts the heating becomes inhomogeneous as well. Local heating remains a problematic issue in almost all experimental studies.

It was reported that  $\text{Ca}_2\text{RuO}_4$  exhibits strong diamagnetism and anomalous transport properties [21] at moderate current densities of 1 to 2 A/cm<sup>2</sup>. At low temperature the magnetoresistance turns negative and the Hall coefficient exhibits a sign change [21]. However, the evidence for strong diamagnetism was recently shown to arise from an experimental artifact [25]. Strong diamagnetism contrasts with the ferromagnetic or quasiferromagnetic instabilities reported for the metallic phases reached by applying pressure or by substitution [12,16,26,27].

For moderate current densities, nano-imaging optical techniques report nanostripe structured areas of phase

\*braden@ph2.uni-koeln.de

coexistence with different optical reflectivity [24]. This documents that the real structure of current carrying  $\text{Ca}_2\text{RuO}_4$  can be nonhomogeneous. Diffraction experiments at a high current density of  $10 \text{ A/cm}^2$  proposed new structural phases in a current carrying sample [28], but the crystal structures strongly resemble those  $\text{Ca}_2\text{RuO}_4$  exhibits at higher temperatures and pressure [10–12]. Other diffraction experiments on a crystal with 3% Mn substitution report evidence for a modified orbital arrangement [22]. The later study, furthermore, does not find any evidence for strong diamagnetism.

Here we report transport and single-crystal diffraction studies using neutron and x-ray radiation. The diffraction experiments with a careful recording of the sample temperature indicate complex phase coexistence of at least three different phases distinguished by different  $c$  lattice parameters. In particular, at low current densities, in addition to the initial metallic and insulating phases an additional component appears.

## II. EXPERIMENT

Single crystals of  $\text{Ca}_2\text{RuO}_4$  were grown by the floating-zone technique and characterized by resistivity and magnetization measurements [15,29]. Due to the metal-insulator transition at 357 K and the accompanied structural transition the crystals tend to shatter into mm-sized pieces upon cooling to room temperature in the furnace. A small amount of 1% Ti substitution broadens the transition, which can result in large single crystals of up to  $1 \text{ cm}^3$  volume. Additionally, and more importantly for this study, Ti-substituted crystals permit to pass the metal-insulator transition several times without destroying the sample. The magnetism is not strongly influenced by the Ti since it is isovalent to Ru and nonmagnetic [29]. In the experiments presented here crystals containing 1% of Ti and pure ones were used. For the application of the DC current in the quasistatic conductance and in the diffraction experiments, the plate-shaped crystals were glued to a copper plate using conductive silver paste. The  $ab$  planes are parallel to the plate. The copper plate as well as the sample were contacted with copper wires, resulting in a current direction parallel to the  $c$  axis. We choose this current direction because it offers the best conditions for thermalizing the sample thereby reducing heating issues. In addition, cracking of the sample in thin plates parallel to the current is suppressed.

Time-resolved pulsed transport measurements were performed in a high bandwidth coaxial setup suitable for frequencies up to the GHz range employing a current source KEITHLEY 2400 together with a 200 MHz oscilloscope AGILENT U2702A and a fast pre-amplifier STANFORDRESEARCH 560. The time-resolved temperature measurements were performed using a fast, thin ( $250 \mu\text{m}$ ) foil-type thermocouple [T-type] with a response time in the millisecond range. The sample was prepared as a small platelet with a thickness of 0.5 mm and a cross section of  $0.8 \text{ mm}^2$  covered with silver electrodes.

The x-ray diffraction (XRD) experiments were conducted on a D5000 powder diffractometer using  $\text{Cu } K_\alpha$  radiation equipped with a He cryostat where the sample chamber is cooled by He flow. Thermal contact to the single crystalline samples is guaranteed by the exchange gas inside the chamber.

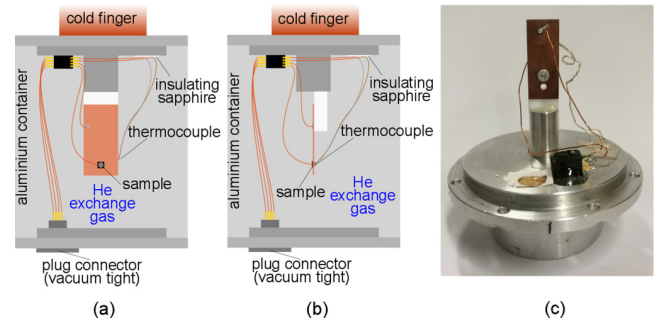


FIG. 1. Illustration of the experimental setup to perform x-ray and neutron diffraction experiments on  $\text{Ca}_2\text{RuO}_4$  with a current flowing parallel to the crystallographic  $c$  direction (perpendicular to the Ru layers). Note that the thermal couple opposite to the sample crystal allows for improved estimate of the sample temperature.

For the neutron diffraction experiments the sample setup was incorporated into a sealed aluminum can including He exchange gas and a vacuum tight connector. The can was then cooled using closed-cycle refrigerators. The elastic neutron scattering experiments were performed at the thermal two-axis diffractometer 3T1 at the Laboratoire Léon Brillouin (LLB). Neutrons with a wavelength of  $2.4 \text{ \AA}$  were extracted by a vertically focusing pyrolytic graphite (002) monochromator. To achieve the high resolution required to distinguish the different contributions in  $\text{Ca}_2\text{RuO}_4$  we used collimations of  $15'$  and  $10'$  before the monochromator and detector, respectively, and higher-order contaminations were suppressed with a pyrolytic graphite filter. To apply the current and to read the voltage generated by the thermocouple a KEITHLEY 2400 source meter and a KEITHLEY 2128 nanovoltmeter were used.

To monitor the sample temperature as exactly as possible in the neutron experiment one contact of a thermal couple was placed on the backside of the 0.5-mm-thick copper plate, precisely at the sample position. As the reference temperature of the thermocouple the cryostat sensor was used, so that we can precisely determine the temperature at the sample position. The experimental mounting used in most of the neutron experiments is shown in Fig. 1. In the x-ray diffraction experiment the thermocouple had to be mounted at the same side of the copper plate at a distance of 2 mm from the crystal.

## III. RESULTS

### A. Quasistatic transport studies of the insulator metal transition

Nakamura *et al.* [18] found that the insulator-metal transition in  $\text{Ca}_2\text{RuO}_4$  can be induced when applying an electric field of  $E = 40 \text{ V/cm}$  at room temperature. At this field the sample resistance drops leading to a jump in current density  $j$ . For the transport studies we use a two-contact circuit with a finite preresistance that limits the current when the samples becomes metallic, and we drive the sample with controlled voltage. In contrast, for the temperature-dependent diffraction studies we drive the crystal by controlling the current, as otherwise the current would strongly change with temperature. When ramping the current up in the current-controlled mode the electronics regulate the voltage to reach the demanded

current and initially exceeds the critical voltage or electric field and thus enforces the partial insulator-metal transition. We confirm the current-induced insulator-metal transition [18] in both samples, pure and Ti substituted ones, with critical electric fields of the same order (Fig. 2). The critical field denotes the value, at which the material changes from insulating to conducting characteristics. Upon cooling the sample resistivity increases and the critical electric field increases as well [Figs. 2(g) and 2(h)] similar to reports in Refs. [18,30]. The more insulating the sample becomes, the higher fields are necessary to transform it to the metallic state. For this reason any changes of current or voltage in the XRD and neutron experiments were applied above 250 K, where the samples are still conductive enough and where stronger cooling power is provided.

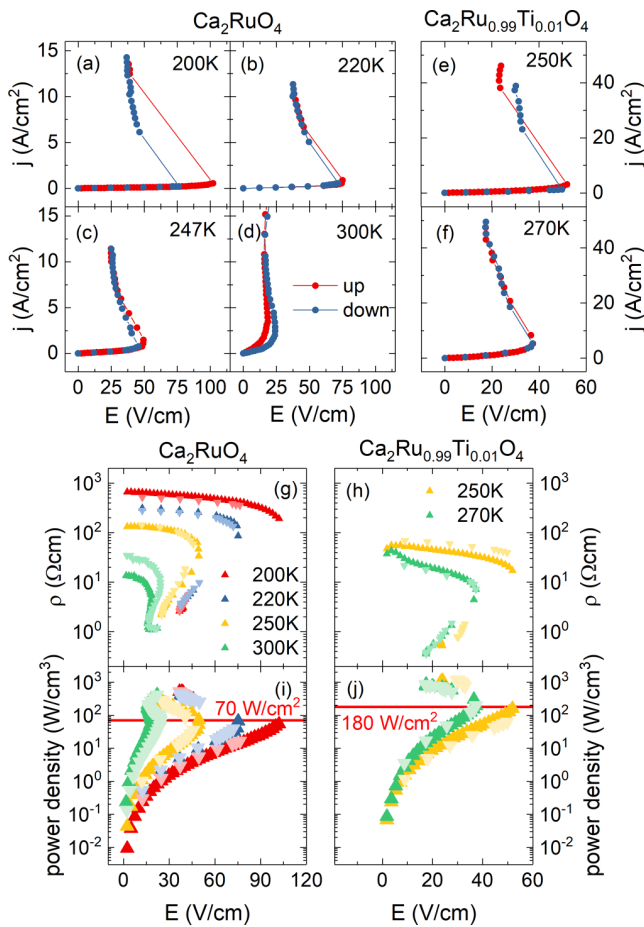


FIG. 2. Switching characteristics of pure and 1% Ti-substituted  $\text{Ca}_2\text{RuO}_4$  in dependency of temperature. (a)–(f) Characteristic  $j$ - $E$  curves display the current-induced phase transition in a voltage controlled setup (the electric field has been corrected for the circuit resistance effects). Here red coloring denotes data taken for ramping the voltage up and blue for ramping down. (g, h) The calculated resistivities from the two-point measurements above show a clear drop at a temperature-dependent critical electric field. (i) and (j) represent the corresponding power densities in the  $j$ - $E$  characteristic. The threshold power density, at which the switching occurs, is constant for all measured temperatures. Dark coloring is used for the up direction, light coloring for the down direction.

While the critical electric field increases, the critical current density decreases with decreasing temperature. The resulting critical power density does not exhibit a temperature dependence but stays constant for the measured temperature range between 220 and 300 K [Figs. 2(i) and 2(j)], which indicates that the current-induced insulator-metal transition is not simply due to heating of the entire crystal. Many aspects of the electric-field-driven insulator-metal transition in  $\text{Ca}_2\text{RuO}_4$  resemble that in  $\text{VO}_2$ , for which it was also reported that the threshold power density does not vary with temperature [31]. Both  $\text{Ca}_2\text{RuO}_4$  samples, pure and substituted ones, show comparable switching behavior. The substituted sample exhibits a slightly lower resistivity which is connected to higher critical current densities. The threshold electrical power density is therefore more than a factor of 2 higher than that in the pure sample [Figs. 2(i) and 2(j)]. Nevertheless the Ti substitution does not effect the current-induced insulator-metal transition significantly, for which reason the substitution can be disregarded for the following analysis of results.

The form of the  $j$ - $E$  characteristic, see Fig. 2, that has consistently been reported by many groups [18,23,30] inevitably leads to the formation of inhomogeneous current-carrying states. This effect has been shown on general grounds, and it is well known in the physics of semiconductors [32] that the state with negative differential resistance  $\frac{dI}{dV} < 0$  is absolutely unstable. Therefore, the  $S$ -shaped  $j$ - $E$  (or  $I$ - $V$ ) characteristic leads to the formation of filaments predominantly parallel to the current (but in the real system usually forming a percolation network), whereas the  $N$ -shaped  $I$ - $V$  curve results in the formation of insulating and metallic domains (Gunn domains) perpendicular to the current (Gunn domains usually move with current leading to the oscillating behavior–Gunn oscillations). The formation of metallic filaments in an insulating matrix is well documented in many systems with insulator-metal transitions, notably in  $\text{VO}_2$  [31,33–35] and in  $\text{SrTiO}_3$  [36]; they lead to a percolation picture of conduction and to switching phenomena. Due to the impact of strain, however, the arrangement of the metallic parts can essentially change, see discussion below.

As a result of the inhomogeneous state the current is predominantly concentrated in narrow metallic channels, in which the local current density is much higher than the average one, so that the local Joule heating  $jEV = \rho j^2$  (in the current-controlled regime, as used in most experiments) and the resulting local temperature in the current carrying parts will also be higher than that estimated by bulk probes. The question whether the metal-insulator switching often observed in systems with metal-insulator transition is due to intrinsic effects or caused by local heating is difficult to answer.

## B. Time-resolved analysis of the current-induced insulator-metal transition

To elucidate the question of what induces the rise in conductivity, the electric field connected to the forced current or simple Joule heating, we performed time-resolved pulsed experiments as illustrated in Fig. 3. Most likely one has to consider phase separation into an insulating and a percolating phase carrying most of the current. The idea of the time-resolved study is to disentangle timescales of a field-driven

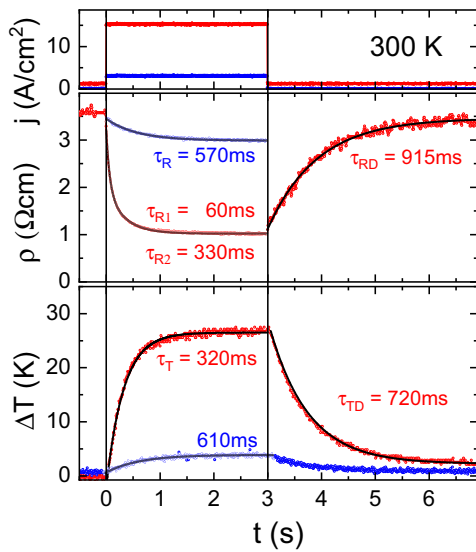


FIG. 3. Pulsed current measurements of sample resistivity (middle panel) and temperature (bottom) in  $\text{Ca}_2\text{RuO}_4$ . For driving currents below the threshold ( $3 \text{ A/cm}^2$ , blue, top panel) the resulting change in  $\rho$  can be modeled with an mono-exponential decay with a decay time similar to the rise time found for the concomitant heating (bottom panel). For larger driving currents above the threshold ( $15 \text{ A/cm}^2$ , red, top panel) the change in  $\rho$  only can be modeled employing a bi-exponential decay: A slowly relaxing component  $\tau_{R2} \approx 300 \text{ ms}$  in accord with the rise time of temperature (bottom) and a significantly faster process with  $\tau_{R1} \approx 60 \text{ ms}$ , which seems to be directly induced via the current, or correspondingly, via the electric field.

switching process and of presumably unavoidable heating effects.

The upper panel of Fig. 3 displays the pulse pattern used to induce additional conductivity. Switching-on a smaller current of about  $3 \text{ A/cm}^2$  leads to a mono-exponential drop in resistivity (middle panel) of about 15% with a slow time constant of  $\tau_R = 570 \text{ ms}$ . At the same time the sample temperature rises with a similar time constant saturating  $3.2 \text{ K}$  above the starting value of  $298 \text{ K}$ . Obviously, the resistivity changes in this below-threshold regime are coupled to the heating. After switching-off the current at  $t = 3 \text{ s}$  the temperature decays to  $298 \text{ K}$  again. Considering a power dissipation of about  $\rho j^2 \approx 15 \text{ W/cm}^3$ , and thus still of the order of  $6 \text{ mW}$  in the sample crystal even for this smaller driving current, such heating has to be expected. The red curves in Fig. 3 denote results for the larger driving current of  $15 \text{ A/cm}^2$ . Here a small base current of  $1 \text{ A/cm}^2$  is applied before and after the pulse to enable the determination of the resistivity in these regimes. The drop in resistivity now amounts up to 70% but it is not possible to describe the underlying time dependence using only one relaxation time. A bi-exponential fit reveals a much faster decay time of  $\tau_{R1} \approx 60 \text{ ms}$ , together with a slower one of  $\tau_{R2} \approx 330 \text{ ms}$ . This last is in accord with the corresponding rise time of the temperature (bottom). The faster process seems not to be induced by simple heating (even though a considerable increase in temperature of up to  $28 \text{ K}$  can be monitored). This second mechanism has to be attributed to the direct induction of a more conductive phase

via the current or, correspondingly, via the electric field. It is interesting to note that after switching-off this larger driving current, the electrical relaxation time exceeds the thermal one. The field-induced phase appears to be metastable which is in accord with the observed hysteresis in the  $j$ - $E$  curves, see [18] and Fig. 2.

The observation of two relaxation rates in the resistance unambiguously confirms an intrinsic origin of the current induced switching. There are several processes that can be associated with the faster conductance enhancement, such as a purely electronic mechanism or filament formation. The fact that even this faster process happens on a timescale above milliseconds suggest some structural implication.

### C. X-ray and neutron diffraction studies as function of current density and temperature

Since the metallic and insulating phases in  $\text{Ca}_2\text{RuO}_4$  differ strongly in their lattice constants, diffraction is a suitable experimental technique to investigate phase changes in this material. Specifically, the lattice parameter  $c$  strongly increases by  $\approx 3\%$  between the insulating phase at room temperature and the metallic phase at  $\sim 360 \text{ K}$  [10,11], which allows one to distinguish these two phases. However, a good resolution is required in neutron diffraction experiments. One expects to observe (00L) reflections at lower  $2\theta$  values when the material becomes metallic. The metallic phase (MP) of  $\text{Ca}_2\text{RuO}_4$  was initially labeled as  $L$  phase due to its longer  $c$  axis, while the insulating phase (IP) is frequently labeled as  $S$  (for short) phase [7,10].

As described above, switching the  $\text{Ca}_2\text{RuO}_4$  crystals from the insulating to the metallic state involves large power densities. Note that a power density of  $100 \text{ W/cm}^3$  would result in a temperature drift of  $36 \text{ K/s}$  for a material without any thermal contact just by taking the specific heat into account [37]. As illustrated in the time-resolved experiments, heating of the sample during the diffraction studies cannot be completely avoided and must be carefully taken into consideration. The controversial diffraction results [18,22,28,30] most likely stem from differing heating conditions. With an additional sensor placed close to the crystal and with the good electric and thermal contact of the sample to a large Cu plate heating effects could be reduced and better documented in most of our experiments.

As a first example, we show the ramping up of the current density in a neutron diffraction experiment in Fig. 4. The cryostat temperature was set to  $250 \text{ K}$ , which is advantageous compared to simple experiments at ambient conditions because it provides strong cooling power. The thermocouple with its sensor placed opposite to the crystal on the Cu plate shows that heating occurs even at these rather low current densities. Note that the thermocouple can only give a lower estimate of the true sample temperature. Similar to several other studies we observe an increase of the  $c$  lattice parameter of the insulating phase. Half of this can be attributed to the temperature change detected in the thermal couple and thus to heating of the entire sample, but most likely an even larger part of the  $c$  parameter enhancement is simply due to heating. In the scenario of phase separation the metallic parts will sense even higher local heating.

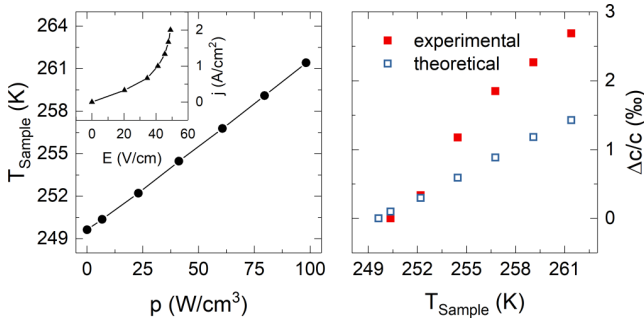


FIG. 4. Sample temperature (thermocouple) in comparison to power density and relative lattice change while ramping up current at the fixed cryostat temperature of 250 K. The purely temperature-driven relative lattice change (open squares) is taken from Ref. [11] for the given temperature range. The experimental lattice change is derived from the (006) reflection in the neutron diffraction experiment.

Some studies seem to partially ignore the heating and report an important intrinsic change of the insulating phase with small currents, a modified short- $c$  phase. However, this modified short- $c$  phase in Ref. [28] exhibits a  $c$  lattice constant increase just up to the maximum value that the insulating  $\text{Ca}_2\text{RuO}_4$  phase reaches upon heating without a current (before the insulator-metal transition takes place at 357 K). Furthermore, the modified short- $c$  phase proposed at 130 K with a large current density of  $10 \text{ A/cm}^2$  perfectly agrees with the current-free insulating phase at the temperature of 240 K: The lattice constants reported in Ref. [28] amount to  $a = 5.404$ ,  $b = 5.547$ , and  $c = 11.848 \text{ \AA}$  compared to  $a = 5.407$ ,  $b = 5.560$ , and  $c = 11.854 \text{ \AA}$  for current-free  $\text{Ca}_2\text{RuO}_4$  at 240 K, taken from Ref. [11], and also the internal parameters perfectly agree [38].

XRD experiments with a Ti-free sample show a second (002) reflection appearing when the current density is increased to  $j = 69 \text{ A/cm}^2$  at a temperature of 294 K [Fig. 5(a)]. Note, however, that the sample was already mounted into a cryostat and temperature stabilized in order to reduce the local heating. The characteristic  $j$ - $E$  curve [Fig. 5(c)] and the resistivity [Fig. 5(e)] indicate that the sample becomes already conductive at much lower current densities ( $\approx 2.6 \text{ A/cm}^2$ ), where no significant change in the diffraction pattern is observable [Fig. 5(a)]. At high temperature, the Bragg reflection associated with the metallic phase exhibits a similar intensity as that of the insulating phase, but it becomes rapidly weaker upon cooling [Figs. 5(b) and 5(d)] in spite of the rather large current flowing. The  $c$  lattice parameter of the metallic phase stays constant upon cooling in agreement with measurements on Sr-substituted materials, in which the metal-insulator transition occurs at lower temperatures [11] [Fig. 5(f)]. The  $2\theta$  value of the Bragg peak associated with the insulating phase increases upon cooling following the pronounced shortening of the  $c$  lattice parameter of the insulating phase at low temperature. The cryostat temperature has been corrected by the offset indicated by the thermal couple scaled by a factor of 2.5 to take the slight displacement of the thermocouple in the x-ray diffraction experiment into account. Nevertheless the observed  $c$

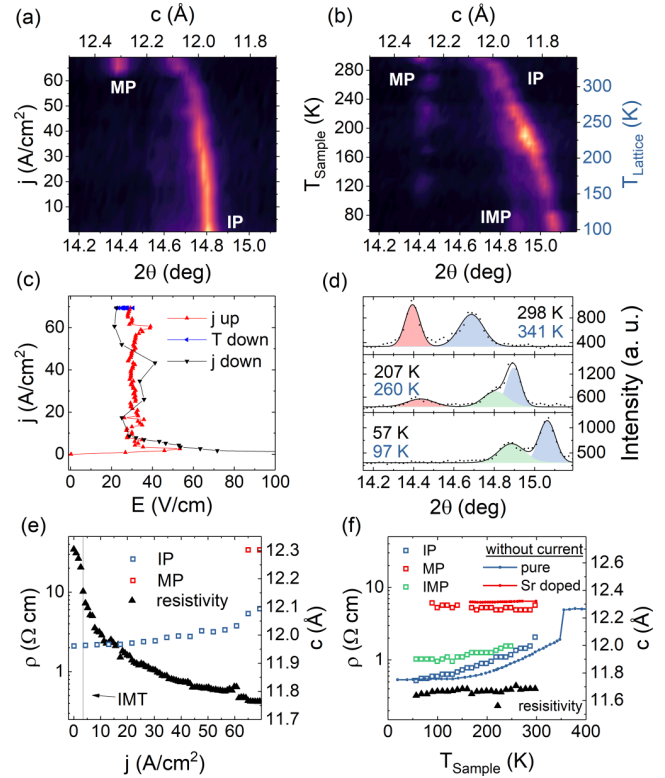


FIG. 5. X-ray diffraction study of the (002) reflection under an applied current density of up to  $j = 69 \text{ A/cm}^2$  on pure  $\text{Ca}_2\text{RuO}_4$ . Panels (a) and (b) show the evolution of different phases characterized by different  $c$  lattice parameters while ramping up current and cooling down with constant current, respectively. The coexistence of phases, visible in the three reflections, is strongly temperature dependent. (c) The  $j$ - $E$  curve is measured simultaneously to the XRD experiment while ramping up current, cooling down, and decreasing the current. (d) The quantitative analysis of  $2\theta$  scans clearly displays the phase mixture of three phases. Here the metallic (MP) and insulating (IP) phases are colored in red and blue, respectively. The third phase is colored in green and is labeled as intermediate phase (IMP).  $T_{\text{Sample}}$  (black) represents the cryostat temperature corrected by the thermocouple while  $T_{\text{Lattice}}$  (blue) is calculated by comparing the reflection angle of insulating phase to the temperature dependency of a current free sample, taken from Ref. [11], i.e., ignoring any intrinsic change. (e, f) Resistivity and lattice parameter in dependence to current density and sample temperature, respectively. The resistivity displays the occurrence of the insulator-metal transition long before the metallic phase becomes visible in (e) the XRD measurement and (f) the decreasing resistivity while cooling down coincides with the phase existence of the intermediate phase. The temperature dependency of  $c$  lattice parameter of  $\text{Ca}_2\text{RuO}_4$ , from Ref. [11], is added for comparison. The low-temperature lattice parameter of the metallic phase (red line) is taken from data of  $\text{Ca}_{1.9}\text{Sr}_{0.1}\text{RuO}_4$  from the same reference.

values of the insulating phase lie above the reported temperature dependence of the insulating phase without any current [Fig. 5(f)]. At high temperature, the insulating phase reflection exhibits significant broadening, see Fig. 5(d), which can be easily recognized from the comparison with the metallic phase peak [Fig. 5(d)]. Below  $\sim 260 \text{ K}$  a third reflection appears

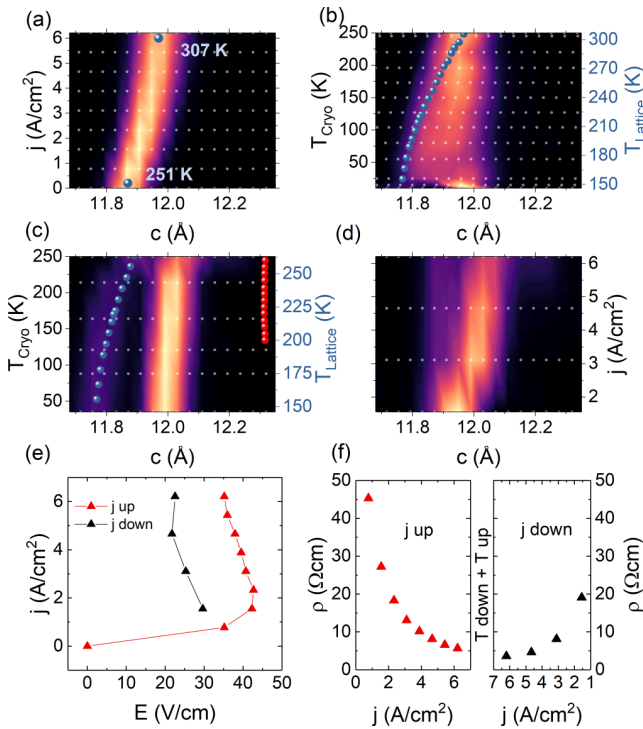


FIG. 6. Evolution of  $c$  lattice parameter recorded by elastic neutron scattering in a measuring sequence of (a) increasing current, (b) decreasing temperature, (c) increasing temperature, and (d) decreasing current. Longitudinal scans are taken across the (006) reflection in pure  $\text{Ca}_2\text{RuO}_4$  at various current densities and temperatures. The blue circles represent the temperature dependency of  $\text{Ca}_2\text{RuO}_4$  lattice parameters without current, taken from Ref. [11] and is used to determine  $T_{\text{Lattice}}$  from the experimental lattice parameter of the insulating phase. The low-temperature lattice parameter of the metallic phase (red balls) is taken from data of  $\text{Ca}_{1.9}\text{Sr}_{0.1}\text{RuO}_4$  from the same reference and plotted against  $T_{\text{Lattice}}$ . The small gray dots represent the measured points and the color maps are obtained with an interpolation algorithm. (e) The  $j$ - $E$  curve is measured simultaneously to the neutron diffraction experiment while ramping up current, cooling down, heating up, and decreasing the current. (f) Sample resistivity is derived from the two-point measurement and displayed for the measurement sequence.

that unambiguously indicates phase coexistence of at least three phases with different  $c$  lattice parameters: Besides the insulating phase (IP) and the metallic phase (MP) there is an intermediate phase (IMP), see Fig. 5(d).

The coexistence of three phases is confirmed by neutron diffraction experiments which also aim to characterize the magnetic ordering in the low current-density range. In a first set of experiments (Fig. 6) the current density was ramped up to  $j = 6.2 \text{ A/cm}^2$ . An additional thermocouple could not be used in this experiment. The color maps in Figs. 6(a) to 6(d) represent the lattice parameter  $c$  extracted from longitudinal scans across the (006) Bragg position and its change during a full measurement cycle of ramping up the current, cooling, reheating, and ramping the current down. At a cryostat temperature of 250 K the current increase leads to an increased  $c$  lattice parameter while no additional reflection becomes visible [Fig. 6(a)]. The  $j$ - $E$  curve clearly

indicates a transition from insulating to metallic state at only  $j = 1.55 \text{ A/cm}^2$ , see Fig. 6(f). The shift of the insulating phase reflection can mostly be assigned to a thermal drift of the sample and therefore it can be used to roughly estimate the sample temperature, although this will overestimate the temperature due to the neglecting of the intrinsic shift, see discussion below. A current density of  $j = 6.2 \text{ A/cm}^2$  heats up the sample by  $\sim 50 \text{ K}$ . When cooling the sample under fixed current a phase separation at low temperatures occurs similar to the XRD observation. The significant broadening of the insulating phase peak increases until two reflections can be distinguished, which we assign to the insulating phase and the intermediate phase [Fig. 6(b)]. Interestingly this phase segregation is not reversible as the two distinct reflections stay separated when increasing the temperature again, see Fig. 6(c). The phase separation and the appearance of the intermediate phase is associated with a reduction of the resistance, see Figs. 6(e) and 6(f), which also reduces the sample heating. Therefore, the sample temperature with the cryostat stabilized at 250 K is lower after the cooling and heating cycle. In addition to the insulating and intermediate phase reflections a weak third peak becomes visible at high temperatures with a  $c$  lattice parameter close to the metallic phase. This third phase also disappears quickly when reducing the current density at  $T_{\text{cryo}} = 250 \text{ K}$  at the end of the full cycle. Below  $3 \text{ A/cm}^2$  the intermediate phase reflection fades out and only one reflection persists [Fig. 6(d)]. The presented full measurement cycle documents a complex real structure arising from phase segregation with strong hysteresis. The amount of insulating, intermediate and metallic phase are not only determined by current strength and temperature but also depend on the history of the sample, similar to reports in Ref. [22].

The mappings of the reflection against longitudinal (00 $\xi$ ) and transversal ( $\xi$ 00) directions clearly reveal the phase coexistence (see Fig. 7). At high current densities the phase separation is already visible at high temperatures whereas at low current densities the coexistence only appears at low temperatures. It can be concluded that the samples show more than the two conventional insulating and metallic phases at low temperatures. The different positions of the Bragg peaks in the transverse direction (see Fig. 7) indicate that the different lattices are slightly tilted against each other similar to ferroelastic domains in a martensitic transition, see, e.g., Refs. [39,40].

Using a two-axis diffractometer the accessible  $\mathbf{Q}$  space is limited to a scattering plane spanned by two crystallographic directions. Therefore, a full structural analysis is not possible. But the twinning of the crystals with respect to the orthorhombic distortion allows one to measure the (200) and (020) reflections in addition to the (006) reflection [Fig. 8(a)]. In this set of neutron experiments with a stronger closed cycle refrigerator SUMITOMO RDK 205D and with a thermocouple mounted as indicated in Fig. 1, we cooled the crystal with a further reduced current density of  $j = 1.5 \text{ A/cm}^2$ . We find qualitatively the same phase segregation and the appearance of the intermediate phase reflection below  $\sim 50 \text{ K}$ , as it is shown in the longitudinal scan across the (006) Bragg position, see Fig. 8(a). The longitudinal scans across (200) show two reflections. The  $a$ -axis twin results in higher  $2\theta$  values

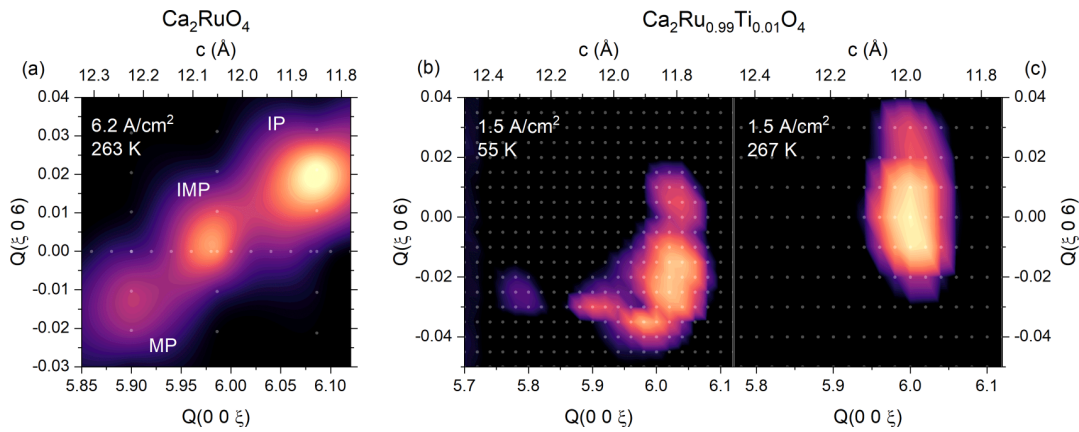


FIG. 7. Mapping of reflections around (006) Bragg peak for two different samples, temperatures, and current densities. The small gray dots represent the measured points and the color maps are obtained with an interpolation algorithm.

and the *b*-axis twin in lower values, respectively, because the lattice parameter *a* is smaller than *b*. The *a*-axis peak does not exhibit a strong temperature dependence, neither in  $2\theta$  nor in peak width. However, the *b*-axis reflection shifts to higher  $2\theta$  values synonymous with the decrease of the lattice parameter *b*. Only at 39 K the lattice parameter *b* increases again. Additionally to the shift, the Bragg peak of the *b*-axis twin is significantly broadened below 50 K [Fig. 8(c)]. This broadening can be attributed to the appearance of the intermediate phase, whose *b* lattice parameter is expected to be slightly smaller since it exhibits a more metallic character. Both the appearance of the intermediate phase and the broadening of the *b*-axis reflection below 50 K, coincide with a drop in sample re-

sistance [Figs. 8(b) and 8(c)]. This again connects the appearance of the intermediate phase to an increased conductivity.

Sow *et al.* showed that below 50 K  $\text{Ca}_2\text{RuO}_4$  exhibits anomalous properties under applied current [21]. In their magnetization measurements they could not find any anti-ferromagnetic transition for nonzero current densities. Ti-substituted  $\text{Ca}_2\text{RuO}_4$  exhibits the B-centered AFM order [29], which leads to a magnetic (101) Bragg reflection [29]. We studied this reflection depending on temperature and under applying a small current density (Fig. 9). Without current application the peak intensity rapidly decreases only close to the transition temperature  $T_N = 110$  K and becomes zero already at 119 K [Fig. 9(a)]. Single point counts on the

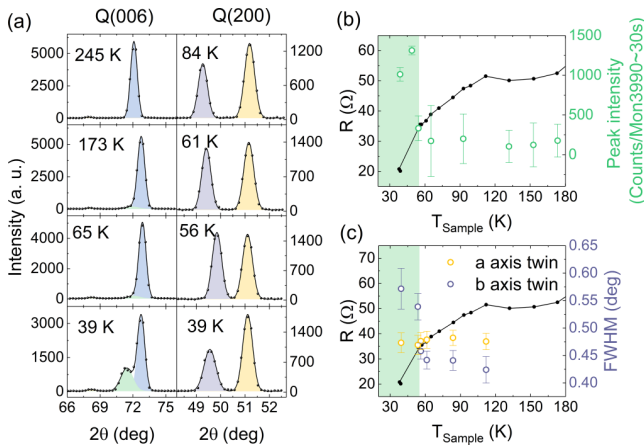


FIG. 8. (a) Longitudinal scans across the (006) Bragg peak, left column, and (200) Bragg peaks, right column, at various temperatures and with applied current ( $j = 1.5 \text{ A/cm}^2$ ) on pure  $\text{Ca}_2\text{RuO}_4$ . The black line represents the sum of Gaussians while the single contributions are marked by the colored areas. In the left column the blue area illustrates the metallic phase, green the intermediate phase whereas the different twin fractions visible in the longitudinal scans of (200) are displayed in yellow (*a* axis twin) and purple (*b* axis twin). (b) Comparison of the temperature dependence of the sample resistance and the fitted peak intensity of intermediate phase. (c) Comparison of the temperature dependence of the resistance and the fitted peak width of both twin fractions.

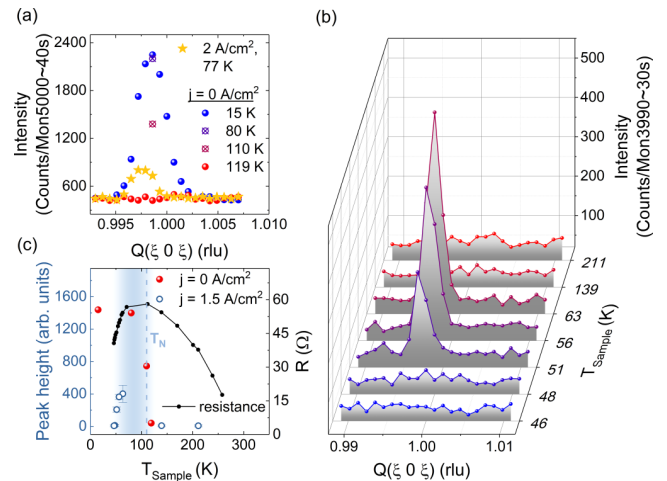


FIG. 9. Influence of current application on the magnetic (101) reflection in substituted  $\text{Ca}_2\text{RuO}_4$ . (a) Longitudinal scans over (101) and single-point count rates at different temperatures. The magnetic signal is reduced but persists with a low current density of  $j = 1.5 \text{ A/cm}^2$ . (b) Temperature dependence of longitudinal scans over the (101) reflection with an applied current density of  $j = 1.5 \text{ A/cm}^2$ . (c) Temperature dependence of the sample resistance recorded simultaneously with the neutron scattering in comparison to the peak heights from panel (b) (obtained by fitting with Gaussians). The red spheres represent the peak height of the (101) reflection measured without current from panel (a).

maximum of the longitudinal scan over (101) at 80 K show that the intensity has little changed up to this temperature in agreement with previous reports [10,29]. While applying a current of 120 mA ( $j = 2 \text{ A/cm}^2$ ) the lowest sample temperature reached is 70 K as determined by the thermocouple. At this experimental configuration ( $T_{\text{sample}} = 77 \text{ K}$ ,  $j = 2 \text{ A/cm}^2$ ) the (101) reflection remains visible, although with reduced intensity compared to the current-free phase at 80 K. It can be clearly stated that magnetically ordered regions survive the application of small currents. The reduction of peak intensity can be caused by various factors such as reduction of ordered phase volume or reduction of the transition temperature and ordered moment. By applying lower current densities ( $j = 1.5 \text{ A/cm}^2$ ) it is possible to cool the sample below 50 K (as indicated by the thermocouple), see Fig. 9(b) for the temperature-dependent evolution of the (101) reflection. The peak intensities in Fig. 9(c) reflect the appearance of the magnetic Bragg peak at 63 K, well below the transition temperature of current free  $\text{Ca}_2\text{RuO}_4$ . Surprisingly the Bragg peak at the magnetic position does not persist to low temperatures but suddenly disappears upon further cooling. The suppression of the AFM ordering can be associated with the appearance of the intermediate phase and the reduction of the resistance, see Figs. 8 and 9.

#### IV. DISCUSSION

The totality of diffraction studies in our and in previous [18,22,28,30] experiments remains puzzling and cannot be fully reconciled. Most likely different experimental conditions—in particular concerning temperature control and measurement—have a large impact on the real structure of the  $\text{Ca}_2\text{RuO}_4$  crystals that carry finite current density below the metal-insulator transition. Our comprehensive diffraction studies indicate that for the largest part of the studied current and temperature ranges the samples are structurally inhomogeneous presenting a complex phase coexistence. Phase coexistence must even be expected in view of the  $S$ -shaped  $j$ - $E$  characteristics [32].

Our experiments for currents perpendicular to the planes as well as all previous experiments agree concerning the fact that only very high current densities applied at elevated temperature result in strong Bragg scattering that can be associated with the high-temperature metallic state of  $\text{Ca}_2\text{RuO}_4$ , i.e., a  $c$  lattice constant close to  $12.25 \text{ \AA}$ . When ramping up a high current density of the order of  $j = 10 \text{ A/cm}^2$  and above, it seems unavoidable to heat the crystal and several groups report that the  $c$  value of the insulating phase increases close to  $\sim 12.05 \text{ \AA}$  [18,22,28], which is the largest  $c$  value the insulating phase of  $\text{Ca}_2\text{RuO}_4$  attains upon heating (without current) before it transforms to the metallic phase [11]. Even though there is no doubt that metallic conduction is induced at temperatures well below the metal-insulator transition as can be seen in, e.g., our time-resolved studies, any results with large current densities have to be considered with great care. Our temperature-dependent measurements at large current densities unambiguously show that even in this case the metallic phase Bragg contributions rapidly diminish upon cooling, see Figs. 5(a), 5(b), 5(d), and Fig. 6(c). When analyzing the total scattering one must, however, keep the spatial extension

of the different phases in mind. If the spatial extension of the metallic phase falls below the coherence length of the diffraction experiment, the metallic phase scattering will become broadened in  $Q$  space. For our XRD experiment with a conventional x-ray tube we can estimate the spatial coherence to be in the range of 40 nm [41], while the coherence length in the neutron experiments amounts to around 20 nm. In our and all previous diffraction studies the use of tiny crystals [18,22,28] rendered it impossible to characterize such weak diffuse scattering.

The low-current state in  $\text{Ca}_2\text{RuO}_4$  exhibits a large negative magnetoresistance [21] that is difficult to explain without magnetism. However, a similar observation in an imperfect bulk-insulating topological insulator was attributed to the Zeeman effect on barely correlating current paths [42].

Small metallic phase regions embedded in an insulating matrix will nevertheless impact the Bragg scattering of the insulating phase because the average  $c$  lattice constant within the coherence volume increases. Such effects can explain the behavior of the Bragg contributions of insulating and intermediate phases. The  $c$  constant of the insulating phase with finite current is very close to that of the current-free insulating phase, and the small deviations can stem from some current-induced heating combined with the admixture of short-range (i.e., extension below the coherence length) metallic parts, but the diffraction studies cannot exclude an intrinsic effect due to, e.g., homogeneous loss of orbital polarization. In particular, when ramping the current density up the inclusion of more and more metallic phase regions yields a continuous increase of  $c$ . The crystal structure reported for a large current density of  $10 \text{ A/cm}^2$  at 130 K [28] exactly corresponds to that of current-free  $\text{Ca}_2\text{RuO}_4$  at 240 K [11,38], therefore it can also be explained by metallic admixtures (combined with heating). However, the density functional theory (DFT) analysis proposing this structure as semimetallic [28] can be questioned in view of the well established insulating properties of  $\text{Ca}_2\text{RuO}_4$  at 240 K.

In pure and in substituted crystals we find the intermediate phase under various conditions, and evidence for a similar phase can also be found in the room temperature x-ray studies by Cirillo *et al.* [30]. The intermediate phase appears to be crucial for the understanding of the anomalous properties at low current densities, which must result from some important intrinsic change. Our neutron experiments for current densities of 1 to  $2 \text{ A/cm}^2$  suggest that the intermediate phase appears or becomes enhanced in the temperature range below 100 K. In addition we still find Bragg scattering at the position where AFM order contributes a Bragg peak in the normal insulating state. This observation indicates that AFM ordering can coexist with current carrying parts in one crystal, see Fig. 9. However, the AFM Bragg scattering disappears when the intermediate phase forms. Most likely the intermediate phase represents a more regular and more homogeneous arrangement compared to the modified insulating phase, but again a homogeneous loss of electronic order cannot be excluded on the basis of the diffraction studies. In the percolative picture of small metallic phase regions in an insulating matrix the intermediate phase is attributed to a stronger and more homogeneous content of metallic

regions with most likely also a more regular arrangement. The occurrence of the intermediate phase is accompanied with an enhanced conductance in agreement with a more regular arrangement.

The optical room-temperature studies by Zhang *et al.* [24] reveal a regular microstripe pattern of metallic phase and insulating phase regions. Such a regular arrangement is common in martensitic phase transitions that create strong local strain [39,40,43–45]. In martensite transitions the domains may even form well-defined superstructures [40,46] arising from a regular arrangement of very small domain sizes causing superlattice reflections. A similar strain mechanism was also proposed to explain stripe-like phenomena in various transition-metal oxides [47]. Indeed the differences in the lattice constants between metallic phase and insulating phase in  $\text{Ca}_2\text{RuO}_4$  without currents are huge. And these differences strongly increase upon cooling. The low-temperature  $c$  parameter of insulating  $\text{Ca}_2\text{RuO}_4$  is  $\sim 0.5$  Å shorter than that of the metallic phase, and the difference in the orthorhombic  $b$  parameter amounts to  $\sim 0.25$  Å. In contrast the  $a$  parameter is almost identical. The optical experiment examines an  $a, b$  surface and finds stripes perpendicular to orthorhombic  $b$ , which is the expected arrangement for martensitic domains that reduce the strong in-plane strain along  $b$ . Similar domain arrangements must, however, also exist perpendicular to the planes, as the  $c$  strain would be even larger. Both strain effects should result in a relative tilting of metallic phase and insulating phase domains. Since the relative strains will increase by a factor of 3 upon cooling, the microstripe pattern will considerably change. The lattice strain seems to be the driving force for the rearrangement of the phase volumes and in particular for the occurrence of the intermediate phase at low temperatures. We speculate that the intermediate phase is a more fine mesh of insulating and metallic parts, so that the average is better defined with intermediate lattice constants. For this finer mesh there is enhanced mutual influence of one state on the other state, which explains the disappearance of AFM ordering. However, studies with local probes are required to fully resolve the structural nature of the intermediate phase. Considering the strain effects and the fact that the insulator-metal transition can be induced by only moderate hydrostatic pressure above 0.5 GPa [12,16], one may assume that  $\text{Ca}_2\text{RuO}_4$  grown on a substrate causing tetragonal strain will even more easily undergo the insulator-metal transition at low temperature.

It also appears most important to understand the relation between the two mechanisms explained above: The formation of conducting filaments typically parallel to the current arising from the general phase instability [32] and the impact of the crystal strain due to the large differences in lattice constants that will also favor domain formation similar to the well-known effects in martensite transitions [39,40]. One may only speculate how these two phenomena actually couple: under the influence of current, in a negative part of the  $j$ - $E$  curve of Fig. 2, the system becomes unstable. It first tends to form conducting filaments predominantly parallel to the current, in which the insulator-metal transition and local heating imply strong structural changes. But then the strong strain imposes its own pattern in this inhomogeneous state leading to the formation of more complicated microstructures, with metallic

inclusions not just parallel to the current, but largely determined by strain. Therefore, the current has to meander, which finally leads to percolating network. The general picture of the origin and of the main characteristics of the current carrying state in  $\text{Ca}_2\text{RuO}_4$  are certainly related to both mechanisms.

## V. CONCLUSION

X-ray and neutron diffraction studies as a function of temperature and applied current density reveal a complex real structure indicating that phase segregation and phase coexistence are essential for the physics of the current carrying state in  $\text{Ca}_2\text{RuO}_4$ . Evidence for phase segregation is deduced from the S-shaped quasistatic  $j$ - $E$  curves and from two distinct timescales visible in pulsed transport measurements. When crystals are cooled with controlled current density we observe three different contributions to the Bragg peaks that can be easily assigned to phases with distinct  $c$  lattice parameters. Except at very high current densities and at elevated temperatures, there are only minority phases corresponding to the high-temperature metallic state of  $\text{Ca}_2\text{RuO}_4$  with  $c$  lattice constants of the order of 12.25 Å. The relative weight of these metallic contributions to the Bragg scattering continuously decreases upon cooling. The suppression of the Bragg peaks associated with the long- $c$ -axis metallic state, however, does not exclude the persistence of such regions. The spatial extent of metallic regions can just become considerably lower than the coherence length of the diffraction experiment (of the order of 20 to 40 nm). For the lower current densities, below  $j = 2$  A/cm<sup>2</sup>, for which anomalous low-temperature properties have been reported, metallic long- $c$  Bragg scattering is irrelevant. The two other Bragg scattering contributions correspond to  $c$  lattice parameters close to the much smaller values expected for the insulating state. One phase, labeled insulating phase, exhibits rather similar though significantly larger  $c$  values compared to the current-free insulating state, while an intermediate contribution, intermediate phase, appears with about  $\sim 0.1$  Å larger  $c$  constants. Upon cooling, heating, and ramping the current densities up or down the phase ratio between insulating and intermediate states considerably varies, which is associated with changes in the resistance. Most importantly, we find evidence for AFM ordering even in samples carrying moderate current densities, but this AFM ordering seems to be suppressed when parts of the sample transform to the intermediate state.

The characters of the insulating and intermediate phases in the current carrying states cannot yet be fully established, but it cannot be excluded that they simply arise from phase coexistence and regular microarrangements of metallic and insulating regions. The general tendency to phase segregate and the impact of the local strain are proposed to drive the complex real structure in current carrying  $\text{Ca}_2\text{RuO}_4$  at low temperature.

## ACKNOWLEDGMENTS

This work was funded by the Deutsche Forschungsgemeinschaft (DFG, German Research Foundation) Project No. 277146847 - CRC 1238, projects A02, B02, and B04.

- [1] F. Chudnovskiy, S. Luryi, and B. Spivak, Switching device based on first-order metal-insulator transition induced by external electric field, in *Future Trends in Microelectronics: The Nano Millennium* (Wiley, New York, 2002), p. 148.
- [2] C. Vaju, L. Cario, B. Corraze, E. Janod, V. Dubost, T. Cren, D. Roditchev, D. Braithwaite, and O. Chauvet, Electric-pulse-driven electronic phase separation, insulator-metal transition, and possible superconductivity in a mott insulator, *Adv. Mater.* **20**, 2760 (2008).
- [3] M. M. Qazilbash, M. Brehm, B.-G. Chae, P.-C. Ho, G. O. Andreev, B.-J. Kim, S. J. Yun, A. V. Balatsky, M. B. Maple, F. Keilmann, H.-T. Kim, and D. N. Basov, Mott transition in VO<sub>2</sub> revealed by infrared spectroscopy and nano-imaging, *Science* **318**, 1750 (2007).
- [4] A. S. McLeod, E. Van Heumen, J. G. Ramirez, S. Wang, T. Saerbeck, S. Guenon, M. Goldflam, L. Anderegg, P. Kelly, A. Mueller, M. K. Liu, I. K. Schuller, and D. N. Basov, Nanotextured phase coexistence in the correlated insulator V<sub>2</sub>O<sub>3</sub>, *Nat. Phys.* **13**, 80 (2017).
- [5] J. Jeong, N. Aetukuri, T. Graf, T. D. Schladt, M. G. Samant, and S. S. P. Parkin, Suppression of metal-insulator transition in VO<sub>2</sub> by electric field-induced oxygen vacancy formation, *Science* **339**, 1402 (2013).
- [6] K. Szot, R. Dittmann, W. Speier, and R. Waser, Nanoscale resistive switching in SrTiO<sub>3</sub> thin films, *Phys. Status Solidi RRL* **1**, R86 (2007).
- [7] S. Nakatsuji, S.-I. Ikeda, and Y. Maeno, Ca<sub>2</sub>RuO<sub>4</sub>: New Mott insulators of layered ruthenate, *J. Phys. Soc. Jpn.* **66**, 1868 (1997).
- [8] S. Nakatsuji, T. Ando, Z. Mao, and Y. Maeno, Metal insulator transition in Ca<sub>2-x</sub>Sr<sub>x</sub>RuO<sub>4</sub>, *Physica B* **259-261**, 949 (1999).
- [9] C. S. Alexander, G. Cao, V. Dobrosavljevic, S. McCall, J. E. Crow, E. Lochner, and R. P. Guertin, Destruction of the Mott insulating ground state of Ca<sub>2</sub>RuO<sub>4</sub> by a structural transition, *Phys. Rev. B* **60**, R8422(R) (1999).
- [10] M. Braden, G. André, S. Nakatsuji, and Y. Maeno, Crystal and magnetic structure of Ca<sub>2</sub>RuO<sub>4</sub>: Magnetoelastic coupling and the metal-insulator transition, *Phys. Rev. B* **58**, 847 (1998).
- [11] O. Friedt, M. Braden, G. André, P. Adelman, S. Nakatsuji, and Y. Maeno, Structural and magnetic aspects of the metal-insulator transition in Ca<sub>2-x</sub>Sr<sub>x</sub>RuO<sub>4</sub>, *Phys. Rev. B* **63**, 174432 (2001).
- [12] P. Steffens, O. Friedt, P. Alireza, W. G. Marshall, W. Schmidt, F. Nakamura, S. Nakatsuji, Y. Maeno, R. Lengsdorf, M. M. Abd-Elmeguid, and M. Braden, High-pressure diffraction studies on Ca<sub>2</sub>RuO<sub>4</sub>, *Phys. Rev. B* **72**, 094104 (2005).
- [13] Z. Fang and K. Terakura, Magnetic phase diagram of Ca<sub>2</sub>RuO<sub>4</sub> governed by structural distortions, *Phys. Rev. B* **64**, 020509(R) (2001).
- [14] G. Zhang and E. Pavarini, Mott transition, spin-orbit effects, and magnetism in Ca<sub>2</sub>RuO<sub>4</sub>, *Phys. Rev. B* **95**, 075145 (2017).
- [15] S. Kunkemöller, D. Khomskii, P. Steffens, A. Piovano, A. A. Nugroho, and M. Braden, Highly Anisotropic Magnon Dispersion in Ca<sub>2</sub>RuO<sub>4</sub>: Evidence for Strong Spin Orbit Coupling, *Phys. Rev. Lett.* **115**, 247201 (2015).
- [16] F. Nakamura, T. Goko, M. Ito, T. Fujita, S. Nakatsuji, H. Fukazawa, Y. Maeno, P. Alireza, D. Forsythe, and S. R. Julian, From Mott insulator to ferromagnetic metal: A pressure study of Ca<sub>2</sub>RuO<sub>4</sub>, *Phys. Rev. B* **65**, 220402 (2002).
- [17] S. Nakatsuji and Y. Maeno, Quasi-Two-Dimensional Mott Transition System Ca<sub>2</sub>RuO<sub>4</sub>, *Phys. Rev. Lett.* **84**, 2666 (2000).
- [18] F. Nakamura, M. Sakaki, Y. Yamanaka, S. Tamaru, T. Suzuki, and Y. Maeno, Electric-field-induced metal maintained by current of the Mott insulator Ca<sub>2</sub>RuO<sub>4</sub>, *Sci. Rep.* **3**, 2536 (2013).
- [19] S. Whitehead, *Dielectric Breakdown of Solids* (Oxford University Press, Oxford, 1953).
- [20] Y. Taguchi, T. Matsumoto, and Y. Tokura, Dielectric breakdown of one-dimensional Mott insulators Sr<sub>2</sub>CuO<sub>3</sub> and SrCuO<sub>2</sub>, *Phys. Rev. B* **62**, 7015 (2000).
- [21] C. Sow, S. Yonezawa, S. Kitamura, T. Oka, K. Kuroki, F. Nakamura, and Y. Maeno, Current-induced strong diamagnetism in the Mott insulator Ca<sub>2</sub>RuO<sub>4</sub>, *Science* **358**, 1084 (2017).
- [22] H. Zhao, B. Hu, F. Ye, C. Hoffmann, I. Kimchi, and G. Cao, Nonequilibrium orbital transitions via applied electrical current in calcium ruthenates, *Phys. Rev. B* **100**, 241104 (2019).
- [23] R. Okazaki, Y. Nishina, Y. Yasui, F. Nakamura, T. Suzuki, and I. Terasaki, Current-induced gap suppression in the Mott insulator Ca<sub>2</sub>RuO<sub>4</sub>, *J. Phys. Soc. Jpn.* **82**, 103702 (2013).
- [24] J. Zhang, A. S. McLeod, Q. Han, X. Chen, H. A. Bechtel, Z. Yao, S. N. Gilbert Corder, T. Ciavatti, T. H. Tao, M. Aronson, G. L. Carr, M. C. Martin, C. Sow, S. Yonezawa, F. Nakamura, I. Terasaki, D. N. Basov, A. J. Millis, Y. Maeno, and M. Liu, Nano-Resolved Current-Induced Insulator-Metal Transition in the Mott Insulator Ca<sub>2</sub>RuO<sub>4</sub>, *Phys. Rev. X* **9**, 011032 (2019).
- [25] G. Mattoni, S. Yonezawa, and Y. Maeno, Diamagnetic-like response from localized heating of a paramagnetic material, *Appl. Phys. Lett.* **116**, 172405 (2020).
- [26] O. Friedt, P. Steffens, M. Braden, Y. Sidis, S. Nakatsuji, and Y. Maeno, Strongly Enhanced Magnetic Fluctuations in a Large-Mass Layered Ruthenate, *Phys. Rev. Lett.* **93**, 147404 (2004).
- [27] P. Steffens, O. Friedt, Y. Sidis, P. Link, J. Kulda, K. Schmalzl, S. Nakatsuji, and M. Braden, Magnetic excitations in the metallic single-layer ruthenates Ca<sub>2-x</sub>Sr<sub>x</sub>RuO<sub>4</sub> studied by inelastic neutron scattering, *Phys. Rev. B* **83**, 054429 (2011).
- [28] J. Bertinshaw, N. Gurung, P. Jorba, H. Liu, M. Schmid, D. T. Mantadakis, M. Daghofer, M. Krautloher, A. Jain, G. H. Ryu, O. Fabelo, P. Hansmann, G. Khaliullin, C. Pfeleiderer, B. Keimer, and B. J. Kim, Unique Crystal Structure of Ca<sub>2</sub>RuO<sub>4</sub> in the Current Stabilized Semimetallic State, *Phys. Rev. Lett.* **123**, 137204 (2019).
- [29] S. Kunkemöller, E. Komleva, S. V. Streltsov, S. Hoffmann, D. I. Khomskii, P. Steffens, Y. Sidis, K. Schmalzl, and M. Braden, Magnon dispersion in Ca<sub>2</sub>Ru<sub>1-x</sub>Ti<sub>x</sub>O<sub>4</sub>: Impact of spin-orbit coupling and oxygen moments, *Phys. Rev. B* **95**, 214408 (2017).
- [30] C. Cirillo, V. Granata, G. Avallone, R. Fittipaldi, C. Attanasio, A. Avella, and A. Vecchione, Emergence of a metallic metastable phase induced by electrical current in Ca<sub>2</sub>RuO<sub>4</sub>, *Phys. Rev. B* **100**, 235142 (2019).
- [31] A. Mansingh, R. Singh, and S. Krupanidhi, Electrical switching in single crystal VO<sub>2</sub>, *Solid-State Electron.* **23**, 649 (1980).
- [32] A. F. Volkov and S. M. Kogan, Physical phenomena in semiconductors with negative differential conductivity, *Sov. Phys. Usp.* **11**, 881 (1969).
- [33] S. Kumar, M. D. Pickett, J. P. Strachan, G. Gibson, Y. Nishi, and R. S. Williams, Local temperature redistribution and structural

- transition during joule-heating-driven conductance switching in VO<sub>2</sub>, *Adv. Mater.* **25**, 6128 (2013).
- [34] C. N. Berglund, Thermal filaments in vanadium dioxide, *IEEE Trans. Electron Devices* **16**, 432 (1969).
- [35] S. Zhang, M. A. Kats, Y. Cui, Y. Zhou, Y. Yao, S. Ramanathan, and F. Capasso, Current-modulated optical properties of vanadium dioxide thin films in the phase transition region, *Appl. Phys. Lett.* **105**, 211104 (2014).
- [36] S. Stille, C. Lenser, R. Dittmann, A. Koehl, I. Krug, R. Muenstermann, J. Perlich, C. M. Schneider, U. Klemradt, and R. Waser, Detection of filament formation in forming-free resistive switching SrTiO<sub>3</sub> devices with ti top electrodes, *Appl. Phys. Lett.* **100**, 223503 (2012).
- [37] The specific heat at room temperature is taken from Ref. [48] for 8.5% Mn-doped Ca<sub>2</sub>RuO<sub>4</sub>. The temperature increase rate is calculated with  $\Delta T = \frac{p}{C_p n_V}$ , where  $p$  is the power density in W cm<sup>-3</sup>,  $C_p$  the specific heat in Jmol<sup>-1</sup> K<sup>-1</sup>, and  $n_V$  the amount of substance in molcm<sup>-3</sup>.
- [38] The values of atomic distance between the Ru site and the basal oxygen sites Ru-O(1)(avg.) reported in Ref. [28] for the S\* phase at 130 K (in Refs. [10,11] for the S phase at 240 K) amount to 2.003(2.004) Å. The Ru-O(2) distance amounts in both cases to 1.979 Å, which yields an averaged Ru-O distance of 1.995(1.996) Å. The rotation angle  $\Phi$  of the RuO<sub>6</sub> octahedra around the  $c$  axis amounts to 11.874(11.91) degrees. The basal plane is titled in respect to the  $ab$  plane by  $\Theta$ -O(1) 12.43(12.23) degrees and the tilt angle  $\Theta$ -O(2) between the Ru-O(2) bond and the  $c$  axis amounts to 10.65(10.2) degrees.
- [39] A. Khachaturian, *Theory of Structural Transformations in Solids* (Wiley, New York, 1983).
- [40] A. G. Khachatryan, S. M. Shapiro, and S. Semenovskaya, Adaptive phase formation in martensitic transformation, *Phys. Rev. B* **43**, 10832 (1991).
- [41] S. Bartzsch and U. Oelfke, Line focus x-ray tubes a new concept to produce high brilliance x-rays, *Phys. Med. Biol.* **62**, 8600 (2017).
- [42] O. Breunig, Z. Wang, A. A. Taskin, J. Lux, A. Rosch, and Y. Ando, Gigantic negative magnetoresistance in the bulk of a disordered topological insulator, *Nat. Commun.* **8**, 15545 (2017).
- [43] J. Dec, Paraelastic and ferroelastic interfaces, *Phase Transit.* **45**, 35 (1993).
- [44] A. L. Roytburd, Elastic domains and polydomain phases in solids, *Phase Transit.* **45**, 1 (1993).
- [45] J. W. Seo and D. Schryvers, TEM investigation of the microstructure and defects of CuZr martensite. Part I: Morphology and twin systems, *Acta Mater.* **46**, 1165 (1998).
- [46] S. Kaufmann, U. K. Röbler, O. Heczko, M. Wuttig, J. Buschbeck, L. Schultz, and S. Fähler, Adaptive Modulations of Martensites, *Phys. Rev. Lett.* **104**, 145702 (2010).
- [47] D. I. Khomskii and K. I. Kugel, Why stripes? Spontaneous formation of inhomogeneous structures due to elastic interactions, *Europhys. Lett.* **55**, 208 (2001).
- [48] T. F. Qi, O. B. Korneta, S. Parkin, J. Hu, and G. Cao, Magnetic and orbital orders coupled to negative thermal expansion in Mott insulators Ca<sub>2</sub>Ru<sub>1-x</sub>M<sub>x</sub>O<sub>4</sub> (M = Mn and Fe), *Phys. Rev. B* **85**, 165143 (2012).

## 3.2 Magnetic Correlations and Oxygen Moment

### 3.2.1 Introduction

A result of spin-orbit coupling in Ca<sub>2</sub>RuO<sub>4</sub> is the connection of electronic and magnetic transitions with the lattice structure. Starting with the metal-insulator transition in Ca<sub>2</sub>RuO<sub>4</sub> the shape of the RuO<sub>6</sub> octahedra is strongly temperature dependent when cooling down to lower temperatures. Below the metal-insulator transition the octahedra are still elongated but flatten further with the simultaneous expansion of the basal plane along the orthorhombic  $b$  axis [22, 25]. These structural distortions saturate at the onset of magnetic order around  $T_N = 110$  K. The magnetic order corresponds to a simple G-type antiferromagnetic order where the magnetic moments point along the  $b$  direction, i.e. along the longest basal plane direction. The changing distortion inside the insulating state suggests that the orbital ordering proposed for this Mott insulator continues to develop until the onset of magnetic order. An interesting issue to investigate is therefore the possible relation between the orbital polarization and the magnetic correlations above the Néel temperature which should be still measurable outside the ordered phase due to the layered character of Ca<sub>2</sub>RuO<sub>4</sub>. A close connection between orbital polarization and magnetism is the main property of colossal magneto-resistance in manganites and also discussed in the FeAs-based superconductors [91, 92]. The availability of a large untwinned crystal grown by the floating-zone method in our institute enables a thorough neutron scattering study of the magnetic correlations above the three dimensional antiferromagnetic ordering temperature. It is possible to quantify the assumed layered character and search for a connection between the magnetic correlations and the orbital polarization connected with the temperature dependent distortions of the octahedra.

Furthermore in combination with polarized neutrons it is possible to validate the existence of magnetic moment on the apical oxygen position. In various other layered ruthenates like SrRuO<sub>3</sub> and Ca<sub>1.5</sub>Sr<sub>0.5</sub>RuO<sub>4</sub> neutron scattering studies and DFT calculations confirmed the existence of magnetic oxygen moment [14, 93]. First evidence for magnetic moment residing on the apical oxygen in Ca<sub>2</sub>RuO<sub>4</sub> was found by Kunkemöller *et al.* with the finding of a low-energy magnon mode which was attributed to the excitation of the magnetic moment of oxygen [37]. The appearance of magnetic moment in the vicinity of the Ru position is the consequence of larger hopping (or  $p$ - $d$  hybridization) in the  $4d$  ruthenates. The determination of the magnetic structure factor which encodes the magnetic structure and the moment distribution can be achieved by the measurement of a large set of magnetic Bragg reflections with elastic neutron scattering. Here we have to use polarized neutrons because the antiferromagnetic order occurs in the strongly distorted phase of Ca<sub>2</sub>RuO<sub>4</sub> and it does not break translation symmetry but only the glide mirror planes of space group  $Pbca$ . In order to separate nuclear and magnetic contributions for a large set of magnetic Bragg reflection intensities, it is necessary to use polarization analysis. A comparison of the extracted magnetic structure factors with structure factor models can identify the existing magnetic moment distribution inside the RuO<sub>6</sub> octahedra.

### 3.2.2 Results and Analysis

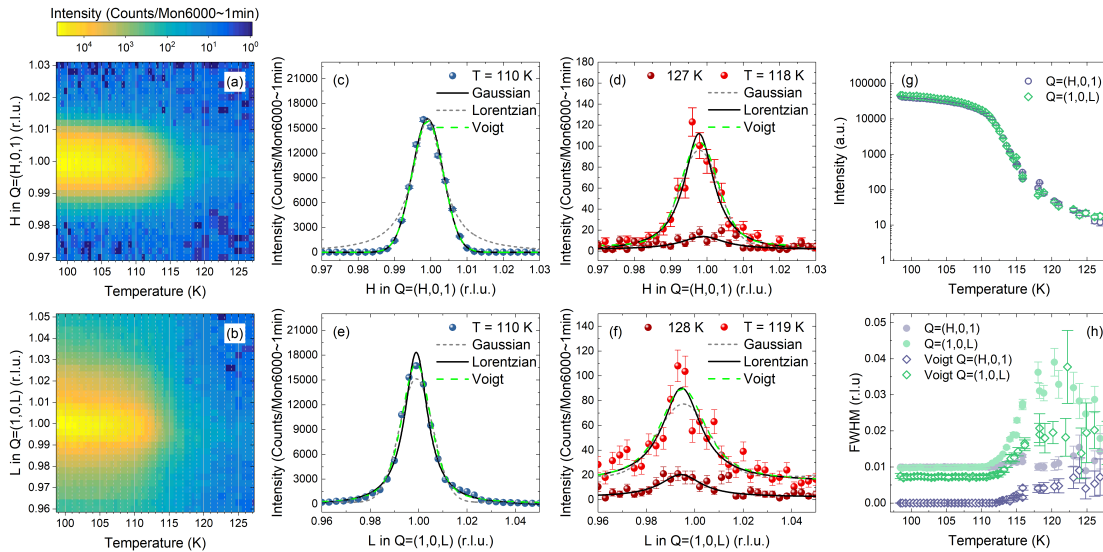


**Figure 3.1: Temperature dependence of the magnetic Bragg peak  $Q = (1, 0, 1)$  and width analysis in  $\text{Ca}_2\text{Ru}_{0.99}\text{Ti}_{0.01}\text{O}_4$ .** The magnetic Bragg reflection  $Q = (1, 0, 1)$  is measured along the  $[H, 0, 0]$  and  $[0, 0, L]$  directions in the proximity of the phase transition with the untwinned sample. (a) and (b) show the vanishing of the peak intensity in the elastic scans with increasing temperature. To extract the line width the scans are fitted with different line shape models (Lorentzian, Gaussian, Voigt). Scans below and above the phase transition are shown exemplary for the  $[H, 0, 0]$  ((c),(d)) and the  $[0, 0, L]$  direction ((e),(f)) respectively. Here the three different line shape models are included and compared with each other. (e) The fitted peak intensities display the phase transition from antiferromagnetic to paramagnetic state. (f) The peak widths show direction depending behavior leaving the magnetically ordered phase as the line width of the  $[0, 0, L]$  direction increases more than in  $[H, 0, 0]$  direction with increasing temperature. The width extracted from the Gaussian and Lorentzian line shape model (full symbols) is compared also with the results for the Lorentzian contribution from the fit using the Voigt profile (open symbols). The FWHM of the Lorentzian contribution in the Voigt profile is reduced but exhibits qualitatively the same direction and temperature dependence.

The investigation of the magnetic correlations close to the phase transition is carried out by measuring the scattering at the magnetic Bragg reflection  $Q = (1, 0, 1)$  in  $[H, 0, 0]$  and  $[0, 0, L]$  directions for different energies. Above the transition the scattering becomes diffuse magnetic scattering stemming from fluctuations which form temporarily ordered regions in the sample as the long-range order disappears. Here a unpolarized cold triple-axis spectrometer (4F2) with low background and a higher  $q$  resolution is used to achieve a good signal-to-noise ratio while possible nuclear scattering contamination like multiple diffraction can be separated. Figure 3.1(a) and (b) display the measured scans in both directions in a two-dimensional intensity map against the temperature. The vanishing of scattering intensities is clearly visible around 112 K. Additionally the scattering intensity in the antiferromagnetic phase seems to be more spread in the  $[0, 0, L]$  direction. The scans in  $Q$  space not only deliver information about the magnetic ordering temperature and magnetic moment size via the peak amplitude, but also the spatial length of magnetic correlations can be quantified via the peak width. Therefore the peaks at the mag-

netic Bragg reflection position are analyzed for each temperature and described with different peak profiles (or line shape models). Examples of the peak fitting and comparison of different line shapes are given for both directions below and above the transition temperature in Figure 3.1(c)-(f). The data in  $[H, 0, 0]$  direction below the phase transition are well described by a Gaussian peak profile while above the phase transition the Lorentzian peak profile seems to be more suitable. In the case of the  $[0, 0, L]$  direction the scans below and above the transition temperature are described well by the Lorentzian peak profile. The fitted amplitude is depicted in Figure 3.1(g) and visualizes the vanishing of magnetic scattering intensity around  $112\text{ K}$ <sup>1</sup>. The temperature dependent change in the line shape can be explained by taking the instrumental resolution into account. The line shape of signals in neutron scattering experiments is determined by the convolution of the instrumental function with the inherent scattering intensity distribution connected with the sample. In the case of a nuclear and magnetic Bragg reflections the scattering intensity is given by a delta function which, by convolution with the instrumental resolution function, results in a Gaussian peak profile governed by the instrument. However, the intensity of diffuse magnetic scattering is given by a Lorentzian distribution whose line width is proportional to the inverse of the magnetic correlation length and changes therefore around the phase transition. This may lead to a change of line shape in the experimental result from Gaussian where the convolution of the instrumental function with delta function or a narrow Lorentzian stays Gaussian shaped to the case where the Lorentzian is broader than the resolution function and the convolution is more Lorentzian shaped. While the data of the  $[H, 0, 0]$  direction show exactly this behavior, the scans along the  $[0, 0, L]$  direction seem to exhibit the Lorentzian line shape for all temperatures pointing to a broader magnetic scattering intensity distribution already in the magnetic phase. Without performing sophisticated fitting of the data taken the instrumental resolution into account like the software tool `ResLib` would do, the inherent magnetic reflection line width can also be determined by fitting the data using a Voigt peak profile<sup>2</sup> [94]. This profile is exactly a convolution of Gaussian and Lorentzian peak profile and resembles therefore the convolution of the instrumental function with the inherent Lorentzian shaped magnetic scattering function. The data for both directions and all temperatures are fitted by such a Voigt peak profile where the line width of the Gaussian function is fixed at  $0.01\text{ r.l.u.}$  stemming from the Gaussian peak profile fits of the scans in  $[H, 0, 0]$  direction below the phase transition. This leaves the width of the Lorentzian shaped contribution as a fitting parameter and it can be quantified. Figure 3.1(h) compares the temperature dependence of the Lorentzian line width in the Voigt peak profile for both directions. In addition the line widths from the pure Gaussian or Lorentzian peak profiles are also included. It can be clearly seen that the line width, independent of the fitted peak profile, stays constant in the magnetic phase, but increases above the phase transition up to a certain plateau. At higher temperatures the error bars increase since the vanishing intensity of the magnetic reflection hinders the accurate description of the line shape. In Figure 3.1(d) and (f) the data of highest measured temperatures ( $T = 127\text{ K}$  and  $128\text{ K}$ ) are included

---

<sup>1</sup>The intensity difference at low temperatures between both directions originates from a misalignment of the  $H$  component in the  $[1, 0, L]$  scan

<sup>2</sup>The fitting is done using `Originlab OriginPro2107` with the integrated fitfunction `voigt5.fdf`

to show the further decrease of peak height above the phase transition. Nevertheless there seems to be still a small signal left at the position of the magnetic Bragg reflection which can be fitted. This rest intensity can stem from multiple diffraction and is therefore of nuclear origin and temperature independent.

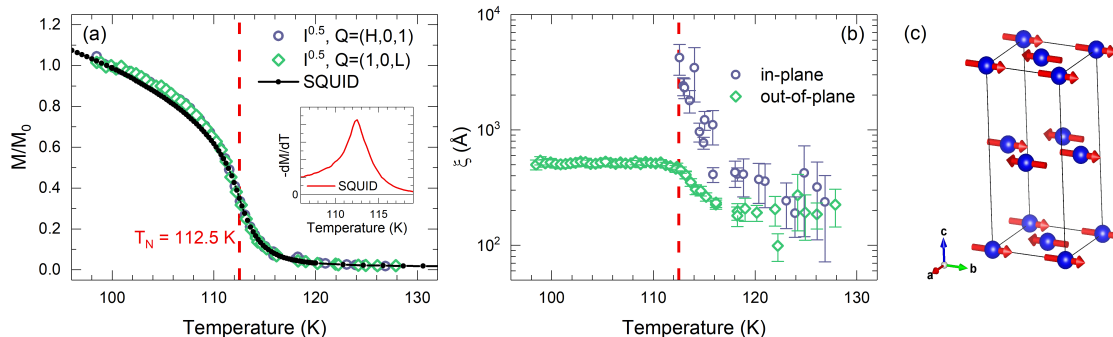


**Figure 3.2: Magnetic order around  $T_N$  in  $\text{Ca}_2\text{Ru}_{0.99}\text{Ti}_{0.01}\text{O}_4$ .** (a) The magnetization data measured with SQUID (field cooled,  $H = 0.1 \text{ T} \parallel a$ , taken from [37]) are compared to the square root of the fitted intensities from Figure 3.1(e). The data sets are individually normalized to their value at  $T = 100 \text{ K}$ . The Néel temperature  $T_N = 112.5 \text{ K}$  is determined by the derivative of the magnetization (inset). (b) The in-plane and out-of-plane coherence lengths are calculated from the Lorentzian contribution in the Voigt model for both scan directions and compared in its temperature dependence.  $T_N$  is marked by the red dashed line. (c) displays the schematic representation of the dominant B-centered magnetic structure in  $\text{Ca}_2\text{Ru}_{0.99}\text{Ti}_{0.01}\text{O}_4$ . The centering depends on the direction of the interlayer moments. The picture is created with VESTA [95].

The fitted amplitude as well as the FWHM of the magnetic Bragg reflection correspond to physical quantities connected to the magnetic correlations. The magnetic scattering is proportional to the squared magnetization  $M^2$  while the line width of the magnetic Bragg peak is connected to the correlation length following  $\xi = \frac{a_i}{2\pi\text{FWHM}}$  with the respective lattice constant  $a_i$ <sup>3</sup>. Figure 3.2(a) compares the temperature dependence of fitted amplitude with the magnetization measured with SQUID around the transition temperature. The transition temperature can be determined by the first derivative of  $M(T)$  (see inset graph) and amounts to  $112.5 \text{ K}$  which is close to the reported  $T_N \approx 112.5 \text{ K}$ . For the comparison the neutron data as well as the SQUID data are normalized to the value at  $100 \text{ K}$ . The square root of the peak amplitudes of the peak at the magnetic Bragg reflection  $\mathbf{Q} = (1, 0, 1)$  in both directions nicely follows the temperature dependence of the magnetization confirming the relation  $I \propto M^2$ . As mentioned above the line width of the Lorentzian contribution extracted from the Voigt peak profile analysis in Figure 3.1 can be translated into the correlation length giving the spatial range of magnetic correlations in the crystal. The temperature dependence of the correlation lengths is displayed in Figure 3.2(b) The different scan directions hereby probe the magnetic correlations in-plane ( $[H, 0, 0]$ ) and out-of-plane ( $[0, 0, L]$ ). For visualization of the  $\text{RuO}_2$  planes the B-centered magnetic structure of  $\text{Ca}_2\text{RuO}_4$  which is relevant for the here used sample is depicted in Figure 3.2(c). Below the transition temperature the in-plane and out-of-plane correlation lengths stay constant while

<sup>3</sup>In this case the lattice constants are  $a = 5.385 \text{ \AA}$  for the  $[H, 0, 0]$  direction and  $c = 11.76 \text{ \AA}$  for the  $[0, 0, L]$  direction

the absolute amount strongly differs. The out-of plane correlation length is 500 Å while the in-plane correlation length cannot be determined properly. It is infinite without the resolution. For this reason the absolute value of the correlation lengths can only be determined above  $T_N$ . Nevertheless it can be stated that the in-plane correlations are stronger than the out-of-plane correlations. As the transition temperature is exceeded both correlation lengths start to decrease until they reach both rather constant values around 250 Å. This value seems to be rather high and might stem from the influence of multiple diffraction which creates a nuclear, temperature independent peak at  $\mathbf{Q} = (1, 0, 1)$  and therefore becomes a systematic error to the absolute values of the correlation lengths in form of a constant offset. However this correlation lengths in Figure 3.2(b) are not corrected for this offset since the fitting of scans with low peak intensities become more unstable and the correction would create high uncertainty. The onset of decrease for both in- and out-of-plane correlation seems to be right at the transition temperature of 112.5 K. This is in contrast to the cuprates where the in-plane correlations survive even above the phase transition [96, 97].

Additionally to the study of the magnetic correlations close to the phase transition we investigate also the magnetic structure in more detail with polarized neutron scattering. Especially the question if there is experimental evidence for magnetic moment on the apical oxygen position in the  $\text{RuO}_6$  octahedra which appears in DFT calculations [37] can be answered by neutron scattering. We therefore measured a set of magnetic Bragg reflections on the cold triple-axis spectrometer 4F1 with longitudinal polarization analysis which allows for the separation of magnetic moment components along the crystal axis. By measuring rocking scans ( $\omega$  scans) at different  $\mathbf{Q}$  vectors in the six possible spin flip channels it is possible to determine the direction of the magnetic moment. The integrated intensity is a measure for the magnetic structure factor which can be compared with the theoretical structure factor of different magnetic moment distributions.

Figure 3.3(a)-(f) show exemplary the six spin flip channels of the rocking scans at  $\mathbf{Q} = (1, 0, -1)$ . The  $x, y, z$  labels refer to the standard coordinate system of the longitudinal polarization analysis (see Section 6.2.2). The spin-flip channels are labeled in the following with  $\text{SF}i$  and the non-spin-flip channels with  $\text{nSF}i$ . The magnetic Bragg reflection of the B-centered magnetic structure of  $\text{Ca}_2\text{RuO}_4$  appears to a full extent in the  $\text{SF}x$ ,  $\text{SF}y$ , and  $\text{nSF}z$  channel [(a),(c),(f)]. The other three channels collect intensities by a factor of 10 smaller. While  $\text{nSF}x$  and  $\text{nSF}y$  show comparable intensity the  $\text{SF}z$  intensity is further reduced. The intensity distribution in the spin flip channels can be explained with the known magnetic structure for  $\text{Ca}_2\text{RuO}_4$  and Table 6.2 as following. The main moment points along the orthorhombic  $b$  direction which is coaligned with the  $z$  axis of the polarization coordinate system for  $\mathbf{Q} = (H, 0, L)$ . Therefore the main magnetic intensity appears in the  $\text{SF}y$  channel which is sensitive to the  $M_z$ . Accordingly also the channels  $\text{SF}x$  and  $\text{nSF}z$  measure the main magnetic scattering.  $\text{nSF}x$  measures the nuclear scattering contribution which appears also in  $\text{nSF}y$  and is only a minor contribution in  $\text{nSF}z$  compared to the magnetic scattering. The small intensity in  $\text{SF}z$  could point to a moment component along  $y$  but is more likely the contamination of the  $\text{nSF}z$  channel due to the finite flipping ratio. This is supported by the fact that the intensity in  $\text{nSF}y$  is not equal to the sum of nuclear contribution ( $\text{nSF}x$ ) and  $\text{SF}y$ . Indeed when con-

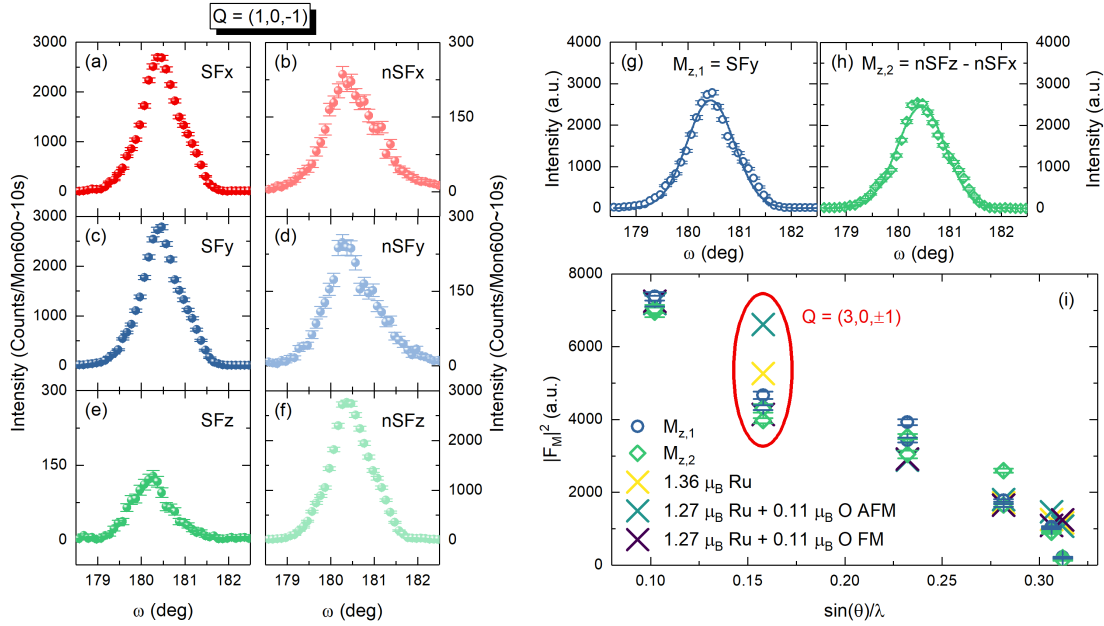


**Figure 3.3: Polarization analysis of magnetic Bragg peaks in  $\text{Ca}_2\text{Ru}_{0.99}\text{Ti}_{0.01}\text{O}_4$ .** (a)-(f) Rocking scans in the six spin channels of the longitudinal polarization analysis at  $\mathbf{Q} = (1, 0, -1)$  were measured with the untwinned sample. The intensities are not corrected for a finite flipping ratio. (g)+(h) The magnetic moment component along  $b$  can be extracted by two different ways. The data are corrected by the finite flipping ratio and then fitted by Gaussians to determine the integrated intensities. (i) The experimentally determined magnetic structure factor is compared with the theoretical calculation of the magnetic structure factor of three different moment distributions. The theoretical values are normalized by the experimental results for  $\mathbf{Q} = (1, 0, \pm 1)$ .

ducting the flipping ratio correction the intensity in SFz vanishes. As expected the magnetic scattering only stems from a magnetic moment component along the crystallographic axis  $b$ . Following this qualitative analysis the magnetic scattering intensity for  $\mathbf{Q} = (H, 0, L)$  can be extracted by using the SFy channel ( $M_{z,1}$ ) and the difference between nSFz and nSFx ( $M_{z,2}$ ). These two ways should give the same result. Figure 3.3(g) and (h) show indeed that the intensity is comparable. For the comparison with different magnetic structures the rocking scans are fitted by Gaussians and the integrated intensity is then given by the area of the fit function. This gives a set of integrated intensities for different magnetic Bragg reflections which are proportional to the respective magnetic structure factor ( $|F_M|^2$ ) and can be displayed against  $\sin(\theta)/\lambda$  [Figure 3.3(i)]<sup>4</sup>. To calculate the theoretical magnetic structure factors of different magnetic moment distributions Fullprof [98] is used. Here three different scenarios are calculated:

1. all magnetic moment on Ru in the B-centered antiferromagnetic (AFM) order  
→ conventional moment distribution
2. conventional distribution with reduced moment on Ru +  $0.11 \mu_B$  on apical oxygen antiferromagnetically ordered (AFM)

<sup>4</sup>For each Bragg reflection also its equivalent is recorded which gives in combination with the two different magnetic intensity extractions a total of four experimental points per  $\sin/\lambda$  value

3. conventional distribution with reduced moment on Ru +  $0.11 \mu_B$  on apical oxygen ferromagnetically ordered (FM)

The amounts of moment are taken from the DFT calculation in [37]. The software calculates the magnetic structure factors using the form factor of  $\text{Ru}^+$ . To compare the theoretical structure factors with the experiment the theoretical values were normalized to the experimental structure factor for  $\mathbf{Q} = (1, 0, \pm 1)$  and plotted also against  $\sin(\theta)/\lambda$ . The different moment distributions only differ at the measured Bragg reflections  $\mathbf{Q} = (3, 0, \pm 1)$ . Here the result of scenario of the conventional distribution with reduced moment on Ru and ferromagnetically ordered moment on the apical oxygen lays closest to the experimental data. One has to state here that no other magnetic Bragg reflections where the calculations of the different moment distributions would differ could be collected due to the instrumental restrictions. A triple-axis spectrometer is not perfectly suitable for collection of a reasonable amount of relevant Bragg reflections. In addition the determination of the real integrated intensities is difficult since the peak profile is dependent on the instrumental resolution given by the instrumental setup (diaphragms, collimators etc.) and the angles between the spectrometer arms. Nevertheless this experimentally confirms the DFT results and the presence of magnetic moment on the oxygen position.

### 3.2.3 Section Summary

In this section the characteristics of the magnetic order in  $\text{Ca}_2\text{RuO}_4$  were investigated in more detail. The study of magnetic correlations confirms that the in-plane correlations are dominant inside the magnetically ordered phase which qualifies  $\text{Ca}_2\text{RuO}_4$  for a rather two-dimensional material. However, above the transition both the in-plane and out-of-plane correlation lengths decrease simultaneously and rather rapidly until both are constant and comparable in size above 125 K.

In addition experimental evidence of magnetic moment on the apical oxygen position in the  $\text{RuO}_6$  octahedra was presented. By collecting integrated intensities for several magnetic Bragg reflections in different spin flip channel by longitudinal polarization analysis the experimental magnetic structure factor can be compared with structure factor calculations for different magnetic moment distributions taken the magnetic oxygen into account. The experimental data are best represented by the magnetic moment distribution with a ferromagnetically ordered moment on the position of the apical oxygen confirming the DFT calculations.

### 3.3 Discussion

In the scope of this chapter the different aspects connected to the complex phase diagram of  $\text{Ca}_2\text{RuO}_4$  were addressed. On the one hand the neutron and X-ray scattering study of the impact of current to the electronic, structural and magnetic state displays the interlacement of the corresponding properties while illustrating the importance of the consideration of phase coexistence in the interpretation of experimental results. On the other hand the study of magnetic correlations above the transition temperature and the experimental evidence for magnetic moment on the apical oxygen position in the  $\text{RuO}_6$  octahedra further characterizes the known antiferromagnetic order in  $\text{Ca}_2\text{RuO}_4$ .

The current application leads to a complex real structure with up to three different structural phases coexisting in a sample which can be attributed to the metallic, the insulating, and an intermediate state. The volume ratios are dependent strongly on temperature, current, and even measurement history. This complex real structure under current application complicates the identification of a possible new non-equilibrium steady state which is connected to the reported anomalies like a negative magnetoresistance or the sign change in the Hall coefficient [83]. The here-found structural intermediate state indicates a different magnetic state as its appearance coincides with the vanishing of the magnetic Bragg reflection and therefore with the suppression of the antiferromagnetic order. In the context of the found complex real structure however it cannot be excluded that the intermediate phase simply arises from phase coexistence and regular microarrangements of metallic and insulating regions.

The analysis of magnetic correlations using the temperature dependence of the magnetic Bragg reflection  $\mathbf{Q}_{\text{AFM}} = (1, 0, 1)$  confirms the rather two dimensional character of  $\text{Ca}_2\text{RuO}_4$ . The correlations length can be extracted from the line width of the Bragg reflection which enables the determination of absolute values for both in- and out-of-plane correlations. While the in-plane correlations length are infinite in the ordered phase the out-of-plane correlations expands over  $\approx 40$  unit cells in  $c$  direction. The temperature dependence of the correlation lengths reveals the stability of the in-plane correlations as expected for a two dimensional material since their correlation lengths decrease slower than the out-of-plane correlation lengths. However the magnetic correlations vanish rather rapidly within  $\approx 13$  K above the Néel temperature which is in contrast to the highly two-dimensional cuprates where the in-plane magnetic correlations survive well above the transition temperature [96, 97]. Since the magnetic correlation disappear rather fast there is no possibility to identify a connection between the magnetic properties and the orbital polarization connected to the octahedra distortion above the magnetic phase transition.

Our polarized neutron scattering study supports the existence of magnetic moment on the apical oxygen position as predicted by DFT calculations [37]. The determined magnetic structure factors for selected Bragg reflections are the best comparable to the structure model where the B-centered antiferromagnetic order with a reduced moment of  $1.27 \mu_B$  on the Ru position and a moment of  $0.11 \mu_B$  on the apical oxygen position (ferromagnetically ordered to Ru moment). This result confirms the  $p$ - $d$  hybridization in the  $4d$  ruthenates which causes the anisotropic magnetic moment distribution reported also in  $\text{SrRuO}_3$  [14] and  $\text{Ca}_{1.5}\text{Sr}_{.5}\text{RuO}_4$  [93]. The existence of magnetic oxygen in  $\text{Ca}_2\text{RuO}_4$  also supports the finding of an oxy-

gen magnon mode reported in an inelastic neutron scattering study of the magnon dispersion [37].

## 3.4 Methods

### Material Information

$\text{Ca}_2\text{RuO}_4$  crystallizes in the orthorhombic space group  $Pbca$  with the lattice parameters  $a = 5.4097 \text{ \AA}$ ,  $b = 5.4924 \text{ \AA}$ , and  $c = 11.9613 \text{ \AA}$  at room temperature [25]. The lattice parameters exhibit a strong temperature dependence with a first-order structural transition where the lattice symmetry is conserved but the  $\text{RuO}_6$  octahedra distortion changes abruptly which results in strong changes in lattice parameters [22]. This structural transition at  $T_{MI} = 357 \text{ K}$  is accompanied with a metal-insulator transition. At low temperatures  $\text{Ca}_2\text{RuO}_4$  is therefore a Mott insulator. Additionally it exhibits antiferromagnetic order below  $T_N = 110 \text{ K}$  which follows the G-type scheme where both inter-layer and intra-layer coupling is antiferromagnetic. This type of antiferromagnetism can be A-centered ( $\text{La}_2\text{CuO}_4$  type) or B-centered ( $\text{La}_2\text{NiO}_4$  type) which differ in the time reversal symmetry. The B-centered order is dominant in  $\text{Ca}_2\text{RuO}_4$  with Ti substitution or oxygen excess while the pure compound shows the A-centered order [25, 37].

The crystals of  $\text{Ca}_2\text{RuO}_4$  used in the reported experiments are grown in the II. Institute of Physics at University of Cologne by S.K. and by the author using the floating-zone method (Section 6.1). Due to the first order structural transition at  $T_{MI} = 357 \text{ K}$  the crystals tend to shatter into sub-millimeter pieces when cooling down. To counter this the transition can be broadened by substituting Ru with small amounts of Ti without altering the magnetic behavior. This enables the growth of large single crystals which can be used for neutron scattering studies [37]. The current-induced effects were investigated using millimeter pieces of both Ti doped and pure  $\text{Ca}_2\text{RuO}_4$  crystals. The magnetic correlations in Section 3.2 were studied with the 1% Ti doped  $\text{Ca}_2\text{RuO}_4$  crystal shown in Figure 3.4. In earlier experiments this crystal was found to show essentially no twinning which facilitates the analysis.



**Figure 3.4:** Mounted  $\text{Ca}_2\text{Ru}_{1-y}\text{Ti}_y\text{O}_4$  ( $y = 0.01$ ) crystal. The big 1% Ti doped  $\text{Ca}_2\text{RuO}_4$  and essentially untwinned crystal ( $V \approx 150 \text{ mm}^2$ ) is mounted and oriented for the neutron scattering experiment.

### Neutron scattering

The neutron scattering experiments were conducted at triple-axis spectrometers at the Laboratoire Léon Brillouin (LLB) in Saclay, France. All involved beam times including the instrument and the experimental setting are listed in Table 3.1. The triple-axis spectrometers are used with pyrolytic graphite crystals as monochromator and analyzer with a fixed  $k_f$ . Note that all the experiments investigated elastic signals where  $k_f = k_i$ . In the experiment at 4F2 a Be filter in front of the analyzer is used to suppress higher order scattering and the neutron beam is collimated to  $15'$  in front of the monochromator, to  $20'$  in front of the analyzer and to  $20'$  in front of the detector.

**Polarized Neutron Scattering**

For the polarized neutron scattering experiment the neutron beam is polarized by a polarizing supermirror (bender). The neutron polarization at the sample is defined with a XYZ-Helmholtz-coil setup. In combination with two Mezei-flippers in front and behind the sample and a Heusler analyzer this setup facilitates the full polarization analysis. The flipping ratio was measured at the nuclear Bragg peak  $(0, 0, -6)$  and amounts to  $\approx 22$ .

**Table 3.1: Involved neutron beam times with the instrumental settings.**

Beam Time	Facility	Instrument	$k_f$ [ $\text{\AA}^{-1}$ ] ( $k_i$ )	Mono./Ana.	Filter	comment
02-2017	LLB	4F1	2.57	PG(002)/Heusler(111)	PG	full polarization analysis
09-2018	LLB	4F2	1.52	PG(002)/PG(002)	cooled Be	collimation (15'—20'—20')
02-2019	LLB	3T1	(2.69)	PG(002)/PG(002)	—	no analyzer
04-2019	LLB	3T1	(2.69)	PG(002)/PG(002)	—	no analyzer
06-2019	LLB	3T1	(2.69)	PG(002)/PG(002)	—	no analyzer



# Sr<sub>2</sub>RuO<sub>4</sub>: Characteristics of Magnetic Fluctuations

## 4.1 Introduction

Since the discovery of superconductivity in Sr<sub>2</sub>RuO<sub>4</sub> in 1994 the pairing mechanism is under investigation [5]. Although structurally very similar to the cuprate high-T<sub>C</sub> superconductors the superconductivity of this Ruddlesden-Popper ruthenate with a T<sub>C</sub> of 1.5 K has different characteristics. Since the sister compound SrRuO<sub>3</sub> [12] exhibits ferromagnetic order it was early proposed that ferromagnetic fluctuations drive the superconductivity. The spin-triplet pairing with which ferromagnetic fluctuations are connected is also found in the A-phase of superfluid <sup>3</sup>He [11, 99]. Chiral *p*-wave superconductivity [100] was considered for a long time to best describe the findings of the majority of experimental studies [101, 102]. Nevertheless there was always experimental evidence which could not be incorporated into the theoretical description [103, 104]. More recently uniaxial strain experiments reveal an enhancement of T<sub>C</sub> by a factor of two [105, 106]. However the strain dependence of the transition temperature close to zero is flat while for a chiral state it is expected to be linearly dependent [105, 107]. The revision of two key experiments which yielded the strongest support for spin-triplet pairing contest the picture of chiral *p*-wave superconductivity strongly. The Knight shift in NMR [49, 50] and polarized neutron diffraction [51] indeed display a drop of electronic susceptibility which is inconsistent with triplet pairing. These findings open up the discussion about the symmetry of the superconducting state and the pairing mechanisms where mostly some *d*-wave state is invoked [52–57, 108, 109]. While the *p*-wave triplet pairing seems to be excluded due to the suppression of electronic susceptibility a chiral state is still supported by the observation of broken time-reversal symmetry in muon spin relaxation experiments [45, 110] and measurements of the magneto-optical Kerr effect [111]. Based on these experimental findings a complex combination of components in the superconducting state is discussed [52–57, 108].

In BCS theory the superconductivity is mediated by bosons which can have the form of phonons, magnetic fluctuations or a combination of both [112]. In Sr<sub>2</sub>RuO<sub>4</sub> there have been found anomalies in the phonon dispersion which could be interpreted as fingerprints of electron phonon coupling [113, 114]. There is also evidence for strong magnetic fluctuations coming from NMR [115] and inelastic neutron scattering experiments [46–48, 116–119]. The magnetic fluctuations are dominated by an incommensurate signal stemming from the nesting between the two one-dimensional bands of the Fermi surface which can be associated with *d*<sub>xz</sub> and *d*<sub>yz</sub> orbitals. This

instability towards an incommensurate spin-density wave seems to be relevant for Sr<sub>2</sub>RuO<sub>4</sub> since minor substitution of Ru with Ti [116] or Sr with Ca [6, 120] leads to static magnetic order exactly at the same  $\mathbf{q}$  position. Also the closeness to a quantum critical point in pure Sr<sub>2</sub>RuO<sub>4</sub> is confirmed by the temperature dependence of the incommensurate magnetic fluctuations [116]. DFT calculations using the random phase approximation (RPA) [26] can explain these nesting-induced fluctuations but their role in the superconducting pairing mechanism stays under discussion [121]. Because magnetic excitations are particle-hole excitations in the most simple case the magnetic gap should be comparable to twice the superconducting gap. This can be excluded for the incommensurate magnetic fluctuations by inelastic neutron scattering where no opening of a large gap is detected [14]. These findings are also confirmed by time-of-flight neutron scattering which additionally reports evidence for suppression of spectral weight at very low energies in the superconducting state as well as the occurrence of a spin resonance mode at the incommensurate position with a finite  $L$  component perpendicular to the RuO<sub>2</sub> layers [122]. This would indicate a modulation of the superconducting gap function perpendicular to the layers in this two-dimensional compound.

There is a second contribution to the magnetic fluctuations beside the nesting-driven incommensurate fluctuations. As multiple measurements like NMR [115, 123], magnetic susceptibility [40] and polarized neutron scattering [47, 48] reveal, there exist weak magnetic fluctuations at the zone center of the Brillouin zone which can be associated with ferromagnetism. Static ferromagnetic short-range order has also been found in Co doped Sr<sub>2</sub>RuO<sub>4</sub> [59] which will be discussed in detail in Chapter 5. These quasi-ferromagnetic fluctuations in pure Sr<sub>2</sub>RuO<sub>4</sub> exhibit no temperature-dependence as seen in all the experimental techniques. Recent dynamical mean field theory (DMFT) calculations of the magnetic fluctuations finds local fluctuations superposed with the known nesting-driven fluctuations [124]. While the calculations are qualitatively in agreement with the experimentally found ferromagnetic response the neutron study disagrees with the local character of the fluctuations as they exhibit a finite  $q$  dependence [48].

Here a detailed investigation of the magnetic fluctuations in SrRuO<sub>3</sub> by neutron scattering is presented. By combining triple-axis spectrometer including polarized neutron scattering and time-of-flight spectrometer we collect a complementary data set which can be analyzed for the changes of magnetic fluctuations in  $\mathbf{q}$ - $E$  space going from the normal into the superconducting state. This study can also help for a general understanding of magnetic excitations in a strongly correlated electron system. In particular the results are connected to the out-of-plane dispersion of the magnetic response in the superconducting and normal phase, the shape of the nesting signal away from the incommensurate position, and the non-local character of the quasi-ferromagnetic fluctuations and their temperature dependence.

The publication of these results in *Physical Review B* in 2021 is included in this thesis [125].

## 4.2 Contribution to Publication and its Relevance in Thesis

The crystals used for the neutron experiment were grown by Z.Q. Mao and Y. Maeno. The coalignment of the crystal assembly was executed by S. Kunkemöller and by the author. The neutron scattering data presented in this publication were measured by the author at different neutron facilities under supervision of M. Braden and with support of R. Bewley, Y. Sidis, and P. Steffens. The data analysis and modeling of the neutron data were conducted by the author. For the text the author contributed all figures including their captions. The author contributed to the writing of the text.

The presented results arise from a combination of different neutron scattering techniques and instruments creating a detailed picture of magnetic fluctuations in the normal and superconducting phase of  $\text{Sr}_2\text{RuO}_4$ . The publication illustrates the complementary use of triple-axis spectrometer and time-of-flight spectrometer in the context of low-energy magnetic fluctuations where physical questions push the boundaries of instrumental techniques.

Neutron scattering studies on spin fluctuations in Sr<sub>2</sub>RuO<sub>4</sub>K. Jenni,<sup>1,\*</sup> S. Kunkemöller,<sup>1</sup> P. Steffens,<sup>2</sup> Y. Sidis,<sup>3</sup> R. Bewley,<sup>4</sup> Z. Q. Mao,<sup>5,6,7</sup> Y. Maeno,<sup>5</sup> and M. Braden<sup>1,†</sup><sup>1</sup>*II. Physikalisches Institut, Universität zu Köln, Zùlpicher Strasse 77, D-50937 Köln, Germany*<sup>2</sup>*Institut Laue Langevin, 71 avenue des Martyrs, 38000 Grenoble, France*<sup>3</sup>*Laboratoire Léon Brillouin, CEA/CNRS, F-91191 Gif-sur-Yvette Cedex, France*<sup>4</sup>*ISIS Neutron and Muon Source, Rutherford Appleton Laboratory, Harwell Oxford, Didcot OX11 0QX, United Kingdom*<sup>5</sup>*Department of Physics, Graduate School of Science, Kyoto University, Kyoto 606-8502, Japan*<sup>6</sup>*Department of Physics, Tulane University, New Orleans, Louisiana 70118, USA*<sup>7</sup>*Department of Physics, Pennsylvania State University, University Park, Pennsylvania 16802, USA*

(Received 17 December 2020; revised 12 February 2021; accepted 9 March 2021; published 18 March 2021)

The magnetic excitations in Sr<sub>2</sub>RuO<sub>4</sub> are studied by polarized and unpolarized neutron scattering experiments as a function of temperature. At the scattering vector of the Fermi-surface nesting with a half-integer out-of-plane component, there is no evidence for the appearance of a resonance excitation in the superconducting phase. The body of existing data indicates weakening of the scattered intensity in the nesting spectrum to occur at very low energies. The nesting signal persists up to 290 K but is strongly reduced. In contrast, a quasiferromagnetic contribution maintains its strength and still exhibits a finite width in momentum space.

DOI: [10.1103/PhysRevB.103.104511](https://doi.org/10.1103/PhysRevB.103.104511)

## I. INTRODUCTION

A quarter century after the discovery of superconductivity in Sr<sub>2</sub>RuO<sub>4</sub> [1], its character and its pairing mechanism remain mysterious. Inspired by the ferromagnetic order appearing in the metallic sister compound SrRuO<sub>3</sub> [2], it was initially proposed that ferromagnetic fluctuations drive the superconductivity in Sr<sub>2</sub>RuO<sub>4</sub> rendering its superconductivity similar to the A-phase of superfluid <sup>3</sup>He [3,4]. For a long time, chiral *p*-wave superconductivity with spin-triplet pairing has been considered to best describe the majority of experimental studies [5,6], although the absence of detectable edge currents [7] and the constant Knight-shift observed for fields perpendicular to the Ru layers [8] were not easily explained in this scenario [9]. Further insight was gained from experiments performed under large uniaxial strain that revealed a considerable enhancement of the superconducting transition temperature by more than a factor 2 [10,11], similar to the enhancement in the eutectic crystals [6]. However, the breaking of the fourfold axis should split the superconducting transition of the chiral state in contradiction with a single anomaly appearing in the specific heat under strain [12]. Furthermore, the strain dependence of the transition temperature close to zero strain is flat [10,13], whereas one expects a linear dependence for the chiral state.

The picture of chiral *p*-wave superconductivity was fully shaken when the two experiments yielding the strongest support for triplet pairing [14,15] were revised. The new studies of the Knight shift in NMR [16,17] and those of the polarized neutron diffraction [18] reveal an unambiguous drop of the

electronic susceptibility that is inconsistent with spin-triplet pairs parallel to Ru layers. Since then, numerous proposals for the superconducting state were made mostly invoking some *d*-wave state, and the discussion of the superconducting pairing has become very active [19–26]. The observations of broken time-reversal symmetry in muon spin relaxation experiments [27,28] and in measurements of the magneto-optical Kerr effect [29] may require interpretations other than the chiral *p*-wave scenario. Many theories discuss a superconducting state with a complex combination of components [19–25].

Assuming a simple boson-mediated pairing following BCS theory, phonons and magnetic fluctuations or a combination of both [30] can be relevant. There are anomalies in the phonon dispersion that could be fingerprints of electron phonon coupling [31,32]. The phonon mode that describes the rotation of the RuO<sub>6</sub> octahedra around the *c* axis exhibits an anomalous temperature dependence and severe broadening [31]. This mode can be associated with the structural phase transition and with the shift of the van Hove singularity in the  $\gamma$  band through the Fermi level. Both effects occur upon small Ca substitution [33,34]. In addition, the Ru-O bond-stretching modes that exhibit an anomalous downward dispersion in many oxides with perovskite-related structure [35] exhibit an anomalous dispersion in Sr<sub>2</sub>RuO<sub>4</sub> as well [32]. Comparing the first-principles calculated [36] and measured [32] phonon dispersion in Sr<sub>2</sub>RuO<sub>4</sub>, the agreement is worst for these longitudinal bond-stretching modes, which exhibit a flatter dispersion indicating better screening compared to the density functional theory (DFT) calculations. Note, however, that perovskite oxides close to charge ordering exhibit a much stronger renormalization of the zone-boundary modes with breathing character that is frequently labeled overscreening [35,37].

\*jenni@ph2.uni-koeln.de

†braden@ph2.uni-koeln.de

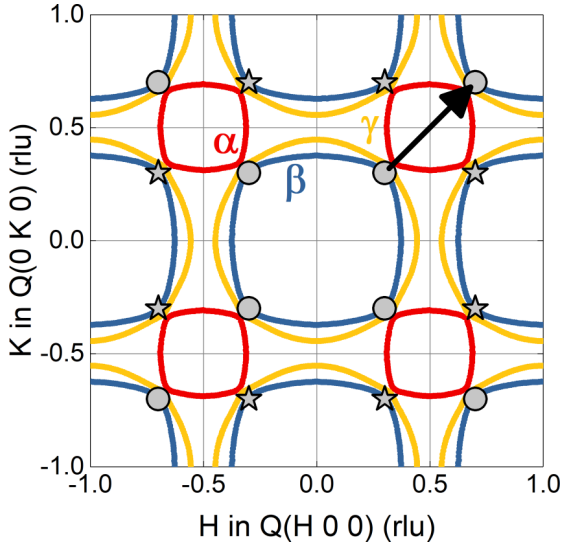


FIG. 1. Fermi surface of  $\text{Sr}_2\text{RuO}_4$  for  $k_z = 0$ . The bands are based on LDA+SO calculations from [60] and marked by different colors. The black arrow represents the dominant nesting vector between the one-dimensional sheets  $\alpha$  (red) and  $\beta$  (blue). The incommensurate positions of the in-plane nesting signal are marked by different symbols. The circles represent the crystallographically equivalent positions  $(\pm 0.3, \pm 0.3)$  and  $(\pm 0.7, \pm 0.7)$ . The positions  $(\pm 0.3, \pm 0.7)$  and  $(\pm 0.7, \pm 0.3)$  shown by stars are equivalent to those on the diagonals only in a purely two-dimensional picture, because  $(1\ 0\ 0)$  is not an allowed Bragg peak in the body-centered lattice.

On the other side there is clear evidence for strong magnetic fluctuations deduced from NMR [38] and inelastic neutron scattering (INS) experiments [39–45]. The dominating magnetic signal is incommensurate and stems from nesting in the one-dimensional bands associated with  $d_{xz}$  and  $d_{yz}$  orbitals; see Fig. 1. The relevance of this instability toward an incommensurate spin-density wave (SDW) is underlined by the observation of static magnetic order emerging at this  $\mathbf{q}$  position in reciprocal space for minor substitution of Ru by Ti [46] or of Sr by Ca [47,48]. A repulsive impurity potential was recently proposed to form the nucleation center for the magnetic ordering that should strongly couple to charge currents [49]. Furthermore, the temperature dependence of these incommensurate magnetic fluctuations in pure  $\text{Sr}_2\text{RuO}_4$  agrees with a closeness to a quantum critical point [40]. These nesting-induced magnetic fluctuations can easily be explained by DFT calculations using the random phase approximations (RPA) [50], but their relevance for the superconducting pairing remains controversial [51]. Inelastic neutron scattering in the superconducting state can exclude the opening of a large gap for these nesting-driven fluctuations [52]. Since magnetic excitations are particle-hole excitations, one expects in the simplest isotropic case a magnetic gap comparable to twice the superconducting one, which can be safely excluded. However, the anisotropy of the gap function and interactions can strongly modify the magnetic response in the superconducting state. A more recent time-of-flight (TOF) inelastic neutron scattering experiment confirms the absence of a large gap but reports weak evidence for suppression of spectral weight

at very low energies [53]. This experiment also claims the occurrence of a spin resonance mode at the nesting position with a finite perpendicular wave-vector component, which would point to an essential modulation of the superconducting gap perpendicular to the  $\text{RuO}_2$  layers but which is inconsistent with the results of this work.

In addition to the incommensurate nesting-induced fluctuations, macroscopic susceptibility [54], NMR [38,55], and also polarized inelastic neutron scattering experiments [42,45] reveal the existence of magnetic fluctuations centered at the origin of the Brillouin zone, which typically can be associated with ferromagnetism. Furthermore, a small concentration of Co doping can lead to static short-range ferromagnetic order [56]. All techniques find almost temperature-independent quasiferromagnetic excitations in pure  $\text{Sr}_2\text{RuO}_4$ . This ferromagnetic response agrees qualitatively with a recent dynamical mean-field theory (DMFT) analysis of magnetic fluctuations [57], which finds essentially local magnetic fluctuations superposed on the well-known nesting signal. However, the neutron data disagree with a fully local character as they show a finite  $q$  dependence [45]. The quasiferromagnetic fluctuations also disagree with the expectations for a nearly ferromagnetic system that exhibits paramagnon scattering [45,58].  $\text{SrRuO}_3$  clearly exhibits such paramagnon scattering with its well-defined structure in  $q$  and energy space [59].

Here we present additional neutron scattering experiments on the magnetic fluctuations in  $\text{Sr}_2\text{RuO}_4$ , which focus on several aspects that are particularly relevant for the superconducting pairing mechanism involving magnetic fluctuations or for the general understanding of magnetic excitations in a strongly correlated electron system. We discuss the possibility of important out-of-plane dispersion in the magnetic response in the superconducting and normal states, the shape of nesting scattering away from the peak position, and the nonlocal character of the quasiferromagnetic response.

## II. EXPERIMENT

INS experiments were carried out on the ThALES [61,62] and IN20 [63] triple-axis spectrometers (TAS) at the Institut Laue Langevin and on the LET [64] TOF spectrometer at the ISIS Neutron and Muon Source. We used an assembly of 12  $\text{Sr}_2\text{RuO}_4$  crystals with a total volume of  $2.2\text{ cm}^3$  in all experiments. At Kyoto University, the crystals were grown using the floating zone method, and similar crystals were studied in many experiments [5,6]. The crystal assembly was oriented in the  $[100]/[010]$  scattering plane (corresponding to a vertical  $c$  axis) to study the in-plane physics of the Ru layers. Additionally, with the instruments ThALES and LET it was possible to access parts of the  $q$  space perpendicular to the plane, which enables an analysis of the out-of-plane dispersion of the magnetic response. To conduct experiments inside the superconducting phase, a dilution refrigerator was used, reaching a temperature of  $\sim 200\text{ mK}$ , well below the transition temperature of  $\sim 1.5\text{ K}$ . ThALES and LET are operating with a cold neutron source providing the energy resolution to study the magnetic response down to  $\sim 200\text{ }\mu\text{eV}$ . The TOF spectrometer LET records data simultaneously with four different values of the incidental energies,  $E_i$ , and

resolutions, while the energy resolution of the TAS ThALES is determined by the chosen final neutron wave vector  $k_f$  of  $1.57 \text{ \AA}^{-1}$  combined with the collimations. On ThALES the best intensity-to-background ratio was achieved by using a Si(111) monochromator and PG(002) analyzer combined with a radial collimator in front of the analyzer for further background reduction. The same configuration was also used in an earlier study [52].

A polarized neutron scattering experiment was performed on the thermal TAS IN20 using Heusler crystals as monochromator and analyzer. A spin flipper in front of the analyzer enabled the polarization analysis. The scans were performed with a fixed final momentum of  $k_f = 4.1 \text{ \AA}^{-1}$ , where the graphite filter in front of the analyzer cuts higher-order contaminations. Longitudinal polarization analysis was performed with a set of Helmholtz coils.

### III. RESULTS AND DISCUSSION

#### A. $q$ dependence of fluctuations associated with nesting

The TOF technique enables an imaging of the complete  $\mathbf{Q}$ - $E$  space, which gives insight on the distribution of scattering intensity in reciprocal space. Throughout the paper, the scattering vector,  $\mathbf{Q} = (H, K, L)$ , and the propagation vector in the first Brillouin zone,  $\mathbf{q} = (q_h, q_k, q_l)$ , are given in reciprocal-lattice units (rlu). We mostly consider only the planar wave vector  $\mathbf{Q}_{2d} = (H, K)$  projection. Figure 2 shows the inelastic scattering plotted against the  $H, K$  components of the scattering vector in the superconducting phase. The four different panels display sections of the two-dimensional  $(H, K)$  plane for different incident energies and hence different resolutions. The intensities are fully integrated along the energy transfer (depending on the incident energy) and along the out-of-plane component of the scattering vector,  $-0.7 < L < 0.7$ . The high scattering intensities at the incommensurate positions  $(\pm 0.3, 0.3)$ ,  $(\pm 0.3, 0.7)$ , and  $(\pm 0.7, 0.7)$  are clearly visible, arising from the well-known antiferromagnetic fluctuations [39–41,43,44]. Additionally, there are ridges of scattering intensities connecting these positions in the  $[\xi, 0]$  and  $[0, \xi]$  directions that were first reported in [43,44]. The arc visible in Fig. 2(d) connecting  $(-0.3, 0.3)$  and  $(0.3, 0.3)$  is a spurious signal; it does not appear for the other incidental energies.

Neglecting electronic dispersion perpendicular to the planes and assuming an idealized scheme of flat one-dimensional bands originating from the  $d_{xz}$  and  $d_{yz}$  orbitals, one expects nesting-induced magnetic excitations for any two-dimensional vector  $\mathbf{Q}_{2d} = (0.3, \xi)$  and  $(\xi, 0.3)$  and accordingly a peak at  $(0.3, 0.3)$  [50]. The peaks clearly dominate but the ridges are also detectable—mostly for the positions connecting the nesting peaks, i.e.,  $0.3 < \xi < 0.7$ . This is in accordance with the calculation of the bare susceptibility, which shows an enhanced signal only between the peaks, i.e., for the paths from  $(0.3, 0.3)$  to  $(0.7, 0.3)$  [50].

To analyze the ridge scattering and the anisotropy of the incommensurate signals in detail, Fig. 3(a) shows one-dimensional cuts along the ridge in the  $[\xi, 0]$  direction calculated from the data taken with  $E_i = 14.13 \text{ meV}$  [Fig. 2(a)]. By subtracting the background obtained from the

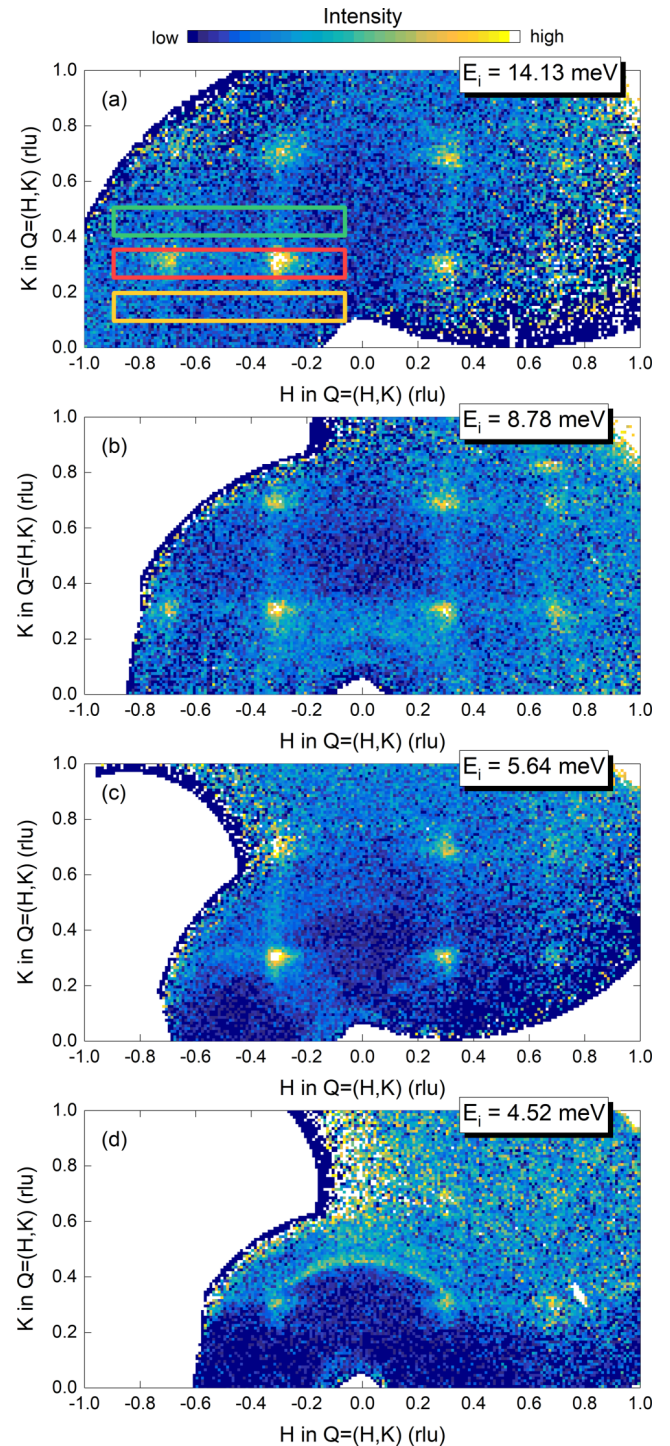


FIG. 2. In-plane scattering in the superconducting phase ( $T = 0.2 \text{ K}$ ). The TOF data at four different incidental energies display the magnetic scattering distribution in the  $ab$  plane. The intense signal at the incommensurate positions  $(0.3, 0.3)$ ,  $(0.7, 0.7)$ , and  $(0.3, 0.7)$  is visible for all  $E_i$ . Additionally, there is magnetic scattering between the incommensurate positions in the  $[\xi, 0]$  and  $[0, \xi]$  directions, respectively. To increase the statistics, the data are integrated over the maximum  $L$  range of  $[-0.7, 0.7]$  and the full  $E$  range depending on the incidental energy ( $1.75 < E < 10$  for  $E_i = 14.13 \text{ meV}$ ,  $0.8 < E < 6.7$  for  $E_i = 8.78 \text{ meV}$ ,  $0.7 < E < 4.5$  for  $E_i = 5.64 \text{ meV}$ , and  $0.5 < E < 3.5$  for  $E_i = 4.52 \text{ meV}$ ). The overlaid rectangles in (a) represent the integration area of the one-dimensional cuts displayed in Figs. 3(a)–3(c).

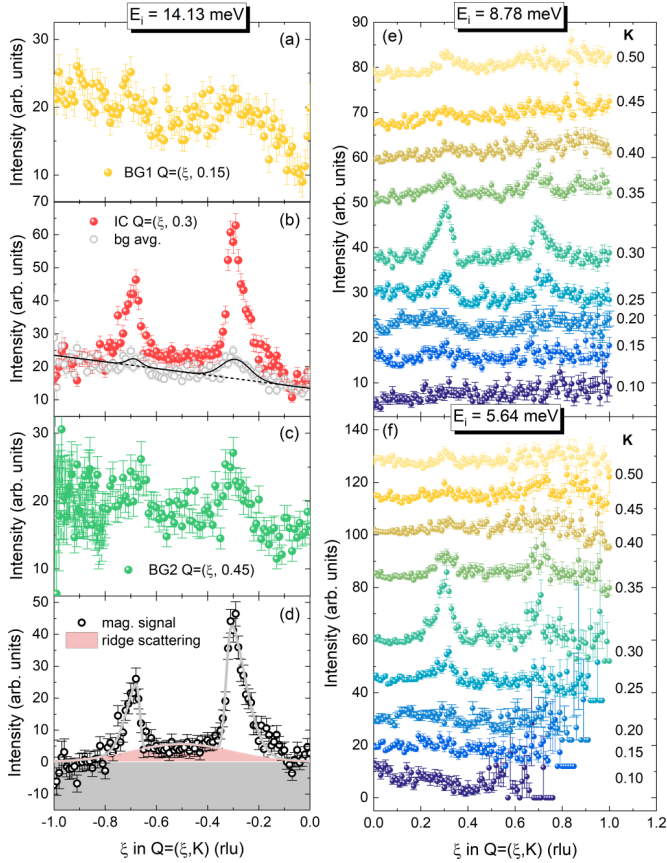


FIG. 3. Magnetic scattering along the connection of the incommensurate positions. Parts (a)–(c) show one-dimensional cuts from Fig. 2(a) along the  $(\xi, K)$  paths for  $K = 0.15$  (a),  $0.3$  (b), and  $0.45$  (c). The background at both sides of the incommensurate positions is displayed in (a) and (c) [represented by the same colored rectangles as in (a)]. An averaged background is formed from both (gray open circles) and fitted with a linear contribution and two Gaussians (black solid line). This is compared to the incommensurate signal in (b). In (d) the linear background contribution (black dashed line) is subtracted, and the signal along the  $[\xi, 0]$  direction is fitted with two skew Gaussians for the incommensurate signal and a broad Gaussian fixed at  $\xi = 0.5$  (red area), taking into account the ridge scattering. Parts (e) and (f) represent one-dimensional cuts for different  $K$  and two different incident energies  $8.78$  and  $5.64$  meV taken from Figs. 2(b) and 2(c). The integration range in the  $[0, \xi]$  direction is  $\pm 0.025$  around the  $K$  value, and the scans are shifted vertically for better visibility.

average of  $(\xi, 0.15)$  and  $(\xi, 0.45)$ , shown in Figs. 3(b) and 3(c), respectively, we isolate the signal along the line  $(\xi, 0.3)$  shown in Fig. 3(d). The ridge scattering is mainly detectable between the peaks at the incommensurate positions, as it is visible in the two one-dimensional cuts representing the background parallel to the ridge on both sides [Figs. 3(b) and 3(c)]. While the  $(\xi, 0.15)$  cut exhibits only a weak signal around  $(-0.3, 0.15)$ , the  $(\xi, 0.45)$  cut shows clearly two peaks at the  $(-0.7, 0.45)$  and  $(-0.3, 0.45)$  positions representing the ridges in the  $[0, \xi]$  direction. The rounding of the one-dimensional Fermi-surface sheets suppresses the susceptibility at  $(0.3, \xi)$  with  $\xi$  lower than  $0.3$ , but this suppression is not abrupt. Besides the ridge scattering, we may also confirm

the pronounced asymmetry of the nesting peak with a shoulder near  $(0.25, 0.3)$  and equivalent positions. This shoulder was reported in [40] and was also found in the full RPA calculations.

The asymmetry of the nesting peaks and the ridge scattering between the incommensurate positions can also be seen in the data of lower incident energies [see Figs. 3(e) and 3(f)]. The one-dimensional cuts for different  $K$  values confirm the asymmetric shape of the nesting peaks. A thorough analysis of the pure magnetic signal as in the case of  $E_i = 14.13$  meV is not possible due to uncertainty in the background. Furthermore, the ridge scattering is less pronounced in the data obtained with lower incident energies, which indicates a higher characteristic energy of the ridge scattering. This further explains why the much weaker scattering in the ridges has not been detected in early TAS studies [39–41].

### B. Search for a gap opening or a resonance mode below $T_c$

The opening of a superconductivity-induced gap in the spectrum of magnetic fluctuations would have a strong impact on the discussion of the superconducting character in  $\text{Sr}_2\text{RuO}_4$ . Previous INS experiments using a TAS revealed the clear absence of a large gap at the nesting position [52], whereas a recent TOF experiment reports a tiny gap, although the statistics remained very poor [53]. Studying the magnetic response of  $\text{Sr}_2\text{RuO}_4$  in its superconducting phase by INS is challenging, because one needs to focus on small energies of the order of  $0.2$ – $0.5$  meV. At these energies, the signal in the normal state is at least one order of magnitude below its maximum strength at  $6$  meV, and the required high-energy resolution further suppresses statistics. Figure 4 presents the TOF data obtained with  $E_i = 3$  meV by calculating the energy dependence at the nesting position integrated over all  $L$  values. The full  $L$  integration is needed to enhance the statistics. In Figs. 4(a) and 4(b), we compare the raw data for both temperatures with the background signal. In Fig. 4(c), the background-subtracted magnetic response in the superconducting phase is compared to that in the normal phase. There is no evidence for the opening of a gap within the statistics of this TOF experiment. Also, a resonance at a finite energy cannot be detected. Admittedly, the statistics of these TOF data is too poor to detect small signals or their suppression.

Following the claim of Iida *et al.* [53], the TOF data are also analyzed in terms of a possible resonance mode appearing at a finite value of the  $L$  component, i.e., at  $(0.3, 0.3, 0.5)$ . Therefore, the  $L$  dependence of the magnetic signal at  $(0.3, 0.3, L)$  is determined by background subtraction and compared for the two temperatures (see Fig. 5). The different panels represent the energy ranges from Ref. [53], where a resonance appearing at  $0.56$  meV is proposed for  $L = 0.5$ . In our data shown in Fig. 5(b), there is no difference visible between superconducting and normal phase at  $L = \pm 0.5$ .

To study the low-energy response and its  $L$  dependence in more detail and with better statistics, the TAS is better suited since measurements can be focused on single  $\mathbf{Q}, \mathbf{E}$  points. Using ThALES and its high flux and energy resolution, constant- $\mathbf{Q}$  scans at the incommensurate position  $(0.3, 0.7, L)$  with  $L = 0, 0.25$ , and  $0.5$  were measured to investigate the  $L$  dependence of the low-energy response (see Fig. 6). This incommensurate position was chosen due to a better

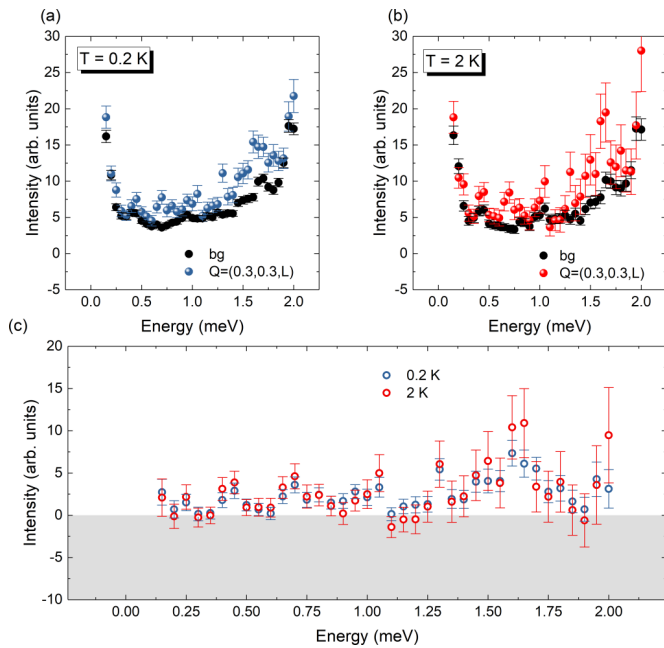


FIG. 4. Low-energy dependence of the incommensurate signal below and above the superconducting transition extracted from TOF data. Parts (a) and (b) display the energy scans at  $q = (0.3, 0.3)$  below ( $T = 0.2$  K) and above ( $T = 2$  K) the superconducting phase transition. The background in both panels is derived from the constant  $Q$  cut at  $(0.09, 0.41)$  for both temperatures ( $|\mathbf{Q}_{\text{IC}}| = |\mathbf{Q}_{\text{bg}}|$ ). To increase statistics, the TOF data with an incidental energy of 3 meV are fully integrated over  $L$  (range  $[-0.7, 0.7]$ ) and symmetrized by folding in  $q$  space at  $(0.3, 0.7)$  along the  $(1, -1, 0)$  plane. The  $H$  and  $K$  components are integrated with the range  $[0.25, 0.35]$ . (c) The background subtraction and Bose factor correction yield the pure magnetic response at low energies, which is compared inside and outside the superconducting phase.

signal-to-noise ratio compared to  $(0.3, 0.3, L)$  and because the larger  $|Q|$  value allows one to reach finite  $L$  values by tilting the cryostat. Similar to Figs. 4(a) and 4(b), the raw data for two temperatures are shown in Figs. 6(a)–6(c). The background was measured by rotating  $\omega$  by  $20^\circ$  for each  $L$  value and then combining all three backgrounds to an average. For all  $L$  values, the intensity of the incommensurate signal increases approximately linearly for small energies, following the established single relaxor behavior. Comparing the two temperatures, there is no difference noticeable for any  $L$  value down to the energy resolution. Especially around 0.56 meV, where Iida *et al.* [53] propose a resonance at the incommensurate position  $(0.3, 0.3, 0.5)$ , the two temperatures yield comparable signals. It should be noted here that while the incommensurate positions  $(0.3, 0.3, 0)$  and  $(0.3, 0.7, 0)$  are crystallographically not equivalent, both positions become equivalent with the  $L$  component 0.5; see Fig. 1. Therefore, the data taken at  $(0.3, 0.3, 0.5)$  and  $(0.7, 0.3, 0.5)$  can be compared. To emphasize the absence of a resonance mode around 0.56 meV, the data from Fig. 6 are plotted with a larger energy binning to further increase the statistics (see Fig. 7, which also indicates the broad energy integration used in [53]). There is no significant deviation from the general linear behavior for any  $L$  value at low temperatures detectable. Iida *et al.*

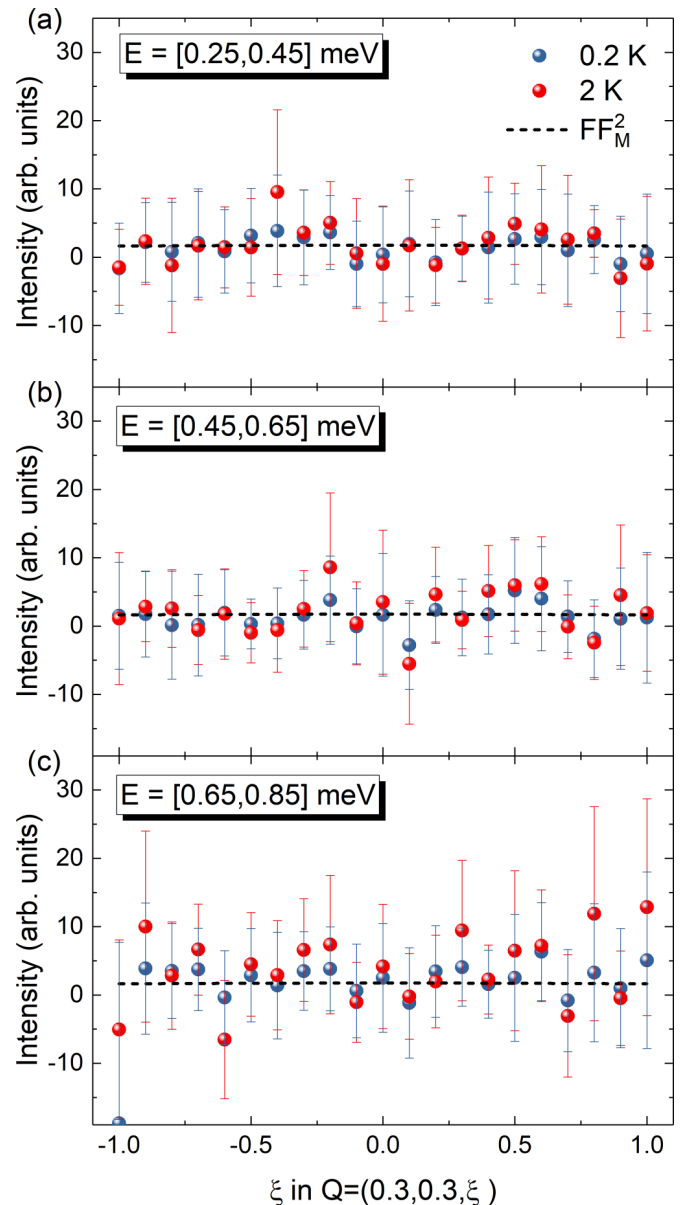


FIG. 5.  $L$  dependence of the incommensurate signal at low energies extracted from TOF data. Constant  $E$  cuts with an integration width of 0.2 meV at the incommensurate position  $(0.3, 0.3, L)$  were adjusted for the measured background at the same energy at  $(0.09, 0.41, L)$  and corrected for the Bose factor. The  $L$  dependence of the magnetic response in the superconducting phase (blue) is compared to the normal phase (red). Additionally, the square of the  $\text{Ru}^{1+}$  form factor is depicted in each panel (black dashed line). There is no evidence for a peak at  $L = 0.5$ .

[53] report a signal increase of  $\sim 60\%$  for  $L = 0.5$  in the superconducting phase, which clearly is incompatible with our data that offer higher statistics.

Since no  $L$  dependence of the magnetic low-energy response can be established (Figs. 6 and 7), we merge the data and compare them with the previously published low-energy dependence of the incommensurate signal [52] (see Fig. 8). The new experiments below  $T_c$  fully confirm that the nesting excitations in  $\text{Sr}_2\text{RuO}_4$  do not exhibit a large gap, i.e., a magnetic gap comparable to twice the superconducting one.

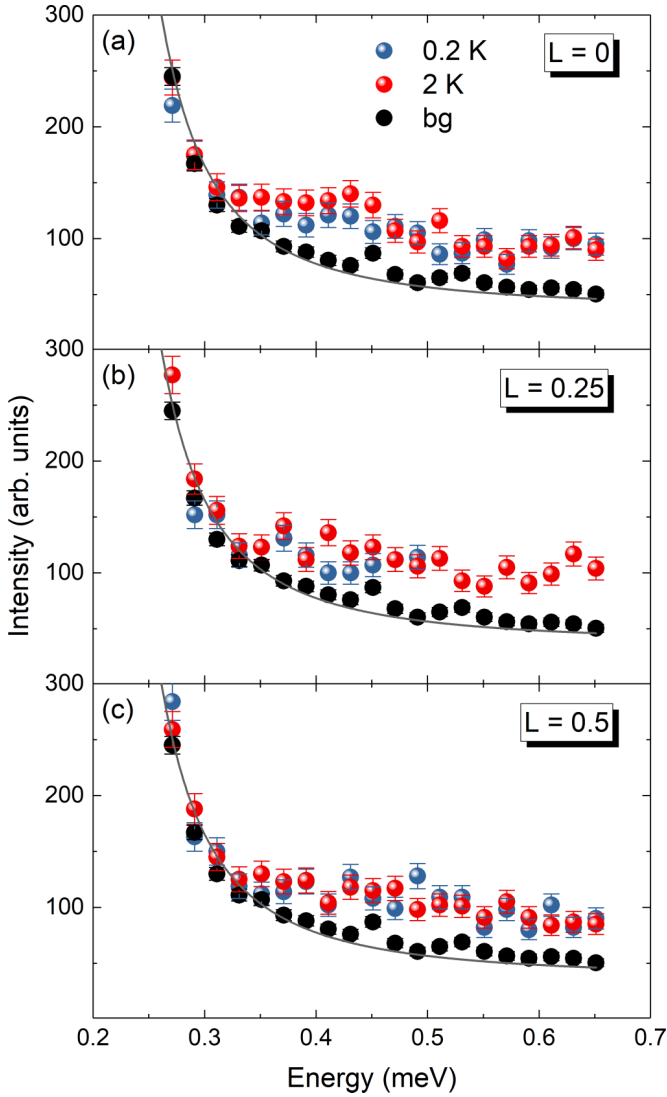


FIG. 6.  $L$  dependence of the incommensurate signal at low energies extracted from TAS data. The constant- $q$  scans were conducted at the incommensurate positions  $(0.3, 0.7, L)$  with  $L = 0, 0.25$ , and  $0.5$  in the superconducting and normal phase. The background for each  $L$  is measured after  $\omega$  rotation of  $20^\circ$ , thus keeping  $|q|$  constant, and later averaged for all scans, yielding the presented background (black circles) and its fit (gray). The intensity is normalized with 1 980 000 monitor counts, which corresponds to a measuring time of about 15 min per point.

Combining all the previous and new data, there is, however, some weak evidence for the suppression of magnetic scattering at very low energies below 0.25 meV. With the neutron instrumentation of today it seems very difficult to further characterize the suppression of the small signal at such low energy.

For the previously assumed superconducting state, detailed theoretical analyses of the magnetic response were reported [51], but concerning the more recently proposed superconducting symmetries [19–26], such investigations are lacking. The  $d_{x^2-y^2}$  state deduced from quasiparticle interference imaging [26] exhibits nodes at Fermi-surface positions that are connected through the nesting vector. This implies that even

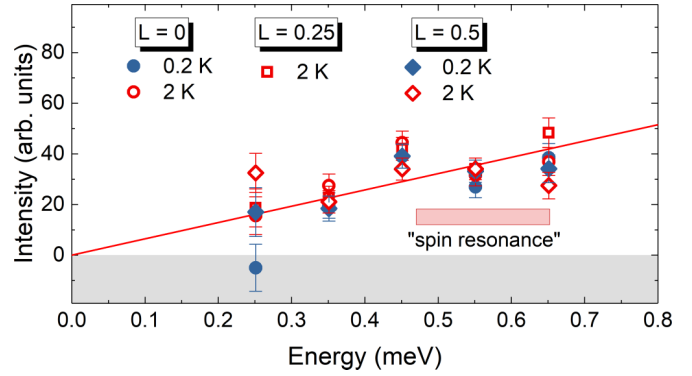


FIG. 7. Comparison of the background-free incommensurate signal  $Q = (0.3, 0.7, L)$  for different  $L$  values and temperatures. The compared data originate from the constant- $q$  scans shown in Fig. 6. The binning is increased to  $\Delta E = 0.1$  meV, which yields better statistics. A linear fit (red line) provides a guide to the eye. The energy range of the proposed spin resonance [53] is indicated by the red box.

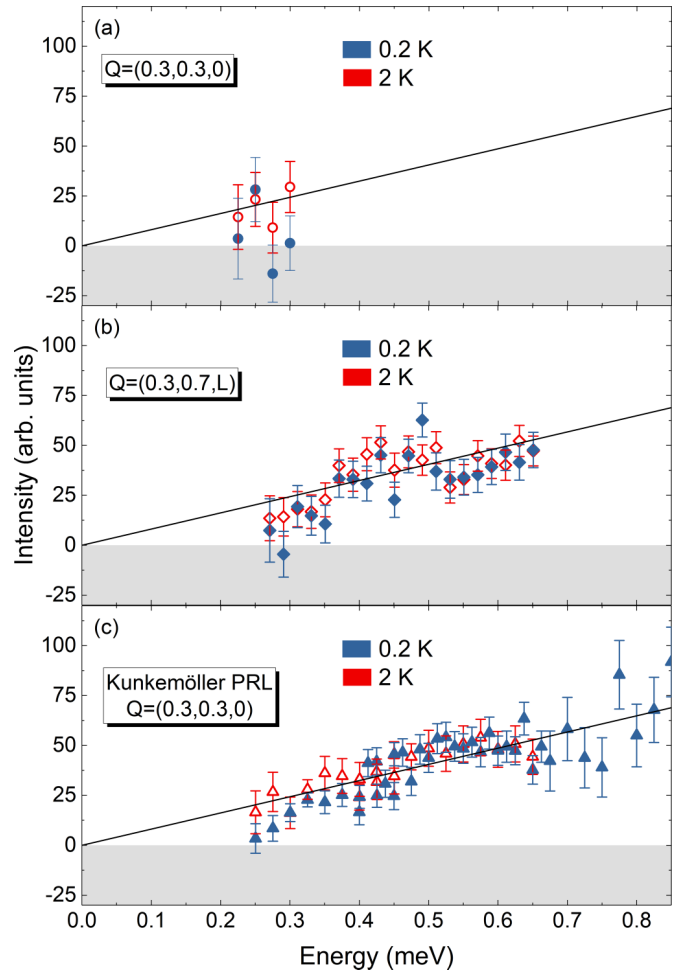


FIG. 8. Comparison of the energy dependence of the incommensurate signal with former published data from [52] (labeled Kunkemöller PRL). Background-corrected data recorded at  $(0.3, 0.3, 0)$  (circles) is given in panel (a); the background free signal at  $(0.3, 0.7)$  is averaged over all  $L$  values for both temperatures (diamonds), panel (b), and the incommensurate signal reported in [52] (triangles) is shown in (c). Data were corrected for the Bose and magnetic form factors.

at very low energies, the nesting-induced excitations are not fully suppressed in such a  $d_{x^2-y^2}$  superconducting state, in agreement with the experimental absence of a large gap in the nesting spectrum [52]. Within the  $d_{x^2-y^2}$  superconducting state, the nesting vector also connects Fermi-surface regions with maximum and minimum gap values, and it connects either two regions of the  $\beta$  sheet or one  $\beta$  region with an  $\alpha$  region. Therefore, the conditions for a spin-resonance mode are more complex and less favorable than in the case of the FeAs-based superconductors, where the  $s^{+-}$  superconducting symmetry and the nesting magnetic fluctuations perfectly match each other [65].

### C. Shape of the quasiferromagnetic fluctuations

The polarization analysis of inelastic neutron scattering provides the separation of the magnetic contribution from any other scattering contribution. It is therefore possible to identify a tiny magnetic response that is little structured in  $\mathbf{q}$  space. This technique was used to detect quasiferromagnetic fluctuations and to determine their strength in comparison to the incommensurate fluctuations in  $\text{Sr}_2\text{RuO}_4$  [45]. We wished to extend this study focusing on the  $\mathbf{q}$  dependence of the magnetic quasiferromagnetic response. Recent DMFT calculations [57] find evidence for local fluctuations superposing the well-established nesting excitations, which agree qualitatively with the experimental quasiferromagnetic signal. However, while the neutron experiments indicate a finite suppression of the quasiferromagnetic response toward the boundaries of the Brillouin zone, the DMFT calculation obtains an essentially local feature without such a  $\mathbf{q}$  dependence.

The polarized neutron study was performed on the thermal TAS IN20, and the results are shown in Fig. 9. An example of the raw data with different spin channels that are needed for the polarization analysis is given in Fig. 9(a), where a diagonal constant energy scan at 8 meV, reaching from the zone boundary (0.5,0.5) over the incommensurate position (0.7,0.3) to the zone center (1,0), is shown. The  $x$ ,  $y$ ,  $z$  indices refer to the common coordinate system used in neutron polarization analysis with respect to the scattering vector  $\mathbf{Q}$  [45]. The three spin-flip channels  $\text{SF}_x$ ,  $\text{SF}_y$ , and  $\text{SF}_z$  clearly exhibit a maximum at the incommensurate position. While  $\text{SF}_y$  and  $\text{SF}_z$  exhibit comparable amplitudes,  $\text{SF}_x$  carries the doubled intensity as it senses both magnetic components perpendicular to the scattering vector. There is an enhancement of magnetic excitations polarized along the  $c$  direction that can be seen in the stronger  $\text{SF}_y$  and that was studied in Ref. [42]. Assuming a polarization-independent background,  $2I(\text{SF}_x) - I(\text{SF}_y) - I(\text{SF}_z)$  yields the background-free magnetic signal; see the discussion in Ref. [45].

Figure 9(b) displays the magnetic signal, corrected for the Bose factor, i.e., the imaginary part of the susceptibility, for different energies and temperatures. The data agree well with the results for 8 meV and 1.6 K presented in [45]. Additionally, the data at 290 K indicate a significant drop of the incommensurate nesting signal, which, however, is still finite and clearly observable. The temperature dependence of the incommensurate signal was first discussed in Ref. [39], where the neutron scattering results are compared to the NMR results from Ref. [38]. The incommensurate

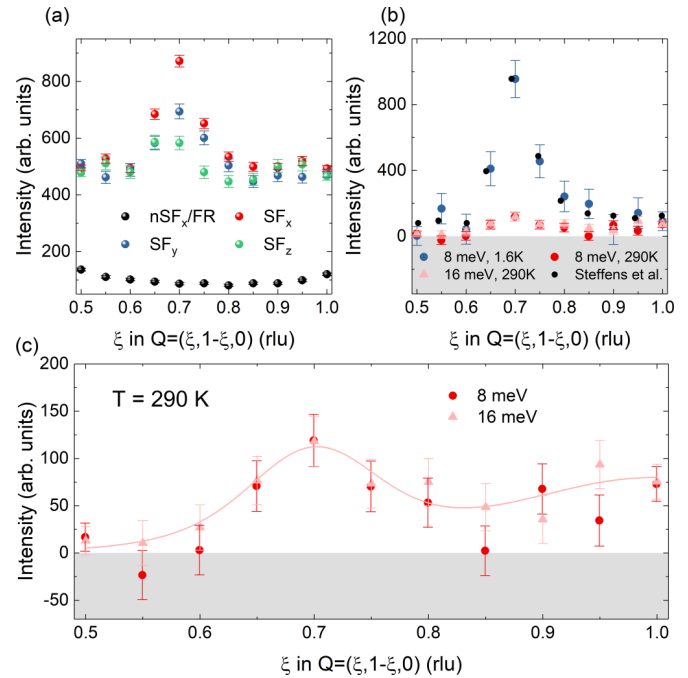


FIG. 9. Polarized neutron analysis of the scattering along the diagonal of the first Brillouin zone. (a) An example of constant energy scans for all three spin-flip channels displays the increased scattering at the incommensurate position (0.7,0.3,0) at 8 meV and 1.6 K. The polarization analysis of all channels yields the purely magnetic scattering signal displayed in (b) for different energies and temperatures. The black circles represent data of the previously reported polarization analysis, taken from [45]. This dataset was also measured at 8 meV and 1.6 K. (c) The magnetic signal at 290 K can be described by the susceptibility model used in [45] (light red line). The intensity in (a) is normalized with 7 800 000 monitor counts, which corresponds to a measuring time of about 20 min per point.

signal was found to strongly decrease with increasing temperature up to room temperature, while the ferromagnetic component of the NMR is nearly temperature-independent. Also, the previous polarized neutron experiment found the quasiferromagnetic contribution to be almost identical at 1.6 and 160 K [45]. As indicated in Fig. 9(b), the quasiferromagnetic signal does not change up to 290 K, thus the peak heights of incommensurate and quasiferromagnetic contributions are comparable at ambient temperature. Taking the much broader  $q$  shape of the quasiferromagnetic excitations into account, the  $q$ -integrated spectral weight of the latter clearly dominates. Around room temperature, therefore, the quasiferromagnetic fluctuations have a larger impact on any integrating processes such as electron scattering. The quasiferromagnetic fluctuations at 290 K, however, do not exhibit a local character as the signal is significantly reduced at the antiferromagnetic zone boundary (0.5,0.5,0) [Fig. 9(c)]. This confirms the conclusion of Steffens *et al.* [45] that the quasiferromagnetic fluctuations are sharper in  $q$  space than expected from the calculations. Also, at the other zone boundary (0.5,0,0) there is no significant magnetic signal detectable (see Fig. 10).

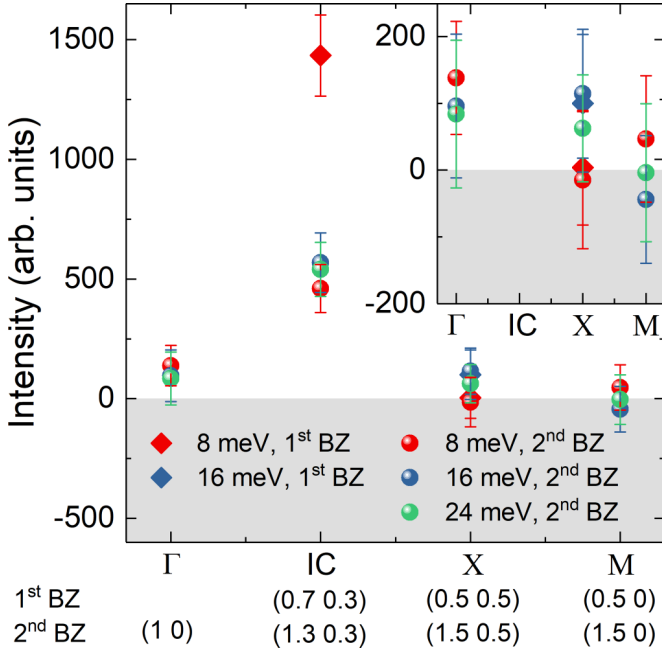


FIG. 10. Comparison of magnetic scattering ( $T = 1.6$  K) at prominent points in  $k$ -space with  $L = 0$ . The magnetic signal was extracted using the polarization analysis [ $2I(SF_x) - I(SF_y) - I(SF_z)$ ] and is displayed for the points in the Brillouin zone and different energies:  $\Gamma$  point, the incommensurate position, and the different zone boundaries X and M. The inset magnifies the intensity region around zero.

#### IV. CONCLUSION

Polarized and unpolarized neutron scattering experiments were performed to study several aspects of the magnetic fluctuations in  $\text{Sr}_2\text{RuO}_4$  that are particularly relevant for a

possible superconducting pairing scenario. The TOF instrument LET yields full mapping of the excitations and reveals the well-studied incommensurate fluctuations at  $(0.3, 0.3)$  in two-dimensional reciprocal space. There is also ridge scattering at  $(0.3, \xi)$  reflecting the one-dimensional character of the  $d_{xz}$  and  $d_{yz}$  bands, as first reported in Refs. [43,44]. These ridges are stronger between the four peaks surrounding  $(0.5, 0.5)$ , i.e., for  $\xi > 0.3$ , but the suppression of the signal at smaller  $\xi$  is gradual. The TOF data confirm the pronounced asymmetry of the nesting peaks. Concerning the study of the nesting fluctuations at very low energy in the superconducting phase, TAS experiments yield higher statistics due to the possibility to focus the experiment on the particular position in  $\mathbf{Q}, E$  space. Data taken at different out-of-plane components of the scattering vector exclude a sizable resonance mode emerging at  $L = 0.5$  in the superconducting phase. Only by combining the results of several experiments can one obtain some evidence for the suppression of spectral weight at very low energies.

With neutron polarization analysis, the magnetic excitations were further characterized at 290 K. The incommensurate nesting signal is strongly reduced but still visible, while the quasiferromagnetic contribution is almost unchanged. At this temperature, there is a suppression of this quasiferromagnetic scattering at the Brillouin-zone boundaries, which underlines that this response is not fully local.

#### ACKNOWLEDGMENTS

We acknowledge stimulating discussions with I. Eremin. This work was funded by the Deutsche Forschungsgemeinschaft (DFG, German Research Foundation)–Project No. 277146847–CRC 1238, project B04, the JSPS KAKENHI Grants No. JP15H05852 and No. JP17H06136, and the JSPS core-to-core Program No. JPJSCCA20170002.

- [1] Y. Maeno, H. Hashimoto, K. Yoshida, S. Nishizaki, T. Fujita, J. G. Bednorz, and F. Lichtenberg, Superconductivity in a layered perovskite without copper, *Nature (London)* **372**, 532 (1994).
- [2] G. Koster, L. Klein, W. Siemons, G. Rijnders, J. S. Dodge, C. B. Eom, D. H. A. Blank, and M. R. Beasley, Structure, physical properties, and applications of  $\text{SrRuO}_3$  thin films, *Rev. Mod. Phys.* **84**, 253 (2012).
- [3] G. Baskaran, Why is  $\text{Sr}_2\text{RuO}_4$  not a high  $T_c$  superconductor? Electron correlation, Hund's coupling and p-wave instability, *Phys. B* **223**, 490 (1996).
- [4] T. M. Rice and M. Sgrist,  $\text{Sr}_2\text{RuO}_4$ : an electronic analogue of  $^3\text{He}$ ?, *J. Phys. Condens. Matter* **7**, L643 (1995).
- [5] A. P. Mackenzie and Y. Maeno, The superconductivity of  $\text{Sr}_2\text{RuO}_4$  and the physics of spin-triplet pairing, *Rev. Mod. Phys.* **75**, 657 (2003).
- [6] Y. Maeno, S. Kittaka, T. Nomura, S. Yonezawa, and K. Ishida, Evaluation of spin-triplet superconductivity in  $\text{Sr}_2\text{RuO}_4$ , *J. Phys. Soc. Jpn.* **81**, 011009 (2012).
- [7] C. W. Hicks, J. R. Kirtley, T. M. Lippman, N. C. Koshnick, M. E. Huber, Y. Maeno, W. M. Yuhasz, M. B. Maple, and K. A. Moler, Limits on superconductivity-related magnetization in  $\text{Sr}_2\text{RuO}_4$  and  $\text{PrOs}_4\text{Sb}_{12}$  from scanning SQUID microscopy, *Phys. Rev. B* **81**, 214501 (2010).
- [8] H. Murakawa, K. Ishida, K. Kitagawa, Z. Q. Mao, and Y. Maeno, Measurement of the  $^{101}\text{Ru}$ -Knight Shift of Superconducting  $\text{Sr}_2\text{RuO}_4$  in a Parallel Magnetic Field, *Phys. Rev. Lett.* **93**, 167004 (2004).
- [9] C. Kallin, Chiral p-wave order in  $\text{Sr}_2\text{RuO}_4$ , *Rep. Prog. Phys.* **75**, 042501 (2012).
- [10] C. W. Hicks, D. O. Brodsky, E. A. Yelland, A. S. Gibbs, J. A. N. Bruin, M. E. Barber, S. D. Edkins, K. Nishimura, S. Yonezawa, Y. Maeno, and A. P. Mackenzie, Strong increase of  $T_c$  of  $\text{Sr}_2\text{RuO}_4$  under both tensile and compressive strain, *Science* **344**, 283 (2014).
- [11] A. Steppke, L. Zhao, M. E. Barber, T. Scaffidi, F. Jerzembeck, H. Rosner, A. S. Gibbs, Y. Maeno, S. H. Simon, A. P. Mackenzie, and C. W. Hicks, Strong peak in  $T_c$  of  $\text{Sr}_2\text{RuO}_4$  under uniaxial pressure, *Science* **355**, 6321 (2017).
- [12] Y. S. Li, N. Kikugawa, D. A. Sokolov, F. Jerzembeck, A. S. Gibbs, Y. Maeno, C. W. Hicks, M. Nicklas, and A. P. Mackenzie, High sensitivity heat capacity measurements on  $\text{Sr}_2\text{RuO}_4$  under uniaxial pressure, *Proc. Natl. Acad. Sci.* **118**, e2020492118 (2021).

- [13] M. E. Barber, F. Lechermann, S. V. Streltsov, S. L. Skornyakov, S. Ghosh, B. J. Ramshaw, N. Kikugawa, D. A. Sokolov, A. P. Mackenzie, C. W. Hicks, and I. I. Mazin, Role of correlations in determining the Van Hove strain in  $\text{Sr}_2\text{RuO}_4$ , *Phys. Rev. B* **100**, 245139 (2019).
- [14] K. Ishida, H. Mukuda, Y. Kitaoka, K. Asayama, Z. Q. Mao, Y. Mori, and Y. Maeno, Spin-triplet superconductivity in  $\text{Sr}_2\text{RuO}_4$  identified by  $^{17}\text{O}$  Knight shift, *Nature (London)* **396**, 658 (1998).
- [15] J. A. Duffy, S. M. Hayden, Y. Maeno, Z. Mao, J. Kulda, and G. J. McIntyre, Polarized-Neutron Scattering Study of the Cooper-Pair Moment in  $\text{Sr}_2\text{RuO}_4$ , *Phys. Rev. Lett.* **85**, 5412 (2000).
- [16] A. Pustogow, Y. Luo, A. Chronister, Y. S. Su, D. A. Sokolov, F. Jerzembeck, A. P. Mackenzie, C. W. Hicks, N. Kikugawa, S. Raghu, E. D. Bauer, and S. E. Brown, Constraints on the superconducting order parameter in  $\text{Sr}_2\text{RuO}_4$  from oxygen-17 nuclear magnetic resonance, *Nature (London)* **574**, 72 (2019).
- [17] K. Ishida, M. Manago, K. Kinjo, and Y. Maeno, Reduction of the  $^{17}\text{O}$  Knight shift in the superconducting state and the heat-up effect by NMR pulses on  $\text{Sr}_2\text{RuO}_4$ , *J. Phys. Soc. Jpn.* **89**, 034712 (2020).
- [18] A. N. Petsch, M. Zhu, M. Enderle, Z. Q. Mao, Y. Maeno, I. I. Mazin, and S. M. Hayden, Reduction of the Spin Susceptibility in the Superconducting State of  $\text{Sr}_2\text{RuO}_4$  Observed by Polarized Neutron Scattering, *Phys. Rev. Lett.* **125**, 217004 (2020).
- [19] H. S. Røising, T. Scaffidi, F. Flicker, G. F. Lange, and S. H. Simon, Superconducting order of  $\text{Sr}_2\text{RuO}_4$  from a three-dimensional microscopic model, *Phys. Rev. Research* **1**, 033108 (2019).
- [20] A. T. Rømer, D. D. Scherer, I. M. Eremin, P. J. Hirschfeld, and B. M. Andersen, Knight Shift and Leading Superconducting Instability from Spin Fluctuations in  $\text{Sr}_2\text{RuO}_4$ , *Phys. Rev. Lett.* **123**, 247001 (2019).
- [21] W.-S. Wang, C.-C. Zhang, F.-C. Zhang, and Q.-H. Wang, Theory of Chiral  $p$ -Wave Superconductivity with Near Nodes for  $\text{Sr}_2\text{RuO}_4$ , *Phys. Rev. Lett.* **122**, 027002 (2019).
- [22] Z. Wang, X. Wang, and C. Kallin, Spin-orbit coupling and spin-triplet pairing symmetry in  $\text{Sr}_2\text{RuO}_4$ , *Phys. Rev. B* **101**, 064507 (2020).
- [23] H. G. Suh, H. Menke, P. M. R. Brydon, C. Timm, A. Ramires, and D. F. Agterberg, Stabilizing even-parity chiral superconductivity in  $\text{Sr}_2\text{RuO}_4$ , *Phys. Rev. Research* **2**, 032023(R) (2020).
- [24] A. T. Rømer, A. Kreisel, M. A. Müller, P. J. Hirschfeld, I. M. Eremin, and B. M. Andersen, Theory of strain-induced magnetic order and splitting of  $T_c$  and  $T_{\text{TRSB}}$  in  $\text{Sr}_2\text{RuO}_4$ , *Phys. Rev. B* **102**, 054506 (2020).
- [25] S. A. Kivelson, A. C. Yuan, B. Ramshaw, and R. Thomale, A proposal for reconciling diverse experiments on the superconducting state in  $\text{Sr}_2\text{RuO}_4$ , *npj Quantum Mater.* **5**, 43 (2020).
- [26] R. Sharma, S. D. Edkins, Z. Wang, A. Kostin, C. Sow, Y. Maeno, A. P. Mackenzie, J. C. S. Davis, and V. Madhavan, Momentum-resolved superconducting energy gaps of  $\text{Sr}_2\text{RuO}_4$  from quasiparticle interference imaging, *Proc. Natl. Acad. Sci. (USA)* **117**, 5222 (2020).
- [27] G. M. Luke, Y. Fudamoto, K. M. Kojima, M. I. Larkin, J. Merrin, B. Nachumi, Y. J. Uemura, Y. Maeno, Z. Q. Mao, Y. Mori, H. Nakamura, and M. Sgrist, Time-reversal symmetry-breaking superconductivity in  $\text{Sr}_2\text{RuO}_4$ , *Nature (London)* **394**, 558 (1998).
- [28] V. Grinenko, R. Sarkar, K. Kihou, C. H. Lee, I. Morozov, S. Aswartham, B. Büchner, P. Chekhonin, W. Skrotzki, K. Nenkov, R. Hühne, K. Nielsch, S. L. Drechsler, V. L. Vadimov, M. A. Silaev, P. A. Volkov, I. Eremin, H. Luetkens, and H. H. Klauss, Superconductivity with broken time-reversal symmetry inside a superconducting  $s$ -wave state, *Nat. Phys.* **16**, 789 (2020).
- [29] J. Xia, Y. Maeno, P. T. Beyersdorf, M. M. Fejer, and A. Kapitulnik, High Resolution Polar Kerr Effect Measurements of  $\text{Sr}_2\text{RuO}_4$ : Evidence for Broken Time-Reversal Symmetry in the Superconducting State, *Phys. Rev. Lett.* **97**, 167002 (2006).
- [30] I. Schnell, I. I. Mazin, and A. Y. Liu, Unconventional superconducting pairing symmetry induced by phonons, *Phys. Rev. B* **74**, 184503 (2006).
- [31] M. Braden, A. H. Moudden, S. Nishizaki, Y. Maeno, and T. Fujita, Structural analysis of  $\text{Sr}_2\text{RuO}_4$ , *Phys. C* **273**, 248 (1997).
- [32] M. Braden, W. Reichardt, Y. Sidis, Z. Mao, and Y. Maeno, Lattice dynamics and electron-phonon coupling in  $\text{Sr}_2\text{RuO}_4$ : Inelastic neutron scattering and shell-model calculations, *Phys. Rev. B* **76**, 014505 (2007).
- [33] Z. Fang and K. Terakura, Magnetic phase diagram of  $\text{Ca}_{2-x}\text{Sr}_x\text{RuO}_4$  governed by structural distortions, *Phys. Rev. B* **64**, 020509(R) (2001).
- [34] O. Friedt, M. Braden, G. André, P. Adelman, S. Nakatsuji, and Y. Maeno, Structural and magnetic aspects of the metal-insulator transition in  $\text{Ca}_{2-x}\text{Sr}_x\text{RuO}_4$ , *Phys. Rev. B* **63**, 174432 (2001).
- [35] M. Braden, W. Reichardt, S. Shiryayev, and S. Barilo, Giant phonon anomalies in the bond-stretching modes in doped  $\text{BaBiO}_3$ : comparison to cuprates manganites and nickelates, *Physica C* **378-381**, 89 (2002).
- [36] Y. Wang, J. J. Wang, J. E. Saal, S. L. Shang, L.-Q. Chen, and Z.-K. Liu, Phonon dispersion in  $\text{Sr}_2\text{RuO}_4$  studied by a first-principles cumulative force-constant approach, *Phys. Rev. B* **82**, 172503 (2010).
- [37] M. Braden, L. Pintschovius, T. Uefuji, and K. Yamada, Dispersion of the high-energy phonon modes in  $\text{Nd}_{1.85}\text{Ce}_{0.15}\text{CuO}_4$ , *Phys. Rev. B* **72**, 184517 (2005).
- [38] T. Imai, A. W. Hunt, K. R. Thurber, and F. C. Chou,  $^{17}\text{O}$  NMR evidence for orbital dependent ferromagnetic correlations in  $\text{Sr}_2\text{RuO}_4$ , *Phys. Rev. Lett.* **81**, 3006 (1998).
- [39] Y. Sidis, M. Braden, P. Bourges, B. Hennion, S. Nishizaki, Y. Maeno, and Y. Mori, Evidence for Incommensurate Spin Fluctuations in  $\text{Sr}_2\text{RuO}_4$ , *Phys. Rev. Lett.* **83**, 3320 (1999).
- [40] M. Braden, Y. Sidis, P. Bourges, P. Pfeuty, J. Kulda, Z. Mao, and Y. Maeno, Inelastic neutron scattering study of magnetic excitations in  $\text{Sr}_2\text{RuO}_4$ , *Phys. Rev. B* **66**, 064522 (2002).
- [41] F. Servant, B. Fåk, S. Raymond, J. P. Brison, P. Lejay, and J. Flouquet, Magnetic excitations in the normal and superconducting states of  $\text{Sr}_2\text{RuO}_4$ , *Phys. Rev. B* **65**, 184511 (2002).
- [42] M. Braden, P. Steffens, Y. Sidis, J. Kulda, P. Bourges, S. Hayden, N. Kikugawa, and Y. Maeno, Anisotropy of the Incommensurate Fluctuations in  $\text{Sr}_2\text{RuO}_4$ : A Study with Polarized Neutrons, *Phys. Rev. Lett.* **92**, 097402 (2004).
- [43] K. Iida, M. Kofu, N. Katayama, J. Lee, R. Kajimoto, Y. Inamura, M. Nakamura, M. Arai, Y. Yoshida, M. Fujita, K. Yamada, and S.-H. Lee, Inelastic neutron scattering study of the magnetic fluctuations in  $\text{Sr}_2\text{RuO}_4$ , *Phys. Rev. B* **84**, 060402(R) (2011).

- [44] K. Iida, J. Lee, M. B. Stone, M. Kofu, Y. Yoshida, and S. Lee, Two-dimensional incommensurate magnetic fluctuations in  $\text{Sr}_2(\text{Ru}_{0.99}\text{Ti}_{0.01})\text{O}_4$ , *J. Phys. Soc. Jpn.* **81**, 124710 (2012).
- [45] P. Steffens, Y. Sidis, J. Kulda, Z. Q. Mao, Y. Maeno, I. I. Mazin, and M. Braden, Spin Fluctuations in  $\text{Sr}_2\text{RuO}_4$  from Polarized Neutron Scattering: Implications for Superconductivity, *Phys. Rev. Lett.* **122**, 047004 (2019).
- [46] M. Braden, O. Friedt, Y. Sidis, P. Bourges, M. Minakata, and Y. Maeno, Incommensurate Magnetic Ordering in  $\text{Sr}_2\text{Ru}_{1-x}\text{Ti}_x\text{O}_4$ , *Phys. Rev. Lett.* **88**, 197002 (2002).
- [47] J. P. Carlo, T. Goko, I. M. Gat-Malureanu, P. L. Russo, A. T. Savici, A. A. Aczel, G. J. MacDougall, J. A. Rodriguez, T. J. Williams, G. M. Luke, C. R. Wiebe, Y. Yoshida, S. Nakatsuji, Y. Maeno, T. Taniguchi, and Y. J. Uemura, New magnetic phase diagram of  $(\text{Sr}, \text{Ca})_2\text{RuO}_4$ , *Nat. Mater.* **11**, 323 (2012).
- [48] S. Kunkemöller, A. A. Nugroho, Y. Sidis, and M. Braden, Spin-density-wave ordering in  $\text{Ca}_{0.5}\text{Sr}_{1.5}\text{RuO}_4$  studied by neutron scattering, *Phys. Rev. B* **89**, 045119 (2014).
- [49] B. Zinkl and M. Sigrist, Impurity induced double transitions for accidentally degenerate unconventional pairing states, *Phys. Rev. Research* **3**, L012004 (2021).
- [50] I. I. Mazin and D. J. Singh, Competitions in Layered Ruthenates: Ferromagnetism Versus Antiferromagnetism and Triplet Versus Singlet Pairing, *Phys. Rev. Lett.* **82**, 4324 (1999).
- [51] J.-W. Huo, T. M. Rice, and F.-C. Zhang, Spin Density Wave Fluctuations and  $p$ -Wave Pairing in  $\text{Sr}_2\text{RuO}_4$ , *Phys. Rev. Lett.* **110**, 167003 (2013).
- [52] S. Kunkemöller, P. Steffens, P. Link, Y. Sidis, Z. Q. Mao, Y. Maeno, and M. Braden, Absence of a Large Superconductivity-Induced Gap in Magnetic Fluctuations of  $\text{Sr}_2\text{RuO}_4$ , *Phys. Rev. Lett.* **118**, 147002 (2017).
- [53] K. Iida, M. Kofu, K. Suzuki, N. Murai, S. Ohira-Kawamura, R. Kajimoto, Y. Inamura, M. Ishikado, S. Hasegawa, T. Masuda, Y. Yoshida, K. Kakurai, K. Machida, and S. Lee, Horizontal line nodes in  $\text{Sr}_2\text{RuO}_4$  proved by spin resonance, *J. Phys. Soc. Jpn.* **89**, 053702 (2020).
- [54] Y. Maeno, K. Yoshida, H. Hashimoto, S. Nishizaki, S.-i. Ikeda, M. Nohara, T. Fujita, A. Mackenzie, N. Hussey, J. Bednorz, and F. Lichtenberg, Two-dimensional Fermi liquid behavior of the superconductor  $\text{Sr}_2\text{RuO}_4$ , *J. Phys. Soc. Jpn.* **66**, 1405 (1997).
- [55] H. Mukuda, K. Ishida, Y. Kitaoka, K. Asayama, Z. Q. Mao, Y. Mori, and Y. Maeno,  $^{17}\text{O}$  NMR probe of spin fluctuations in triplet superconductor  $\text{Sr}_2\text{RuO}_4$ , *Phys. B* **259-261**, 944 (1999).
- [56] J. E. Ortmann, J. Y. Liu, J. Hu, M. Zhu, J. Peng, M. Matsuda, X. Ke, and Z. Q. Mao, Competition between antiferromagnetism and ferromagnetism in  $\text{Sr}_2\text{RuO}_4$  probed by Mn and Co doping, *Sci. Rep.* **3**, 2950 (2013).
- [57] H. U. R. Strand, M. Zingl, N. Wentzell, O. Parcollet, and A. Georges, Magnetic response of  $\text{Sr}_2\text{RuO}_4$ : Quasi-local spin fluctuations due to Hund's coupling, *Phys. Rev. B* **100**, 125120 (2019).
- [58] T. Moriya, *Spin Fluctuations in Itinerant Electron Magnetism* (Springer-Verlag, Berlin, 1985).
- [59] K. Jenni, S. Kunkemöller, D. Brünig, T. Lorenz, Y. Sidis, A. Schneidewind, A. A. Nugroho, A. Rosch, D. I. Khomskii, and M. Braden, Interplay of Electronic and Spin Degrees in Ferromagnetic  $\text{SrRuO}_3$ : Anomalous Softening of the Magnon Gap and Stiffness, *Phys. Rev. Lett.* **123**, 017202 (2019).
- [60] C. N. Veenstra, Z. H. Zhu, B. Ludbrook, M. Capsoni, G. Levy, A. Nicolaou, J. A. Rosen, R. Comin, S. Kittaka, Y. Maeno, I. S. Elfimov, and A. Damascelli, Determining the Surface-to-Bulk Progression in the Normal-State Electronic Structure of  $\text{Sr}_2\text{RuO}_4$  by Angle-Resolved Photoemission and Density Functional Theory, *Phys. Rev. Lett.* **110**, 097004 (2013).
- [61] K. Jenni, M. Braden, Y. Sidis, and P. Steffens, Interplay of magnetic excitations and superconductivity in  $\text{Sr}_2\text{RuO}_4$  (2018), Institut Laue-Langevin (ILL), doi:10.5291/ILL-DATA.4-02-537.
- [62] K. Jenni, M. Braden, Y. Sidis, and P. Steffens,  $\pi, \pi$  resonance mode in the superconducting state of  $\text{Sr}_2\text{RuO}_4$  (2020), Institut Laue-Langevin (ILL), doi:10.5291/ILL-DATA.4-02-586.
- [63] K. Jenni, M. Braden, Y. Sidis, and P. Steffens, Electronic interaction in the unconventional superconductor  $\text{Sr}_2\text{RuO}_4$  (2020), Institut Laue-Langevin (ILL), doi:10.5291/ILL-DATA.4-02-565.
- [64] M. Braden, K. Jenni, D. Vonshen, Y. Sidis, P. Steffens, and S. Kunkemöller, Low-energy magnetic excitations in the superconducting state of  $\text{Sr}_2\text{RuO}_4$ : opening of a gap? (2017), STFC ISIS Neutron and Muon Source, doi:10.5286/ISIS.E.RB1710381.
- [65] I. I. Mazin, D. J. Singh, M. D. Johannes, and M. H. Du, Unconventional Superconductivity with a Sign Reversal in the Order Parameter of  $\text{LaFeAsO}_{1-x}\text{F}_x$ , *Phys. Rev. Lett.* **101**, 057003 (2008).

## 4.4 Methods

### Material Information

Sr<sub>2</sub>RuO<sub>4</sub> crystallizes in a tetragonal lattice (space group  $I4/mmm$ ) with the lattice parameters  $a = 3.8730 \text{ \AA}$  and  $c = 12.7323 \text{ \AA}$  at room temperature [126]. It is isostructural to the high-T<sub>C</sub> superconductors of the cuprates and also shows superconductivity. However its T<sub>C</sub> is strongly reduced in comparison to the cuprates and amounts to T<sub>C</sub> = 1.5 K. Since the transition temperature is highly sensitive to impurities the floating-zone method with a mirror furnace (Section 6.1) as a non-contact crystal growth method is well established in producing high-quality samples. The crystals of Sr<sub>2</sub>RuO<sub>4</sub> used in the reported experiments were grown by Z. Q. Mao at Kyoto university using the floating-zone method.

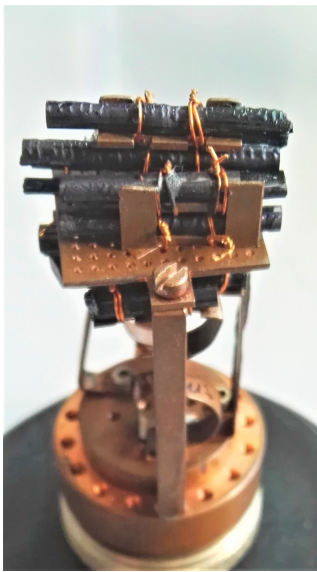


**Figure 4.1: Crystal setup for neutron scattering experiments.** The 12 single crystals are mounted and coaligned on a copper holder which facilitates measurements in the superconducting phase.

The flipping ratio was measured with a phonon at  $\mathbf{Q} = (-0.3, 2, 0)$ ,  $E = 10 \text{ meV}$  and amounts to  $\approx 8$ . The sample holder of Cu which is normally used to measure at  $T < T_C$  unfortunately produces high background at the high energies studied on IN20.

### Neutron scattering

The neutron scattering experiments were conducted at triple-axis spectrometers at the Institut Laue-Langevin (ILL) in Grenoble, France and the time-of-flight instrument LET at ISIS Neutron and Muon source in Didcot, United Kingdom. All involved beam times including the instrument and the experimental setting are listed in Table 4.1. The triple-axis spectrometers are operated with pyrolytic graphite (PG) crystals as analyzer with a fixed  $k_f$ . For decreased background a Si(111) monochromator was used for the cold neutron instrument ThALES. To clean the neutron signal of higher orders and further decrease the background a cooled Be filter in combination with a radial collimator was used at ThALES. At the thermal instrument IN20 a graphite filter was used to suppress higher orders.

The sample is oriented in the  $[1, 0, 0]/[0, 1, 0]$  scattering plane for all scattering experiments.

### Polarized Neutron Scattering

For the polarized neutron scattering experiment at IN20 the neutron beam is polarized by a Heusler monochromator. The neutron polarization at the sample is defined with a XYZ-Helmholtz-coil setup. In combination with one Mezei-flipper behind the sample and a Heusler analyzer this setup facilitates the full polarization analysis.

Table 4.1: Involved neutron beam times with the instrumental settings.

Beam Time	Facility	Instrument	$k_f$ ( $\text{\AA}^{-1}$ ) ( $E_i$ (meV))	Mono./Ana.	Filter	comment
05-2017	ISIS	LET	(3, 4.52, 5.64, 8.78, 14.13)	–	–	
10-2018	ILL	ThALES	1.57	Si(111)/PG(002)	cooled Be + radial collimator	
01-2020	ILL	IN20	4.1	Heusler(111)/ Heusler(111)	graphite	full polarization analysis
09-2020	ILL	ThALES	1.57	Si(111)/PG(002)	cooled Be + radial collimator	



# Sr<sub>2</sub>Ru<sub>1-y</sub>Co<sub>y</sub>O<sub>4</sub>: Search for Magnetic Order

## 5.1 Introduction

Like in many unconventional superconductors the superconducting state in Sr<sub>2</sub>RuO<sub>4</sub> exists in the proximity of static magnetic order. This resulted in the proposal that spin fluctuations may play a role in the pairing mechanism of unconventional superconductors. In the case of Sr<sub>2</sub>RuO<sub>4</sub> extended efforts have been made to clarify to which static magnetic order the superconducting state lies adjacent. The most prominent spin fluctuations are the antiferromagnetic fluctuations at the incommensurate scattering vector  $\mathbf{Q}_{\text{IC}} = (0.3, 0.3, 0)$  stemming from the Fermi surface nesting between the  $\alpha$  and  $\beta$  sheets derived from the Ru  $4d_{xz/yz}$  orbitals. These incommensurate fluctuations can be stabilized by small Ti doping or significant Ca doping into short-range static magnetic order in the form of spin-density wave ordering which was found by neutron scattering [6, 116]. While these antiferromagnetic fluctuations are expected to favor  $d$ -wave pairing other experimental evidence and the ferromagnetism in the infinite layered Ruddlesden-Popper ruthenate SrRuO<sub>3</sub> suggested a spin-triplet  $p$ -wave pairing with which ferromagnetic fluctuations coincide [26]. This led to the detailed study of spin fluctuations in Sr<sub>2</sub>RuO<sub>4</sub> and indeed there is experimental evidence for ferromagnetic fluctuations [48, 115]. However the inelastic neutron scattering study suggests that the ferromagnetic fluctuations are rather weak compared to the antiferromagnetic fluctuations. While the two main experimental results supporting the triplet  $p$ -wave pairing symmetry [43, 44] had to be retracted after both experimental studies were revised [50, 51] the study of ferromagnetic spin fluctuations is still going on. Also in the scenario of weak ferromagnetic fluctuations coexisting with antiferromagnetic fluctuations it should be possible to stabilize the ferromagnetic fluctuations by chemical doping similar to the case of Ti doping stabilizing the incommensurate fluctuations. Indeed La substitution is enhancing the ferromagnetic fluctuations which has been interpreted as the electron doping from La<sup>3+</sup> bringing the Fermi level of Ru  $4d_{xy}$  bands close to the van Hove singularity [127, 128]. In 2013 Ortman *et al.* reported that small Co doping seems to stabilize short-range ferromagnetic order while Mn doping stabilizes the incommensurate order known from Ti and Ca doping [59]. While they present neutron scattering data for Mn doped samples showing the spin-density wave ordering peak close to  $\mathbf{Q}_{\text{IC}} = (0.3, 0.7, 0)$ , there is no reported neutron scattering data for the Co doped samples showing evidence for static ferromagnetic order. After the successful growth of large single crystals of the Sr<sub>2</sub>Ru<sub>1-y</sub>Co<sub>y</sub>O<sub>4</sub> series with differ-

ent Co contents in our institute we investigated the magnetic order in Co doped Sr<sub>2</sub>RuO<sub>4</sub> and searched for static ferromagnetic order confirmed by neutron scattering experiments. Here the results of the neutron scattering study are combined with magnetization measurements and single crystal X-ray diffraction to clarify the origin of magnetic order in Co doped Sr<sub>2</sub>RuO<sub>4</sub>.

## 5.2 Results and Analysis

The crystal growth in the mirror furnace yielded 3 nominally different doping levels of Co. All crystals were characterized using the standard measurement techniques (see Section 5.4). The measurements confirm qualitatively the results reported in [59]. Comparing the magnetization of the three crystals it is apparent that the signatures of short-range ferromagnetic order, namely the non-linear and hysteretic behavior of the field dependent magnetization, are visible for all Co doping but seem to become more pronounced with increasing nominal Co content. Here Figure 5.1(a) and (b) compare the temperature and field dependence of the magnetization for different doping levels with the magnetic field pointing along  $c$ . The temperature of irreversibility  $T_{\text{ir}}$  where the zero-field cooled and the field cooled measurements separate increases with increasing Co content. Same is true for the coercitive fields of the low temperature hystereses. The temperature dependent resistivity shows an increase in residual resistivity compared to the pure compound with increasing Co content which is expected because the Co introduces disorder to the system. The temperature dependence for both in- and out-of-plane resistivity indicates the preserved metallic behavior of  $\text{Sr}_2\text{RuO}_4$  under Co doping. The insets in Figure 5.1(c) and (d) focus on the temperature area of  $T_{\text{ir}}$  stemming from the magnetization. There is no evidence for anomalies in the resistivity at this temperatures.

In the scope of the characterization all samples were also analyzed by single crystal X-ray diffraction (scXRD) and refined using JANA2006 [132]. A summary of the refinement results are given in Table 5.1. The structural data can be refined with good R values below 2 and the determined structural parameters show no strong influence of the Ru substitution by Co on the crystal structure which is essentially identical to the parent compound. For each sample the structure was refined with and without Co doping and the inclusion of Co into the refinement yields an improvement of the R value in every case<sup>1</sup>. When the Ru/Co ratio is refined alongside the structural parameters then scXRD can also yield a quantitative value of the amount of Co incorporated into the lattice. For all samples the determined relative amount of Co is always less than the nominal values. In the case of the 1.5% doped sample the Co amount reduces to 1% while the refinement of the 5% doped crystal structure determines a Co amount of 3.2%. Surprisingly the refinement of the nominal 10% Co doped sample determines a Co amount of 1.5% which is lower than the determined value of the nominal 5% sample. Also here the improvement in R value is the lowest for all samples. Firstly this indicates a solution limit of Co in the structure of the parent compound which was also observed in [59]. Secondly the discrepancy between nominal and by scXRD determined Co content points to inhomogeneities in the crystals. Some areas of the crystal have a Co excess which leads to the formation of magnetic Co clusters which cannot be resolved by scXRD and influence the bulk magnetization. Single crystal X-ray diffraction only measures the amount of Co which is incorporated into the lattice in the Ru positions and therefore contribute to the long-range order. Evidence for such localized Co clusters or magnetic droplets were also found in the specific heat measurements in [59]. For consistency the samples will be still labeled with their nominal Co contents in the following.

Unfortunately the crystal growth of samples with 10% Co doping did not yield a

---

<sup>1</sup>The R value of the refinement without Co is indicated by  $R_w^{\text{pure}}$  in Table 5.1.

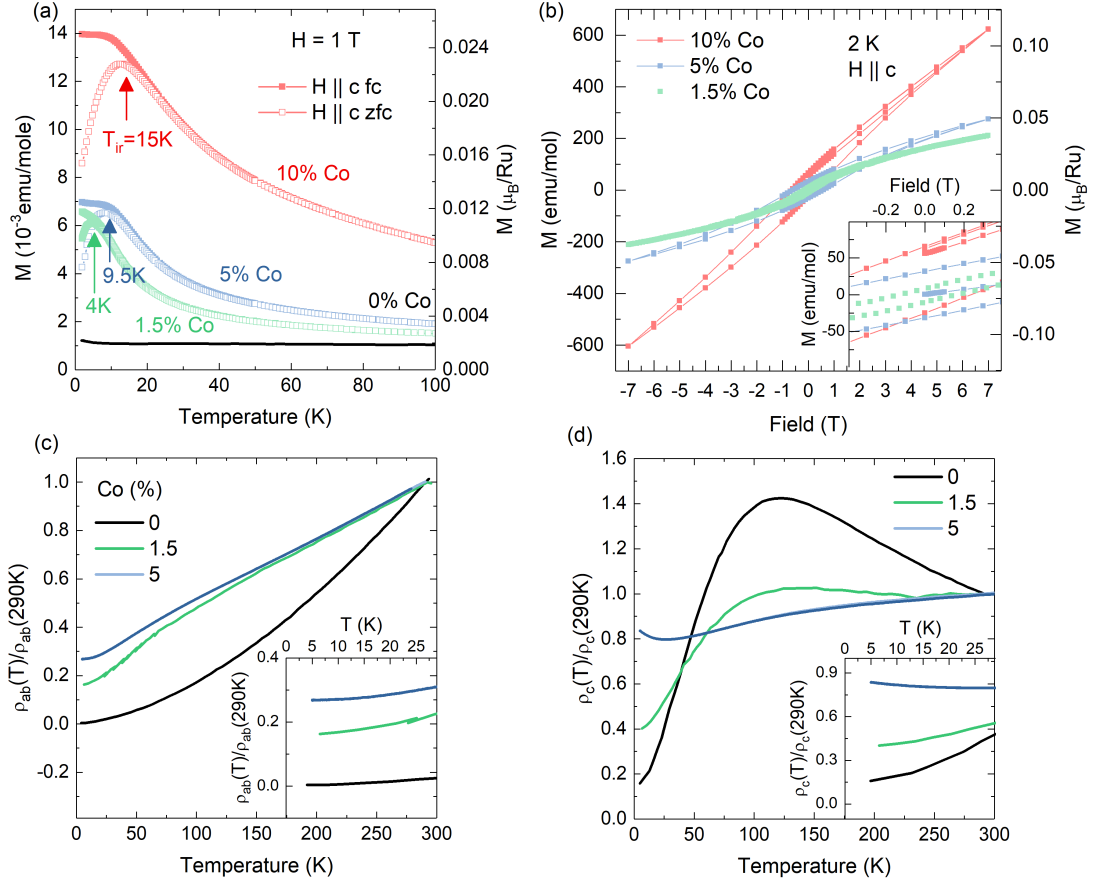


**Figure 5.1: Comparison of the temperature and field dependence of magnetization and resistivity for different Co contents in Sr<sub>2</sub>Ru<sub>1-x</sub>Co<sub>x</sub>O<sub>4</sub>.** (a) The temperature dependent magnetization shows an increase of magnetic moment at low temperature with increasing Co doping. In addition the temperature of irreversibility  $T_{ir}$  is also increasing with Co content. (b) The field dependence of the magnetization shows the increase of magnetic moment with the increase of Co content. Additionally the coercitive fields of the hystereses increase with Co content. The magnetization data for the pure Sr<sub>2</sub>RuO<sub>4</sub> are taken from [129], for the 1.5% Co doped sample from [130]. (c)-(d) The temperature dependence of the resistivity in *ab* and *c* direction respectively shows a reduction of the RRR with increasing Co content. The insets focus on the temperature range of  $T_{ir}$ . The resistivity data for the pure Sr<sub>2</sub>RuO<sub>4</sub> are taken from [131], for the 1.5% Co doped sample from [130].

large enough pure sample volume for a thorough neutron scattering study. Therefore the following neutron data only refer to the 1.5% and 5% Co doped samples. The scope of the neutron scattering study of samples of the Sr<sub>2</sub>Ru<sub>1-y</sub>Co<sub>y</sub>O<sub>4</sub> series was the investigation of possible magnetic order which is introduced by Co doping. As reported before doping of Sr<sub>2</sub>RuO<sub>4</sub> with either Mn or Ti stabilizes the antiferromagnetic fluctuations and leads to a spin-density wave signal appearing in the vicinity of the incommensurate position  $\mathbf{Q}_{IC} = (0.3, 0.3, 0)$ . This makes the incommensurate position a point of interest also for this neutron scattering study. However the main point of interest is the search for evidence of the stabilization of ferromagnetic fluctuations which do coexist with the more pronounced antiferromagnetic fluctuations in Sr<sub>2</sub>RuO<sub>4</sub>[48]. As mentioned above, the magnetization of the Co doped samples

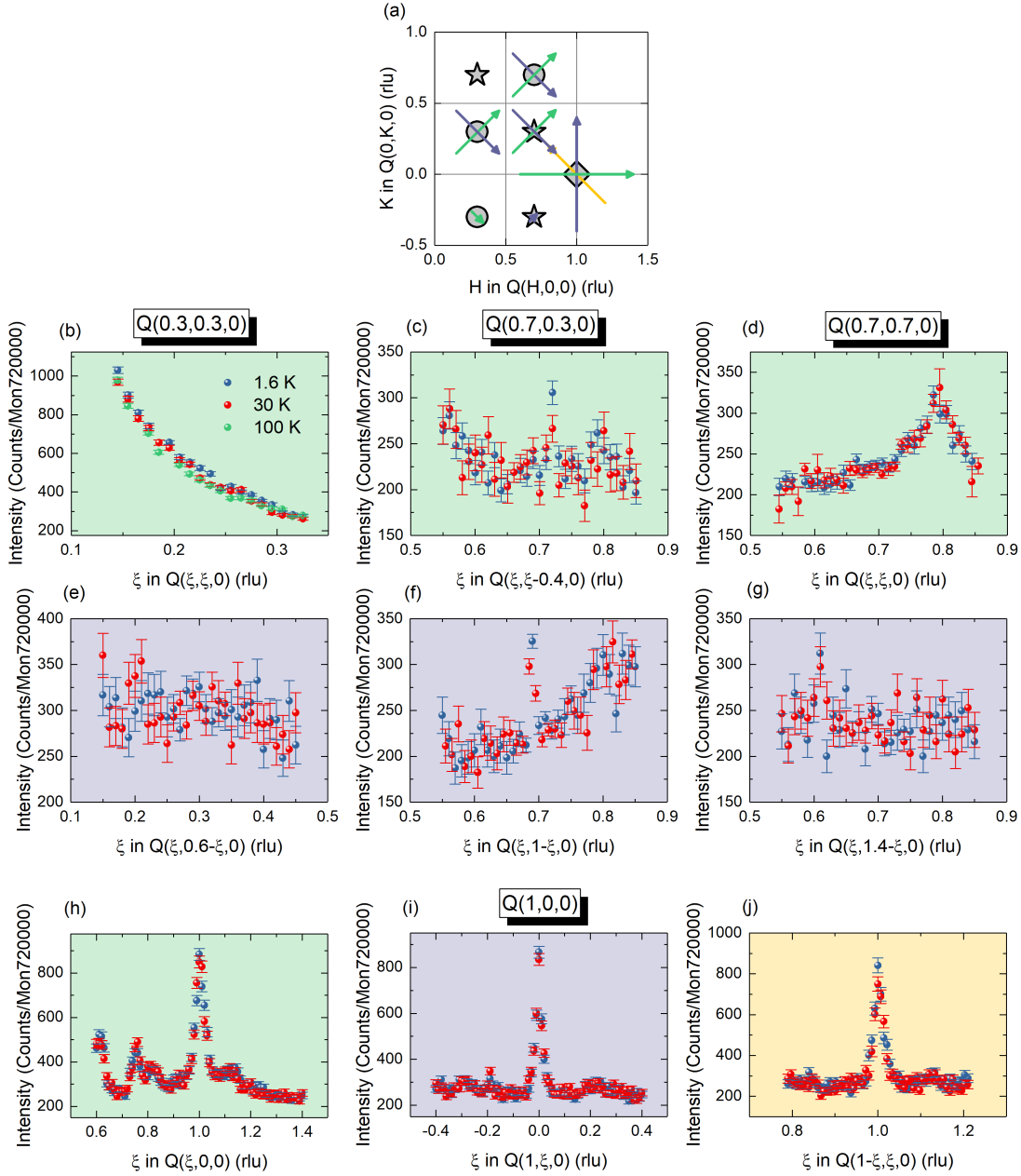
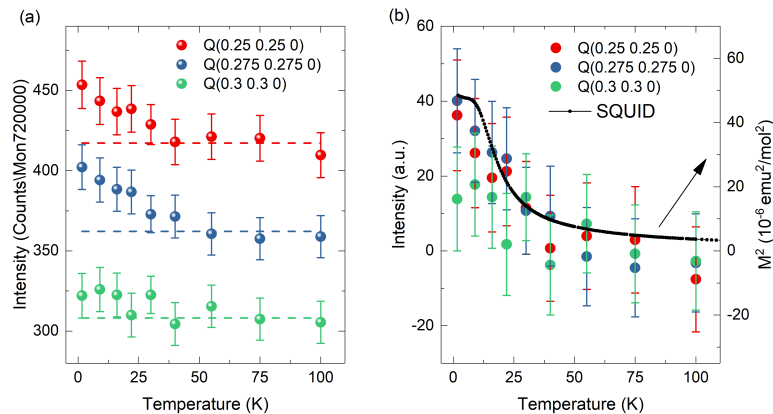


**Figure 5.2: Checking for magnetic order in  $\text{Sr}_2\text{Ru}_{0.95}\text{Co}_{0.05}\text{O}_4$  using elastic scans at various  $Q$  vectors of interests.** (a) The schematic representation of the scattering plane displays the incommensurate positions  $(0.3, 0.3, 0)$  (circles),  $(0.7, 0.3, 0)$  (stars), and equivalent positions, and the ferromagnetic commensurate position  $(1, 0, 0)$  (diamond). The arrows indicate the different scan directions: longitudinal in respect to the scattering vector (green), transversal (purple), and diagonal (yellow). (b)-(g) The longitudinal and transversal scans for different temperatures show no elastic magnetic signal appearing at low temperature in the vicinity of the incommensurate positions. (h)-(j) There is also no elastic magnetic signal appearing in the vicinity of the ferromagnetic position  $(1, 0, 0)$ .

indicate an existing static ferromagnetic order. In neutron scattering experiments with these samples ferromagnetic order would result in changes in the scattering in the vicinity of  $Q_{\text{FM}} = (1, 0, 0)$ . Therefore constant energy scans with  $E = 0$  meV in the vicinity of the incommensurate position (and equivalent) and the ferromagnetic

position are performed in various direction for both samples. In Figure 5.2 the data are shown for the 5% doped sample where, according to the magnetization data, the magnetic order should be easier to measure than for the 1.5% doped sample since the higher magnetic moment produces higher magnetic scattering intensities. The schematic in Figure 5.2(a) represents the different elastic scans over the points of interest in different directions. The directions are color coded where green represents longitudinal, purple represents transversal and yellow represents diagonal scan directions. This color code is also applied to the background of the panels in the figure. To identify any change of scattering when going into the ordered state the same scans were taken at 1.6 K and 30 K. The panels (b)-(g) in Figure 5.2 compare the elastic scans around the incommensurate positions (0.3, 0.3.0), (0.7, 0.3.0), and (0.7, 0.7.0) for both temperatures. There is no consistent peak noticeable in both scan directions and especially there is no clear difference visible at any scattering vector between the two temperatures. At the incommensurate positions there is no sign of enhanced scattering at low temperatures which would indicate a spin-density-wave order similar to that in Ti or Ca doped Sr<sub>2</sub>RuO<sub>4</sub> [6]. All features in the scans like the single enhanced counts in Figure 5.2(c) or the broad peak in (d) are not temperature dependent and therefore either spurious or instrumental background effects. The elastic scans around the ferromagnetic position (1, 0, 0) in Figure 5.2(h)-(j) show a pronounced peak at (1, 0, 0). Since the nuclear scattering at this position is forbidden the origin of scattering at this point stems most likely from multiple scattering. In addition there are numerous smaller peaks visible, depending on the scan direction, but mostly visible in the longitudinal scan direction in Figure 5.2(h). They can be assigned to smaller crystallites with slightly different orientation indicating that the sample is not fully single crystalline. Large crystals of ruthenates grown with the floating zone method can have a more polycrystalline skin which forms due to overflowing melt during the growth. This skin is hard to remove and its volume amounts, especially in large samples, only to a small percentage of the bulk volume for which reason these samples are still suitable for neutron scattering studies. Nevertheless the smaller crystallites produce elastic signals different to the main bulk crystal orientation which was determined by nuclear Bragg peaks such as (1,1,0). This Bragg peak produces a scattering intensity of  $\approx 1.5$  Million counts for the same monitor used in Figure 5.2 which puts the 800 counts of the biggest elastic signal at (1,0,0) into perspective. For this investigation the measurable contaminations are not affecting the analysis since any scattering contribution due to magnetic ordering can be easily identified by the comparison of different temperature data. As for the incommensurate position, the data around the ferromagnetic position do not indicate any temperature dependent scattering intensity at  $\mathbf{Q}_{\text{FM}} = (1, 0, 0)$  or at any of the other peaks confirming their nuclear nature. Similar results are achieved for the 1.5% doped sample where there is no temperature dependent scattering intensity measurable at the points of interest and in their vicinity. There is no indication for any static long-range magnetic order.

Looking closely again to Figure 5.2(b) there seems to be a small enhancement of scattering at low temperatures between (0.2, 0.2, 0) and (0.3, 0.3, 0). This temperature dependent scattering is added on top of the higher background scattering which increases for smaller  $Q$  since the instrument approaches the direct beam. This hinders the analysis. Therefore the scattering intensities at three different scattering vectors in this area are counted while heating up. The results are presented in



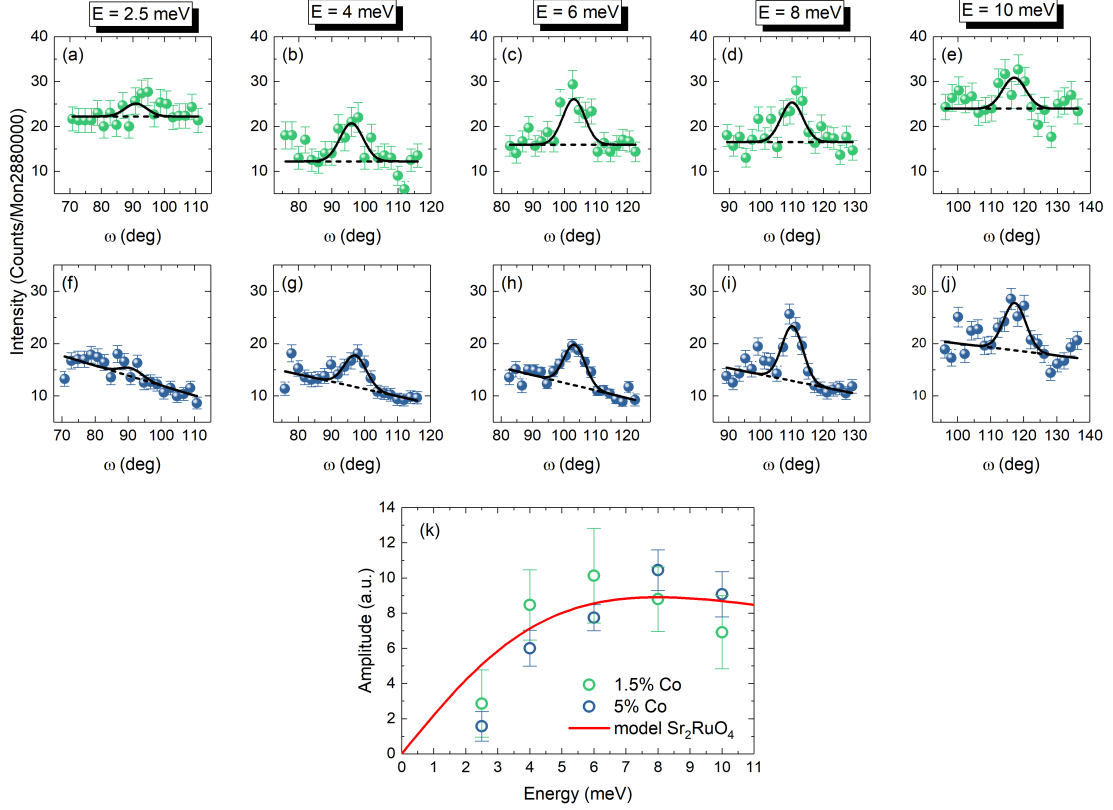
**Figure 5.3: Temperature dependence of elastic scattering in the low  $Q$  regime in  $\text{Sr}_2\text{Ru}_{0.95}\text{Co}_{0.05}\text{O}_4$ .** (a) Single points at different low  $Q$  vectors in the vicinity of the incommensurate position  $\mathbf{Q}_{\text{IC}} = (0.3, 0.3, 0)$  are counted while heating the sample. A constant background (dashed lines) is fitted using the four highest temperature points. (b) The temperature dependent scattering is extracted by individually subtracting the background for each  $\mathbf{Q}$  and compared to the squared magnetization measured with SQUID. The y axis range of the neutron data is chosen to give the best overlap with the magnetization data.

Figure 5.3. Panel (a) displays the temperature dependent single counts at the three distinct scattering vectors <sup>2</sup>. A constant background was fitted to each temperature dependence to extract the pure temperature dependent and therefore magnetic scattering intensity. The magnetic intensity is displayed in panel (b) of Figure 5.3 and compared with the temperature dependent squared magnetization for the 5% doped sample. The magnetic intensity increases with decreasing absolute value of the scattering vector. The temperature dependence resembles strongly that of the magnetization measured with SQUID which indicates that both the bulk magnetization and the neutron scattering intensity share the same origin.

Since there is no indication of an elastic incommensurate signal at the nesting vector  $\mathbf{Q}_{\text{IC}} = (0.3, 0.3, 0)$  and equivalent positions the Co doping does not stabilize the antiferromagnetic fluctuations in  $\text{Sr}_2\text{RuO}_4$ . Nevertheless the Co doping could influence the fluctuations which is investigated for the two different Co contents. Figure 5.4(a)-(e) and (f)-(j) displays rocking scans for increasing energy at  $\mathbf{Q}_{\text{IC}} = (0.7, 0.3, 0)$  for the 1.5% and 5% Co doped sample respectively. The scans are fitted with a Gaussian and the energy dependence of the fitted amplitudes is compared in panel (k) for Co contents with the single relaxor susceptibility model with a characteristic energy of 8 meV for  $\text{Sr}_2\text{RuO}_4$  [46, 116] <sup>3</sup>. Inside the error margins there is no noticeable difference between the different Co contents. They both follow the susceptibility model of  $\text{Sr}_2\text{RuO}_4$  except with a slight reduction at lower energies which can also be attributed to the low energy resolution of the thermal triple-axis spectrometer.

<sup>2</sup>The data are not shifted artificially. The vertical offset stems from the already mentioned background increase for smaller  $Q$ .

<sup>3</sup>The amplitudes are made comparable by extracting a scaling factor from phonon measurements at  $\mathbf{Q}_{\text{ph}} = (2, \xi, 0)$  for both samples ( $\text{Amplitude}(1.5\%) = \text{Amplitude}(5\%) * 0.873$ ).



**Figure 5.4: Energy dependence of incommensurate signal at  $Q_{\text{IC}} = (0.7, 0.3, 0)$  in  $\text{Sr}_2\text{Ru}_{0.985}\text{Co}_{0.015}\text{O}_4$  and  $\text{Sr}_2\text{Ru}_{0.95}\text{Co}_{0.05}\text{O}_4$  at 1.6 K.** The energy dependence of the incommensurate signal for different Co doped samples is measured using rocking ( $\omega$ ) scans for different energies at  $Q = (0.7, 0.3, 0)$  at 1.6 K. Here the top row ((a)-(e), green) displays the data for  $\text{Sr}_2\text{Ru}_{0.985}\text{Co}_{0.015}\text{O}_4$  while the middle row ((f)-(j), blue) displays the data for  $\text{Sr}_2\text{Ru}_{0.95}\text{Co}_{0.05}\text{O}_4$ . The data are fitted using a Gaussian in combination with a constant or a sloped background. (k) The energy dependence of the fitted signal amplitudes is shown for both Co contents and compared to the single relaxor susceptibility model with a characteristic energy of  $\Gamma = 8$  meV for  $\text{Sr}_2\text{RuO}_4$  [46, 116].

### 5.3 Discussion

The successful growth of large crystals of the  $\text{Sr}_2\text{Ru}_{1-y}\text{Co}_y\text{O}_4$  series enables a thorough investigation of the magnetic order appearing in these materials. The characterization of these crystals ensures the sample quality and confirms already reported characteristics concerning the electronic and magnetic bulk properties [59]. The results of the magnetization measurements imply a short-range ferromagnetic order appearing when introducing Co into the parent compound  $\text{Sr}_2\text{RuO}_4$ . This manifests in non-linear hysteretic behavior of the field dependent magnetization and the splitting of zero-field cooled and field cooled histories of the temperature dependent magnetization. These fingerprints of ferromagnetic order become more pronounced with increasing Co content as the coercitive fields and the point of irreversibility  $T_{\text{ir}}$  increase. An issue to resolve is the question whether the ferromagnetic magnetization stems from the stabilization of ferromagnetic fluctuations inherent in the parent compound  $\text{Sr}_2\text{RuO}_4$  [48] or from the forming of magnetic Co clusters in the crystal dominate the bulk magnetization. In the scope of the sample characterization single crystal X-ray diffraction enables a quantitative determination of the Co amount incorporated into the crystal structure. As a result the structural refinements of the different samples with nominally different Co content indicate an incomplete incorporation of Co at the Ru positions in the lattice since the refined Co ratio is always below the nominal value. Especially the case the nominal 10% doped sample, where the refined Co content with  $\approx 1\%$  is below the value of the 5% doped sample while the ferromagnetic order appearing in the bulk magnetization is enhanced, points to the scenario of magnetic Co clusters which form from the not in the lattice incorporated Co. This of course assumes that the evaporation of Ru and Co during the crystal growth does not account for the complete difference between nominal and incorporated Co content.

A way to investigate the nature of magnetic order is provided by neutron scattering experiments. We conducted various scans at points of interest, i.e. the nesting vector  $\mathbf{Q}_{\text{IC}} = (0.3, 0.3, 0)$  and the ferromagnetic zone center  $\mathbf{Q}_{\text{FM}} = (1, 0, 0)$ , for low and high temperatures which yield no evidence for any long-range magnetic order. Neither a spin-density wave at the incommensurate position as a stabilization of the antiferromagnetic fluctuations in  $\text{Sr}_2\text{RuO}_4$  nor a clear magnetic signal at  $\mathbf{Q}_{\text{FM}}$  indicating the stabilization of ferromagnetic fluctuations into long-range order is not measurable. Nevertheless magnetic scattering intensity can be extracted in the small  $Q$  regime. This intensity does not seem to be localized in  $Q$  space but rather increases with decreasing  $Q$  which can be attributed to the magnetic form factor. Furthermore its temperature dependence is qualitatively comparable with the bulk magnetization which links the ferromagnetic order in these Co doped compounds to a in real space rather localized source of magnetization. This supports the scenario of short-range ferromagnetic order stemming from magnetic Co clusters. In the case of Co clusters the low  $Q$  magnetic signal is the only with neutron scattering measurable feature of magnetic order while for long-range magnetic order the low  $Q$  signal appears in combination with magnetic scattering at distinct points in the Brillouin zone like  $(1,0,0)$ . There is a report of a new commensurate order with wave vector  $\mathbf{q}_{\text{c}} = (0.25, 0.25, 0)$  in Fe doped  $\text{Sr}_2\text{RuO}_4$  [133] which could explain the low- $Q$  magnetic signal. In principal it cannot be excluded that the measured magnetic scattering is commensurate and the magnetic form factor and the small

sample volume do not allow the measurement of magnetic scattering at equivalent points in  $\mathbf{Q}$  space with this experimental setup. There is definitely no indication of magnetic scattering at the equivalent points (0.75,0.75,0) and (0.75,0.25,0) which were covered by the elastic scans.

Additionally the antiferromagnetic fluctuations do still appear in the Co doped samples and their energy dependence is describable to the single relaxor behavior with the same characteristic energy as in Sr<sub>2</sub>RuO<sub>4</sub>. This indicates further that the Co doping does not change the magnetic characteristics of the parent compound and the fingerprint of ferromagnetic order appearing in the bulk magnetization stems from magnetic inhomogeneities, e.g. Co clusters.

## 5.4 Methods

### Material Information

A series of  $\text{Sr}_2\text{Ru}_{1-y}\text{Co}_y\text{O}_4$  crystals with different amounts of Co doping were successfully grown by N. Baldauf and A. A. Nugroho in our institute. The following material information are based on the characterization of these crystals conducted by N. Baldauf in the scope of his bachelor thesis [130] and by the author himself. Samples with 1.5%, 5% and 10% Co are characterized by powder X-ray diffraction, single crystal X-ray diffraction, resistivity, and magnetization measurements. An example of the characterization data for the 5% Co doped sample is given in Figure 5.6.  $\text{Sr}_2\text{Ru}_{1-y}\text{Co}_y\text{O}_4$  crystallizes in a tetragonal lattice (space group  $I4/mmm$ ) with similar lattice parameters as the parent compound  $\text{Sr}_2\text{RuO}_4$ . The Co doping increases the  $a/c$  ratio insignificantly (0.6 % with 10% Co doping [130]). The refinement of single crystal X-ray diffraction data with Jana2006 [132] confirms the small structural changes the Co doping introduces to the structure of the parent compound (see Table 5.1). Different structure models with and without Co are tested and used to quantitatively determine the amount of Co incorporated into the structure. The refinements of all crystals yield improved R values when Co is taken into account.

The temperature dependence of the resistivity indicates metallic behavior with higher out-of-plane resistivity than in-plane resistivity which is quantitatively comparable to the parent compound (see Figure 5.6(b)). The quadratic behavior at low temperatures confirms that the Fermi liquid ground state of the undoped compound survives in the Co doped crystals. The doping introduces higher disorder which is evident in the strong reduction of the residual resistivity ratio (RRR) from 245 in  $\text{Sr}_2\text{RuO}_4$  [131] to 3.7 in the 5% Co doped compound for the in-plane direction.

The temperature and field dependent behavior of the magnetization in Co doped compounds differs from the magnetization of the parent compound. The temperature dependence in Figure 5.6(c) exhibits an increase of magnetic moment at low temperatures with an irreversibility between zero-field cooled (zfc) and field cooled (fc) histories appearing at  $T_{\text{ir}} = 10$  K. Notably this irreversibility appears for magnetic fields parallel to  $c$  whereas for magnetic fields parallel to  $ab$  the separation between the two histories is more subtle and  $T_{\text{ir}}$  is shifted to very low temperatures. This Ising anisotropy in the susceptibility is consistent with the measurements in Mn and Ti doped samples [59, 129]. The field dependent magnetization shows a nonlinear behavior for temperatures below  $T_{\text{ir}}$  with the opening of a hysteresis (see Figure 5.6(d) and (e)). This implies that the Co doping results in static ferromagnetic order. The missing step increase in the magnetization at low temperatures which is expected for long-range ferromagnetic order and the appearing splitting of zfc and fc data indicates short-range order. The features of short-range ferromag-



**Figure 5.5: Mounted crystal of  $\text{Sr}_2\text{Ru}_{0.95}\text{Co}_{0.05}\text{O}_4$ .** A big single crystal of the 5% Co doped compound is mounted on an aluminium sample holder for neutron scattering experiments. A LiF shield is used to decrease background by avoiding scattering stemming from aluminium.

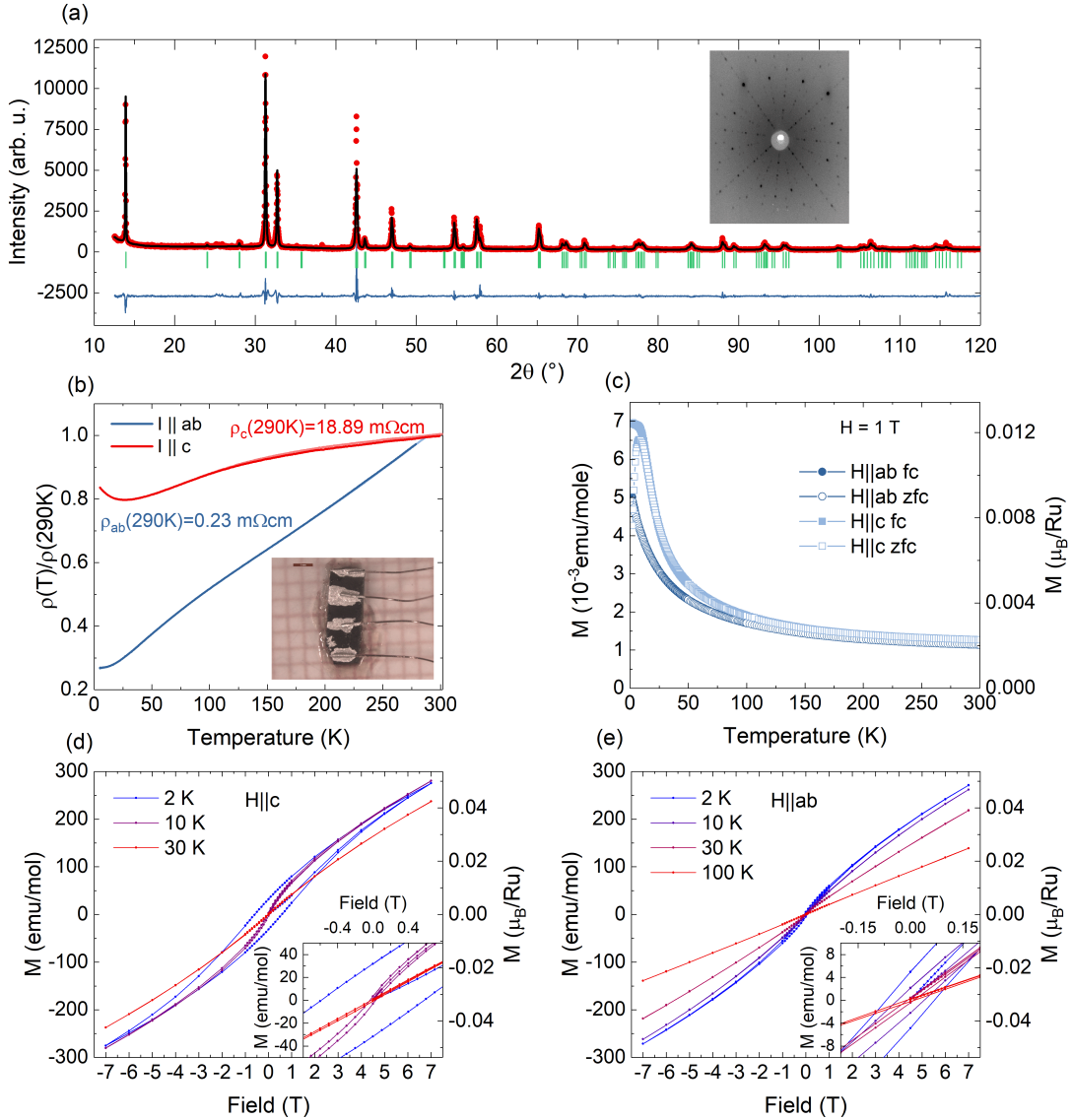


**Figure 5.6: Characterization measurements of Sr<sub>2</sub>Ru<sub>0.95</sub>Co<sub>0.05</sub>O<sub>4</sub>.** (a) The powder XRD data are refined using the Rietveld method to ensure phase purity and determine the lattice parameters. The inset shows a Laue picture visualizing the single crystal quality. (b) The temperature dependent in-plane ( $I \parallel ab$ ) and out-of-plane ( $I \parallel c$ ) resistivity displays the two-dimensional character of this compound. The RRR value for the in-plane direction of 3.7 is highly reduced compared to the pure compound Sr<sub>2</sub>RuO<sub>4</sub> with a RRR of 245 [131] verifying the disorder introduced by Co. (c)-(e) The temperature and field dependent magnetization measurements exhibit an moment increase in addition to a hysteretic field dependence at low temperatures indicating magnetic order below 10 K. These markers of magnetic order are more pronounced in the  $c$  direction.

netic order are more pronounced when the magnetic field points out-of-plane ( $H \parallel c$ ).

### Neutron scattering

The neutron scattering experiments were conducted at triple-axis spectrometers at the Institut Laue-Langevin (ILL) in Grenoble, France and at Laboratoire Léon Brill-

louis in Saclay, France. All involved beam times including the instrument and the experimental setting are listed in Table 5.2. The triple-axis spectrometers are operated with pyrolytic graphite (PG) crystals as monochromator and analyzer with a fixed  $k_f$ . To clean the neutron signal of higher orders and decrease the background a cooled Be filter at the cold spectrometer 4F2 was installed. At the thermal instrument IN22 a graphite filter was used to suppress higher orders.

The sample is oriented in the  $[1, 0, 0]/[0, 1, 0]$  scattering plane for all scattering experiments.

**Table 5.1: Refinement results of room temperature scXRD of Sr<sub>2</sub>Ru<sub>1-y</sub>Co<sub>y</sub>O<sub>4</sub>.** For comparison the structural data of Sr<sub>2</sub>RuO<sub>4</sub> at 295 K are taken from [134]. The lattice parameters of Sr<sub>2</sub>Ru<sub>1-y</sub>Co<sub>y</sub>O<sub>4</sub> result from the orientation matrix of the refinement.

compound	Sr <sub>2</sub> RuO <sub>4</sub>	Sr <sub>2</sub> Ru <sub>0.985</sub> Co <sub>0.015</sub> O <sub>4</sub>	Sr <sub>2</sub> Ru <sub>0.95</sub> Co <sub>0.05</sub> O <sub>4</sub>	Sr <sub>2</sub> Ru <sub>0.9</sub> Co <sub>0.1</sub> O <sub>4</sub>
label	–	nb004	Ag5Co1	Ag10Co2
nominal y (%)	–	1.5	5	10
Space group	<i>I4/mmm</i>	<i>I4/mmm</i>	<i>I4/mmm</i>	<i>I4/mmm</i>
a,b (Å)	3.8694(4)	3.8762(4)	3.8724(2)	3.8729(3)
c (Å)	12.746(2)	12.7544(18)	12.7514(5)	12.7511(5)
R <sub>w</sub> (%)	1.68	2.06	1.84	2.15
refined y (%)	–	1.0(4)	3.2(4)	1.5(5)
R <sub>w</sub> <sup>pure</sup> (%)	–	2.07	2.03	2.19
Reflect. total (obs/all)	–	19213/25346	21670/25884	19904/25457
Reflect. unique (obs/all)	–	345/353	350/353	325/328
Ru				
x	0	0	0	0
y	0	0	0	0
z	0	0	0	0
U <sub>11</sub>	0.0029(3)	0.00288(7)	0.0016(5)	0.00296(7)
U <sub>22</sub>	0.0029(3)	0.00288(7)	0.00169(12)	0.00296(7)
U <sub>33</sub>	0.0066(5)	0.00431(7)	0.00089(10)	0.00370(8)
Co				
x	–	0	0	0
y	–	0	0	0
z	–	0	0	0
U <sub>11</sub>	–	0.00288(7)	0.0016(5)	0.00296(7)
U <sub>22</sub>	–	0.00288(7)	0.00169(12)	0.00296(7)
U <sub>33</sub>	–	0.00431(7)	0.00089(10)	0.00370(8)
Sr				
x	0	0	0	0
y	0	0	0	0
z	0.35320(7)	0.353193(15)	0.353188(14)	0.353168(16)
U <sub>11</sub>	0.0042(2)	0.00725(8)	0.0068(6)	0.00734(8)
U <sub>22</sub>	0.0042(2)	0.00725(8)	0.00634(14)	0.00734(8)
U <sub>33</sub>	0.0039(3)	0.00520(8)	0.00239(12)	0.00468(9)
O(1)				
x	0	0	0	0
y	0.5	0.5	0.5	0.5
z	0	0	0	0
U <sub>11</sub>	0.004(2)	0.0129(7)	0.0121(10)	0.0133(7)
U <sub>22</sub>	0.013(3)	0.0042(5)	0.0027(6)	0.0040(6)
U <sub>33</sub>	0.011(3)	0.0103(6)	0.0084(8)	0.0103(6)

O(2)				
x	0	0	0	0
y	0	0	0	0
z	0.1611(5)	0.16164(15)	0.16169(14)	0.16179(16)
U <sub>11</sub>	0.011(2)	0.0101(4)	0.009(5)	0.0100(4)
U <sub>22</sub>	0.011(2)	0.0101(4)	0.0077(10)	0.0100(4)
U <sub>33</sub>	0.007(3)	0.0049(4)	0.0024(7)	0.0044(4)

Table 5.2: Involved neutron beam times with the instrumental settings.

Beam Time	Facility	Instrument	$k_f$ ( $\text{\AA}^{-1}$ ) ( $E_i$ (meV))	Mono./Ana.	Filter	comment
02-2018	LLB	4F2	1.55	PG(002)/PG(002)	cooled Be + graphite	
06-2019	ILL	IN22	2.663	PG(002)/PG(002)	graphite	

# Experimental Methods

Since this thesis gives insights into the physics of ruthenates based on experimental evidence it is worth to explain how this evidence is gathered. Especially in the context of this thesis the experimental methods depict the complete journey of experimental work in condensed matter research: Beginning with the crystal growth of ruthenates, followed by the characterization of the crystals using different diffraction and transport methods, ending in complex neutron scattering studies at state-of-the-art research facilities. In this chapter an introduction in the respective experimental methods is given which were used to collect the data presented in this thesis. The explanations and descriptions are held brief but will go more into detail when applied in the data analysis. For more general and complete information it will be referred to the particular literature.

## 6.1 Crystal Growth of layered Ruthenates

All experimental condensed matter research starts with materials with interesting physical characteristics. To study the physics in this materials it is necessary to possess samples where the requirements to their quality, size and shape are depending on the experimental methods which are applied to study the material. In the case of neutron scattering and especially for inelastic neutron scattering big single crystals (Volume  $\gtrsim 1 \text{ cm}^3$ ) are needed to collect decent intensities of scattered neutrons. Also the crystal quality in terms of crystallinity and purity is of importance as it cannot only influence the physical effects but also determines the signal strength and experimental resolution in scattering experiments. A good example for the necessity of high-quality, big crystals is the study of superconductivity in  $\text{Sr}_2\text{RuO}_4$ . The transition temperature is highly sensitive to defects [135]. To study the magnetic fluctuations which are possibly involved in the superconducting pairing inelastic neutron scattering is best suited but requires big sample volumes. Therefore the samples which are now used for more than 25 years in research are grown by the floating-zone technique using a mirror furnace. This growth technique which is also used to grow silicon single crystals for the wafer fabrication in industrial scale enables the growth of single crystals with high purity and large volumes. During the growth the sample is floating in a controlled atmosphere and heated contactless by halogen lamps. The melting zone does therefore never come into contact with possible contamination sources like crucibles which ensures the high purity of the single crystals. However the growth of ruthenates using this method can be challenging since the  $\text{RuO}_2$  is evaporating at the melting temperature which has to be accounted for in the powder mixture by using a Ru excess. In the scope of this thesis single crystals of ruthenates of the Ruddlesden-Popper series were grown with the floating-zone technique inside a mirror furnace which then have been characterized and further studied by neutron scattering. The successful attempts yield single crystals of the following ruthenate systems:

- $\text{SrRuO}_3$
- $\text{Ca}_2\text{Ru}_{1-y}\text{Ti}_y\text{O}_4$  with  $y = 0, 0.01$
- (•  $\text{Sr}_2\text{Ru}_{1-y}\text{Co}_y\text{O}_4$  with  $y = 0.015, 0.05, 0.1$ )<sup>1</sup>

Details of the used parameters in the growth will be given in Table 6.1.

### 6.1.1 Powder Sintering

In the beginning of the growth the starting materials are weighted stoichiometrically while using a  $\text{RuO}_2$  excess to account for the increased evaporation during growth. In first sintering steps the powder mixture is heated multiple times for several hours in a muffle furnace with intermediated mixing in a ball mortar. After the powder is pressed into rod shape using a hydraulic press and then finally sintered in a tube furnace at temperatures below the melting point. This procedure ensures the homogeneous mixture of the materials as well as the reaction of the components into

---

<sup>1</sup>These cystals were grown in the scope of the bachelor thesis of N. Baldauf by himself and A. A. Nugroho. The characterization was done by the author.

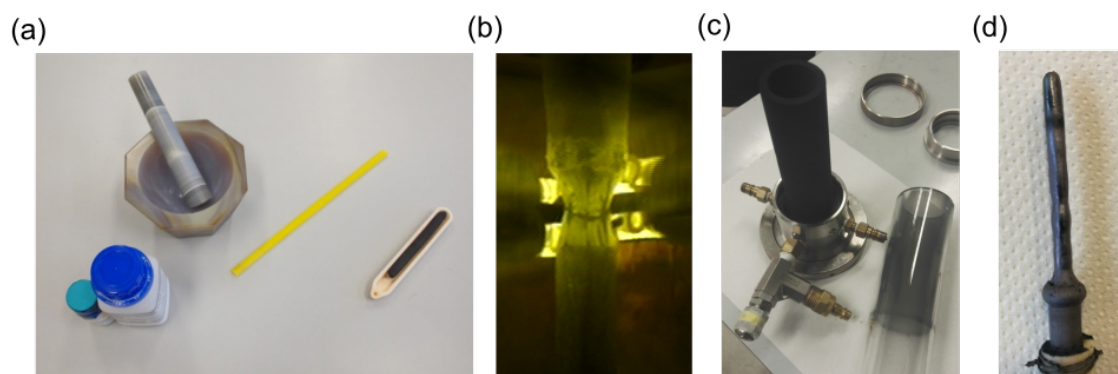


**Figure 6.1: Different stages of crystal growth process.** (a) The stoichiometric mixture of starting materials is sintered and pressed into a powder rod. (b) The melting zone is stabilized throughout the growth in the mirror furnace by adjusting the lamp power, growth speed and atmosphere. (c) The cold trap is preventing the  $\text{RuO}_2$  condensation on the quartz tube around the melting zone. (d) The resulting crystal can now be cut and characterized.

layered ruthenates. Since the  $\text{RuO}_2$  evaporation during the single crystal growth in the mirror furnace changes the material composition drastically the powder rod cannot purely be the desired material from which a single crystal should grow. Therefore the sintering steps before the crystal growth do not differ strongly between the different compounds.

### 6.1.2 Mirror Furnace

The optical floating-zone technique in crystal growth uses mirror furnaces to heat and melt the starting material. As the name of these furnaces suggest they create the high temperatures (up to  $2000\text{ }^\circ\text{C}$ ) by focusing the light of halogen lamps into a focal point in the center of the furnace. The powder feed rod is attached with a wire hook on the upper shaft which can be rotated and moved vertically. Same is valid for the lower shaft where the seed (either powder rod or single crystal) is attached inside an aluminum oxide tube. The surrounding atmosphere is concealed by a quartz tube and can be controlled by a vacuum pump and gas flow. Here an Ar/O mixture gas flow can be set with a pressure of up to 10 bar. This avoids the contamination during the crystal growth and also gives an additional parameter to adjust. A water cooled metal cylinder, i.e. cold trap, inside the quartz tube has to be used for the growth of ruthenates since there is an increased evaporation of  $\text{RuO}_2$ . To avoid the condensation of the black powder on the inside of the quartz tube which reduces the light transmission the cold trap gives a condensation source. At the beginning of the growth the lower end of the feed rod is melted and then connected with the seed rod. The goal is to establish a stable melting zone. The crystal growth proceeds by moving the upper and lower shaft with a constant vertical velocity downwards. By doing so the lower part of the melting zone cools down and crystallizes accordingly to the crystal orientation of the seed. If the seed is also a powdered material there will be a competition of crystallites with different orientations where one will eventually succeed. With a length of the feed rod of around 7 cm the length of a resulting single crystal ranges from 1 cm to up to 5 cm and therefore produces large samples which are suitable for neutron scattering experiments.

A detailed description of the optical floating-zone technique can be found in [136].

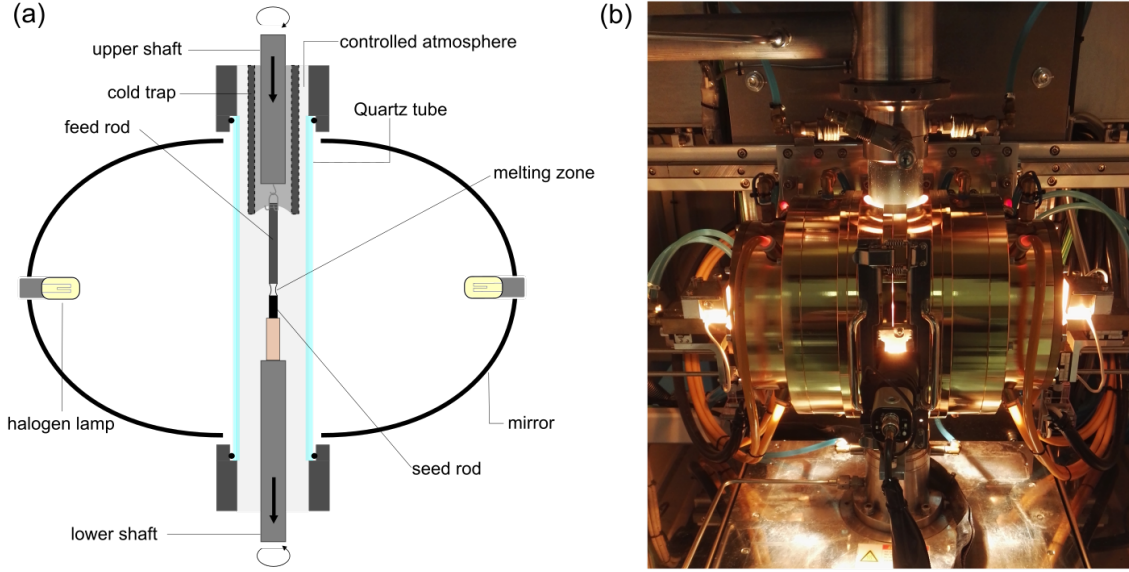


**Figure 6.2: Mirror furnace for crystal growth.** (a) In the schematic representation of the furnace all essential components are labeled. (b) The photograph shows the outside of the mirror furnace during the crystal growth.

**Table 6.1: Parameters of the crystal growth in the mirror furnace.** The parameters used in the crystal growth are given for the different sample groups presented in this thesis.

	$\text{SrRuO}_3$	$\text{Ca}_2\text{Ru}_{1-y}\text{Ti}_y\text{O}_4$	$\text{Sr}_2\text{Ru}_{1-y}\text{Co}_y\text{O}_4$
Feed rod preparation			
Ru excess	90%	35%	20%
sintering	$2 \times 12\text{h}@1000^\circ\text{C} + 3\text{h}@1370^\circ\text{C}$		
hydraulic pressure (pressing of rod)	$\frac{15\text{ t}\cdot\text{g}}{7.8\text{ cm}^2} \approx 188\text{ MPa}$		
Mirror furnace			
Gas mixture ( $\text{Ar}:\text{O}_2$ )	3:1.5	2.5:0.25	2.25:0.25
total flow (l/min)	4.5	2.75	2.5
pressure (bar)	9.3	9.3	3
growth rate (mm/h)	40	20	40
lamp power range (V)	93-95	79-80	71-73

### 6.1.3 Sample Characterization

For the determination of a successful crystal growth the samples have to be characterized in terms of purity, crystallinity and transport properties. The character-

ization is crucial for the iterative process of the crystal growth since it is basis for optimizing growth parameters. The samples which were grown in the scope of this thesis were characterized using the following methods.

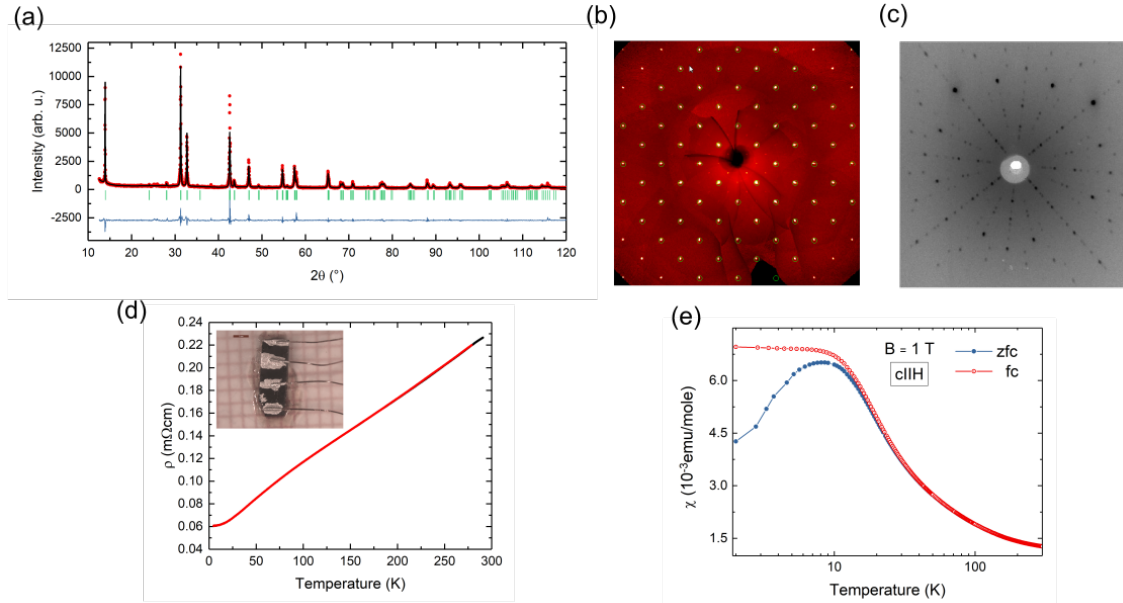


**Figure 6.3: Exemplary sample characterization with X-ray diffraction and transport measurements.** (a) The Rietveld refinement of the powder diffraction pattern gives insight in the phase purity of the sample. (b) Single crystal X-ray diffraction can be used to quantify dopants in the system. (c) The Laue method ensures the mono-domain state and the overall crystallinity of the sample. (d) The temperature dependence of the resistivity yields comparability with literature and gives the residual resistivity. (e) Temperature dependent magnetization reveals magnetic order phase transition temperatures which can be used to categorize sample quality.

### XRD - powder diffraction

X-ray diffraction is a powerful tool to gather structural information of the sample. Specific experimental setups can be used to focus on different parts of sample characteristics. The diffraction pattern of a powdered sample can be analyzed in terms of phase purity and gives precise measures of the lattice constants of the material. Therefore small portions along the grown crystalline sample are crushed and measured in a powder diffractometer. Knowing the structure of the desired material and common impurity phases the data are refined using the software **Fullprof** [98]. This software package offers the refinement of powder and single crystal diffraction patterns using the Rietveld method [137]. In the case of the crystal growth of Ruddlesden-Popper ruthenates the structure of the most common phases which can form during the growth are known from literature. These structures (space group, atomic positions, and lattice parameters) can be inserted into the software and the pattern analysis yields a phase distribution of the different possible ruthenates. In addition to this control of phase purity the refined lattice parameters can be checked against the literature values.

### XRD - single crystal diffraction

The diffraction pattern of single crystals is normally used to identify the structural

symmetry and the spacial distribution of atoms in the unit cell of a material. In the scope of the characterization of grown samples it can be used to quantize the amount of dopants in the sample which were introduced before the growth. Since the X-ray diffraction with single crystals can be more efficiently analyzed for atomic distributions this experimental method can identify the ratio of different atoms in the unit cell. A sufficient deviation between the form factors of the different atoms is crucial for the precision of the analysis. In the case of the grown ruthenate systems where Sr is substituted by Ca and Ru is replaced by Ti or Co the form factors are sufficiently different to give a quantitative result.

### **XRD - Laue diffraction**

Another diffraction method which uses single crystalline samples is the Laue method. For the characterization this method can be used to ensure the single crystallinity of a sample. As the Laue diffraction patterns encode the orientation of the probed crystal domain monodomain samples can be identified by probing several points in a cross section. If each measurement yields the same pattern, the crystal orientation is identical and the sample is a single crystal. The reflection spot shape itself gives a qualitative measure of the mosaic spread of the crystal (small relative deviation between microscopic crystallite orientations). Circular well defined reflections indicate a structural long-range order with good periodicity. This method is also used to orient and coalign the multi-crystal setups used for neutron scattering experiments.

### **Resistivity**

The low-temperature resistivity (residual resistivity) in metals is proportional to the defect density in the crystal and can therefore be used to quantify the crystallinity of the grown samples. Beside this the temperature dependence of the resistivity can indicate phase transitions where the transition temperatures give also a measure of sample quality and can be compared to literature values. The resistivity is measured by a four-point measurement on a dipstick which is cooled in a He bath.

### **SQUID**

The field and temperature dependence of the magnetization quantifies parameters like magnetic order transition temperatures, saturation magnetizations and more. These parameters give as well a measure for sample quality and enable the comparison of the grown samples with samples reported in the literature. The magnetization is measured using a SQUID (superconducting quantum interference device).

The crystal growth is a iterative procedure where the sample after the growth is first checked for sample purity, then single crystallinity and finally the transport properties are determined to compare with former successful growths and literature. If the sample does not fulfill the requirements at any step the results of the characterization measurements are used to optimize the growth parameters in the next growth cycle. In the end the optimization yields a sample which can be studied further by neutron scattering and other methods.

## 6.2 Neutron Scattering

Shull and Smart observed antiferromagnetism for the first time in 1949 by neutron diffraction [138], shortly after the discovery of the neutron by Chadwick in 1932 [139]. The magnetic moment of the neutron makes the magnetic scattering possible and is the perfect probe for scattering experiments. The scattering technique was extended by Brockhouse and Stewart in 1955 where they also managed to observe inelastic scattering processes of excitations [140]. Since then the flux of neutron sources around the world has increased significantly while on the same time the experimental techniques were perfected. Up to now neutron scattering is a powerful, versatile and well established technique to study physical properties in natural sciences.

Here a short introduction of the theoretical concepts behind neutron scattering is given. The focus will lay on the most important aspects which are needed in the scope of this thesis. For more detailed description the reader may be referred to the numerous textbooks which give extensive insight into the theory of neutron scattering and its experimental consequences [141–144].

### 6.2.1 Basics

The neutron is not only one of the building blocks of atoms; this subatomic particle by itself has interesting properties which makes it the perfect probe. The neutron has a comparable mass to the proton however with vanishing electronic charge in average. Which makes it interesting in terms of interaction, the neutron as a spin  $1/2$  particle posses a magnetic moment  $\boldsymbol{\mu}_n = \frac{g_n \mu_N}{\hbar} \mathbf{s}_n = \gamma_n \mathbf{s}_n$  with  $\mathbf{s}_n = \frac{\hbar}{2} \hat{\boldsymbol{\sigma}}_n$ <sup>2</sup>. The g-factor of the neutron  $g_n = -3.826$  results in a negative gyromagnetic ratio which makes the magnetic moment of the neutron point in the opposite direction as its spin. The energy of propagating neutrons as given by  $E = \frac{1}{2}mv^2$  can be expressed in different units where the most common are: Energy in meV, Temperature in  $T = E/k_B$ , wavelength  $\lambda = h/(mv)$  in Å, and wave vector  $|\mathbf{k}| = 2\pi/\lambda$  in Å<sup>-1</sup>.

The neutron interacts with both the nuclei and the unpaired electrons which is why both interactions have to be considered in the description of neutron scattering. The cross section  $\sigma_{\text{total}} = I_s/I_{\text{total}}$  gives the ratio between the number of scattered neutrons to the number of incoming neutrons, i.e. neutron flux. Experimentally only a part of the scattering cross section can be covered by the detector. This leads to the differential cross section  $\frac{\partial^2 \sigma}{\partial \Omega \partial E}$ , within a the solid angle  $d\Omega$  and the energy interval  $[E, E + dE]$ . In the scattering process the system undergoes a transition from initial state  $i$  to final state  $f$  where the scattering system changes from state  $\lambda_i$  to  $\lambda_f$  while the neutron changes its wave vector and spin state from  $(\mathbf{k}_i, \sigma_i)$  to  $(\mathbf{k}_f, \sigma_f)$ . For such a transition the differential cross section is given by Fermi's Golden Rule:

---

<sup>2</sup>g-factor  $g_n$ , nuclear magneton  $\mu_N$ , gyromagnetic ratio  $\gamma_n = \frac{g_n \mu_N}{\hbar}$ , and the spin operator  $\hat{\boldsymbol{\sigma}}_n$  with the Pauli-matrices as components

$$\begin{aligned}
& \left( \frac{\partial^2 \sigma}{\partial \Omega \partial E} \right)_{\mathbf{k}_i \rightarrow \mathbf{k}_f} \\
&= \left( \frac{m}{2\pi \hbar^2} \right)^2 \frac{k_f}{k_i} \sum_{\lambda_i \sigma_i} p_{\lambda_i} p_{\sigma_i} \sum_{\lambda_f \sigma_f} \left| \langle \mathbf{k}_f \lambda_f \sigma_f | \hat{V} | \mathbf{k}_i \lambda_i \sigma_i \rangle \right|^2 \delta(E + E_{\lambda_i} - E_{\lambda_f}) \quad (6.1)
\end{aligned}$$

Here  $p_j$  gives the probability to find the scattering system or the neutron in the initial state while  $\hat{V}$  denotes the interaction potential. Since this formula describes the most general case of a scattering process it can be called the master formula of neutron scattering and is basis for all neutron experiments.

Since different interaction potentials contribute to the scattering of a neutron the scattering can be categorized accordingly in nuclear and magnetic scattering. For each scattering contribution the interaction potentials depend on different forces. The neutron interacts with the nucleus via the strong-force interaction and the scattering efficiency is determined by the scattering length  $b^{scat}$  which is not correlated systematically with the atomic number. This makes neutron scattering sensitive to scattering from light atoms and also different isotopes can be distinguished. Since the thermal neutron wavelength is one order of magnitude higher than the nucleus dimension the interaction potential can be approximated to a delta function of the atomic positions  $\mathbf{R}_l$  of  $N$  atoms:

$$\hat{V}_N(\mathbf{r}) = \frac{2\pi \hbar^2}{m} \sum_l b_l^{scat} \delta(\mathbf{r} - \mathbf{R}_l) \quad (6.2)$$

In general the scattering length  $b^{scat}$  contains a contribution from the interaction with nuclear spins which are, in the general case, randomly oriented and only create incoherent scattering. Also different isotopes in a system can create such a incoherent contribution. In the following we will focus only on the scattering contributions which show interference effects, i.e. coherent scattering.

The magnetic interaction is governed by the dipole-dipole interaction between the magnetic moment of the neutron and the unpaired electrons of the scattering system. The corresponding interaction potential of the neutron in spin state  $\hat{\boldsymbol{\sigma}}_n$  and the electron with spin  $\mathbf{s}_e$  and momentum  $\mathbf{p}$  can be described with:

$$\hat{V}_M(\mathbf{r}) = -\boldsymbol{\mu}_n \cdot \mathbf{B} = \gamma_n \mu_B \mu_0 \hat{\boldsymbol{\sigma}}_n \left[ \nabla \times \left( \frac{\mathbf{s}_e \times \mathbf{R}}{R^3} \right) + \frac{\mathbf{p} \times \mathbf{R}}{R^3} \right] \quad (6.3)$$

with the Bohr magneton  $\mu_B$ , the gyromagnetic ratio  $\gamma_n$ , and the vacuum permeability  $\mu_0$ . The first term describes the interaction of the neutron with the electron spin while the second part characterizes the interaction with the orbital momentum.

Before these interaction potentials can be evaluated in the master formula (Equation 6.1) they have to be transformed in the momentum space to account for the neutron state described by its wave vector. With this transformation the interactions can be limited to the unit cell and become dependent on the scattering vector  $\mathbf{Q} = \mathbf{k}_i - \mathbf{k}_f = \boldsymbol{\tau} + \mathbf{q}$  with the reciprocal lattice vector  $\boldsymbol{\tau}$ . The Fourier transformation of the potentials yield the structure factors  $F_N(\mathbf{Q})$  (Equation 6.4) and  $\mathbf{F}_{M_\perp}(\mathbf{Q})$  (Equation 6.5).

$$F_N(\mathbf{Q}) = \sum_j b_j^{scat} e^{i\mathbf{Q}r_j} := \hat{N}(\mathbf{Q}) \quad (6.4)$$

$$F_{M_\perp}(\mathbf{Q}) = \sum_j f_j(Q) \frac{1}{2} g\langle S_j \rangle \left[ \tilde{\mathbf{Q}} \times (\tilde{\mathbf{S}}_j \times \tilde{\mathbf{Q}}) \right] e^{i\mathbf{Q}r_j} \hat{\sigma}_j := \hat{M}_\perp(\mathbf{Q}) \cdot \hat{\sigma} \quad (6.5)$$

$f_j(Q)$  is the magnetic form factor which characterizes the magnetic moment distribution in an atom, similar to the atomic form factor. This factor depends on  $Q$  as it decreases with increasing length of the scattering vector. This is in contrast to the nuclear scattering length which is  $Q$  independent. The term  $\tilde{\mathbf{Q}} \times (\tilde{\mathbf{S}}_j \times \tilde{\mathbf{Q}})$  in the magnetic structure factor accounts for the fact that only parts of the magnetic moment perpendicular to the scattering vector  $\mathbf{Q}$  contribute to the scattering.

The elastic scattering from a material with nuclear and magnetic interaction can be described by evaluation of the master formula with the combined interaction potentials yielding the so called Blume-Maleev equation (Equation 6.6)[144]. The explicit derivation of this equation will be described in detail in Section 6.2.2.

$$\frac{d\sigma}{d\Omega} \propto \underbrace{\hat{N}^* \hat{N}}_{\text{nuclear}} + \underbrace{\hat{M}_\perp^\dagger \hat{M}_\perp}_{\text{magnetic}} + \underbrace{\hat{N}^* (\hat{M}_\perp \cdot \mathbf{P}) + (\hat{M}_\perp^\dagger \cdot \mathbf{P}) \hat{N}}_{\text{interference}} + \underbrace{i\mathbf{P} (\hat{M}_\perp^\dagger \times \hat{M}_\perp)}_{\text{chiral}} \quad (6.6)$$

With this equation different scattering contributions can be categorized in nuclear, magnetic, interference, and chiral terms. For an unpolarized neutron beam where the orientation of the neutron spins is randomly distributed the two last contributions cancel out and the scattering intensity becomes:

$$I \propto |F_N|^2 + |F_{M_\perp}|^2 \quad (6.7)$$

The dependency of the scattering cross section on the neutron polarization  $\mathbf{P}$  opens up the possibility to access more information about the scattering system using polarization analysis. The theoretical description of this technique will be discussed in the following section.

## 6.2.2 Polarization Analysis

In the following the theoretical description of the scattering cross section in dependence of the neutron polarization is given based on the density-matrix formalism. The formulas are based on theoretical work of Blume [145], Maleev [146], and Sáenz [147] and summarized in the book of Marshall and Lovesey [141]. The experimental implication of the theory, firstly applied by Moon, Riste, and Koehler [148], will also be discussed. In the end we will apply the theory to describe the inelastic magnetic neutron scattering in a Heisenberg ferromagnet and derive a criterion for the interpretation of experimental results.

The polarization of the neutron beam can be defined as twice the average value of the spins of neutrons in the beam:

$$\mathbf{P}_n = 2\langle \hat{\mathbf{s}}_n \rangle = \langle \hat{\boldsymbol{\sigma}} \rangle \quad (6.8)$$

where the spin operator components  $\hat{\boldsymbol{\sigma}}^\alpha$  are the Pauli matrices.

A partially polarized beam where ( $0 < |\mathbf{P}| < 1$ ) cannot be quantum mechanically described because a wave function cannot be assigned to the spin state of the beam. Therefore the beam polarization can only be defined by a probability distribution which can be expressed by a density matrix operator  $\rho$ :

$$\hat{\rho} = \frac{1}{2}(I + \mathbf{P} \cdot \hat{\boldsymbol{\sigma}}) \quad (0 \leq |\mathbf{P}| \leq 1) \quad (6.9)$$

This density matrix consists of the unity matrix  $I$  and the spin operator  $\hat{\boldsymbol{\sigma}}$ . Using this density matrix to describe the neutron spin state the spin part of the master formula (Equation 6.1) becomes

$$\sum_{\sigma_i \sigma_f} p_{\sigma_i} \langle \sigma_i | \hat{V}^\dagger | \sigma_f \rangle \langle \sigma_f | \hat{V} | \sigma_i \rangle = \text{Tr} \hat{\rho} \hat{V}^\dagger \hat{\boldsymbol{\sigma}} \hat{V}. \quad (6.10)$$

When examine the interaction potentials of nuclear and magnetic interactions a general form of the interaction potential  $\hat{V}$  can be derived:

$$\hat{V} = \hat{\beta} + \hat{\boldsymbol{\alpha}} \cdot \hat{\boldsymbol{\sigma}} \quad (6.11)$$

The general interaction potential is splitted into a part  $\hat{\beta}$  which is independent of the neutron spin and a spin dependent part  $\hat{\boldsymbol{\alpha}} \cdot \hat{\boldsymbol{\sigma}}$ . With this the master formula can be simplified to

$$\begin{aligned} & \left( \frac{\partial^2 \sigma}{\partial \Omega \partial E} \right)_{\mathbf{k}_i \rightarrow \mathbf{k}_f} \\ &= \left( \frac{m}{2\pi \hbar^2} \right)^2 \frac{k_f}{k_i} \sum_{\lambda_i \lambda_f} p_{\lambda_i} \text{Tr} \hat{\rho} \left| \langle \mathbf{k}_f \lambda_f | \hat{V} | \mathbf{k}_i \lambda_i \rangle \right|^2 \delta(E + E_{\lambda_i} - E_{\lambda_f}). \end{aligned} \quad (6.12)$$

The scattering cross section is therefore determined by the term  $\text{Tr} \hat{\rho} \hat{V}^\dagger \hat{V}$  with which also the final polarization  $\mathbf{P}_f$  can be calculated. Using the general interaction potential from Equation 6.11 these expressions become

$$\text{Tr} \hat{\rho} \hat{V}^\dagger \hat{V} = \hat{\boldsymbol{\alpha}}^\dagger \cdot \hat{\boldsymbol{\alpha}} + \hat{\beta}^\dagger \hat{\beta} + \hat{\beta}^\dagger (\hat{\boldsymbol{\alpha}} \cdot \mathbf{P}) + (\hat{\boldsymbol{\alpha}}^\dagger \cdot \mathbf{P}) \hat{\beta} + i\mathbf{P} (\hat{\boldsymbol{\alpha}}^\dagger \times \hat{\boldsymbol{\alpha}}) \quad (6.13)$$

$$\begin{aligned} \mathbf{P}_f &\propto \text{Tr} \hat{\rho} \hat{V}^\dagger \hat{\boldsymbol{\sigma}} \hat{V} \\ &= \hat{\beta}^\dagger \hat{\boldsymbol{\alpha}} + \hat{\boldsymbol{\alpha}}^\dagger \hat{\beta} + \hat{\beta}^\dagger \hat{\beta} \mathbf{P} + \hat{\boldsymbol{\alpha}}^\dagger (\hat{\boldsymbol{\alpha}} \cdot \mathbf{P}) + (\hat{\boldsymbol{\alpha}}^\dagger \cdot \mathbf{P}) \hat{\boldsymbol{\alpha}} - \mathbf{P} (\hat{\boldsymbol{\alpha}}^\dagger \cdot \hat{\boldsymbol{\alpha}}) \\ &\quad - i\hat{\boldsymbol{\alpha}}^\dagger \times \hat{\boldsymbol{\alpha}} + i\hat{\beta}^\dagger (\hat{\boldsymbol{\alpha}} \times \mathbf{P}) + i(\mathbf{P} \times \hat{\boldsymbol{\alpha}}^\dagger) \hat{\beta} \end{aligned} \quad (6.14)$$

The first expression (Equation 6.13) determines in principal the scattering amplitude and choosing  $\hat{\beta} = \hat{N}$  and  $\hat{\alpha} = \hat{M}_\perp$  for the combination of nuclear and magnetic scattering yields the Blume-Maleev equation Equation 6.6. The final polarization  $\mathbf{P}_f$  and its relation to the initial polarization  $\mathbf{P}$  is given by the second expression (Equation 6.14). These expressions describe the scattering of polarized neutrons in the most general case and simplify depending on the specific case they are applied on.

For example a common application is the elastic polarized neutron scattering with a magnetic material where all the spins are aligned collinear, either parallel or antiparallel to a direction  $\tilde{\mathbf{S}}$ . Here equations (6.13) and (6.14) simplify considerably and it follows:

$$\frac{d\sigma}{d\Omega} \propto \left| \sum_j e^{i\mathbf{Q}r_j} \right|^2 \left\{ |F_N(\mathbf{Q})|^2 + \left[ 1 - (\tilde{\mathbf{Q}} \cdot \tilde{\mathbf{S}})^2 \right] |F_M(\mathbf{Q})|^2 + \tilde{\mathbf{S}} \cdot \mathbf{P}_\perp \operatorname{Re}\{F_N(\mathbf{Q})F_M^*(\mathbf{Q})\} \right\} \quad (6.15)$$

$$\mathbf{P}_f \frac{d\sigma}{d\Omega} \propto \left| \sum_j e^{i\mathbf{Q}r_j} \right|^2 \left\{ \mathbf{P} |F_N(\mathbf{Q})|^2 + \left\{ -\mathbf{P} \left[ 1 - (\tilde{\mathbf{Q}} \cdot \tilde{\mathbf{S}})^2 \right] + 2\tilde{\mathbf{S}} \cdot \mathbf{P}_\perp [\tilde{\mathbf{Q}} \times (\tilde{\mathbf{S}} \times \tilde{\mathbf{Q}})] \right\} |F_M(\mathbf{Q})|^2 + [\tilde{\mathbf{Q}} \times (\tilde{\mathbf{S}} \times \tilde{\mathbf{Q}})] \operatorname{Re}\{F_N(\mathbf{Q})F_M^*(\mathbf{Q})\} - \mathbf{P} \times [\tilde{\mathbf{Q}} \times (\tilde{\mathbf{S}} \times \tilde{\mathbf{Q}})] \operatorname{Im}\{F_N(\mathbf{Q})F_M^*(\mathbf{Q})\} \right\} \quad (6.16)$$

with  $\mathbf{P}_\perp = [\tilde{\mathbf{Q}} \times (\tilde{\mathbf{P}} \times \tilde{\mathbf{Q}})]$ .

Because of the collinearity of moments there is no chiral contribution. The purely nuclear and magnetic contributions (first and second row of Equation 6.15) are not polarization dependent. The vector relation between  $\tilde{\mathbf{Q}}$  and  $\tilde{\mathbf{S}}$  scaling the magnetic structure factor indicates the circumstance that neutrons only interact with the magnetic moment component perpendicular to  $\mathbf{Q}$ . The only polarization dependent part of the scattering intensity comes from the interference of nuclear and magnetic contribution. Analyzing the polarization of neutrons after the scattering event  $\mathbf{P}_f$  in Equation 6.16 one can derive central rules of the polarization analysis:

1. nuclear scattering does not change the neutron polarization  $\rightarrow$  non-spin-flip process
2. magnetic scattering does not change the neutron polarization when the magnetic moment is collinear to the neutron spin  $\rightarrow$  non-spin-flip process
3. magnetic scattering does change the sign of the neutron polarization when the magnetic moment is perpendicular to the neutron spin  $\rightarrow$  spin-flip process

Moon, Riste and Koehler applied the polarization analysis experimentally and derived a description tailored for neutron scattering experiments [148]. Instead of using the vector relation for the final neutron polarization (Equation 6.16) where  $\mathbf{P}_f$  is they are interested in the component along the initial polarization. The experimental setup allows only to measure the polarization components of initial and final polarization along the quantization axis  $Z$  which is given by the magnetic field at the sample. By using spin flippers it is possible to change the initial and final polarization direction along  $Z$  individually from parallel (+) to antiparallel (-). This gives access to for spin state combinations for which the interaction term in Equation 6.1 has to be evaluated. Moon *et al.* introduced therefore the atomic scattering amplitudes for the four possible spin state combinations:

$$U^{++} = b^{scat} - pS_{\perp,Z} \quad (6.17)$$

$$U^{--} = b^{scat} + pS_{\perp,Z} \quad (6.18)$$

$$U^{+-} = -p(S_{\perp,X} + iS_{\perp,Y}) \quad (6.19)$$

$$U^{-+} = -p(S_{\perp,X} - iS_{\perp,Y}) \quad (6.20)$$

$b^{scat}$  denotes the coherent nuclear scattering length and  $\mathbf{S}_{\perp}$  is the atomic spin component perpendicular to the scattering vector  $\mathbf{Q}$ . The magnetic amplitude  $p = (\gamma_n e^2 / 2mc^2) gSf(\mathbf{Q})$  contains the neutron moment in nuclear magnetons  $\gamma_n$ , the atomic moment in Bohr magnetons  $gS$  and the magnetic form factor  $f(\mathbf{Q})$ . The nuclear spin scattering contributions is neglected here since in the general case of randomly distributed nuclear spins the scattering is only incoherent. The indices  $X, Y$ , and  $Z$  refer to the coordinate system with the quantization axis  $Z$  given by the magnetic field at the sample.

The scattering amplitudes in Equation 6.20 illustrate again the general rules of polarization analysis stated before where nuclear scattering is only visible for non-spin-flip processes and spin-flip processes measure pure magnetic scattering when the neutron polarization is collinear with the scattering vector. The nuclear and magnetic scattering contributions can be therefore easily separated using polarization analysis.

A common experimental application is the longitudinal polarization analysis where the neutron polarization is set by a magnetic field at the sample which can point in three orthogonal directions in respect to the scattering vector. Therefore the coordinate system for the neutron polarization is defined as following:

- $x$  is parallel to  $\mathbf{Q}$
- $y$  is perpendicular to  $x$  and within the scattering plane
- $z$  is perpendicular to the scattering plane

Using this coordinate system the spin component perpendicular to the scattering vector which contributes to the magnetic scattering can be split into only two orthogonal components  $\mathbf{M}_{\perp} = (0, M_y, M_z)$ . The neutron polarization along either of this three axis determines the quantization axis  $Z$  in Equation 6.20 which enables the separation of different spin components. The different cross-section contributions resulting from the evaluation of  $|U^{\sigma_i \sigma_f}|^2$  are categorized in Table 6.2 where

$N$  denotes the nuclear scattering amplitude and  $\mathbf{M}$  the magnetic scattering vector. The indices refer to the neutron polarization coordinate system.

**Table 6.2: Scattering contributions to the different spin-flip channels.**

polarization direction	non-spin-flip (nSF: $\pm\pm$ )	spin-flip (SF: $\pm\mp$ )
$x$	$NN^*$	$\mathbf{M}_\perp \cdot \mathbf{M}_\perp^* \mp i(\mathbf{M}_\perp \times \mathbf{M}_\perp^*)_z$
$y$	$NN^* + M_y M_y^* \pm 2 \operatorname{Re}\{NM_y^*\}$	$M_z M_z^*$
$z$	$NN^* + M_z M_z^* \pm 2 \operatorname{Re}\{NM_z^*\}$	$M_y M_y^*$

An illustrative example for the polarization dependence of neutron scattering is the generation of polarized neutron beams with Heusler alloys. Here a magnetic field is applied perpendicular to the scattering plane which fully orients the magnetic moments in the crystals and determines the polarization direction of neutrons. Therefore according to the bottom line of Table 6.2 the elastic neutron scattering consists only of non-spin-flip scattering. For certain Bragg reflections where the nuclear as well as the magnetic structure factor is finite the cross-section becomes:

$$\left(\frac{d\sigma}{d\Omega}\right)^{\pm\pm} = |F_N(\mathbf{Q}) \pm F_M(\mathbf{Q})|^2 \quad (6.21)$$

When now additionally the nuclear and the magnetic structure factor are equal only neutrons with parallel polarization are scattered by the Heusler alloy crystals which creates a monochromatized and polarized neutron beam. The polarization performance is expressed by the so called flipping ratio (FR) which is connected to the total beam polarization  $P = |\mathbf{P}|$  by

$$P = \frac{I^- - I^+}{I^- + I^+} = \frac{FR - 1}{FR + 1} \quad (6.22)$$

The intensity ratio of neutrons with polarization parallel and antiparallel to the quantization axis defines the flipping ratio  $FR = I^-/I^+$  and can be experimentally determined by measuring the intensity ratio between spin-flip and non-spin-flip channel for e.g. a purely nuclear Bragg reflection.

### **Example: Polarization dependence of inelastic magnetic neutron scattering in a Heisenberg ferromagnet**

In the following the polarization dependence of neutron scattering will be derived for the special case of magnon scattering in a Heisenberg ferromagnet. Therefore the inelastic magnetic scattering contribution is considered and evaluated for the spin correlations following the Heisenberg model of ferromagnets. This example case is derived from [141, 148].

So far the scattering cross section was only determined by the evaluation of the interaction term in Equation 6.1 which lead to the proportionality described in Equation 6.6. Here only the elastic case is assumed where  $E_{\lambda_i} = E_{\lambda_f}$  and the sums over initial and final states do not change the result. The general case allows inelastic

scattering processes where the final state of the scattering system is different from the initial state and the time dependence of the interaction potentials have to be considered. While the evaluation of the interaction term for magnetic and nuclear interaction described above still hold true in the general case the different scattering cross section contributions in Equation 6.6 have to be calculated with correlation functions like:

$$\langle AB^* \rangle_\omega = \sum_\lambda p_\lambda \frac{1}{2\pi} \int_{-\infty}^{\infty} e^{-i\omega t} dt \sum_j e^{i\mathbf{Q}\cdot\mathbf{r}_j} A(\mathbf{0}, 0) B^*(\mathbf{r}_j, t) \quad (6.23)$$

The correlation function  $\langle \dots \rangle_\omega$  illustrates the thermal average over the double Fourier transformation where one is executed in real space  $\mathbf{r}$  and one in time  $t$ .

In the case of purely magnetic scattering only the terms  $\langle \hat{\mathbf{M}}_\perp^\dagger \hat{\mathbf{M}}_\perp \rangle_\omega$  and  $i\mathbf{P} \langle \hat{\mathbf{M}}_\perp^\dagger \times \hat{\mathbf{M}}_\perp \rangle_\omega$  contribute. With Equation 6.5 the scattering cross section for magnetic scattering of polarized neutrons becomes:

$$\begin{aligned} \left( \frac{\partial^2 \sigma}{\partial \Omega \partial E} \right) &= \left( \frac{\gamma_n e^2}{m_e c^2} \right) \frac{k_f}{k_i} \sum_{j,j'} e^{i\mathbf{Q}\cdot\mathbf{r}_j} \frac{1}{2} g_j f_j^*(\mathbf{Q}) \frac{1}{2} g_{j'} f_{j'}(\mathbf{Q}) \\ &\cdot \frac{1}{2\pi\hbar} \int_{-\infty}^{\infty} e^{-i\omega t} \left[ \langle \hat{\mathbf{S}}_{j,\perp}(0) \cdot \hat{\mathbf{S}}_{j',\perp}(t) \rangle + i\mathbf{P} \langle \hat{\mathbf{S}}_{j,\perp}(0) \times \hat{\mathbf{S}}_{j',\perp}(t) \rangle \right] \quad (6.24) \end{aligned}$$

Note here that the thermal average is executed with  $p_\lambda$  as the Boltzmann distribution and the  $\perp$  index denotes the moment component perpendicular to the scattering vector  $\hat{\mathbf{S}}_\perp(t) = \tilde{\mathbf{Q}} \times (\hat{\mathbf{S}}(t) \times \tilde{\mathbf{Q}})$ . This formula simplifies significantly when assuming that the total component of spin of the scattering target is a constant of motion. We define the direction of this component to be the unit vector  $\tilde{\mathbf{S}}$ . With this constraint which is valid for a Heisenberg ferromagnet the two spin dependent terms in Equation 6.24 can be transformed into expressions which depend on the spin ladder operators  $\hat{S}^+$  and  $\hat{S}^-$  and the scattering cross section simplifies into:

$$\begin{aligned} \left( \frac{\partial^2 \sigma}{\partial \Omega \partial E} \right) &= \left( \frac{\gamma_n e^2}{m_e c^2} \right) \frac{k_f}{k_i} \left| \frac{1}{2} g f(\mathbf{Q}) \right|^2 \sum_{l,l'} e^{i\mathbf{Q}\cdot(\mathbf{l}-\mathbf{l}')} \frac{1}{2\pi\hbar} \int_{-\infty}^{\infty} e^{-i\omega t} \\ &\cdot \frac{1}{4} \left\{ [1 + (\tilde{\mathbf{Q}} \cdot \tilde{\mathbf{S}})^2 + 2(\mathbf{P} \cdot \tilde{\mathbf{Q}})(\tilde{\mathbf{Q}} \cdot \tilde{\mathbf{S}})] \langle \hat{S}_l^-(0) \hat{S}_{l'}^+(t) \rangle \right. \\ &\left. + [1 + (\tilde{\mathbf{Q}} \cdot \tilde{\mathbf{S}})^2 - 2(\mathbf{P} \cdot \tilde{\mathbf{Q}})(\tilde{\mathbf{Q}} \cdot \tilde{\mathbf{S}})] \langle \hat{S}_l^+(0) \hat{S}_{l'}^-(t) \rangle \right\} \quad (6.25) \end{aligned}$$

The scattering cross sections depends now on the correlation functions  $\langle \hat{S}_l^\mp(0) \hat{S}_{l'}^\pm(t) \rangle$  and the vector relations between the scattering vector, the neutron polarization vector and the quantization axis of spin determines the magnitude of their contribution to the scattering cross section. When the polarization and the magnetization are collinear to the scattering vector than only one of the two correlation functions contribute.

The correlation functions of the spin ladder operators appearing in the cross section can be evaluated for a Heisenberg ferromagnet.

$$\langle \hat{S}_l^\mp(0) \hat{S}_{l'}^\pm(t) \rangle = \frac{2S}{N} \sum_{\mathbf{q}} \exp(\pm i\mathbf{q} \cdot (\mathbf{l} - \mathbf{l}') \mp i\omega_{\mathbf{q}}t) \begin{cases} n_{\mathbf{q}} \\ (n_{\mathbf{q}} + 1) \end{cases} \quad (6.26)$$

with  $n_{\mathbf{q}} = \left[ \exp\left(\frac{\hbar\omega_{\mathbf{q}}}{k_bT}\right) - 1 \right]^{-1}$

The energy of a magnon with wave vector  $\mathbf{q}$  is marked by  $\hbar\omega_{\mathbf{q}}$ . With this expression for the correlation functions the cross section of polarized neutron scattering with a Heisenberg ferromagnet results in:

$$\left( \frac{\partial^2 \sigma}{\partial \Omega \partial E} \right)^\pm = \left( \frac{\gamma_n e^2}{m_e c^2} \right) \frac{k_f}{k_i} \left| \frac{1}{2} g f(\mathbf{Q}) \right|^2 \frac{1}{2} S \frac{(2\pi)^3}{v_0^2} \sum_{\mathbf{q}, \tau} (n_{\mathbf{q}} + \frac{1}{2} \pm \frac{1}{2}) \cdot \delta(\hbar\omega \mp \hbar\omega_{\mathbf{q}}) \delta(\mathbf{Q} \mp \mathbf{q} - \boldsymbol{\tau}) \left[ 1 + (\tilde{\mathbf{Q}} \cdot \tilde{\mathbf{S}})^2 \mp 2(\mathbf{P} \cdot \tilde{\mathbf{Q}})(\tilde{\mathbf{Q}} \cdot \tilde{\mathbf{S}}) \right] \quad (6.27)$$

Here the superscripts denote the processes of magnon creation (+) and annihilation (-). The vector relations between the scattering vector  $\mathbf{Q}$ , the neutron polarization vector  $\mathbf{P}$  and the quantization axis of spin  $\tilde{\mathbf{S}}$  determine for which experimental configuration the magnon signal can be measured. Since the correlation functions in Equation 6.26 for a Heisenberg ferromagnet are determined by the commutation relation of spin components the vector relation term states the criterion for which polarized neutron scattering channel measures which handedness of spin excitations. This criterion is used to interpret the results in Section 2.3.

### 6.2.3 Triple-Axis Spectrometer

Using continuous, reactor-based neutron sources the triple-axis spectrometer is the most versatile experimental tool of neutron scattering to navigate through  $\mathbf{Q}$ - $E$  space. Since its first version built by Brockhouse in 1956 it enables neutron scattering studies of fundamental excitations in condensed matter. Also in this thesis this experimental instrument is used extensively to investigate the magnetic correlations in Ruthenates.

In reactor-based sources like the ILL in Grenoble, the LLB in Saclay, or the FRM-II in Garching the nuclear fission of  $^{235}\text{U}$  provides a continuous beam of free neutrons with an energy in the MeV regime. While this energy is typical for nuclear processes the high-energy neutrons cannot be used for spectroscopy in the meV regime and therefore have to be moderated. The neutron energy depends on the moderator temperature as the high energy neutrons thermalize via scattering processes in the different moderators. and the respective energy distribution is given by the Maxwell-Boltzmann distribution. Following the neutron energy after moderation the neutron sources can be categorized into *cold* ( $T_{\text{mod}} \lesssim 50\text{K}$ ), *thermal* ( $T_{\text{mod}} \approx 300\text{K}$ ), and *hot* ( $T_{\text{mod}} \gtrsim 1000\text{K}$ ). The different neutron sources provide particular neutron energy ranges with corresponding energy resolutions of the spectrometers which, depending on the physical problem, has to be considered. Since the energy distribution of every source is rather broad the white neutron beam has to be monochromatized for neutron scattering spectrometry. This is achieved by nuclear diffraction of the neutron beam on single crystals of a certain material and

yields a neutron beam with defined initial wave vector  $\mathbf{k}_i$ . The materials and their particular Bragg reflection determine further the energy range of the spectrometer. Common monochromators are using the (0, 0, 2) reflection of pyrolytic graphite (PG), the (1, 1, 1) reflection of Cu, or the (1, 1, 1) reflection of Si. The Bragg reflection (1, 1, 1) of the Heusler alloy  $\text{Cu}_2\text{MnAl}$  creates both a monochromatized and polarized neutron beam. Details of the creation of polarized neutrons by Heusler alloys are given in Section 6.2.2. The monochromator represents the first axis of a triple-axis spectrometer. Behind the monochromator, in the primary spectrometer arm, the so called monitor is installed which is a very inefficient neutron detector. By capturing every 10000<sup>th</sup> neutron it gives a measure for the incident neutron flux at the sample which can be used to normalize data. The second axis of a triple-axis spectrometer is represented by the sample stage where, depending on the desired sample environment, cryostats and magnets can be installed. On the end of the secondary spectrometer arm the analyzer is placed and is responsible for the energy discrimination of the scattered neutrons. The analyzer uses analogous to the monochromator the Bragg diffraction on single crystals for the determination of the final wave vector  $\mathbf{k}_f$  of the detected neutrons. The analyzer represents the third axis of a triple-axis spectrometer. The neutrons behind the analyzer are detected by  $^3\text{He}$  detector. The shape of the neutron beam profile can be altered using collimators on primary and secondary spectrometer arms which is used for background optimization. To avoid higher order contamination, i.e. scattering by  $\frac{\lambda}{2}$  neutrons, Be or graphite filters can be placed on the spectrometer arms depending on the neutron energy. A more sophisticated method to filter out higher order neutrons is the velocity selector which transmits only neutrons in a certain velocity window, i.e. energy range. In the case of polarization analysis the spectrometer arms are equipped by permanent magnets which create a polarization conserving guide field along the scattered neutron path. The polarization direction of the neutrons at the sample position can be determined by a setup of three Helmholtz coils (*XYZ* method, longitudinal polarization analysis) or the CRYOPAD<sup>3</sup> (spherical polarization analysis) which can orient the neutron polarization in an arbitrary direction. Additionally spin flippers can be installed in front and behind the sample stage to flip the neutron spin in respect to the guide field. The in the presented experiments used Mezei flippers facilitates the spin flip by a non-adiabatic 90° field change in a flat coil. This results in the Larmor precession of the neutron moment around the perpendicular magnetic field direction. By tuning the field magnitude a phase difference of  $\pi$  can be achieved.

Figure 6.4 represents a schematic to illustrate the principal setup of a triple-axis spectrometer with its possible components. The paths through  $\mathbf{Q}$ - $E$  space can be experimentally realized by continuously changing the six possible angles of the instrument<sup>4</sup>. The angle rotations change  $\mathbf{k}_i$  and  $\mathbf{k}_f$  and enable the access to defined  $(\mathbf{Q}, E)$  points in  $\mathbf{Q}$ - $E$  space. Since the rotation of the monochromator and analyzer is confined in the horizontal plane the triple-axis spectrometer can only operate in a two-dimensional part of the reciprocal space. The part is determined by the sample orientation which defines the scattering plane. The scattering vector  $\mathbf{Q}$  determined by  $\mathbf{k}_i$  and  $\mathbf{k}_f$  has to lay therefore in the scattering plane. For some experimental

<sup>3</sup>more information: <https://www.ill.eu/users/instruments/instruments-list/d3/how-it-works/spherical-polarimetry-with-cryopad>

<sup>4</sup>The angles notation (A1-A6) follows the notation used by the ILL.

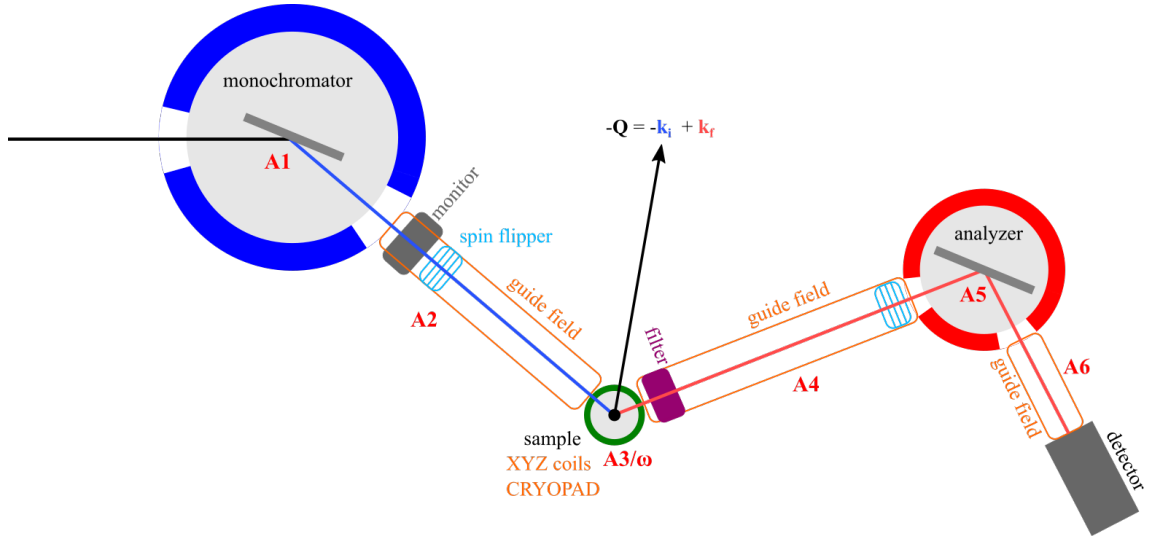


**Figure 6.4: Schematic representation of a triple-axis spectrometer.** The monochromator (A1) determines the initial wave vector  $\mathbf{k}_i$ . The monochromatized neutron beam passes the monitor which captures a small portion and measures therefore the incident neutron flux. Along the primary (A2) and secondary (A4) spectrometer arms there can be higher order filters as well as guide fields and spin flippers for the polarization analysis installed. The sample stage (A3) represents the second axis of the spectrometer. The neutron polarization direction can be defined by  $XYZ$  Helmholtz coils or the CRYOPAD for the polarization analysis. The third axis of the spectrometer is represented by the analyzer (A5) and combined with the tertiary spectrometer arm (A6) defines the probed final wave vector  $\mathbf{k}_f$ .

setups also a small out-of-plane component of the scattering vector in respect to the original scattering plane can be achieved by tilting the sample stage which changes the sample orientation in respect to the horizontal plane of the instrument (see ??).

Further details of the instrumentation of triple-axis spectrometers are given in [143, 149, 150].

### 6.2.4 Time-of-Flight Spectrometer

In contrast to the triple-axis spectrometer time-of-flight spectrometer are predominantly utilized at spallation sources. Here the energy discrimination of scattered neutrons is accomplished by analyzing the flight time of neutrons after the scattering process. Therefore a pulsed neutron beam with defined time structure has to be used which is provided inherently by spallation sources. A spallation source produces neutrons by bombarding a target, e.g. tungsten metal, with high energy protons created by an accelerator. Since the proton beam is pulsed the resulting neutron beam is also pulsed. This pulsed beam structure can also be achieved with a reactor based neutron source by chopping the continuous beam. The neutron beam is moderated similarly to the reactor-based neutron sources and the initial neutron energy is defined by neutron velocity selection. Technically this is realized by rotating choppers whose angular velocity corresponds to the desired neutron velocity. This determines the energy of the transmitted neutrons and gives the initial wave vector  $\mathbf{k}_i$ . After the scattering process at the sample the neutrons are captured

by a detector array which covers a certain amount of solid angle and also registers the flight time of every single scattered neutron. This flight time together with the known distance between sample and detector can then be translated into the final energy of the scattered neutron which enables the spectrometry. The data collection in a time-of-flight experiment is realized by rotating the sample around the vertical axis. The accessible reciprocal space is given therefore predominantly by the sample orientation, i.e. the scattering plane. Nevertheless since the detector array is usually also arranged out-of-plane it can cover more out-of-plane reciprocal space than the triple-axis spectrometer. While both techniques give access to the  $\mathbf{Q}$ - $E$  space the obtained data differ significantly. The triple-axis spectrometer collects scattered neutron intensity at defined  $(\mathbf{Q}, E)$  points while the time-of-flight spectrometer yields the intensity of the whole accessible  $\mathbf{Q}$ - $E$  space. Since the collected intensity is spread in the four-dimensional space this technique favors the study of low-dimensional systems where the collected data can be integrated along the high-symmetry directions. The analysis of such data sets relies heavily on computational infrastructure because the four-dimensional data sets have to be integrated, sliced and cut to make a visualization and interpretation possible. The computational infrastructure as well as the analysis software HORACE [151] which was used for this thesis is provided by ISIS Neutron and Muon source.

More detailed information about the experimental technique are given in [149, 150].

# Appendix

## A.1 Phonons in SrRuO<sub>3</sub>

The phonon dispersion is studied by inelastic neutron scattering at the thermal triple-axis spectrometer 1T1 at LLB in Saclay, France in the course of two beam times (11-2017 and 02-2019). The monochromator consists of PG(002) crystals and the analyzer is chosen as PG(002) or Cu(111) depending on the energy transfer. For the lower energy transfers below 40 meV PG(002) with  $k_f = 2.662 \text{ \AA}^{-1}$  is used while the higher energy transfers are accessible with the Cu(111) analyzer and  $k_f = 3.84 \text{ \AA}^{-1}$ . The sample is cooled down using a closed-cycle cryostat.

Constant  $Q$  and constant  $E$  scans are conducted in various Brillouin zones around different Bragg peaks to cover most of the different phonon modes. The scans are fitted by Gaussians to extract the peak position which gives the energy-momentum relation for each mode. Figure A.1 displays the dispersion relation for the measured phonon modes. Depending on the direction of the momentum transfer  $q$  the modes are sorted in three categories according to the three high-symmetry directions in the pseudo-cubic lattice:  $\Delta = [1, 0, 0]$ ,  $\Sigma = [1, 1, 0]$ , and  $\Lambda = [1, 1, 1]$ .

Additionally the temperature dependence of the high energy modes at specific Brillouin zone points is studied (Figure A.2). The subscripts 'long' and 'trans' refer to the relation between the vector  $Q$  of the Brillouin zone center and the zone point.

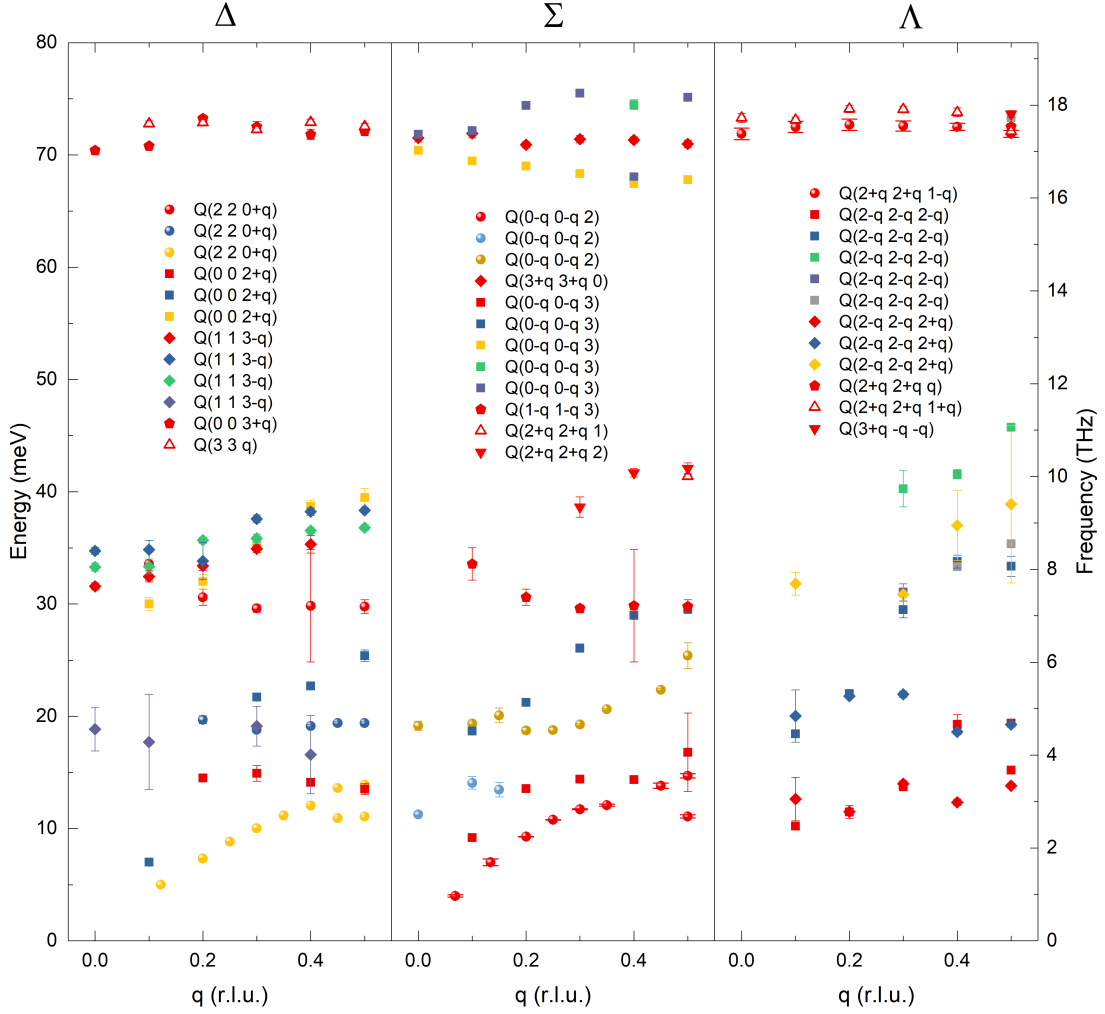


**Figure A.1: Phonon dispersion of SrRuO<sub>3</sub> at T = 10 K investigated by inelastic neutron scattering.** The phonon dispersion is studied by measuring constant  $Q$  and constant  $E$  scans in various Brillouin zones. The scans are fitted with a Gaussian for each phonon mode. The dispersion is displayed by plotting the fitted energy values in meV (and THz) against the momentum transfer  $q$  in relative lattice units. The branches are sorted in the high symmetry directions of the cubic symmetry  $\Delta$ ,  $\Sigma$ , and  $\Lambda$ .

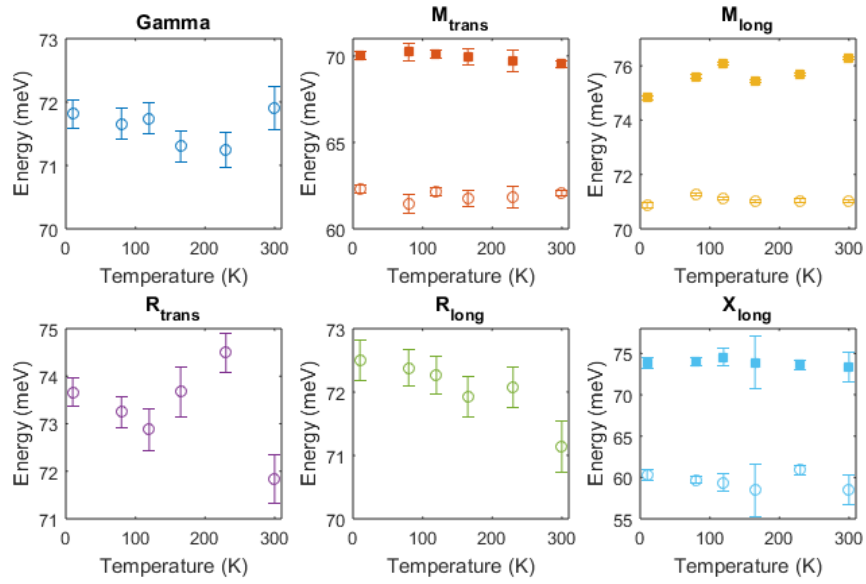


**Figure A.2:** Temperature dependence of high energy phonon modes at high symmetry points in the cubic Brillouin zone. The phonon modes are extracted from fitting constant  $Q$  scans at  $Q = (3, 0, 0)$  and  $(0, 3, 3)$ .

## A.2 Spin-density wave dynamics in $\text{Ca}_{2-x}\text{Sr}_x\text{RuO}_4$

The spin-density wave ordering in  $\text{Ca}_{0.5}\text{Sr}_{1.5}\text{RuO}_4$  is studied by inelastic neutron scattering at the cold triple-axis spectrometer PANDA at FRM-II in Munich, Germany in the course of one beam time (01-2021). The monochromator as well as the analyzer consists of PG(002) crystals. The instrument is operating in constant  $k_f$  mode with  $k_f = 1.55 \text{ \AA}^{-1}$ . To reduce higher-order scattering a cooled Be filter is mounted in front of the analyzer. The sample is cooled down using a closed-cycle cryostat.

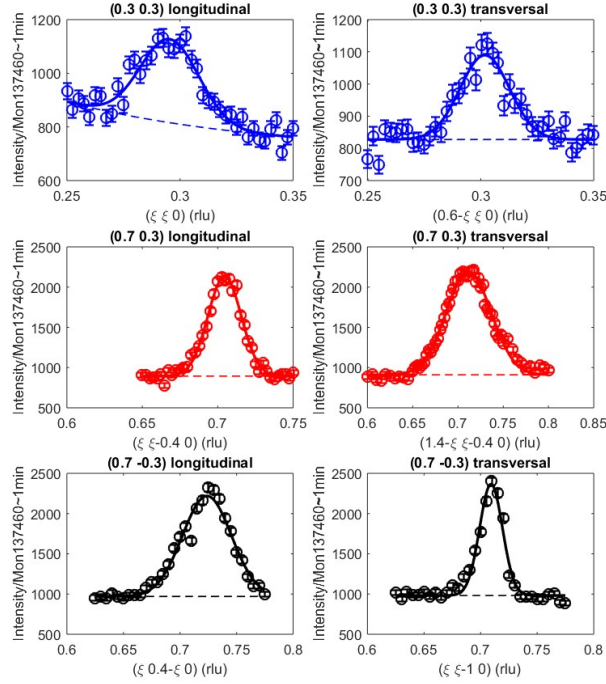


**Figure A.3: Spin-density wave ordering in  $\text{Ca}_{0.5}\text{Sr}_{1.5}\text{RuO}_4$  with the incommensurate wave vector  $\mathbf{q}_{IC} = (0.3, 0.3, 0)$ .** Elastic scans around the equivalent positions corresponding to the wave vector  $\mathbf{q}_{IC}$  in longitudinal and transversal directions. The data color associates to the specific incommensurate position: blue =  $(0.3, 0.3, 0)$ , blue =  $(0.7, 0.3, 0)$ , and black =  $(0.7, -0.3, 0)$ .

In the unconventional superconductor  $\text{Sr}_2\text{RuO}_4$ , inelastic neutron scattering has revealed incommensurate (IC) fluctuations which do not promote the Triplet pairing. These IC fluctuations condensate upon doping with Ti or Ca into static spin-density wave (SDW) order. The inelastic response of this SDW order is investigated in the case of  $\text{Ca}_{0.5}\text{Sr}_{1.5}\text{RuO}_4$ .

Firstly the measurements of the SDW ordering at the IC positions reported in a previous study [6] are reproduced (see Figure A.3). The peak width is depending on the scan direction which can be explained by the focus effect of the experimental resolution. For the inelastic response of the SDW ordering constant energy scans in longitudinal direction over the IC positions are measured (see Figure A.4). Note here that  $(0.3, 0.3, 0)$  is not crystallographically equivalent to  $(0.7, \pm 0.3, 0)$  because  $(1, 0, 0)$  is not a zone center but a  $Z$  point. Nevertheless the IC signal can be measured at

all 3 positions. The data show that the SDW does not disperse in this low energy region, instead the signal stays localized at the IC position. At higher energies the background increases and the separation of magnetic signal becomes more uncertain. It seems that the signal has almost disappeared at 5 meV. The data are fitted by Gaussians in combination with constant or sloped backgrounds. The fit results are presented in Figure A.5. The energy dependence of the signal does not exhibit a clear maximum and the error bars are still large which leaves the description ambiguous. This is also visible in the different result of fitting of the two equivalent positions  $(0.7, \pm 0.3, 0)$ .

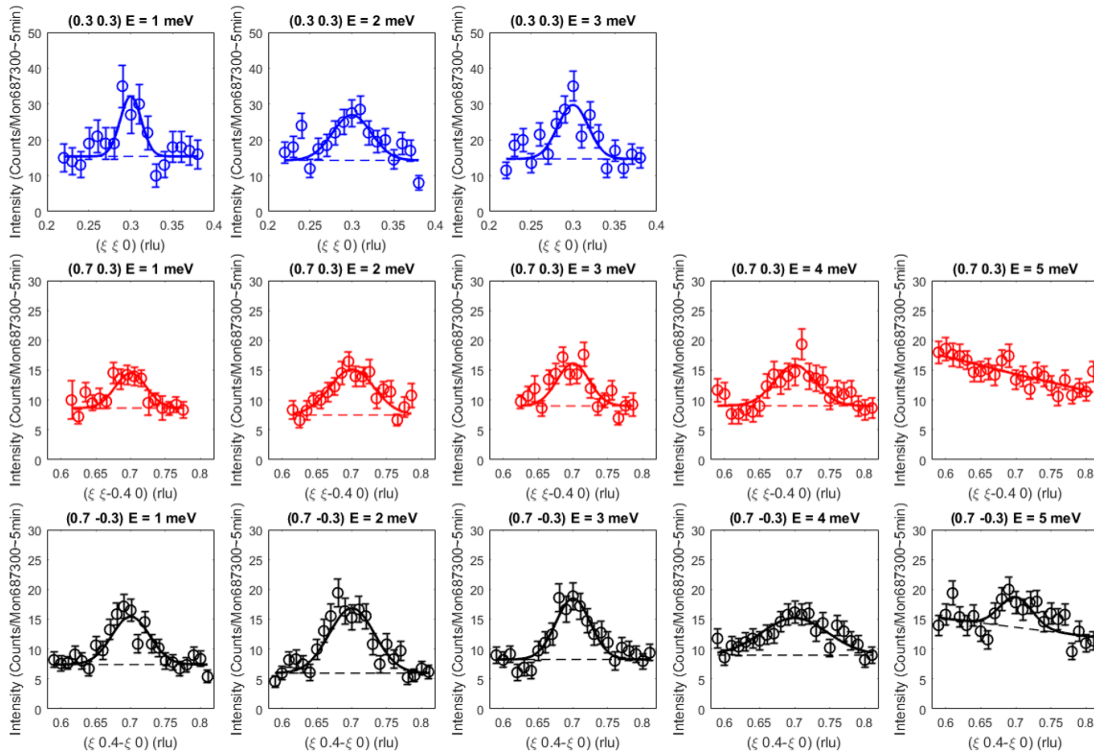


**Figure A.4:** Dispersion of the spin-density wave signal ordering at equivalent incommensurate positions in  $\text{Ca}_{0.5}\text{Sr}_{1.5}\text{RuO}_4$ . Constant energy scans at the equivalent positions corresponding to the wave vector  $q_{IC}$  reveal the energy dependence of inelastic spin-density wave signal. The scans are fitted by a Gaussian in combination with a constant and sloped background respectively. The data color associates to the specific incommensurate position: blue =  $(0.3, 0.3, 0)$ , blue =  $(0.7, 0.3, 0)$ , and black =  $(0.7, -0.3, 0)$ .

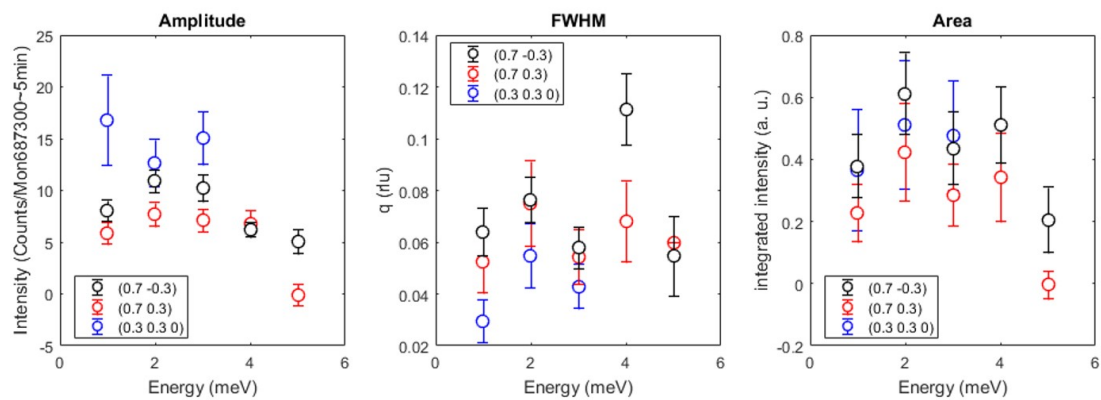


**Figure A.5: Energy dependence of the inelastic signal at the incommensurate positions.** The fit results of the Gaussian fits display the energy dependence of the inelastic signal and its FWHM.

# Bibliography

- [1] J. G. Bednorz and K. A. Müller, “Possible High  $T_C$  Superconductivity in the Ba-La-Cu-O System”, *Z. Phys. B* **64**, 189–193 (1986).
- [2] S. N. Ruddlesden and P. Popper, “New compounds of the  $K_2NiF_4$  type”, *Acta Crystallogr.* **10**, 538–539 (1957).
- [3] S. N. Ruddlesden and P. Popper, “The compound  $Sr_3Ti_2O_7$  and its structure”, *Acta Crystallogr.* **11**, 54–55 (1958).
- [4] F. Lichtenberg, A. Catana, J. Mannhart, and D. G. Schlom, “ $Sr_2RuO_4$ : A metallic substrate for the epitaxial growth of  $YBa_2Cu_3O_{7-\delta}$ ”, *Appl. Phys. Lett.* **60**, 1138–1140 (1992).
- [5] Y. Maeno, H. Hashimoto, K. Yoshida, S. Nishizaki, T. Fujita, J. G. Bednorz, and F. Lichtenberg, “Superconductivity in layered perovskite without copper”, *Nat.* **372**, 532–534 (1994).
- [6] S. Kunkemöller, A. A. Nugroho, Y. Sidis, and M. Braden, “Spin-density-wave ordering in  $Ca_{0.5}Sr_{1.5}RuO_4$  studied by neutron scattering”, *Phys. Rev. B* **89**, 1–6 (2014).
- [7] S. Nakatsuji and Y. Maeno, “Metamagnetic Transition in the Quasi Two-Dimensional Mott Transition System  $Ca_{2-x}Sr_xRuO_4$ ”, *J. Low Temp. Phys.* **117**, 1593–1597 (1999).
- [8] R. A. Borzi, S. A. Grigera, J. Farrell, R. S. Perry, S. J. S. Lister, S. L. Lee, D. A. Tennant, Y. Maeno, and A. P. Mackenzie, “Formation of a Nematic Fluid at High Fields in  $Sr_3Ru_2O_7$ ”, *Science* **315**, 214–217 (2007).
- [9] C. L. Huang, D. Fuchs, M. Wissinger, R. Schneider, M. C. Ling, M. S. Scheurer, J. Schmalian, and H. V. Löhneysen, “Anomalous quantum criticality in an itinerant ferromagnet”, *Nat. Commun.* **6**, 6–10 (2015).
- [10] S. Kunkemöller, F. Sauer, A. A. Nugroho, and M. Braden, “Magnetic anisotropy of large floating-zone-grown single-crystals of  $SrRuO_3$ ”, *Cryst. Res. Technol.* **51**, 299–305 (2016).
- [11] T. M. Rice and M. Sigrist, “ $Sr_2RuO_4$ : an electronic analogue of  $^3He$ ?”, *J. Phys. Cond. Matter* **7**, L643–L648 (1995).
- [12] G. Koster, L. Klein, W. Siemons, G. Rijnders, J. S. Dodge, C.-B. Eom, D. H. A. Blank, and M. R. Beasley, “Structure, physical properties, and applications of  $SrRuO_3$  thin films”, *Rev. Mod. Phys.* **84**, 253–298 (2012).
- [13] S. Kunkemöller, D. Brüning, A. Stunault, A. A. Nugroho, T. Lorenz, and M. Braden, “Magnetic shape-memory effect in  $SrRuO_3$ ”, *Phys. Rev. B* **96**, 220406 (2017).

- [14] S. Kunkemöller, K. Jenni, D. Gorkov, A. Stunault, S. Streltsov, and M. Braden, “Magnetization density distribution in the metallic ferromagnet SrRuO<sub>3</sub> determined by polarized neutron diffraction”, *Phys. Rev. B* **100**, 54413 (2019).
- [15] T. Kiyama, K. Yoshimura, K. Kosuge, Y. Ikeda, and Y. Bando, “Invar effect of SrRuO<sub>3</sub>: Itinerant electron magnetism of Ru 4d electrons”, *Phys. Rev. B* **54**, R756–R759 (1996).
- [16] L. Klein, J. S. Dodge, C. H. Ahn, J. W. Reiner, L. Mieville, T. H. Geballe, M. R. Beasley, and A. Kapitulnik, “Anomalous Spin Scattering Effects in the Badly Metallic Itinerant Ferromagnet SrRuO<sub>3</sub>”, *Phys. Rev. Lett.* **77**, 2774–2777 (1996).
- [17] P. Kostic, Y. Okada, Z. Schlesinger, J. W. Reiner, L. Klein, A. Kapitulnik, T. H. Geballe, and M. R. Beasley, “Non-Fermi liquid behavior of SrRuO<sub>3</sub> - Evidence from infrared conductivity”, *Phys. Rev. Lett.* **81**, 2498–2501 (1998).
- [18] M. S. Laad and E. Müller-Hartmann, “Origin of the non-fermi liquid behavior of SrRuO<sub>3</sub>”, *Phys. Rev. Lett.* **87**, 246402–1–246402–4 (2001).
- [19] Z. Fang, N. Nagaosa, K. S. Takahashi, H. Yamada, M. Kawasaki, and Y. Tokura, “The Anomalous Hall Effect and Magnetic Monopoles in Momentum Space”, *Science* **302**, 1–4 (2003).
- [20] S. Itoh, Y. Endoh, T. Yokoo, S. Ibuka, J. G. Park, Y. Kaneko, K. S. Takahashi, Y. Tokura, and N. Nagaosa, “Weyl fermions and spin dynamics of metallic ferromagnet SrRuO<sub>3</sub>”, *Nat. Commun.* **7**, 1–8 (2016).
- [21] Y. Chen, D. L. Bergman, and A. A. Burkov, “Weyl fermions and the anomalous Hall effect in metallic ferromagnets”, *Phys. Rev. B* **88**, 125110 (2013).
- [22] O. Friedt, M. Braden, G. Andre, G. André, P. Adelman, S. Nakatsuji, and Y. Maeno, “Structural and magnetic aspects of the metal-insulator transition in Ca<sub>2-x</sub>Sr<sub>x</sub>RuO<sub>4</sub>”, *Phys. Rev. B* **63**, 174432 (2001).
- [23] C. S. Alexander, G. Cao, V. Dobrosavljevic, S. McCall, J. E. Crow, E. Lochner, and R. P. Guertin, “Destruction of the Mott insulating ground state of Ca<sub>2</sub>RuO<sub>4</sub> by a structural transition”, *Phys. Rev. B* **60**, R8422–R8425 (1999).
- [24] P. Steffens, O. Friedt, P. Alireza, W. G. Marshall, W. Schmidt, F. Nakamura, S. Nakatsuji, Y. Maeno, R. Lengsdorf, M. M. Abd-Elmeguid, and M. Braden, “High-pressure diffraction studies on Ca<sub>2</sub>RuO<sub>4</sub>”, *Phys. Rev. B* **72**, 94104 (2005).
- [25] M. Braden, G. André, S. Nakatsuji, and Y. Maeno, “Crystal and magnetic structure of Ca<sub>2</sub>RuO<sub>4</sub>: Magnetoelastic coupling and the metal-insulator transition”, *Phys. Rev. B* **58**, 847–861 (1998).
- [26] I. I. Mazin and D. J. Singh, “Competitions in Layered Ruthenates: Ferromagnetism versus Antiferromagnetism and Triplet versus Singlet Pairing”, *Phys. Rev. Lett.* **82**, 4324–4327 (1999).
- [27] T. Mizokawa, L. H. Tjeng, G. A. Sawatzky, G. Ghiringhelli, O. Tjernberg, N. B. Brookes, H. Fukazawa, S. Nakatsuji, and Y. Maeno, “Spin-Orbit Coupling in the Mott Insulator Ca<sub>2</sub>RuO<sub>4</sub>”, *Phys. Rev. Lett.* **87** (2001).

- [28] J. H. Jung, Z. Fang, J. P. He, Y. Kaneko, Y. Okimoto, and Y. Tokura, “Change of Electronic Structure in  $\text{Ca}_2\text{RuO}_4$  Induced by Orbital Ordering”, *Phys. Rev. Lett.* **91**, 056403 (2003).
- [29] T. Hotta and E. Dagotto, “Prediction of Orbital Ordering in Single-Layered Ruthenates”, *Phys. Rev. Lett.* **88**, 17201 (2001).
- [30] A. V. Puchkov, M. C. Schabel, D. N. Basov, T. Startseva, G. Cao, T. Timusk, and Z.-X. Shen, “Layered Ruthenium Oxides: From Band Metal to Mott Insulator”, *Phys. Rev. Lett.* **81**, 2747–2750 (1998).
- [31] A. Liebsch and H. Ishida, “Subband Filling and Mott Transition in  $\text{Ca}_{2-x}\text{Sr}_x\text{RuO}_4$ ”, *Phys. Rev. Lett.* **98**, 1–4 (2007).
- [32] G. Zhang and E. Pavarini, “Mott transition, spin-orbit effects, and magnetism in  $\text{Ca}_2\text{RuO}_4$ ”, *Phys. Rev. B* **95**, 75145 (2017).
- [33] V. I. Anisimov, I. A. Nekrasov, D. E. Kondakov, T. M. Rice, and M. Sigrist, “Orbital-selective Mott-insulator transition in  $\text{Ca}_{2-x}\text{Sr}_x\text{RuO}_4$ ”, *Eur. Phys. J. B* **25**, 191–201 (2002).
- [34] E. Gorelov, M. Karolak, T. O. Wehling, F. Lechermann, A. I. Lichtenstein, and E. Pavarini, “Nature of the Mott Transition in  $\text{Ca}_2\text{RuO}_4$ ”, *Phys. Rev. Lett.* **104**, 1–4 (2010).
- [35] G. Khaliullin, “Excitonic Magnetism in Van Vleck – type  $d^4$  Mott Insulators”, *Phys. Rev. Lett.* **111**, 1–5 (2013).
- [36] S. Nakatsuji and Y. Maeno, “Quasi-Two-Dimensional Mott Transition System  $\text{Ca}_{2-x}\text{Sr}_x\text{RuO}_4$ ”, *Phys. Rev. Lett.* **84**, 2666–2669 (2000).
- [37] S. Kunkemöller, E. Komleva, S. V. Streltsov, S. Hoffmann, D. I. Khomskii, P. Steffens, Y. Sidis, K. Schmalzl, and M. Braden, “Magnon dispersion in  $\text{Ca}_2\text{Ru}_{1-x}\text{Ti}_x\text{O}_4$ : Impact of spin-orbit coupling and oxygen moments”, *Phys. Rev. B* **95**, 214408 (2017).
- [38] T. Vogt and D. J. Buttrey, “Low-temperature structural behavior of  $\text{Sr}_2\text{RuO}_4$ ”, *Phys. Rev. B* **52**, R9843 (1995).
- [39] A. P. Mackenzie, R. K. W. Haselwimmer, A. W. Tyler, G. G. Lonzarich, Y. Mori, S. Nishizaki, and Y. Maeno, “Extremely Strong Dependence of Superconductivity on Disorder in  $\text{Sr}_2\text{RuO}_4$ ”, *Phys. Rev. Lett.* **80**, 161–164 (1998).
- [40] Y. Maeno, K. Yoshida, H. Hashimoto, S. Nishizaki, S.-i. Ikeda, M. Nohara, T. Fujita, A. P. Mackenzie, N. E. Hussey, J. G. Bednorz, and F. Lichtenberg, “Two-Dimensional Fermi Liquid Behavior of the Superconductor  $\text{Sr}_2\text{RuO}_4$ ”, *J. Phys. Soc. Japan* **66**, 1405–1408 (1997).
- [41] A. P. Mackenzie, S. R. Julian, A. J. Diver, G. J. McMullan, M. P. Ray, G. G. Lonzarich, Y. Maeno, S. Nishizaki, and T. Fujita, “Quantum Oscillations in the Layered Perovskite Superconductor  $\text{Sr}_2\text{RuO}_4$ ”, *Phys. Rev. Lett.* **76**, 3786–3789 (1996).
- [42] C. N. Veenstra, Z. H. Zhu, B. Ludbrook, M. Capsoni, G. Levy, A. Nicolaou, J. A. Rosen, R. Comin, S. Kittaka, Y. Maeno, I. S. Elfimov, and A. Damascelli, “Determining the surface-to-bulk progression in the normal-state electronic structure of  $\text{Sr}_2\text{RuO}_4$  by angle-resolved photoemission and density functional theory”, *Phys. Rev. Lett.* **110**, 1–5 (2013).

- [43] K. Ishida, H. Mukuda, Y. Kitaoka, K. Asayama, Z. Q. Mao, Y. Mori, and Y. Maeno, “Spin-triplet superconductivity in  $\text{Sr}_2\text{RuO}_4$  identified by  $^{17}\text{O}$  Knight shift”, *Nat.* **396**, 658–660 (1998).
- [44] J. A. Duffy, S. M. Hayden, Y. Maeno, Z. Mao, J. Kulda, and G. J. McIntyre, “Polarized-Neutron Scattering Study of the Cooper-Pair Moment in  $\text{Sr}_2\text{RuO}_4$ ”, *Phys. Rev. Lett.* **85**, 5412–5415 (2000).
- [45] G. M. Luke, Y. Fudamoto, K. M. Kojima, M. I. Larkin, J. Merrin, B. Nachumi, Y. J. Uemura, Y. Maeno, Z. Q. Mao, Y. Mori, H. Nakamura, and M. Sgrist, “Time-reversal symmetry-breaking superconductivity in  $\text{Sr}_2\text{RuO}_4$ ”, *Nat.* **394**, 558–561 (1998).
- [46] Y. Sidis, M. Braden, P. Bourges, B. Hennion, S. NishiZaki, Y. Maeno, and Y. Mori, “Evidence for Incommensurate Spin Fluctuations in  $\text{Sr}_2\text{RuO}_4$ ”, *Phys. Rev. Lett.* **83**, 3320–3323 (1999).
- [47] M. Braden, P. Steffens, Y. Sidis, J. Kulda, P. Bourges, S. Hayden, N. Kikugawa, and Y. Maeno, “Anisotropy of the Incommensurate Fluctuations in  $\text{Sr}_2\text{RuO}_4$ : A Study with Polarized Neutrons”, *Phys. Rev. Lett.* **92**, 97402 (2004).
- [48] P. Steffens, Y. Sidis, J. Kulda, Z. Q. Mao, Y. Maeno, I. I. Mazin, and M. Braden, “Spin Fluctuations in  $\text{Sr}_2\text{RuO}_4$  from Polarized Neutron Scattering: Implications for Superconductivity”, *Phys. Rev. Lett.* **122**, 47004 (2019).
- [49] A. Pustogow, Y. Luo, A. Chronister, Y.-S. Su, D. A. Sokolov, F. Jerzembeck, A. P. Mackenzie, C. W. Hicks, N. Kikugawa, S. Raghu, E. D. Bauer, and S. E. Brown, “Constraints on the superconducting order parameter in  $\text{Sr}_2\text{RuO}_4$  from oxygen-17 nuclear magnetic resonance”, *Nature* **574**, 72–75 (2019).
- [50] I. Kenji, M. Masahiro, K. Katsuki, and M. Yoshiteru, “Reduction of the  $^{17}\text{O}$  Knight Shift in the Superconducting State and the Heat-up Effect by NMR Pulses on  $\text{Sr}_2\text{RuO}_4$ ”, *J. Phys. Soc. Japan* **89**, 34712 (2020).
- [51] A. N. Petsch, M. Zhu, M. Enderle, Z. Q. Mao, Y. Maeno, I. I. Mazin, and S. M. Hayden, “Reduction of the spin susceptibility in the superconducting state of  $\text{Sr}_2\text{RuO}_4$  observed by polarized neutron scattering”, *Phys. Rev. Lett.* **125**, 217004 (2020).
- [52] H. S. Røising, T. Scaffidi, F. Flicker, G. F. Lange, and S. H. Simon, “Superconducting order of  $\text{Sr}_2\text{RuO}_4$  from a three-dimensional microscopic model”, *Phys. Rev. Res.* **1**, 33108 (2019).
- [53] A. T. Rømer, D. D. Scherer, I. M. Eremin, P. J. Hirschfeld, and B. M. Andersen, “Knight Shift and Leading Superconducting Instability from Spin Fluctuations in  $\text{Sr}_2\text{RuO}_4$ ”, *Phys. Rev. Lett.* **123**, 247001 (2019).
- [54] W.-S. Wang, C.-C. Zhang, F.-C. Zhang, and Q.-H. Wang, “Theory of Chiral  $p$ -Wave Superconductivity with Near Nodes for  $\text{Sr}_2\text{RuO}_4$ ”, *Phys. Rev. Lett.* **122**, 27002 (2019).
- [55] Z. Wang, X. Wang, and C. Kallin, “Spin-orbit coupling and spin-triplet pairing symmetry in  $\text{Sr}_2\text{RuO}_4$ ”, *Phys. Rev. B* **101**, 64507 (2020).
- [56] H. G. Suh, H. Menke, P. M. R. Brydon, C. Timm, A. Ramires, and D. F. Agterberg, “Stabilizing even-parity chiral superconductivity in  $\text{Sr}_2\text{RuO}_4$ ”, *Phys. Rev. Res.* **2**, 32023 (2020).

- [57] S. A. Kivelson, A. C. Yuan, B. Ramshaw, and R. Thomale, “A proposal for reconciling diverse experiments on the superconducting state in  $\text{Sr}_2\text{RuO}_4$ ”, *npj Quantum Mater.* **5**, 43 (2020).
- [58] M. Braden, O. Friedt, Y. Sidis, P. Bourges, M. Minakata, and Y. Maeno, “Incommensurate Magnetic Ordering in  $\text{Sr}_2\text{Ru}_{1-x}\text{Ti}_x\text{O}_4$ ”, *Phys. Rev. Lett.* **88**, 197002 (2002).
- [59] J. E. Ortmann, J. Y. Liu, J. Hu, M. Zhu, J. Peng, M. Matsuda, X. Ke, and Z. Q. Mao, “Competition Between Antiferromagnetism and Ferromagnetism in  $\text{Sr}_2\text{RuO}_4$  Probed by Mn and Co Doping”, *Sci. Rep.*, 1–7 (2013).
- [60] P. B. Allen, H. Berger, O. Chauvet, L. Forro, T. Jarlborg, A. Junod, B. Revaz, and G. Santi, “Transport properties, thermodynamic properties, and electronic structure of  $\text{SrRuO}_3$ ”, *Phys. Rev. B* **53**, 4393–4398 (1996).
- [61] J. J. Neumeier, A. L. Cornelius, and J. S. Schilling, “Influence of pressure on the ferromagnetic transition temperature of  $\text{SrRuO}_3$ ”, *Phys. B Phys. Condens. Matter* **198**, 324–328 (1994).
- [62] S. Blundell, *Magnetism in Condensed Matter* (Oxford University Press, Oxford, 2001).
- [63] A. Zheludev, *ResLib 3.4: 3-axis resolution library for MatLab*, Oak Ridge, TN 37831-6393, USA, 2007.
- [64] J. M. D. Coey, *Magnetism and Magnetic Materials* (Cambridge University Press, New York, 2009).
- [65] M. C. Langner, C. L. S. Kantner, Y. H. Chu, L. M. Martin, P. Yu, J. Seidel, R. Ramesh, and J. Orenstein, “Observation of Ferromagnetic Resonance in  $\text{SrRuO}_3$  by the Time-Resolved Magneto-Optical Kerr Effect”, *Phys. Rev. Lett.* **102**, 177601 (2009).
- [66] K. Jenni, S. Kunkemöller, D. Brüning, T. Lorenz, Y. Sidis, A. Schneidewind, A. A. Nugroho, A. Rosch, D. I. Khomskii, and M. Braden, “Interplay of Electronic and Spin Degrees in Ferromagnetic  $\text{SrRuO}_3$ : Anomalous Softening of the Magnon Gap and Stiffness”, *Phys. Rev. Lett.* **123**, 17202 (2019).
- [67] D. I. Khomskii, *Transition Metal Compounds* (Cambridge University Press, Cambridge, 2014).
- [68] J. Okamoto, T. Okane, Y. Saitoh, K. Terai, S. I. Fujimori, Y. Muramatsu, K. Yoshii, K. Mamiya, T. Koide, A. Fujimori, Z. Fang, Y. Takeda, and M. Takano, “Soft x-ray magnetic circular dichroism study of  $\text{Ca}_{1-x}\text{Sr}_x\text{RuO}_3$  across the ferromagnetic quantum phase transition”, *Phys. Rev. B - Condens. Matter Mater. Phys.* **76**, 1–5 (2007).
- [69] S. Agrestini, Z. Hu, C. Y. Kuo, M. W. Haverkort, K. T. Ko, N. Hollmann, Q. Liu, E. Pellegrin, M. Valvidares, J. Herrero-Martin, P. Gargiani, P. Gegenwart, M. Schneider, S. Esser, A. Tanaka, A. C. Komarek, and L. H. Tjeng, “Electronic and spin states of  $\text{SrRuO}_3$  thin films: An x-ray magnetic circular dichroism study”, *Phys. Rev. B - Condens. Matter Mater. Phys.* **91**, 1–5 (2015).
- [70] H. A. Mook and R. M. Nicklow, “Neutron Scattering Investigation of the Magnetic Excitations in Iron”, *Phys. Rev. B* **7**, 336–342 (1973).

- [71] B. Yan and C. Felser, “Topological materials: Weyl semimetals”, *Annu. Rev. Condens. Matter Phys.* **8**, 337–354 (2017).
- [72] G. I. Eleftheriades and K. G. Balmain, *Negative-Refractive Metamaterials* (Wiley/IEEE Press, New York, 2005).
- [73] M. Onoda, A. S. Mishchenko, and N. Nagaosa, “Left-handed spin wave excitation in ferromagnet”, *J. Phys. Soc. Japan* **77**, 1–4 (2008).
- [74] H. Huang, S. J. Lee, B. Kim, B. Sohn, C. Kim, C. C. Kao, and J. S. Lee, “Detection of the Chiral Spin Structure in Ferromagnetic SrRuO<sub>3</sub> Thin Film”, *ACS Appl. Mater. Interfaces* **12**, 37757–37763 (2020).
- [75] K. Takiguchi, Y. K. Wakabayashi, H. Irie, Y. Krockenberger, T. Otsuka, H. Sawada, S. A. Nikolaev, H. Das, M. Tanaka, Y. Taniyasu, and H. Yamamoto, “Quantum transport evidence of Weyl fermions in an epitaxial ferromagnetic oxide”, *Nat. Commun.* **11**, 4969 (2020).
- [76] F. Chudnovskiy, S. Luryi, and B. Spivak, “Switching device based on first-order metal-insulator transition induced by external electric field”, *Futur. Trends Microelectron. Nano Millenn.*, 148–155 (2002).
- [77] M. M. Qazilbash, M. Brehm, B.-G. Chae, P.-C. Ho, G. O. Andreev, B.-J. Kim, S. J. Yun, A. V. Balatsky, M. B. Maple, F. Keilmann, H.-T. Kim, and D. N. Basov, “Mott Transition in VO<sub>2</sub> Revealed by Infrared Spectroscopy and Nano-Imaging”, *Science* **318**, 1750–1753 (2007).
- [78] A. S. McLeod, E. Van Heumen, J. G. Ramirez, S. Wang, T. Saerbeck, S. Guenon, M. Goldflam, L. Andereg, P. Kelly, A. Mueller, M. K. Liu, I. K. Schuller, and D. N. Basov, “Nanotextured phase coexistence in the correlated insulator V<sub>2</sub>O<sub>3</sub>”, *Nat. Phys.* **13**, 80–86 (2017).
- [79] S. Nakatsuji, S.-I. Ikeda, and Y. Maeno, “Ca<sub>2</sub>RuO<sub>4</sub>: New Mott Insulators of Layered Ruthenate”, *J. Phys. Soc. Japan* **66** (1997).
- [80] S. Nakatsuji, T. Ando, Z. Mao, and Y. Maeno, “Metal–insulator transition in Ca<sub>2–x</sub>Sr<sub>x</sub>RuO<sub>4</sub>”, *Phys. B* **259–261**, 949–950 (1999).
- [81] F. Nakamura, T. Goko, M. Ito, T. Fujita, S. Nakatsuji, H. Fukazawa, Y. Maeno, P. Alireza, D. Forsythe, and S. R. Julian, “From Mott insulator to ferromagnetic metal: A pressure study of Ca<sub>2</sub>RuO<sub>4</sub>”, *Phys. Rev. B* **65**, 220402 (2002).
- [82] F. Nakamura, M. Sakaki, Y. Yamanaka, S. Tamaru, T. Suzuki, and Y. Maeno, “Electric-field-induced metal maintained by current of the Mott insulator Ca<sub>2</sub>RuO<sub>4</sub>”, *Sci. Rep.* **3**, 2536 (2013).
- [83] C. Sow, S. Yonezawa, S. Kitamura, T. Oka, K. Kuroki, F. Nakamura, and Y. Maeno, “Current-induced strong diamagnetism in the Mott insulator Ca<sub>2</sub>RuO<sub>4</sub>”, *Science* **358**, 1084–1087 (2017).
- [84] H. H. Zhao, B. Hu, F. Ye, C. Hoffmann, I. Kimchi, and G. Cao, “Nonequilibrium orbital transitions via applied electrical current in calcium ruthenates”, *Phys. Rev. B* **100**, 241104 (2019).
- [85] R. Okazaki, Y. Nishina, Y. Yasui, F. Nakamura, T. Suzuki, and I. Terasaki, “Current-Induced Gap Suppression in the Mott Insulator Ca<sub>2</sub>RuO<sub>4</sub>”, *J. Phys. Soc. Japan* **82**, 103702 (2013).

- [86] J. Zhang, A. S. McLeod, Q. Han, X. Chen, H. A. Bechtel, Z. Yao, S. N. Gilbert Corder, T. Ciavatti, T. H. Tao, M. Aronson, G. L. Carr, M. C. Martin, C. Sow, S. Yonezawa, F. Nakamura, I. Terasaki, D. N. Basov, A. J. Millis, Y. Maeno, and M. Liu, “Nano-Resolved Current-Induced Insulator-Metal Transition in the Mott Insulator  $\text{Ca}_2\text{RuO}_4$ ”, *Phys. Rev. X* **9**, 011032 (2019).
- [87] G. Mattoni, S. Yonezawa, and Y. Maeno, “Diamagnetic-like response from localized heating of a paramagnetic material”, *Appl. Phys. Lett.* **116**, 172405 (2020).
- [88] K. Jenni, F. Wirth, K. Dietrich, L. Berger, Y. Sidis, S. Kunkemöller, C. P. Grams, D. I. Khomskii, J. Hemberger, and M. Braden, “Evidence for current-induced phase coexistence in  $\text{Ca}_2\text{RuO}_4$  and its influence on magnetic order”, *Phys. Rev. Mater.* **4**, 85001 (2020).
- [89] L. Berger, *Control of the metal insulator transition in calcium ruthenate by electric fields (BSc Thesis)* (2018).
- [90] F. Wirth, *Current induced metallic behaviour in  $\text{Ca}_2\text{RuO}_4$  (BSc Thesis)* (2019).
- [91] B. J. Campbell, S. K. Sinha, R. Osborn, S. Rosenkranz, J. F. Mitchell, D. N. Argyriou, L. Vasiliu-Doloc, O. H. Seeck, and J. W. Lynn, “Polaronic orbital polarization in a layered colossal magnetoresistive manganite”, *Phys. Rev. B* **67**, 020409 (2003).
- [92] E. Bascones, B. Valenzuela, and M. J. Calderon, “Magnetic interactions in iron superconductors: A review”, *Comptes Rendus Phys.* **17**, 36–59 (2016).
- [93] A. Gukasov, M. Braden, R. J. Papoular, S. Nakatsuji, Y. Maeno, and L. Le, “Anomalous Spin-Density Distribution on Oxygen and Ru in  $\text{Ca}_{1.5}\text{Sr}_{0.5}\text{RuO}_4$ : Polarized Neutron Diffraction Study”, *Phys. Rev. Lett.* **89**, 087202 (2002).
- [94] W. Voigt, “Über das Gesetz der Intensitätsverteilung innerhalb der Linien eines Gasspektrums”, *Sitzungsberichte* **25** (1912).
- [95] K. Momma and F. Izumi, “VESTA 3 for three-dimensional visualization of crystal, volumetric and morphology data”, *J. Appl. Crystallogr.* **44**, 1272–1276 (2011).
- [96] G. Shirane, Y. Endoh, R. J. Birgeneau, M. A. Kastner, Y. Hidaka, M. Oda, M. Suzuki, and T. Murakami, “Two-dimensional antiferromagnetic quantum spin-fluid state in  $\text{La}_2\text{CuO}_4$ ”, *Phys. Rev. Lett.* **59**, 1613–1616 (1987).
- [97] R. J. Birgeneau, M. Greven, M. A. Kastner, Y. S. Lee, B. O. Wells, Y. Endoh, K. Yamada, and G. Shirane, “Instantaneous spin correlations in  $\text{La}_2\text{CuO}_4$ ”, *Phys. Rev. B* **59**, 13788–13794 (1999).
- [98] J. Rodriguez-Carvajal, *Fullprof*.
- [99] G. Baskaran, “Why is  $\text{Sr}_2\text{RuO}_4$  not a high  $T_C$  superconductor? Electron correlation, Hund’s coupling and p-wave instability”, *Phys. B Condens. Matter* **223**, 490–495 (1996).
- [100] C. Kallin, “Chiral p-wave order in  $\text{Sr}_2\text{RuO}_4$ ”, *Reports Prog. Phys.* **75**, 42501 (2012).
- [101] A. P. Mackenzie and Y. Maeno, “The superconductivity of  $\text{Sr}_2\text{RuO}_4$  and the physics of spin-triplet pairing”, *Rev. Mod. Phys.* **75**, 657–712 (2003).

- [102] M. Yoshiteru, K. Shunichiro, N. Takuji, Y. Shingo, and I. Kenji, “Evaluation of Spin-Triplet Superconductivity in  $\text{Sr}_2\text{RuO}_4$ ”, *J. Phys. Soc. Japan* **81**, 11009 (2012).
- [103] C. W. Hicks, J. R. Kirtley, T. M. Lippman, N. C. Koshnick, M. E. Huber, Y. Maeno, W. M. Yuhasz, M. B. Maple, and K. A. Moler, “Limits on superconductivity-related magnetization in  $\text{Sr}_2\text{RuO}_4$  and  $\text{PrOs}_4\text{Sb}_{12}$  from scanning SQUID microscopy”, *Phys. Rev. B* **81**, 214501 (2010).
- [104] H. Murakawa, K. Ishida, K. Kitagawa, Z. Q. Mao, and Y. Maeno, “Measurement of the  $^{101}\text{Ru}$ -Knight Shift of Superconducting  $\text{Sr}_2\text{RuO}_4$  in a Parallel Magnetic Field”, *Phys. Rev. Lett.* **93**, 167004 (2004).
- [105] C. W. Hicks, D. O. Brodsky, E. A. Yelland, A. S. Gibbs, J. A. N. Bruin, M. E. Barber, S. D. Edkins, K. Nishimura, S. Yonezawa, Y. Maeno, and A. P. Mackenzie, “Strong Increase of  $T_C$  of  $\text{Sr}_2\text{RuO}_4$  Under Both Tensile and Compressive Strain”, *Science* **344**, 283–285 (2014).
- [106] A. Steppke, L. Zhao, M. E. Barber, T. Scaffidi, F. Jerzembeck, H. Rosner, A. S. Gibbs, Y. Maeno, S. H. Simon, A. P. Mackenzie, and C. W. Hicks, “Strong peak in  $T_c$  of  $\text{Sr}_2\text{RuO}_4$  under uniaxial pressure”, *Science* **355**, 6321 (2017).
- [107] M. E. Barber, F. Lechermann, S. V. Streltsov, S. L. Skornyakov, S. Ghosh, B. J. Ramshaw, N. Kikugawa, D. A. Sokolov, A. P. Mackenzie, C. W. Hicks, and I. I. Mazin, “Role of correlations in determining the Van Hove strain in  $\text{Sr}_2\text{RuO}_4$ ”, *Phys. Rev. B* **100**, 245139 (2019).
- [108] A. T. Rømer, A. Kreisel, M. A. Müller, P. J. Hirschfeld, I. M. Eremin, and B. M. Andersen, “Theory of strain-induced magnetic order and splitting of  $T_c$  and  $T_{\text{TRSB}}$  in  $\text{Sr}_2\text{RuO}_4$ ”, *Phys. Rev. B* **102**, 54506 (2020).
- [109] R. Sharma, S. D. Edkins, Z. Wang, A. Kostin, C. Sow, Y. Maeno, A. P. Mackenzie, J. C. S. Davis, and V. Madhavan, “Momentum-resolved superconducting energy gaps of  $\text{Sr}_2\text{RuO}_4$  from quasiparticle interference imaging”, *Proc. Natl. Acad. Sci.* **117**, 5222–5227 (2020).
- [110] V. Grinenko, R. Sarkar, K. Kihou, C. H. Lee, I. Morozov, S. Aswartham, B. Büchner, P. Chekhonin, W. Skrotzki, K. Nenkov, R. Hühne, K. Nielsch, S. L. Drechsler, V. L. Vadimov, M. A. Silaev, P. A. Volkov, I. Eremin, H. Luetkens, and H.-H. Klauss, “Superconductivity with broken time-reversal symmetry inside a superconducting s-wave state”, *Nat. Phys.* **16**, 789–794 (2020).
- [111] J. Xia, Y. Maeno, P. T. Beyersdorf, M. M. Fejer, and A. Kapitulnik, “High Resolution Polar Kerr Effect Measurements of  $\text{Sr}_2\text{RuO}_4$ : Evidence for Broken Time-Reversal Symmetry in the Superconducting State”, *Phys. Rev. Lett.* **97**, 167002 (2006).
- [112] I. Schnell, I. I. Mazin, and A. Y. Liu, “Unconventional superconducting pairing symmetry induced by phonons”, *Phys. Rev. B* **74**, 184503 (2006).
- [113] M. Braden, A. H. Moudden, S. Nishizaki, Y. Maeno, and T. Fujita, “Structural analysis of  $\text{Sr}_2\text{RuO}_4$ ”, *Phys. C Supercond.* **273**, 248–254 (1997).

- [114] M. Braden, W. Reichardt, Y. Sidis, Z. Mao, and Y. Maeno, “Lattice dynamics and electron-phonon coupling in  $\text{Sr}_2\text{RuO}_4$ : Inelastic neutron scattering and shell-model calculations”, *Phys. Rev. B* **76**, 014505 (2007).
- [115] T. Imai, A. W. Hunt, K. R. Thurber, and F. C. Chou, “ $^{17}\text{O}$  NMR Evidence for Orbital Dependent Ferromagnetic Correlations in  $\text{Sr}_2\text{RuO}_4$ ”, *Phys. Rev. Lett.* **81**, 3006–3009 (1998).
- [116] M. Braden, Y. Sidis, P. Bourges, P. Pfeuty, J. Kulda, Z. Mao, and Y. Maeno, “Inelastic neutron scattering study of magnetic excitations in  $\text{Sr}_2\text{RuO}_4$ ”, *Phys. Rev. B* **66**, 64522 (2002).
- [117] F. Servant, B. Faak, S. Raymond, J. P. Brison, P. Lejay, and J. Flouquet, “Magnetic excitations in the normal and superconducting states of  $\text{Sr}_2\text{RuO}_4$ ”, *Phys. Rev. B* **65**, 184511 (2002).
- [118] K. Iida, M. Kofu, N. Katayama, J. Lee, R. Kajimoto, Y. Inamura, M. Nakamura, M. Arai, Y. Yoshida, M. Fujita, K. Yamada, and S.-H. Lee, “Inelastic neutron scattering study of the magnetic fluctuations in  $\text{Sr}_2\text{RuO}_4$ ”, *Phys. Rev. B* **84**, 60402 (2011).
- [119] K. Iida, J. Lee, M. B. Stone, M. Kofu, Y. Yoshida, and S. Lee, “Two-Dimensional Incommensurate Magnetic Fluctuations in  $\text{Sr}_2\text{Ru}_{0.99}\text{Ti}_{0.01}\text{O}_4$ ”, *J. Phys. Soc. Japan* **81**, 124710 (2012).
- [120] J. P. Carlo, T. Goko, P. L. Russo, A. T. Savici, A. A. Aczel, G. J. Macdougall, J. A. Rodriguez, T. J. Williams, G. M. Luke, C. R. Wiebe, Y. Yoshida, S. Nakatsuji, Y. Maeno, T. Taniguchi, and Y. J. Uemura, “New magnetic phase diagram of  $(\text{Sr,Ca})_2\text{RuO}_4$ ”, *Nat. Mater.* **11**, 323–328 (2012).
- [121] J.-W. Huo, T. M. Rice, and F.-C. Zhang, “Spin Density Wave Fluctuations and p -Wave Pairing in  $\text{Sr}_2\text{RuO}_4$ ”, *Phys. Rev. Lett.* **110**, 167003 (2013).
- [122] K. Iida, M. Kofu, K. Suzuki, N. Murai, S. Ohira-Kawamura, R. Kajimoto, Y. Inamura, M. Ishikado, S. Hasegawa, T. Masuda, Y. Yoshida, K. Kakurai, K. Machida, and S. Lee, “Horizontal Line Nodes in  $\text{Sr}_2\text{RuO}_4$  Proved by Spin Resonance”, *J. Phys. Soc. Japan* **89**, 053702 (2020).
- [123] H. Mukuda, K. Ishida, Y. Kitaoka, K. Asayama, Z. Q. Mao, Y. Mori, and Y. Maeno, “ $^{17}\text{O}$  NMR probe of spin fluctuations in triplet superconductor  $\text{Sr}_2\text{RuO}_4$ ”, *Phys. B Condens. Matter* **259-261**, 944–946 (1999).
- [124] H. U. R. Strand, M. Zingl, N. Wentzell, O. Parcollet, and A. Georges, “Magnetic response of  $\text{Sr}_2\text{RuO}_4$ : Quasi-local spin fluctuations due to Hund’s coupling”, *Phys. Rev. B* **100**, 125120 (2019).
- [125] K. Jenni, S. Kunkemöller, P. Steffens, Y. Sidis, R. Bewley, Z. Q. Mao, Y. Maeno, and M. Braden, “Neutron scattering studies on spin fluctuations in  $\text{Sr}_2\text{RuO}_4$ ”, *Phys. Rev. B* **103**, 104511 (2021).
- [126] Q. Huang, J. L. Soubeyroux, O. Chmaissem, I. N. Sora, A. Santoro, R. J. Cava, J. J. Krajewski, and W. F. Peck, “Neutron powder diffraction study of the crystal structures of  $\text{Sr}_2\text{RuO}_4$  and  $\text{Sr}_2\text{IrO}_4$  at room temperature and at 10K”, *J. Solid State Chem.* **112**, 355–361 (1994).
- [127] I. I. Mazin and D. J. Singh, “Ferromagnetic Spin Fluctuation Induced Superconductivity in  $\text{Sr}_2\text{RuO}_4$ ”, *Phys. Rev. Lett.* **79**, 733–736 (1997).

- [128] N. Kikugawa, C. Bergemann, A. P. Mackenzie, and Y. Maeno, “Band-selective modification of the magnetic fluctuations in  $\text{Sr}_2\text{RuO}_4$ : A study of substitution effects”, *Phys. Rev. B* **70**, 134520 (2004).
- [129] M. Minakata and Y. Maeno, “Magnetic ordering in  $\text{Sr}_2\text{RuO}_4$  induced by non-magnetic impurities”, *Phys. Rev. B* **63**, 180504 (2001).
- [130] N. Baldauf, *Kristallzüchtung von  $\text{Sr}_2\text{Ru}_{1-x}\text{Co}_x\text{O}_4$  (BSc Thesis)*, November (2017), pp. 1–47.
- [131] F. Lichtenberg, “The story of  $\text{Sr}_2\text{RuO}_4$ ”, *Prog. Solid State Chem.* **30**, 103–131 (2002).
- [132] V. Petricek, M. Dusek, and L. Palatinus, “Crystallographic Computing System JANA2006: General features”, *Zeitschrift für Krist. - Cryst. Mater.* **229**, 345–352 (2014).
- [133] M. Zhu, K. V. Shanavas, Y. Wang, T. Zou, W. F. Sun, W. Tian, V. O. Garlea, A. Podlesnyak, M. Matsuda, M. B. Stone, D. Keavney, Z. Q. Mao, D. J. Singh, and X. Ke, “Non-Fermi surface nesting driven commensurate magnetic ordering in Fe-doped  $\text{Sr}_2\text{RuO}_4$ ”, *Phys. Rev. B* **95**, 2–7 (2017).
- [134] L. Walz and F. Lichtenberg, “Refinement of the Structure of  $\text{Sr}_2\text{RuO}_4$  with 100 and 295 K X-ray data”, *Acta Cryst.* **C49**, 1268–1270 (1993).
- [135] Z. Q. Mao, Y. Mori, and Y. Maeno, “Suppression of superconductivity in  $\text{Sr}_2\text{RuO}_4$  caused by defects”, *Phys. Rev. B* **60**, 610–614 (1999).
- [136] G. Dhanaraj, K. Byrappa, V. Prasad, and M. Dudley, *Springer Handbook of Crystal Growth* (2010), pp. 1–1855.
- [137] H. M. Rietveld, “A profile refinement method for nuclear and magnetic structures”, *J. Appl. Crystallogr.* **2**, 65–71 (1969).
- [138] C. G. Shull and J. S. Smart, “Detection of Antiferromagnetism by Neutron Diffraction”, *Phys. Rev.* **76**, 1256 (1950).
- [139] J. Chadwick, “Possible existence of a Neutron”, *Nature* **129**, 312 (1932).
- [140] B. N. Brockhouse and A. T. Stewart, “Scattering of Neutrons by Phonons in an Aluminum Single Crystal”, *Phys. Rev.* **100**, 756 (1955).
- [141] W. G. Marshall and S. W. Lovesey, *Theory of Thermal Neutron Scattering* (Oxford University Press, Oxford, 1971).
- [142] G. Squires, *Introduction to the theory of thermal neutron scattering* (Cambridge University Press, 1978).
- [143] G. Shirane, S. M. Shapiro, and J. M. Tranquada, *Neutron Scattering with a Triple-Axis Spectrometer* (Cambridge University Press, 2004).
- [144] T. Chatterji, *Neutron Scattering from Magnetic Materials* (Elsevier B.V., 2006).
- [145] M. Blume, “Polarization Effects in the Magnetic Elastic Scattering of Slow Neutrons”, *Phys. Rev.* **130**, 1670 (1963).
- [146] S. V. Maleev, “Polarization of Slow Neutrons scattered in Crystals”, *Sov. Phys. JETP* **34**, 10.7868/s0367676513090172 (1958).

- [147] A. W. Sáenz, “Magnetic Scattering of Neutrons by Exchange-Coupled Lattices”, *Phys. Rev.* **119**, 1543 (1960).
- [148] R. M. Moon, T. Riste, and W. C. Koehler, “Polarization Analysis of Thermal-Neutron Scattering”, *Phys. Rev.* **181**, 920 (1969).
- [149] A. Furrer, J. Mesot, and T. Strässle, *Neutron Scattering in Condensed Matter Physics (Neutron Techniques and Applications)* (World Scientific Publishing Company, 2009).
- [150] B. T. M. Willis and C. J. Carlile, *Experimental Neutron Scattering* (Oxford University Press, 2009).
- [151] R. Ewings, A. Buts, M. Le, J. van Duijn, I. Bustinduy, and T. Perring, “Horace : Software for the analysis of data from single crystal spectroscopy experiments at time-of-flight neutron instruments”, *Nucl. Instruments Methods Phys. Res. Sect. A Accel. Spectrometers, Detect. Assoc. Equip.* **834**, 132–142 (2016).



# Abstract

Unconventional Superconductivity is one of the most intriguing phenomena in condensed matter physics and is often the motivation of extensive research of certain material families. Such a material family is represented by the Ruddlesden-Popper ruthenates whose superconducting member  $\text{Sr}_2\text{RuO}_4$  pushed the discovery of other interesting physical phenomena in related ruthenates. The ruthenates provide a rich playground to investigate the interplay of electronic, magnetic and structural properties.

This thesis is a small contribution to the latest ruthenate research and a good example of the variety of fundamental concepts of condensed matter physics which the Ruddlesden-Popper ruthenates cover. It illustrates one complete journey of experimental work in condensed matter research: Beginning with the crystal growth of ruthenates, followed by the characterization of the crystals using different diffraction and transport methods, ending in complex neutron scattering studies at state-of-the-art research facilities. Main focus lays here on the neutron scattering techniques which are a versatile tool to study structural and magnetic properties and are used here to reveal the magnetic correlation in different members of the Ruddlesden-Popper ruthenate family.

The most substantial part of this work covers the magnetic excitations in the ferromagnetic  $\text{SrRuO}_3$  which are extensively studied in their  $Q$ -space dispersion and their temperature dependence revealing the entanglement of charge and spin degrees of freedom in this material. The anomalous temperature dependence of the spin dynamics are explained by the influence of Weyl points near the Fermi surface created by the combination of exchange splitting and spin-orbit coupling. Also basic concepts like the handedness of magnon in ferromagnets are tested. Theoretical predictions claim that the right handedness resulting from the universal commutation relation of spin components can be changed to left handedness under certain conditions involving spin-orbit coupling. Using a technically challenging experimental setup with polarized neutrons the proposed candidate for left-handed magnons  $\text{SrRuO}_3$  is studied and revealed only right-handed excitations in the ferromagnetic phase.

$\text{Ca}_2\text{RuO}_4$ , the counterpart of  $\text{Sr}_2\text{RuO}_4$  in the well known subclass of 214 ruthenates  $\text{Ca}_{2-x}\text{Sr}_x\text{RuO}_4$ , is studied in its structural and magnetic properties using X-ray and neutron scattering under the application of current. Motivated by reported experimental evidence of current-induced diamagnetism, which had to be retracted in the meantime, experimental efforts are made to identify a non-equilibrium phase which differs from the established metallic and insulating phases. The investigation indicate a phase coexistence of metallic and insulating phases in the material under current application. This phase coexistence has to be considered when discussing new non-equilibrium phases since the combination of metallic and insulating

phase could produce ambiguous experimental results. Furthermore the study of the magnetic correlations above the antiferromagnetic phase and the magnetic order in general confirm the two-dimensionality of the material while providing experimental evidence for the existence of magnetic moment on the apical oxygen position as a result of  $p$ - $d$  hybridization.

An investigation of the spin fluctuations in the superconductor  $\text{Sr}_2\text{RuO}_4$  itself using complementary neutron scattering techniques confirmed previous findings of the distribution of antiferromagnetic and quasi-ferromagnetic fluctuations in the in-plane  $Q$  space. The reported spin resonance confirming the horizontal line nodes model can not be found in our investigation of the out-of-plane components of the spin fluctuations. These results are of importance in the discussion of the superconducting pairing symmetry which after recent revisiting of the key experiments of the  $p$ -wave symmetry opened up again.

In the context of identifying the nature of magnetic fluctuations doping is a common tool to characterize such fluctuations when they are stabilized. Here samples of the  $\text{Sr}_2\text{Ru}_{1-y}\text{Co}_y\text{O}_4$  series reveal ferromagnetic order. However, this order is not found to be of long-range character which would be the case for stabilized ferromagnetic fluctuations in the parent compound. One origin of the short-range ferromagnetic order can be inhomogeneities in the sample forming magnetic Co clusters.

# Kurzzusammenfassung

Unkonventionelle Supraleitung ist eine der faszinierendsten Phänomene in der Festkörperphysik und ist oft Motivation für umfangreiche Forschung an bestimmten Materialfamilien. Eine solche Materialfamilie sind die Ruddlesden-Popper Ruthenate, wessen supraleitendes Mitglied  $\text{Sr}_2\text{RuO}_4$  die Entdeckung anderer interessanter physikalischer Phänomene in verwandten Ruthenaten förderte. Die Ruthenate bieten fruchtbaren Boden, um das Zusammenspiel von elektronischen, magnetischen und strukturellen Eigenschaften zu untersuchen.

Diese Arbeit ist ein kleiner Beitrag zur aktuellen Ruthenat-Forschung und ein gutes Beispiel für die Vielfalt an fundamentalen Konzepten der Festkörperphysik, die die Ruddlesden-Popper Ruthenate abdeckt. Sie veranschaulicht einen vollständigen Weg der experimentellen Arbeit in der Festkörperphysik-Forschung: Angefangen bei der Kristallzucht von Ruthenaten, über die Charakterisierung der Kristalle mit Hilfe von Transport- und Diffraktionsexperimenten, bis hin zu Neutronenstreuexperimenten an modernen Forschungsinstituten. Das Hauptaugenmerk liegt hier auf den Neutronenstreutechniken, welche ein vielseitiges Werkzeug zur Untersuchung von strukturellen und magnetischen Eigenschaften sind und welche hier benutzt werden, um die magnetischen Korrelationen in verschiedenen Mitgliedern der Ruddlesden-Popper Ruthenat-Familie zu enthüllen.

Der Großteil dieser Arbeit beschäftigt sich mit den magnetischen Anregungen im ferromagnetischen  $\text{SrRuO}_3$ , die umfangreich in ihrer  $Q$ -Raum Dispersion und ihrer Temperaturabhängigkeit untersucht werden. Dabei legen sie die Verknüpfung von magnetischen und elektronischen Freiheitsgraden in diesem Material offen. Die anormale Temperaturabhängigkeit der Spin-Dynamik lassen sich mit dem Einfluss von Weyl-Punkten nahe der Fermi-Fläche erklären, die durch die Kombination von Austauschwechselwirkung und Spin-Bahn-Kopplung entstehen. Ebenfalls grundlegende Konzepte wie die Händigkeit von Magnonen in einem Ferromagneten werden getestet. Theoretische Vorhersagen behaupten, dass die Rechtshändigkeit, die aus der universellen Kommutator-Beziehung der Spin-Komponenten resultiert, unter gewissen Bedingungen, wie z.B. Spin-Bahn-Kopplung, zur Linkshändigkeit umgewandelt werden kann. Der von der Theorie vorgeschlagene Kandidat für linkshändige Magnonen  $\text{SrRuO}_3$  wird mit Hilfe eines technisch herausfordernden experimentellen Aufbaus mit polarisierten Neutronen untersucht und zeigt nur rechtshändige Anregungen in der ferromagnetischen Phase.

Der Einfluss von Strom auf die strukturellen und magnetischen Eigenschaften von  $\text{Ca}_2\text{RuO}_4$ , dem Gegenstück zu  $\text{Sr}_2\text{RuO}_4$  in der bekannten 214-Unterklasse der Ruthenate  $\text{Ca}_{2-x}\text{Sr}_x\text{RuO}_4$ , wird mit Hilfe von Röntgen- und Neutronenstreuung untersucht. Motiviert von mittlerweile zurückgezogenen experimentellen Ergebnissen für Strom induzierten Diamagnetismus, werden experimentelle Anstrengungen gemacht, um eine Ungleichgewichtsphase zu identifizieren, die sich von den

etablierten metallischer und isolierender Phasen unterscheidet. Die Untersuchung deutet eine Phasenkoexistenz der metallischen und isolierenden Phase unter Strom an. Diese Phasenkoexistenz muss berücksichtigt werden, wenn Ungleichgewichtsphasen diskutiert werden, da die Kombination von metallischer und isolierender Phase zu mehrdeutigen Ergebnissen führen kann. Außerdem bestätigt die Untersuchung der magnetischen Korrelationen oberhalb der Ordnungstemperatur und der magnetischen Ordnung im Allgemeinen die Zweidimensionalität des Materials während sie experimentelle Beweise für magnetisches Moment auf der Position des apikalen Sauerstoffes als Ergebnis einer  $p-d$ -Hybridisierung liefert.

Eine Untersuchung der Spin-Fluktuationen im Supraleiter  $\text{Sr}_2\text{RuO}_4$  mit Hilfe von komplementären Neutronenstreutechniken bestätigt vorherige Ergebnisse von antiferromagnetischen und quasiferromagnetischen Fluktuationen im  $Q$ -Raum parallel zu den zweidimensionalen  $\text{RuO}_2$ -Schichten. Der Bericht über eine Spin-Resonanz, die ein Modell mit horizontalen Knotenlinien bestätigen würde, konnte durch unsere Untersuchung der Spin-Fluktuationskomponenten senkrecht zu den  $\text{RuO}_2$ -Schichten nicht bestätigt werden. Diese Ergebnisse sind wichtig für die Diskussion über die Symmetrie der Bildung der supraleitenden Paare, die nach aktuellen erneuten Durchführung der Schlüsselexperimente für das Szenario der  $p$ -Symmetrie wieder offen ist.

Im Kontext des Identifizierens der Natur der magnetischen Fluktuationen ist Dotieren eine verbreitete Methode, um solche Fluktuationen zu stabilisieren und zu untersuchen. Proben der  $\text{Sr}_2\text{Ru}_{1-y}\text{Co}_y\text{O}_4$  Serie zeigen eine statische ferromagnetische Ordnung. Allerdings besitzt diese Ordnung keine langreichweitigen Charakter, der für stabilisierte ferromagnetische Fluktuationen im Supraleiter  $\text{Sr}_2\text{RuO}_4$  zu erwarten wäre. Eine mögliche Ursache der kurzreichweitigen ferromagnetischen Ordnung können Inhomogenitäten in den Proben sein, die sich zu magnetischen Co Clustern formieren.

# List of Publications

## Publications included in thesis

- **K. Jenni**, S. Kunkemöller, D. Brüning, T. Lorenz, Y. Sidis, A. Schneidewind, A. A. Nugroho, A. Rosch, D. I. Khomskii, M. Braden, "Interplay of Electronic and Spin Degrees in Ferromagnetic SrRuO<sub>3</sub>: Anomalous Softening of the Magnon Gap and Stiffness", *Physical Review Letters* 123, 017202 (2019).  
<https://doi.org/10.1103/PhysRevLett.123.017202>
- **K. Jenni**, F. Wirth, K. Dietrich, L. Berger, Y. Sidis, S. Kunkemöller, C.P. Grams, D.I. Khomskii, J. Hemberger, M. Braden, "Evidence for current-induced phase coexistence in Ca<sub>2</sub>RuO<sub>4</sub> and its influence on magnetic order", *Physical Review Materials* 4, 085001 (2020).  
<https://doi.org/10.1103/PhysRevMaterials.4.085001>
- **K. Jenni**, S. Kunkemöller, P. Steffens, Y. Sidis, R. Bewley, Z.Q. Mao, Y. Maeno, M. Braden, "Neutron scattering studies on spin fluctuations in Sr<sub>2</sub>RuO<sub>4</sub>", *Physical Review B* 103, 104511 (2021).  
<https://doi.org/10.1103/PhysRevB.103.104511>

## Further publications

- S. Kunkemöller, **K. Jenni**, D. Gorkov, A. Stunault, S. Streltsov, M. Braden, "Magnetization density distribution in the metallic ferromagnet SrRuO<sub>3</sub> determined by polarized neutron diffraction", *Physical Review B* 100, 054413 (2019).  
<https://doi.org/10.1103/PhysRevLett.123.017202>

The following publications result from work and results connected to my diploma thesis at Technical University of Kaiserslautern:

- **K. Jenni**, L. Scherthan, I. Faus, J. Marx, C. Strohm, M. Herlitschke, H.-C. Wille, P. Würtz, V. Schünemann, J.A. Wolny, "Nuclear inelastic scattering and density functional theory studies of a one-dimensional spin crossover [Fe(1,2,4-triazole)<sub>2</sub>(1,2,4-triazolato)](BF<sub>4</sub>) molecular chain", *Physical Chemistry Chemical Physics* 19, 18880-18889 (2017).  
<https://doi.org/10.1039/C7CP03690F>

- J.A. Wolny, T. Hochdörffer, S. Sadashivaiah, H. Auerbach, **K. Jenni**, L. Scherthan, A. Li, C. von Malotki, H.-C. Wille, E. Rentschler, V. Schünemann, "Vibrational properties of 1D and 3D polynuclear spin crossover Fe(II) urea-triazoles polymer chains and quantification of intrachain cooperativity", *Journal of Physics: Condensed Matter* 33, 034004 (2020).  
<https://doi.org/10.1088/1361-648X/aba71d>
- S. Sadashivaiah, J. A. Wolny, L. Scherthan, **K. Jenni**, A. Omlor, C. S. Müller, I. Sergueev, M. Herlitschke, O. Leupold, H.-C. Wille, R. Röhlberger, V. Schünemann, "High-Repetition Rate Optical Pump–Nuclear Resonance Probe Experiments Identify Transient Molecular Vibrations after Photoexcitation of a Spin Crossover Material", *The Journal of Physical Chemistry Letters* 12, 3240-3245 (2021).  
<https://doi.org/10.1021/acs.jpcllett.0c03733>

# Danksagung

An dieser Stelle möchte ich mir Zeit nehmen und mich bei den Menschen bedanken, die einen essentiellen Teil, ob inhaltlich oder motivierend, zu dieser Arbeit beigetragen und mich auf meinem Weg begleitet haben. Ohne die Möglichkeit der aktiven Forschung ist eine solche Arbeit natürlich nicht umsetzbar, weshalb mein Dank zuerst Prof. Dr. Markus Braden für die Chance und das in mich gesetzte Vertrauen gilt, als Teil seiner Arbeitsgruppe die Neutronenstreuung kennen und schätzen zu lernen. Natürlich möchte ich mich auch für seine Betreuung und Unterstützung im Rahmen dieser Arbeit bedanken. Dafür geht mein Dank auch an Prof. Dr. Markus Grüninger und Prof. Dr. Simon Trebst, die sich bereit erklärt haben, als Mitglieder der Prüfungskommission meine Arbeit zu beurteilen.

Ich habe die abwechslungsreiche und herausfordernde Zusammenarbeit, die die internationale Neutronenforschung bietet, stets genossen. Der Austausch mit zahlreichen Wissenschaftlern auf Messreisen und Konferenzen war für mich immer ein großer Pluspunkt meiner Arbeit. Hier möchte ich mich bei Paul Steffens, Yvan Sidis, Wolfgang Schmidt und Astrid Schneidewind für die herausragende Betreuung eines Großteils meiner Experimente an den jeweiligen Forschungsinstituten bedanken. Auch die KollegInnen des Instituts und die der Arbeitsgruppe im Speziellen haben einen großen Beitrag am Abschluss dieser Arbeit. Besonderer Dank gilt hier Stefan Kunkemöller, von dem ich die Ruthenat-Forschung geerbt habe, und Florian Waßer, die mir beide den Einstieg in ein neues Thema erleichtert haben. Ich möchte mich auch bei meinen direkten Bürokollegen vom Büro 208, Sebastian Biesenkamp, Philipp Warzanowski und David Maluski, bedanken, mit denen ich sowohl im, als auch außerhalb des Büros viel Spaß hatte.

Gruß und Dank geht ebenfalls an die Arbeitsgruppe von Prof. Dr. Volker Schünemann an der Technischen Universität Kaiserslautern, in der ich während meiner Diplomarbeit die Begeisterung am experimentellen Arbeiten gefunden habe und auch schon dort in den internationalen Forschungsbetrieb an Großforschungsanlagen hineinschnuppern konnte.

Natürlich möchte ich auch meiner Familie danken, die mir stets mit Rat und Tat beiseite steht. Auch wenn ich während der letzten Phase der Promotion vor allem bei meiner Schwester viel Frust verursacht habe, bin ich froh, dass ich bei meiner Familie einen Ort der Unterstützung und des offenen Ohrs habe.

Abschließend möchte ich der wichtigsten Person danken, die wohl auch am meisten, vor allem in der (zu langen) Schreibphase, unter der Promotion hat leiden müssen. Vielen Dank für deine Unterstützung, Sara. Es ist mir unerklärlich, wie du es mit mir ausgehalten hast, und ich kann mich unendlich glücklich schätzen, dich in meinem Leben zu wissen.



# Erklärung

Hiermit versichere ich an Eides statt, dass ich die vorliegende Dissertation selbstständig und ohne die Benutzung anderer als der angegebenen Hilfsmittel und Literatur angefertigt habe. Alle Stellen, die wörtlich oder sinngemäß aus veröffentlichten und nicht veröffentlichten Werken dem Wortlaut oder dem Sinn nach entnommen wurden, sind als solche kenntlich gemacht. Ich versichere an Eides statt, dass diese Dissertation noch keiner anderen Fakultät oder Universität zur Prüfung vorgelegen hat; dass sie - abgesehen von unten angegebenen Teilpublikationen und eingebundenen Artikeln und Manuskripten - noch nicht veröffentlicht worden ist sowie, dass ich eine Veröffentlichung der Dissertation vor Abschluss der Promotion nicht ohne Genehmigung des Promotionsausschusses vornehmen werde. Die Bestimmungen dieser Ordnung sind mir bekannt. Darüber hinaus erkläre ich hiermit, dass ich die Ordnung zur Sicherung guter wissenschaftlicher Praxis und zum Umgang mit wissenschaftlichem Fehlverhalten der Universität zu Köln gelesen und sie bei der Durchführung der Dissertation zugrundeliegenden Arbeiten und der schriftlich verfassten Dissertation beachtet habe und verpflichte mich hiermit, die dort genannten Vorgaben bei allen wissenschaftlichen Tätigkeiten zu beachten und umzusetzen. Ich versichere, dass die eingereichte elektronische Fassung der eingereichten Druckfassung vollständig entspricht.

Teilpublikationen:

- K. Jenni, S. Kunkemöller, D. Brüning, T. Lorenz, Y. Sidis, A. Schneidewind, A. A. Nugroho, A. Rosch, D. I. Khomskii, M. Braden, "Interplay of Electronic and Spin Degrees in Ferromagnetic SrRuO<sub>3</sub>: Anomalous Softening of the Magnon Gap and Stiffness", Physical Review Letters 123, 017202 (2019). <https://doi.org/10.1103/PhysRevLett.123.017202>
- K. Jenni, F. Wirth, K. Dietrich, L. Berger, Y. Sidis, S. Kunkemöller, C.P. Grams, D.I. Khomskii, J. Hemberger, M. Braden, "Evidence for current-induced phase coexistence in Ca<sub>2</sub>RuO<sub>4</sub> and its influence on magnetic order", Physical Review Materials 4, 085001 (2020). <https://doi.org/10.1103/PhysRevMaterials.4.085001>

- K. Jenni, S. Kunkemöller, P. Steffens, Y. Sidis, R. Bewley, Z.Q. Mao, Y. Maeno, M. Braden, "Neutron scattering studies on spin fluctuations in  $\text{Sr}_2\text{RuO}_4$ ", Physical Review B 103, 104511 (2021).  
<https://doi.org/10.1103/PhysRevB.103.104511>

Köln, den 04.10.2021

Kevin Jenni

